

Pyrylium and Pyridinium Fluorescent Probes for pH Sensing and Imaging in Live Cells

By

Sandip Chakraborty

10CC17A39001

A thesis submitted to the
Academy of Scientific and Innovative Research
for the award of the degree of
DOCTOR OF PHILOSOPHY
in
SCIENCE

Under the supervision of
Prof. A. AJAYAGHOSH



**CSIR-National Institute for Interdisciplinary Science and Technology (CSIR-NIIST)
Thiruvananthapuram – 695 019**



**Academy of Scientific and Innovative Research
AcSIR Headquarters, CSIR-HRDC Campus
Sector 19, Kamla Nehru Nagar,
Ghaziabad, Uttar Pradesh – 201 002, India**

October 2021

*Dedicated to Everybody who
Believed in Me*



राष्ट्रीय अंतर्विषयी विज्ञान तथा प्रौद्योगिकी संस्थान
वैज्ञानिक तथा औद्योगिक अनुसंधान परिषद्
इंडस्ट्रियल इस्टेट पी.ओ., पाप्पनकोड, तिरुवनंतपुरम, भारत-695 019
CSIR-NATIONAL INSTITUTE FOR INTERDISCIPLINARY SCIENCE & TECHNOLOGY (CSIR-NIIST)
Council of Scientific & Industrial Research
Industrial Estate P.O., Pappanamcode, Thiruvananthapuram, India-695 019

डॉ. ए. अजयघोष एफएनए, एफटीडब्ल्यूएस
निदेशक



Dr. A. Ajayaghosh FNA, FTW
Director

22-10-2021

CERTIFICATE

*This is to certify that the work incorporated in this Ph. D. thesis entitled, “**Pyrylium and Pyridinium Fluorescent Probes for pH Sensing and Imaging in Live Cells**”, submitted by Mr. Sandip Chakraborty to the Academy of Scientific and Innovative Research (AcSIR) in partial fulfilment of the requirements for the award of the **Degree of Doctor of Philosophy in Sciences**, embodies original research work carried out by the student. We further certify that this work has not been submitted to any other University or Institution in part or full for the award of any degree or diploma. Research materials obtained from other sources and used in this research work have been duly acknowledged in the thesis. Images, illustrations, figures, tables etc., used in the thesis from other sources, have also been duly cited and acknowledged.*

Sandip Chakraborty
Sandip Chakraborty 22/10/21

A. Ajayaghosh
22-10-2021
A. Ajayaghosh
(Thesis Supervisor)

STATEMENTS OF ACADEMIC INTEGRITY

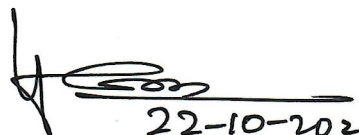
I Sandip Chakraborty, a Ph. D. student of the Academy of Scientific and Innovative Research (AcSIR) with Registration No. 10CC17A39001 hereby undertake that, the thesis entitled “**Pyrylium and Pyridinium Fluorescent Probes for pH Sensing and Imaging in Live Cells**” has been prepared by me and that the document reports original work carried out by me and is free of any plagiarism in compliance with the UGC Regulations on “*Promotion of Academic Integrity and Prevention of Plagiarism in Higher Educational Institutions (2018)*” and the CSIR Guidelines for “*Ethics in Research and in Governance (2020)*”.


Sandip Chakraborty 22/10/21

October 22nd, 2021

Thiruvananthapuram

It is hereby certified that the work done by the student, under my supervision, is plagiarism-free in accordance with the UGC Regulations on “*Promotion of Academic Integrity and Prevention of Plagiarism in Higher Educational Institutions (2018)*” and the CSIR Guidelines for “*Ethics in Research and in Governance (2020)*”.


22-10-2021
Prof. A. Ajayaghosh

October 22nd, 2021

Thiruvananthapuram

DECLARATION

I, Sandip Chakraborty, bearing AcSIR Registration No. 10CC17A39001 declare that my thesis entitled, “**Pyrylium and Pyridinium Fluorescent Probes for pH Sensing and Imaging in Live Cells**” is plagiarism free in accordance with the UGC Regulations on “*Promotion of Academic Integrity and Prevention of Plagiarism in Higher Educational Institutions (2018)*” and the CSIR Guidelines for “*Ethics in Research and in Governance (2020)*”.

I would be solely held responsible if any plagiarised content in my thesis is detected, which is violative of the UGC regulations 2018.


Sandip Chakraborty 24/10/21

October 22nd, 2021

Thiruvananthapuram

ACKNOWLEDGEMENTS

It is with great pleasure that I extend my deep sense of gratitude to Prof. A. Ajayaghosh, my thesis supervisor and Director of CSIR-National Institute for Interdisciplinary Science and Technology (CSIR-NIIST), Thiruvananthapuram, for suggesting the research problem, for his valuable guidance, support, motivation, encouragement and providing the necessary facilities, leading to the successful completion of this work.

I would like to express my gratitude to late Prof. M. V. George for being an inspiration.

My sincere thanks are also due to:

- ✓ Dr. Sreejith Shankar, Senior Scientist (CSTD) and Dr. Animesh Samanta, former Ramanujan Fellow (CSIR-NIIST) for their support, guidance, motivation and fruitful discussion throughout my Ph. D. work.
- ✓ Dr. V. Karunakaran, Dr. C. H. Suresh, and Dr. R. Luxmi Varma present and former AcSIR co-ordinators.
- ✓ Dr. Joshy Joseph, Dr. Kaustabh Kumar Maiti and Dr. Raghu K. G., Doctoral Advisory Committee (DAC) members and the whole AcSIR faculty for the successful completion of the course work.
- ✓ Dr. P. Sujatha Devi, Dr. R. Luxmi Varma present and former Heads of the Chemical Sciences and Technology Division (CSTD).
- ✓ Dr. V. K. Praveen, Dr. J. D. Sudha, Dr. Rakesh K. Mishra, Dr. Sunil Varughese, Dr. Jubi John, for their support and discussion.
- ✓ Dr. K. R. Gopidas, Dr. K. N. Narayanan Unni, Dr. Vijayakumar C., Dr. Biswapriya Deb, Dr. K. Yoosaf, Dr. Suraj Soman, Dr. Ishita Neogi, Dr. Adersh Asok, and Dr. Manas Panda present and former scientists of the Photosciences and Photonics Section, for their help and support.
- ✓ Mr. Chandrakanth C. K., Mr. Kiran J. S., Mr. Robert Philip and Mr. Vishnu Gurjar for general help.
- ✓ Mrs. Saumini Matthew, for NMR, Mrs. Viji S. for mass spectral analyses, Dr. Manu. M. Joseph, Dr. Anivind Kaur Bindra and Prof. Yanli Zhao for cellular studies.
- ✓ Ms. Shamna, Ms. Praveena, Ms. Sreedhaniya, Mr. Arumay and Ms. Persis for their support.

- ✓ Dr. Rahul Dev Mukhopadhyay, Dr. Samrat Ghosh, Dr. Sudheesh K. V., Dr. Satyajit Das, Dr. Saranya Giridharan, Dr. Gourab Das for their support and advice.
- ✓ Dr. Sandeep A., Dr. Vishnu S. Nair, Dr. Divya Susan Philips, Dr. Sandeep C., Dr. Arindam Mal, Dr. Mohamed Hifsudheen B. M., Mr. S. Vijayakumar, Ms. Anjali N., Ms. Indulekha M., Mr. S. Lingamoorthy, Mr. Dipak Patra, Ms. Anagha Thomas, Ms. Priyanka A. S., Ms. Lekshmi L., former and present group members for their help and cooperation.
- ✓ Mr. Sourava C. Pradhan, Mr. Soumallya Banerjee, Mr. Subrata Munan, my roommates.
- ✓ Former and present members of CSTD and friends at CSIR-NIIST, for their help and support.
- ✓ All my teachers for their encouragement at different stages of my academic career.
- ✓ DST-INSPIRE for Research fellowship.

I am deeply and forever grateful to my parents, brother and other family members for their constant source of love, inspiration and blessings. Finally, I would like to thank my friends and relatives for their excellent support and encouragement.

Sandip Chakraborty

TABLE OF CONTENTS

Certificate		i
Statements of Academic Integrity		ii
Declaration		iii
Acknowledgements		iv
Table of Contents		vi
List of Abbreviations		ix
Preface		xii
CHAPTER 1	Fluorescent Probes for pH Sensing and Imaging in Biological Systems	1-49
1.1	Abstract	1
1.2	Introduction	2
1.3	Historical Perspective of pH and pH Indicators	3
1.4	Role of pH in Cellular System	6
1.5	Bioimaging using pH Probes	8
1.6	Fluorescence Imaging	9
1.7	Fluorescent pH Imaging Probes	10
1.8	ON-OFF pH probes	18
1.8.1	Turn-ON pH Probes	18
1.8.2	Turn-OFF pH Probes	25
1.9	Ratiometric pH probe	28
1.10	Development of Novel Fluorescent Cores	34
1.11	Origin, Objectives and Organization of the Thesis	42
1.12	References	44
CHAPTER 2	A New Pentacyclic Pyrylium Probe with Distinct Fluorescence Response to pH Imbalance during Apoptosis	50-89
2.1	Abstract	50
2.2	Introduction	51
2.3	Results and Discussion	57
2.3.1	Synthesis of PS Derivatives	57
2.3.2	Photophysical Studies	61
2.3.3	Aqueous Solubility	64

2.3.4	pH Response and Calculation of pKa	65
2.3.5	Theoretical Calculations	67
2.3.6	Response Time and Reversibility	68
2.3.7	Selectivity of PS-OH towards H ⁺	69
2.3.8	Biocompatibility and Photostability	70
2.3.9	Intracellular pH Response and <i>In-vitro</i> pH Quantification	72
2.3.10	Dynamic pH Quantification during Apoptosis	75
2.4	Conclusions	77
2.5	Experimental Section: Synthesis	77
2.6	Description on Experimental Techniques	83
2.7	References	85
CHAPTER 3	Single Excitation Ratiometric Pyridinium pH probe for Lysosomal Autophagy monitoring in Real-Time	90-131
3.1	Abstract	90
3.2	Introduction	91
3.3	Results and Discussion	99
3.3.1	Synthesis of the Pyridinium Derivatives	99
3.3.2	Photophysical Studies	101
3.3.3	pH Response and Calculation of pKa	105
3.3.4	pH Reversibility and Selectivity	110
3.3.5	Biocompatibility and Photostability	111
3.3.6	Colocalization Experiment	113
3.3.7	Intracellular pH Response	117
3.3.8	Autophagy Monitoring Through pH Change	118
3.4	Conclusions	120
3.5	Experimental Section: Synthesis	121
3.6	Description on Experimental Techniques	124
3.7	References	128
CHAPTER 4	A Pyridinium Fluorophore for pH-assisted ‘Three-in-one’ Imaging of Heat Shock in Endoplasmic Reticulum	132-210
4.1	Abstract	174

4.2	Introduction	133
4.3	Results and Discussion	143
4.3.1	Synthesis of the Pyridinium Derivatives	143
4.3.2	Photophysical Studies	144
4.3.3	pH Response, Calculation of pKa and Microscope Compatibility	146
4.3.4	Photo and Thermal Stabilities	150
4.3.5	Reversibility and Selectivity	152
4.3.6	Biocompatibility, Colocalization and Intracellular Photostability	153
4.3.7	<i>In-vitro</i> pH Response	157
4.3.8	pH Changes during Heat Shock	158
4.4	Conclusions	162
4.5	Experimental Section: Synthesis	164
4.6	Description on Experimental Techniques	168
4.7	References	171
	Abstract of the Thesis	175
	List of Publications	176
	List of Conference Presentations	177

List of Abbreviations

A549	Adenocarcinoma human alveolar basal epithelial cells
ABIR	One-dimensional
ACQ	Aggrigation Caused Quenching
AG5	Two-dimensional
AIE	Aggrigation Induced Emission
ATCC	Atomic force microscopy
ATP	Adenosine Triphosphate
BAF-A1	Bafilomycin A1
BODIPY	4,4-difluoro-4-bora-3a-4a-diaza-s-indacene
BSA	Bovine Serum Albumin
CCCP	<i>m</i> -chlorophenyl hydrazone
CLSM	Confocal Laser Scanning Microscopy
cm	Centimeter
cRGD	Chitosan
CT	Computed Tomography
Cys	Cystine
D-A-D	Donor-Acceptor-Donor
DBU	1,8-Diazabicyclo [5.4.0] undec-7-ene
DMEM	Dulbecco's Modified Eagle Medium
DMF	<i>N, N</i> -Dimethylformamide
DMSO	Dimethyl sulfoxide
DNA	Deoxyribonucleic Acid
EPR	Electron paramagnetic resonance
equiv.	Equivalent
ER	Endoplasmic Reticulum
ESIPT	Excited-state intramolecular proton-transfer
FRET	Förster resonance energy transfer
g	Gram
GFP	Green Fluorescent Protein
GSH	Glutathione
h	Hour

Hcy	Homocysteine
HepG2	liver hepatocellular carcinoma cells
Hg	Mercury
HL-7702	Hepatic immortal cell line
HOMO	Highest occupied molecular orbital
HRMS	High resolution mass spectrometry
HSA	Instrument response function
H ₂ O ₂	Hydrogen Peroxide
ICT	Intramolecular Charge Transfer
LCMS	Liquid Chromatography–mass Spectrometry
LPA	α -lipoic acid
LPS	lipopolysaccharide
LTR	Lysotracker Red
LUMO	Lowest unoccupied molecular orbital
M	Molar
mm	Millimetre
MCF-7	Human breast cancer cells
MDA-MB-231	Epithelial human breast cancer cells
MHz	Mega hertz
min	Minute
mL	Millilitre
mmol	Millimole
MMP	Mitochondrial Membrane Potential
mol	Mole
MRC-5	Diploid human cell culture line
MTR	Mitotracker Red
MTT	3-(4,5-dimethylthiozoly-2)-2,5-diphenyltetrazolium bromide
NAC	<i>N</i> -Acetyl-L-cysteine
NAD(P)H	Nicotinamide adenine dinucleotide phosphate
NEM	<i>N</i> -ethyl maleimide
NIR	Near-infrared
nm	Nanometre
NMR	Nuclear magnetic resonance

NP	Nanoparticle
NOC13	1-hydroxy-2-oxo-3-(3-amino-propyl)-3-methyl-1-triazene
NTR	Nitroreductase
PA	<i>p</i> -Phenyleneethynylene
PBS	Phosphate buffer saline
PET	Photoinduced electron transfer
pH	Hydrogen ion concentration at logarithmic scale
pH _i	Intracellular hydrogen ion concentration at logarithmic scale
pKa	Acid dissociation constant at logarithmic scale
s	Second
t	Time
T	Temperature
TEMPO	Time Correlated Single Photon Counting
TFA	Trifluoroacetic acid
TICT	Twisted Intramolecular Charge Transfer
TLC	Thin layer chromatography
TMS	Tetramethyl silane
TPE	Tetraphenyl ethylene
UV	Ultra-violet
vis	Visible
WI- 38	Wide angle X-ray scattering
XRD	X-ray diffraction
Å	Angstrom
°C	Degree Celsius
Φ_F	Fluorescence quantum yield
λ	Wavelength
λ_{abs}	Wavelength of absorption
λ_{em}	Wavelength of emission
λ_{ex}	Wavelength of excitation
λ_{max}	Wavelength of maximum intensity
µm	Micrometre
µL	Microliter
µM	Micromolar

PREFACE

Non-invasive, reliable, ultrasensitive and low-cost fluorescent sensors have been an effective tool for early-stage disease diagnosis and therapeutic management. Moreover, these sensors have revolutionized the understanding of cellular dynamics in real-time. From elucidating the mechanistic pathways behind various biological processes to tracking cellular abnormalities, fluorescent probes have made biological sensing and imaging simpler, efficient and accurate. pH is one among the most critical cellular parameters and fluorescent sensors have allowed to accurately quantify the pH of various cellular compartments, leading to timely detection of abnormalities by tracking unusual changes in pH at sub-cellular levels. Furthermore, pH probes are being used extensively in screening anti-cancer drugs and monitoring drug efficacy towards personalized cancer therapy. Applications of fluorescent sensors, particularly in bio-imaging, have led to a huge demand for new fluorescent cores as a platform for sensor development. In the present thesis, an overview of various chemical tools to measure pH and the recent progress in fluorescent pH sensors for imaging applications is given. Also, a brief discussion on polycyclic pyrylium and pyridinium molecules as an emerging fluorescent core is provided.

The body of the thesis describes the work carried out in the design, synthesis and studies pertaining to new pyrylium and pyridinium fluorescent probes. We developed a new route for the synthesis of a pentacyclic symmetric pyrylium fluorophore (**PS-OMe**) using a modified Vilsmeier-Haack formylation reaction and proposed the corresponding mechanism.¹ Using this mechanistic understanding, we established an alternative synthesis protocol for **PS-OMe**, with improved yield and reduced reaction

time. We also prepared an ‘ON-OFF’ pH sensor **PS-OH** with excellent sensitivity around the cytosolic pH (7.4), and a 55-fold enhancement in fluorescence intensity between pH 7.4 ($\Phi_F = 0.03$) and 4.0 ($\Phi_F = 0.11$). The probe’s high sensitivity and selectivity in cytosolic pH range was used to monitor minute acidification in cells and related pH dynamics during induced apoptosis.

Conversion of the pyrylium fluorophore into its pyridinium analogs resulted in improved photophysical properties, photostability and ratiometric fluorescence response to changes in pH. Also, the pyridinium chromophores bearing hexyl chains (**PM-C₆** and **PM-C₆-OH**) exhibited lysosomal accumulation without creating any alkalizing effect.² The large Stokes shift of **PM-C₆-OH** further allowed single and multiple excitation ratiometric response. Finally, we used **PM-C₆-OH** to monitor autophagy at sub-cellular levels by monitoring lysosomal pH changes accompanying this process.

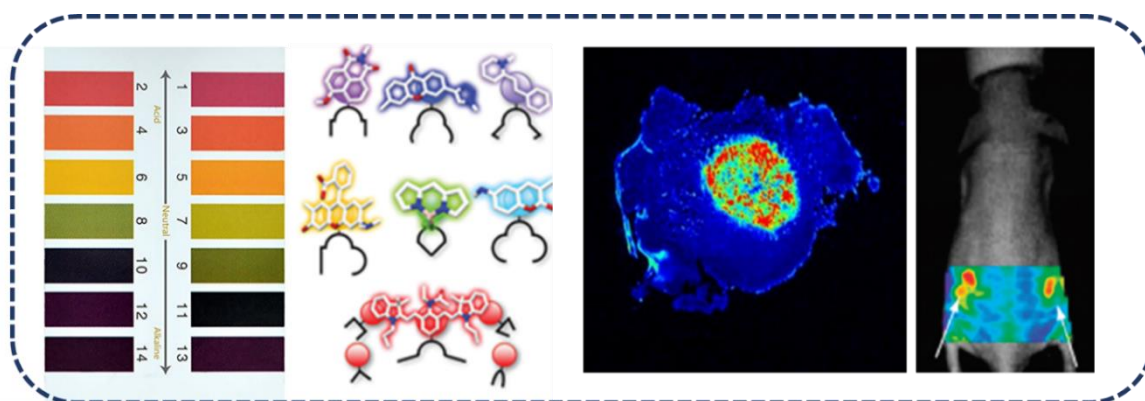
Finally modified pyridinium probes were exploited for the imaging of pH variations in endoplasmic reticulum during heat shock. We converted the pyrylium fluorophore **PS-OMe** to the corresponding endoplasmic reticulum-targeting pyridinium probes (**PM-ER-OMe** and **PM-ER-OH**).³ Due to the presence of a rigid backbone, **PM-ER-OH** did not show any significant changes in pH dependent emission under applied temperature. Using the large Stokes shift of **PM-ER-OH**, we used this single probe as a ‘*three-in-one*’ i.e., ‘turn-ON’, ‘turn-OFF’ and single excitation ratiometric pH sensor just by changing the excitation wavelength and demonstrated its utility towards ‘point-of-care’ and quantitative pH imaging. Also, we established the role of heat shock proteins in protecting cells from extensive damage due to heat related stress. Activation

of heat shock proteins during heat stress leads to lesser acidification and hence lesser damage. In conclusion, the present research work is a detailed investigation on some new pyrylium and pyridinium-based fluorescent dyes as molecular probes for monitoring the pH variations in cells and their application. We envision that this work will motivate the development of new fluorescent core architectures and sensors for monitoring critical cellular functions in real-time, leading to early diagnosis, treatment planning and efficacy.

References

1. **S. Chakraborty**, M. M. Joseph, S. Varughese, S. Ghosh, K. K. Maiti, A. Samanta, and A. Ajayaghosh. “A New Pentacyclic Pyrylium Fluorescent Probe that Responds to pH Imbalance During Apoptosis” *Chem. Sci.*, **2020**, 11, 12695
2. **S. Chakraborty**, M. M. Joseph, K. K. Maiti, A. Samanta, and A. Ajayaghosh “Pyridinium Fluorophore for Single Excitation Ratiometric Imaging of Lysosomal pH Imbalance During Autophagy” (Manuscript Under Preparation)
3. **S. Chakraborty**, A. K. Bindra, S. Munan, A. Samanta, Y. Zhao, and A. Ajayaghosh. “Pyridinium pH Probe for ‘Three-in-one’ Imaging of Heat Shock in Endoplasmic Reticulum. (Manuscript Under Preparation)

Fluorescent Probes for pH Sensing and Imaging in Biological Systems



1.1. Abstract

For the last few decades, pH has been regarded as one of the most important biomarkers in chemical biology. Visualizing and quantifying pH changes during subcellular processes have become easier and effective with the advancements in instrumentation and development of optical pH probes. Among the different optical techniques used for biosensing, fluorescence imaging facilitates a deeper understanding of complex biological systems with superior consistency and a high degree of accuracy. Therefore, the design and development of new fluorescent pH probes has attracted the interest of researchers globally. On similar grounds, the construction of new fluorescent cores with ease of synthesis, possibilities for functional modification, excellent photophysical properties and low biotoxicity has paved the way for engineering new and improved biosensors with multifarious advantages over existing probes. This introductory chapter aims at providing an

overview of the recent developments in fluorescent pH probes, the advantages of small molecule fluorophores and evolution of pyrylium and pyridinium based chromophores as emerging building blocks for constructing new probes for application in disease diagnosis, therapy monitoring and pro-treatment modalities. The origin, objectives and outlook of the thesis are presented towards the end of this chapter.

1.2. Introduction

pH is one among the most widely used analytical parameters in both chemical and biological systems. From the determination of the soil quality for agriculture to quality control of food, categorizing water utilization pathways, ensuring the wellbeing of marine organisms, monitoring wound healing and understanding cellular abnormalities, pH delivers critical information in almost every realm of science and technology.¹⁻⁴ While the application of pH and the related data on soil, food, water and marine life is well documented in literature, the area of biosensing and bioimaging using pH as a primary probe is reasonably less explored.⁵

Biosensing and bioimaging are crucial tools to visualize, understand and investigate the functions associated with various cellular components and regulation of various biological processes.⁶⁻⁸ These probes work as biocompatible miniaturized devices that provide real-time information on complex biochemical processes in a readable format.^{9,10} As it is non-invasive and provides instantaneous results, biosensing and bioimaging probes have revolutionized medical diagnosis and therapy.^{11,12} Bioimaging has enabled precise monitoring of various biomarkers that can be

utilized for disease diagnosis, fixing treatment protocols, and follow therapeutic effects and recovery process.^{13–15}

Among different modalities used for biosensing and bioimaging, fluorescence-based techniques have shown significant attention in terms of sensor development, introduction of new and improved methodologies, and instrumental progression. Such advancement in fluorescence modalities has allowed precise monitoring and analysis of a number of complex biological processes with high spatial and temporal resolution.^{16,17}

Apart from disease diagnosis, fluorescent sensors and imaging agents have profound applications in drug and inhibitor screening, image-guided surgery, therapy monitoring, and personalized medicine.^{18–22} The present chapter summarizes various reports in developing fluorescence-based optical probes for biosensing and bioimaging, particularly using pH as an analytical parameter and possible applications of pH probes in biology and medicine.

1.3. Historical Perspective of pH and pH Indicators

Though for a long time, certain solutions were identified to be acidic in taste, and some gave a burning feeling, the scientific definition of pH was proposed only in the last century. In 1909, Sorensen, a Danish chemist, introduced the concept of pH to conveniently define the acidity of a material. He described pH as the negative logarithm of hydrogen ion concentration,²³ i.e.

$$\text{pH} = -\log [\text{H}^+]$$

Later, in 2002 IUPAC recommendation transposed a more accurate expression for pH and the term ‘concentration of hydrogen ion’ was changed to the activity of hydrogen ion,²⁴ and the final equation was reformulated as,

$$\text{pH} = -\log [a(\text{H}^+)]$$

Differentiation of acid and base in the initial days was achieved by tasting the solution, which was fatal in many cases. Later, in the early 1300s, litmus was prepared from a fermented extract of lichens such as *Rocella tinctoria* and was found to change its color from blue to red in the presence of an acid. Subsequently, test strips were developed to avoid mixing of the test solution and litmus paper or cotton was dipped into an alcoholic solution of litmus and were dried to make the litmus strips.²⁵

While Sorensen defined pH scientifically in 1909, a glass electrode for pH measurement was concurrently reported by Haber and Klemensiewicz. In 1922, Hughes showed that the alkali-silicate glass electrodes are identical to hydrogen electrodes and are reversible to the concentration of H^+ .²⁶ Later, in 1925, Kerridge developed the first glass electrode for the pH analysis of blood samples.²⁷ Glass pH electrodes are considered the golden standard and undoubtedly the most widely used tool to analyze pH due to its accuracy, wide range monitoring capability, stability and fairly fast response (**Figure 1.1a**).

In the 1970s, paper strips were further improved by covalently immobilizing pH-sensitive azo dyes on cellulose and are commonly called pH paper or strips. The test

results are compared to a supplied color chart and have been found to be reasonably accurate in most cases (**Figure 1.1b**).²⁸

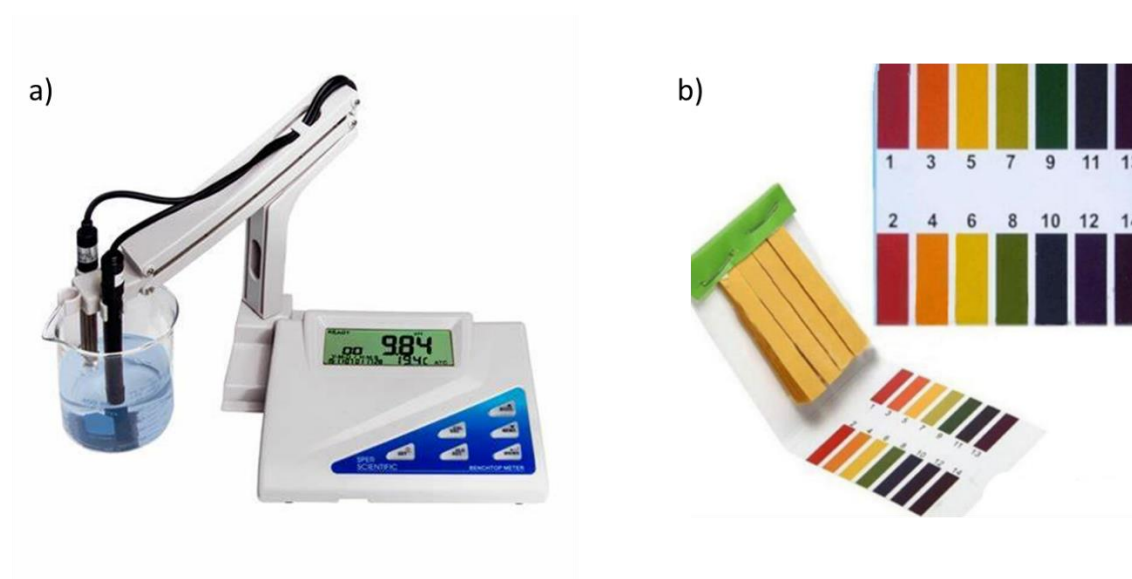


Figure 1.1. Photographs of (a) commercially available glass electrode-based pH meter and (b) pH paper strips with reference color indicator.

While most of the pH analyses using manual comparison of colors were semi-quantitative until the late 1980s, introduction of instruments capable of reading out color changes of such strips increased the popularity of these techniques for accurate quantification of pH based on absorbance and reflectance.²⁹ As most of the test strips are opaque, majority of the instrumental testing is done in a reflectance mode.³⁰

Though litmus solution, test strips, and glass pH electrodes can accurately measure pH of a wide range of materials in the macroscopic scale, its application is limited for microscopic objects like cells. Chemical sensors have thus emerged as potential candidates to deliver real-time and precise information about pH of live cells and cellular components.

1.4. Role of pH in Cellular System

Understanding a cell's internal structure and the chemical conditions within the cells is essential to study cellular behavior.³¹ Hydrogen ions (H^+) are the smallest and most active ions present in living organisms. Virtually every H^+ within a cell is buffered by reversible binding to weak acids and bases.³² Intracellular pH (pH_i) is a crucial parameter for understanding the intracellular environment, since the healthy functioning of cytoplasm and various cellular compartments (organelles) are associated with balanced pH values, strictly adhering within a defined range. Any deviation in the pH of these compartments as compared to the balanced pH indicates an abnormal condition.³³ In fact, intracellular pH modulation is fundamental towards controlling several critical physiological processes, such as protein synthesis, DNA and RNA syntheses, control of the cell cycle, and changes in the membrane ion conduction.³⁴

The pH_i values vary from 4.0 to 8.0 within the cellular medium (**Figure 1.2**). Lysosomes and endosomes are acidic, with a pH of 4.0–5.5 and 4.5– 6.8, respectively. Mitochondria is slightly basic with a pH of 8.0, whereas endoplasmic reticulum (pH 7.2), intracellular fluid (pH 7.4), nucleus (pH 7.2), etc., are nearly neutral.³⁵ Changes in intracellular pH adversely affect all cellular processes, including metabolism, membrane potential, cell growth, cell cycles, etc. Also, the activity of intracellular enzymes involved in cellular metabolism is pH sensitive.³⁶ Alterations on intracellular pH are one of the initial responses of the cells to the presence or introduction of externally applied agents, including growth factors,

hormones and neurotransmitters.³⁷ Changes in intracellular pH are often considered a functional consequence of organelle's dysfunction or exposure to external physicochemical agents and therefore is an indication of an abnormal condition of the cell.³⁸ For instance, the abnormal cell growth in cancer cells correlates with a lower pH as compared to healthy cells.³⁹

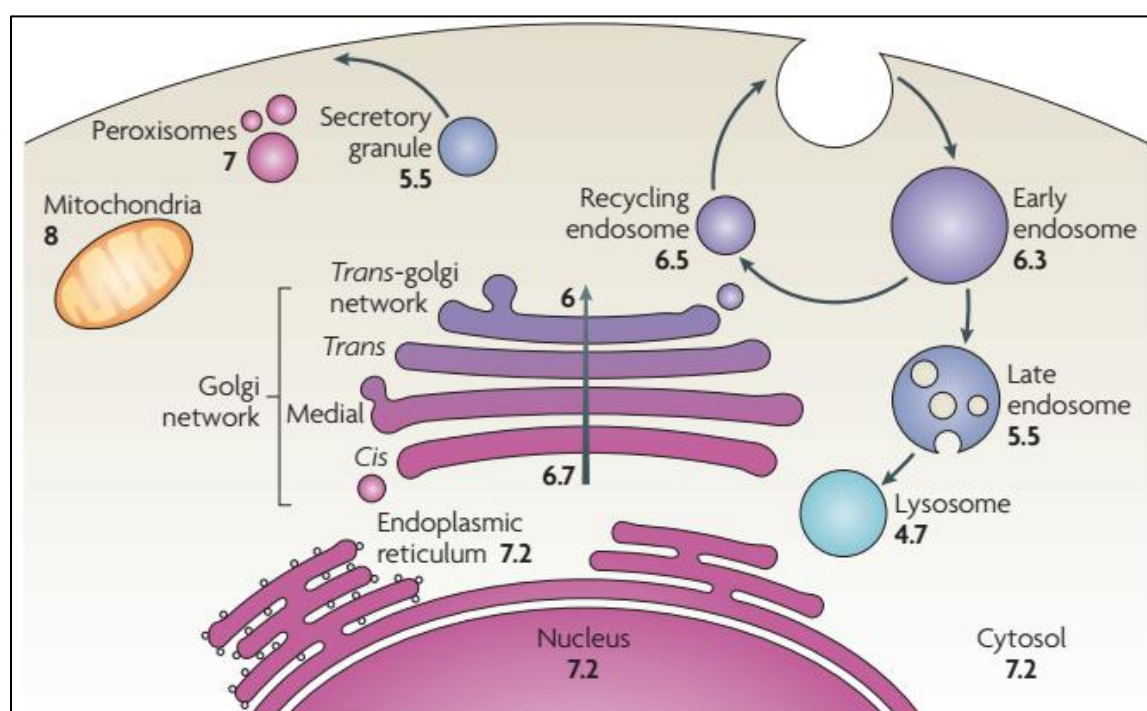


Figure 1.2. Schematic representation of the pH range of individual cellular compartments and organelles in a normal mammalian cell. (Adapted with permission from ref 35).

Several studies have shown that stress associated with endoplasmic reticulum (ER) can trigger autophagy, leading to acidification of the cell and a lowering of pH from the normal pH of 7.2.⁴⁰ Therefore, intracellular pH plays an inevitable role in cellular functions and hence monitoring the pH levels in cells is the first step towards a better understanding of cellular metabolism and other pathological processes.

1.5. Bioimaging using pH Probes

Tracking subcellular interactions in biological systems in real-time has always been an arduous task. For more than a century, most of the cellular processes were investigated using conventional biochemical assays in test tube reactions using pure or isolated biomolecules. Though these assays gave typical information on protein-protein and protein-biomolecule interactions, genetic identification and optimal conditions for enzymatic activity, it was nearly impossible to replicate the actual cellular environment that differed fundamentally from the solution state test tube reactions. Accurate determination of several biologically relevant parameters such as pH, that is dynamic with regard to cellular compartments or surroundings, using such assays, has neither been practical nor straightforward.

Bioimaging, on the other hand, has conferred a unique opportunity to contemplate cells as ‘living’ test tubes and track parameters like pH in real-time in various subcellular processes. A thorough understanding on the pH of different organelles, their dynamics during cellular functions, and any minor abnormalities could thus be obtained and eventually assists in disease diagnosis and deciding treatment modalities. However, a judicious combination of advanced instruments and suitable contrast/imaging agents is the major prerequisite towards achieving this objective. Nevertheless, concerted efforts from chemists, biologists, physicists and device engineers have enabled contemporary imaging modalities with spatial resolution as high as 1-2 nm.

Depending on the source and the type of contrast agent used, different imaging techniques, such as fluorescence imaging, photoacoustic imaging, magnetic resonance imaging (MRI), SERS imaging, computed tomography (CT), positron emission tomography (PET), etc. have emerged. Among these different modalities, fluorescence imaging has attracted significant attention due to multifarious advantages over others in real-time tracking of molecular events in cells with high sensitivity, resolution and reproducibility.

1.6. Fluorescence Imaging

Most of the molecules in the ground state of energy (S_0) absorb energy in the form of light and get excited to a higher energy level (S_1^*). Some energy may then be dissipated through a non-radiative pathway to reach a lower electronic state (S_1). Finally, the molecule comes back to the ground state (S_0) by emitting a lower energy photon. If this release happens through a radiative pathway, it is called fluorescence, and the process generally occurs within a few nanoseconds (**Figure 1.3a**).

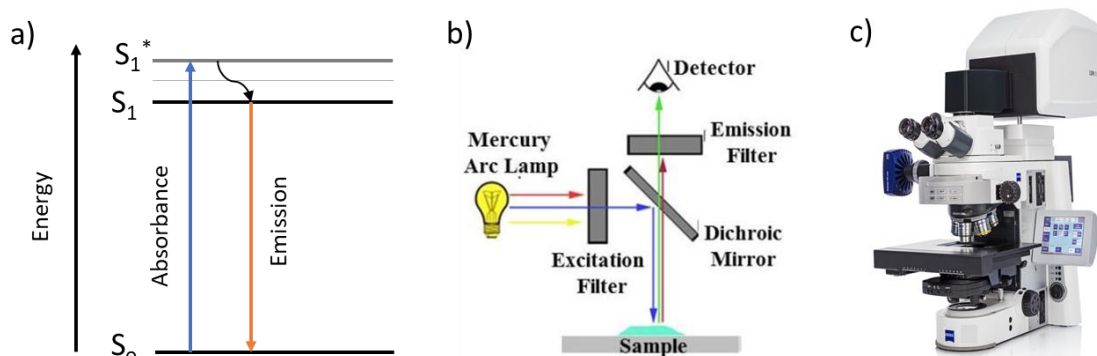


Figure 1.3. (a) Simplified Jablonski diagram representing the key steps involved in emission. (b) Schematic representation of the working principle of a fluorescence microscope. (c) Photograph of a modern-day confocal microscope for imaging applications.

By virtue of its fast response, excellent spatiotemporal resolution, non-invasive nature, and high sensitivity, fluorescence-based techniques have become an indispensable imaging tool in chemical biology.

A state-of-the-art fluorescence microscope is the prime requirement for reliable bioimaging using designed contrast agents. In a fluorescence microscope, the excitation source produces a white light, which passes through an excitation filter and falls on the sample after being reflected by a dichroic mirror. The sample then absorbs the light and emits fluorescence through the emission filter, and is directed to the detector by the objective lens. In an epifluorescence microscope, one of the most commonly used imaging devices, the excitation of the fluorophore as well as the detection of fluorescence occurs through the same light path, i.e., through the objective lens (**Figure 1.3b**).

However, in simple fluorescence microscopes, light falls on the entire specimen and results in a substantial unfocused background that further reduces the image's sharpness. This deterrent can be efficiently addressed using a confocal laser scanning microscope that uses point illumination and a pinhole in an optically conjugate plane in front of the detector to eliminate out-of-focus signals. At the same time, there exists a possibility to choose a particular excitation wavelength and flexible collection wavelengths (**Figure 1.3c**).

1.7. Fluorescent pH Imaging Probes

Fluorescent pH imaging probes show distinct structural changes at different pH, resulting in variations either in the wavelength or intensity of emission. In most

cases, the fluorescence response of such probes corroborates the pH profile of the cell. Several new fluorogenic materials that sense pH under different operational mechanisms have been reported over the last few decades. In this context, imaging of various endogenous systems such as NAD(P)H, tryptophans, and flavins have shed light on various processes happening inside the cell. Development of efficient fluorescent probes has opened a new dimension in understanding such intracellular activities through cellular trafficking, real-time monitoring of cellular dynamics, and following the interactions of various biomolecules.

Several studies have shown that the structure and function of proteins are highly dependent on the intracellular pH.⁴¹ This concept has also been used to develop fluorescent protein-based pH sensors capable of monitoring intracellular pH regulation during several complex biological processes. Yellen *et al.* have reported such a sensor prepared by mutagenesis of the red fluorescent protein mKeima.⁴² This genetically encoded pH sensor, **1** exhibited an emission peak at 610 nm. It features excitation peaks at 440 nm (protonated and neutral) and 585 nm (anionic) that changed the peak intensity ratio with a change in pH. When pH of the medium was adjusted from 6 to 9, a 7-fold decrease in the peak intensity at 585 nm was observed, whereas that at 440 nm increased by 4-fold. The pKa of **1** was found to be 7.8 (**Figure 1.4a**). This ratiometric change in emission intensity with change in pH resulted in a ratiometric signal during intracellular pH imaging.

Wang and coworkers used a combination of an intercalated motif (i-motif) and an aptamer to design a pH probe **2** that selectively imaged an acidic tumor microenvironment.⁴³ The i-motif part of the probe was constructed using two split i-

motif fragments and a linker DNA and was labeled by a quencher. The cancer-targeting aptamer possessed a DNA strand complementary to the linker DNA and was further modified with a fluorophore (**Figure 1.4b**).

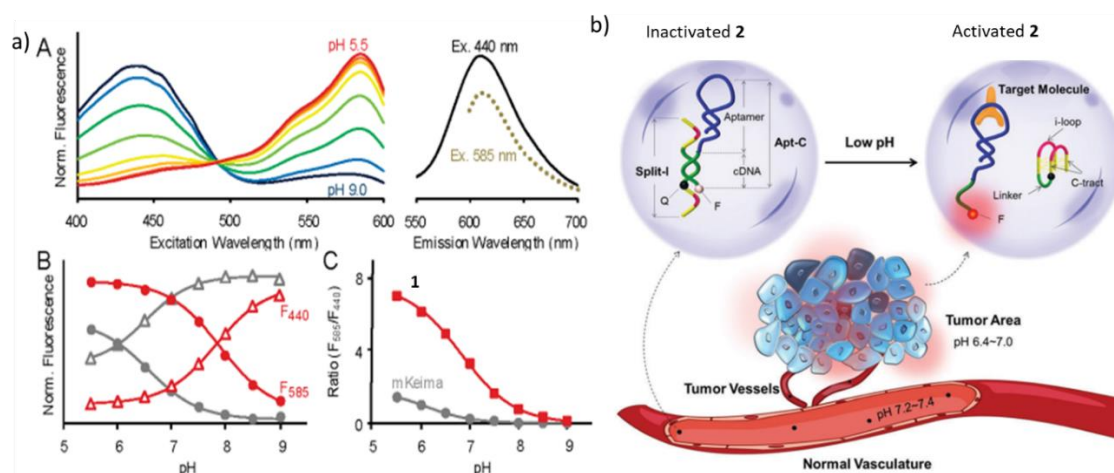


Figure 1.4. (a) (A) Fluorescence excitation and emission spectra of purified compound **1** in solution. pH response of the (B) 440 and 585 nm excitation peak intensities with 620 nm emission, (C) the F₅₈₅/F₄₄₀ ratio, (b) Schematic representation of the construct, and the working principle of the pH-activatable aptamer probe **2** for tumor imaging. (Adapted with permission from ref 42 and 43).

The probe **2** showed fluorescence change in a narrow range of pH with a transition midpoint (pH_T) at 6.77 ± 0.03 and could distinguish tumors from normal cells with high specificity and contrast and was applied to distinguish normal tissues and tumors in a mouse model. Several polymeric materials have also been developed as pH sensors for various biological applications.⁴⁴⁻⁴⁷ Most of these polymers are capable of localizing within a confined part of the cell leading to an increase in local concentration and thereby improving fluorescence images.

Na *et. al.* have reported a green-yellow emitting silicon-based nanoparticle for monitoring intracellular pH change.⁴⁸ The probe **3** was synthesized using a

hydrothermal method using 4-aminophenol as the reducing agent and *N*-aminoethyl γ -aminopropyltrimethoxysilane (DAMO) as the silicon source (**Figure 1.5a**).

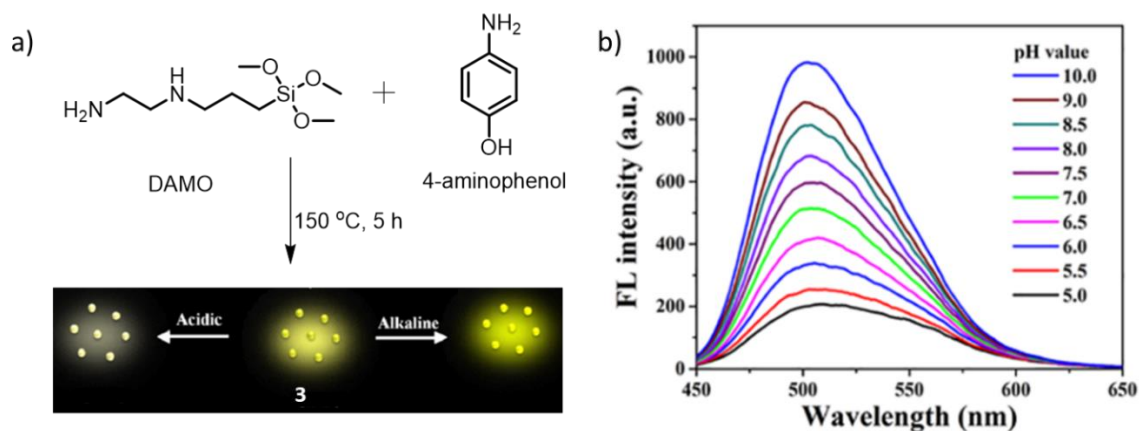


Figure 1.5. (a) Synthesis and pH response of the silicon-based nanoparticle **3**. (b) Emission spectra of **3** at different pH values. (Adapted with permission from ref 44).

It showed an emission maximum at 505 nm, and the intensity increased with an increase in pH. A similar trend was seen in cellular experiments also (**Figure 1.5b**). The crosslinked triphenylamine (TPA) derivatives with polydimethylsiloxane (PDMS) polymer are well-known for their bio-compatibility.⁴⁹ The probe **4**, reported by Zuo and coworkers showed an excellent response to pH due to the presence of a pyridine moiety in it. Protonation and deprotonation of the pyridine moiety with change in pH lead to a ratiometric response to the fluorescence of **4** (**Figure 1.6a**). It showed a green emission ($\lambda_{\text{max}} = 505$ nm) at basic pH which shifted to red region ($\lambda_{\text{max}} = 620$ nm) in acidic medium. Staining HeLa cells with this probe at different pH ranging from 4-8 replicated the fluorescence signals as observed in solution studies (**Figure 1.6b**). Later the probe was also used for monitoring intracellular pH change during autophagy.

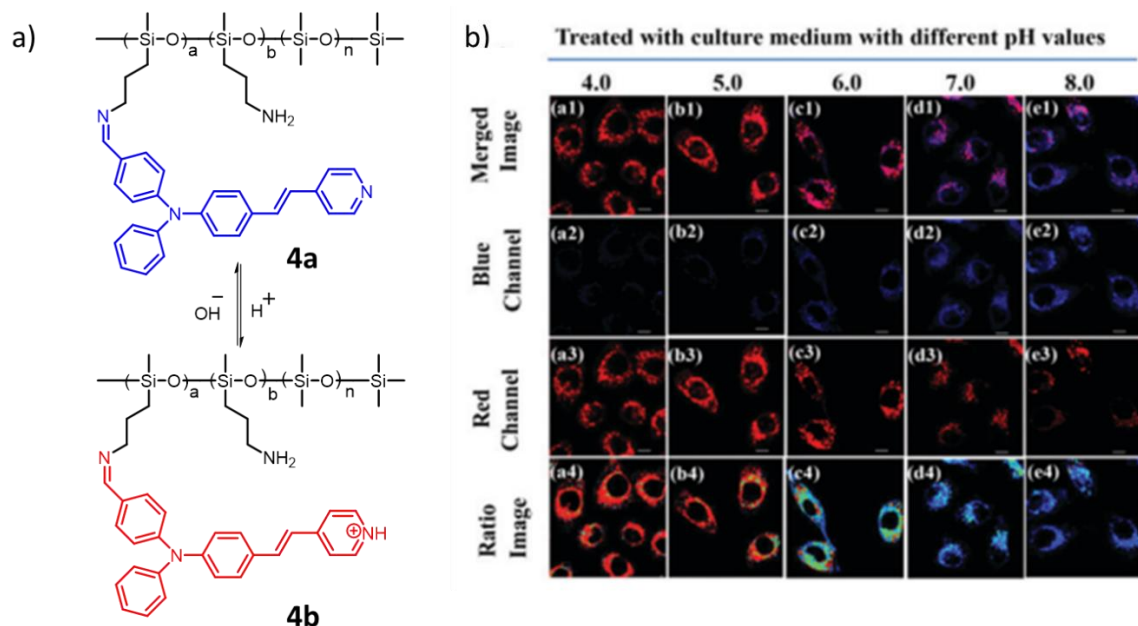


Figure 1.6. (a) Structure of pH probe **4** prepared by crosslinking of pH-responsive triphenyl derivative with polysiloxane and its chemical structure in basic (**4a**) and acidic (**4b**) media. (b) Ratiometric fluorescence imaging using **4** with the variation of intracellular pH. (Adapted with permission from ref 45).

Vijayakumar and coworkers have reported another polymeric material for long-range pH monitoring in biological systems with tunable polymer size and fluorescence response.⁵⁰ A pH probe **5** was prepared via controlled crosslinking of bovine serum albumin (BSA) and covalently attaching Coumarin, Fluorescein, and Rhodamine derivatives in a defined ratio. White emission was observed at pH 7, which changed to purple at pH 1–2, yellow at pH 11, dull green at pH 13, and nearly non-emissive at pH 14 (**Figure 1.7a**). The probe showed excellent biocompatibility, stability and distribution in cellular medium. Cellular imaging using the probe **5** showed heterogeneity in emission, indicating pH variations within various organelles in the cells (**Figure 1.7b**).

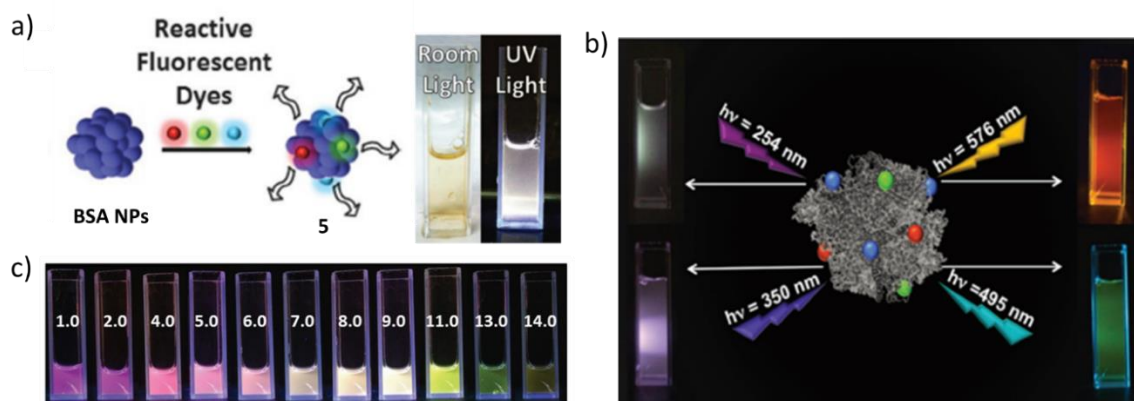


Figure 1.7. (a) Synthesis of **5** by covalent conjugation of coumarin, fluorescein and rhodamine with BSA nanoparticles and its photograph in day light and under UV light. (b) variation of emission of the probe with change in excitation wavelength. (c) Emission change of the probe **5** for broad range pH variation. (Adapted with permission from ref 46).

In another attempt to develop BSA-based pH sensors, Ajayaghosh and coworkers have prepared a tunable two-component system by mixing squaraine nanoparticle **6** with BSA.⁵¹ The hybrid nanoparticles (SqNPs) emit NIR fluorescence at acidic pH through a non-covalent interaction with BSA and green fluorescence in basic medium due to the covalent reaction of BSA with the nanoparticles.

The process was found to be reversible (**Figure 1.8a**) and the active pH range was tuned by varying the ratio of the two components in the nanoparticle. When a 12:1 ratio of BSA and SqNPs was used, the sensor showed a ratiometric change in the pH range of 4.6–6.4. When the corresponding ratio was changed to 6:1, the active region shifted to pH 5.8–7.6, and for a 1:1 ratio, it shifted to pH 7.4–9.0. Based on the cellular pH range, 6:1 ratio of BSA and SqNPs was used for imaging. When the intracellular pH was modulated using nigericin, the hybrid exhibited a consistent fluorescence behavior (**Figure 1.8b**).

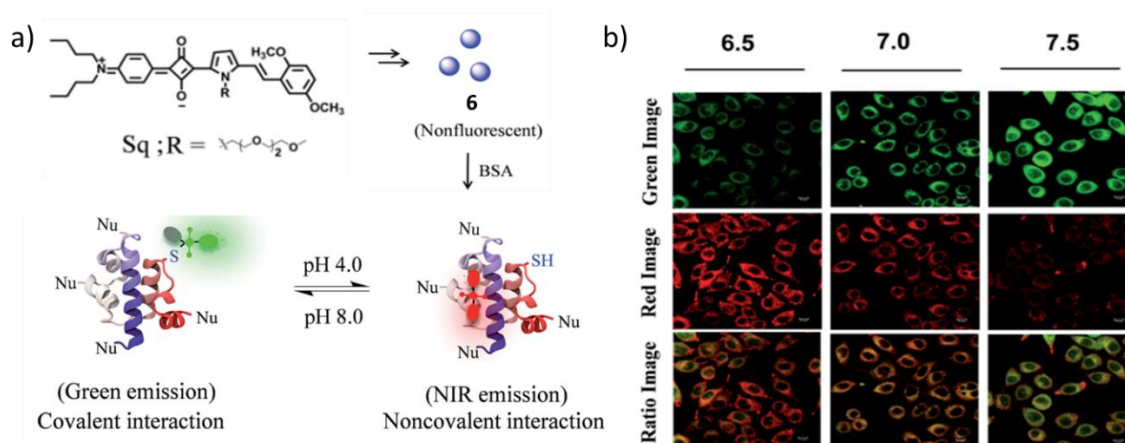


Figure 1.8. (a) Schematic representation of interaction between **6** and BSA at acidic and basic pH, exhibiting ratiometric fluorescence signals. (b) Fluorescence images of the cells incubated with the hybrid prepared by mixing probe **6** and BSA in 6:1 ratio at different intracellular pH values. (Adapted with permission from ref 47).

In-vivo imaging agents have recently emerged as powerful tools for real-time visualization of complex cellular events. NIR-II emitting dyes are among the best-reported candidates for such applications. Zhang and coworkers have recently reported a pKa tunable FRET-based hybrid pH sensor with NIR-II fluorescence response.⁵² The probe was constructed by conjugating a FRET donor aza-BODIPY dye **7** to NIR-II light activable rhodamine hybrid polymethine dye **8**, and subsequently encapsulated using a commercially available material 1,2-distearoyl-sn-glycero-3-phosphoethanolamine-*N*-[methoxy (polyethylene glycol)-2000] (DSPE-PEG2000-OCH₃) that ensured better stability and hydrophilicity (**Figure 1.9a**). The aza-BODIPY dye **7** exhibited an emission maximum at 949 nm, and **8** in acidic medium showed emission maximum at 1026 nm. Mixing these two dyes at 1:1, 1:5 and 1:10 ratio gave a tunable pH range of pH 6.11–6.88, pH 6.43–7.09, and pH 6.63–7.22, respectively. Finally, the probes with suitable ratios of donor and

acceptor were used to quantify dynamic pH variations within a tumor microenvironment under different pH ranges (**Figure 1.9b**).

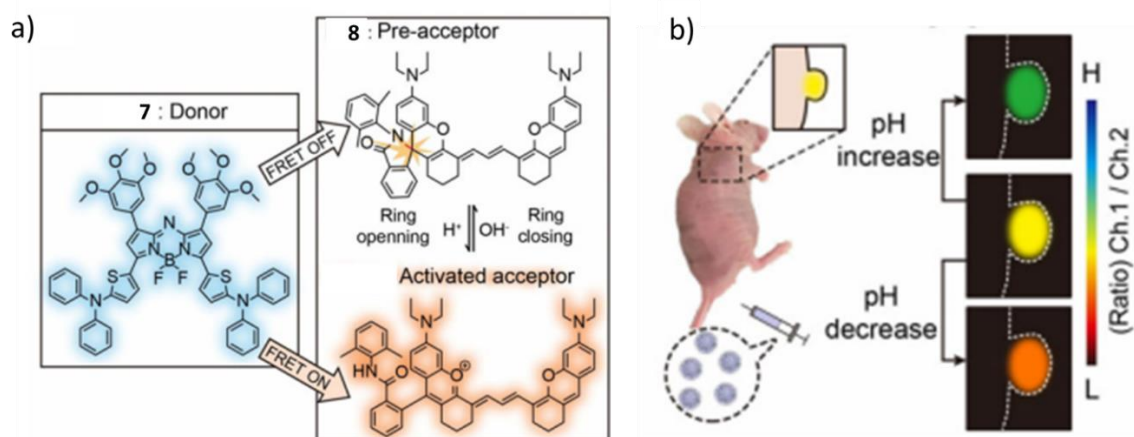


Figure 1.9. (a) Structure of the aza-BODIPY dye, **7** (donor) and Rhodamine dye, **8** (pH-responsive acceptor). (b) Ratiometric fluorescence imaging of *in-vivo* pH dynamics at the tumor site. (Adapted with permission from ref 48).

Though the aforementioned fluorescent probes possess several advantages over conventional biochemical assays, they are not devoid of disadvantages. Complicated synthesis, tedious work-up and purification, slow cellular uptake, cytotoxicity, undesired interaction with biomolecules, low signal-to-noise ratio, etc., restrict their application in several cases.⁵³ Small-molecule fluorescent probes have therefore attracted immense interest as potential bioimaging agents. Small size, ease of synthetic modification, excellent and controlled cellular uptake, high photostability, chemical stability, low cytotoxicity, organelle targeting ability, high spatiotemporal resolution, etc., have made them promising candidates for precisely tracking cellular activities in real-time.⁵⁴ Small-molecule based probes can be designed to follow specific photochemical mechanisms, such as intramolecular charge transfer (ICT), photoinduced electron transfer (PET), twisted intramolecular charge transfer

(TICT), Förster resonance energy transfer (FRET), excited-state intramolecular proton transfer (ESIPT), aggregation-induced emission (AIE), excimer/excimer formation, etc., leading to selectivity, precision and accuracy in subcellular imaging. Depending on the pH modulated output signals, these small-molecule fluorescent probes can be classified into two main categories: (i) ON-OFF pH probe and (ii) Ratiometric pH probe.

1.8. ON-OFF pH Probes

Those probes that alter their response between fluorescent and non-fluorescent states with changes in pH are called ON-OFF probes. These probes are generally preferred for point-of-care detection as it has clear discrimination between the two states that can be distinguished easily. Depending on the application, they are sub-classified as ‘Turn-ON’ and ‘Turn-OFF’ fluorescent probes.

1.8.1. Turn-ON pH Probes

A fluorescent probe that shows a gradual increase in emission from a non-fluorescent state after recognizing the target analyte is called a ‘Turn-ON’ probe. A large number of Turn-ON fluorescent pH probes, with great potential as bioimaging agents, have been reported in the literature.

Achilefu *et al.* have reported a NIR pH probe **9** for the selective detection of breast cancer.⁵⁵ The probe was constructed using a norcyanine dye that absorbs and emits in the NIR region and was attached to $\alpha_v\beta_3$ integrin receptor (ABIR)-avid peptide, cRGD which selectively localizes in breast cancer cells (**Figure 1.10a**). pKa of **9**

was found to be 4.7 and showed a sharp ‘Turn-ON’ response when pH was decreased below 5.0 (**Figure 1.10b**). Both *in-vitro* and *in-vivo* models were used to establish the potential of the probe to exhibit a Turn-ON pH response in acidic medium and selectively mark primary and metastatic breast tumors in subcutaneous and orthotopic mouse models (**Figure 1.9c**).

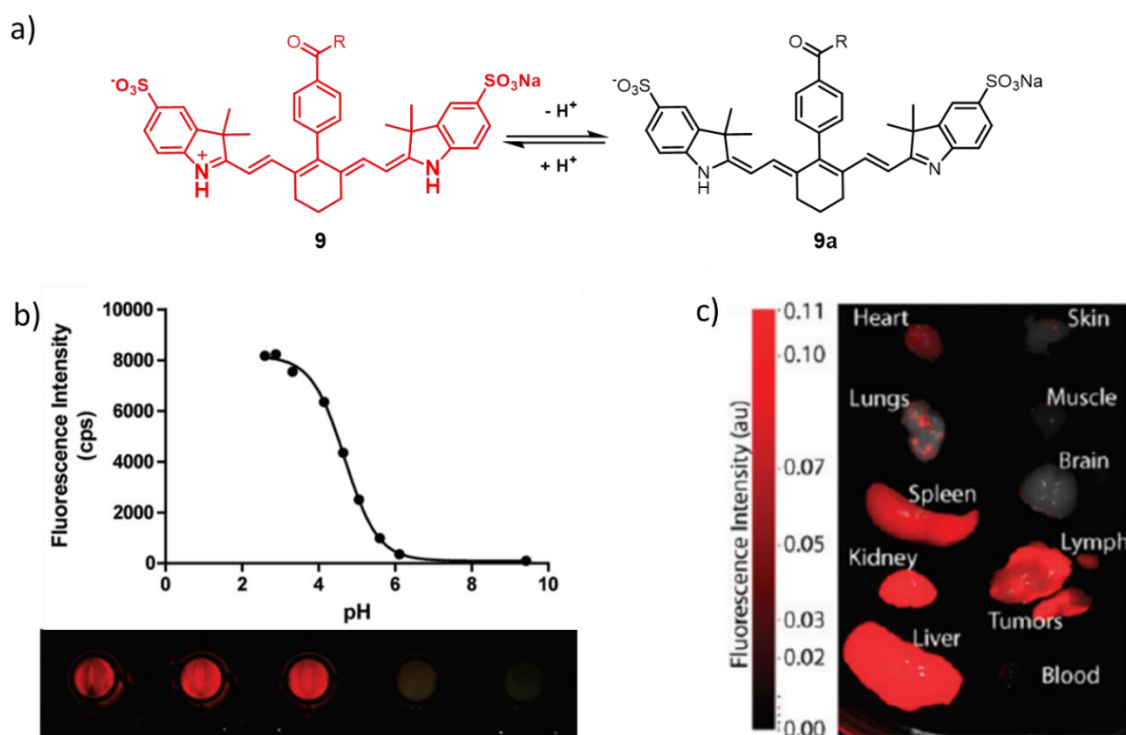


Figure 1.10. (a) pH responsive structural change of the probe **9** where R represents the peptide cRGD. (b) Secondary plot of the fluorescence intensity maxima at different pH values and the photographs of their corresponding fluorescence response in buffer of different pH under UV-light. (c) *Ex-vivo* fluorescence biodistribution image of probe **9** in organ tissues from 4T1/luc orthotopic tumor bearing mice at 24 h post injection. (Adapted with permission from ref 51).

In 2014, Hirose and coworkers reported a series of rhodamine-based pH probes to monitor vesicular dynamics in cells.⁵⁶ The probes were constructed using a photostable and bright dye rhodamine and different *N*-substituted piperazines as pH-responsive units. Among those, **10** was prepared by attaching *N*, *N*-dimethylamino

group for selective acidic vesicle targeting. Another derivative, **10a** had a Halo-Tag for selective protein labeling (**Figure 1.11a**).

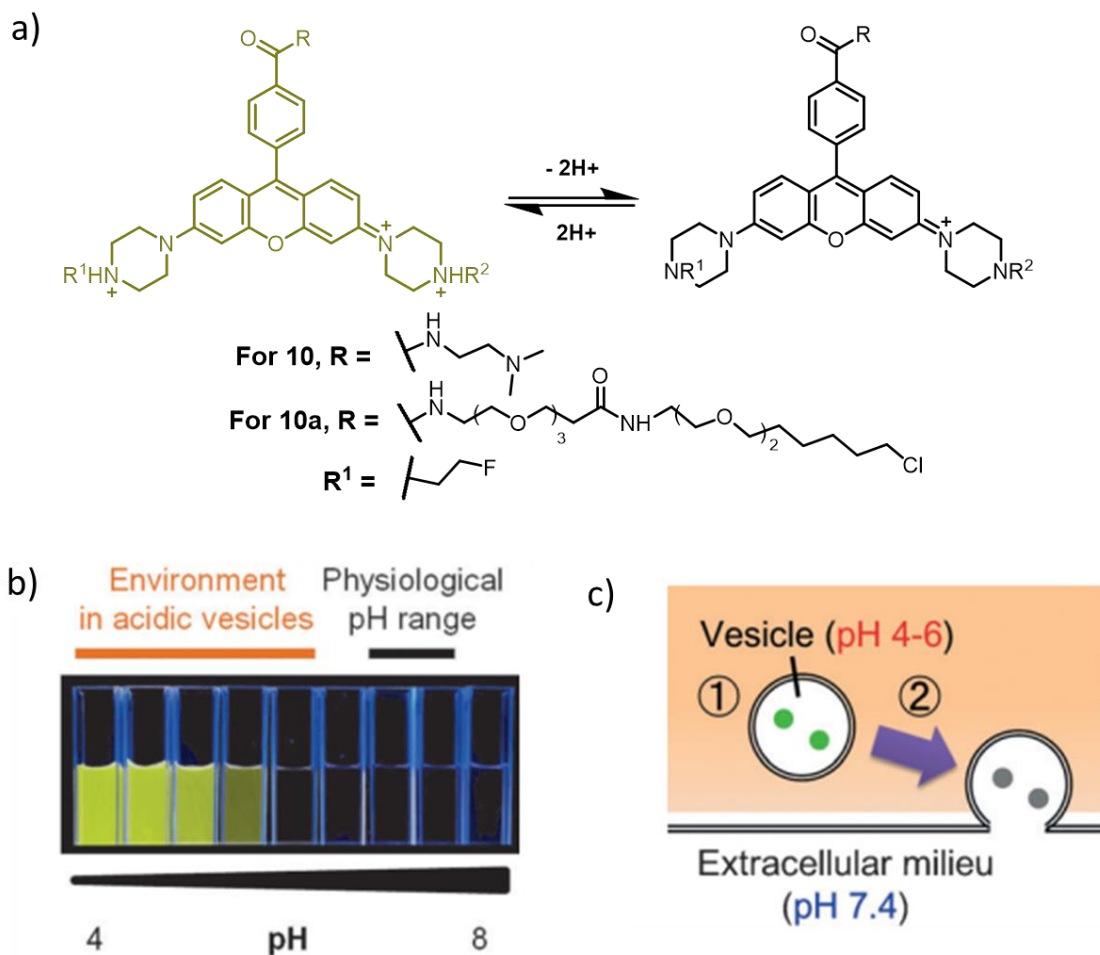


Figure 1.11. (a) Structure of pH probes **10** and **10a** for labelling acidic vesicles and protein, respectively, using a turn-on fluorescence response. (b) Fluorescence response of the probe at different pH conditions. (c) A schematic representation of monitoring the exocytosis and endocytosis dynamics through fluorescence light-up using the probe. (Adapted with permission from ref 52).

Both the molecules were almost non-fluorescent above pH 6 and showed a sharp increase in intensity in the range of pH 4-6 (**Figure 1.11b**). These probes reversibly interact with the target organelle, resulting in an ON-OFF output signal (**Figure 1.11c**). Using these probes, exocytosis, as well as endocytosis/reacidification

processes were imaged using dynamic fluorescence changes in cells during these processes.

O'Shea *et al.* have designed a NIR pH probe **11** that localized in lysosomes without the use of any typical amine protonation mechanism.⁵⁷ They synthesized a BF₂-chelated azadipyrromethene based fluorophore, having a pH-responsive *p*-nitrophenol group and a polyethylene glycol chain as a tumor-targeting moiety (**Figure 1.12a**).

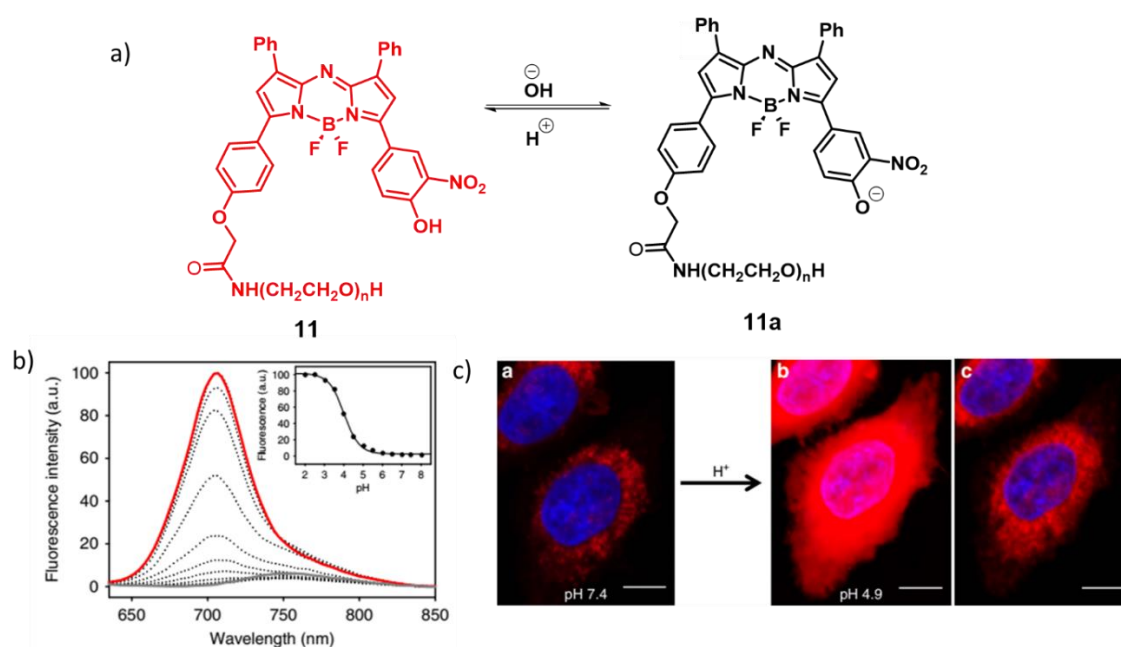


Figure 1.12. (a) Chemical structure of the BODIPY-based pH probe **11** in its fluorescent and non-fluorescent form. (b) pH-dependent emission of the probe and its secondary plot using emission maxima at different pH (inset). (c) Fluorescent images of the cells at pH 7.4 and 4.9 where the red fluorescence intensity is less at higher pH and increases significantly when pH is reduced to 4.9. Later, when the microscope laser power and PMT voltage were adjusted to obtain a non-saturated image, a clear red fluorescence was seen to emerge from the nucleus of the cells due to acidification. (Adapted with permission from ref 53).

The probe was non-emissive at pH 7.4 and showed a sharp increase in fluorescence intensity at pH 4 (**Figure 1.12b**). Unlike most other NIR probes, **11** exhibited excellent photostability and was insensitive to the polarity of the medium at neutral

or acidic pH. The probe was internalized in cells via an endocytosis pathway and showed excellent lysosomal localization. When the pH of the cell was reduced to pH 4.9, red fluorescence was observed from the whole cell. The images clearly showed high fluorescence intensity at the lysosomal pH and was silent at higher pH, characteristic of other organelles (**Figure 1.12c**). The probe **11** was then used to image several complex biological processes, such as endocytosis, organelle trafficking, and efflux. It was also used for *in-vivo* imaging using MDA-MB-231 subcutaneous tumor model. The probe accumulated almost exclusively in the tumor within 24 h of injection, most likely due to PEG conjugation, as reported for its use as a drug delivery vehicle for various anti-cancer drugs.

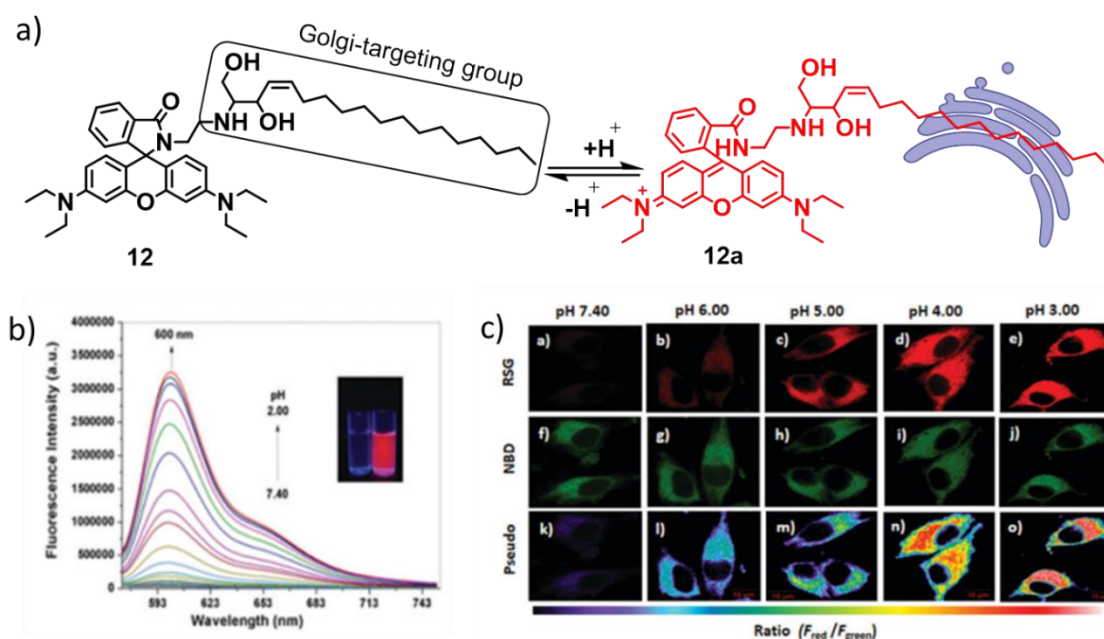


Figure 1.13. (a) The proposed mechanism of pH response and Golgi apparatus targeting by the Rhodamine-based fluorescent probe **12**. (b) Fluorescence change in buffer solution containing probe **12** when the pH of the medium was changed to 2.0 from 7.4. (c) Fluorescence response of the probe in the red channel when the intracellular pH was adjusted using nigericin. A pH-insensitive Golgi-specific commercial green fluorescent dye NBD was used in combination with probe **12** to generate ratiometric images from the cells. (Adapted with permission from ref 54).

Dong *et al.* have reported a small molecule-based pH fluorophore **12** that targeted the Golgi apparatus.⁵⁸ Sphingosine was used as a Golgi targeting group and Rhodamine B as a pH-responsive entity (**Figure 1.13a**). The probe showed a 112-fold increase in fluorescence intensity at 600 nm when pH was changed from pH 7.4 to 2 (**Figure 1.13b**).

Golgi-localization of the probe was confirmed by co-localizing with NBD C6-Ceramide (commercial Golgi-specific green fluorescent dye) with Pearson's coefficient of 0.90. When the pH of the cells stained with **12** was slowly changed from 7.4-3.0, a gradual increase in the fluorescence intensity in the red channel was observed (**Figure 1.13c**). Practical application of the probe was demonstrated by imaging cells that are initially treated with bafilomycin A1 (Baf-A1), a selective inhibitor of H⁺ v-ATPase, and found that the pH of Golgi increased, leading to a corresponding emission change. H₂O₂ and *N*-ethylmaleimide were used to generate stress and an increased pH was witnessed in the first case, whereas a pH drop was observed in the other case, with RSG providing a consistent fluorescence response as expected. It was later used for *in-vivo* imaging using a mouse model and results confirmed its potential as a Golgi-targeting 'Turn-ON' pH probe.

Generally, cancer cells are slightly more acidic in comparison to normal cells. Exploiting this pH difference, Bhuniya and coworkers have demonstrated the use of an amphiphilic fluorescent probe **13** for selective detection of cancer cells using a 'Turn-ON' fluorescence response (**Figure 1.14a**).⁵⁹ The probe showed a weak green fluorescence at pH 8.5, with an 8-fold intensity increment at pH 4 due to self-assembly of the molecule (**Figure 1.14b**). The pK_a of **13** was found to be 5.99 ±

0.09. Consistent results were obtained upon using this probe to image live cells at different pH. In an attempt to investigate whether **13** can selectively label cancer cells, A549 (human lung adenocarcinoma), AGS (human gastric cancer), and MRC-5 (human normal lung fibroblastic cells) cells were treated with CS-1 (20 μM), and fluorescence image analysis revealed that 90% and 82% of A549 and AGS cells, respectively, were labeled. On the contrary, only 20% of MRC-5 cells were labeled under similar conditions. The probe was also found to stain lysosome (P.C. = 0.84 ± 0.04), mitochondria (P.C. = 0.89 ± 0.03), and cell surface (P.C. = 0.68 ± 0.06) in acidic cancer cells, in a time-dependent fashion. Differentiation of A549 and MRC-5 cancer cells in a co-culture was also possible based on fluorescence intensity of **13**.

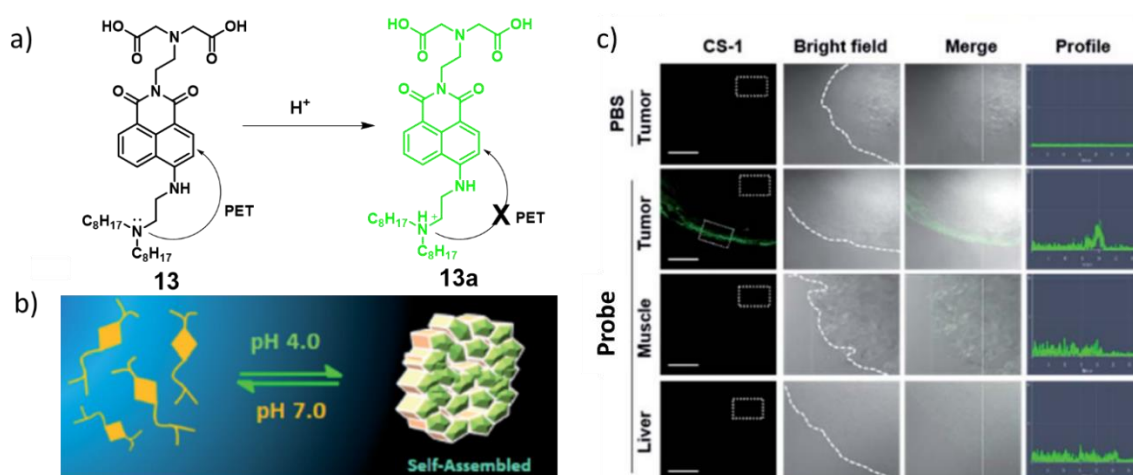


Figure 1.14. (a) The chemical structure and fluorescence response mechanism of probe **13** with change in pH. (b) Schematic representation of the proposed self-assembly of the pH probe in presence of an acid. (c) Change in fluorescence intensity emanating from the cells treated with **13** with the modulation of the intracellular pH. (Adapted with permission from ref 55).

In the case of A549 spheroids and tumors in Balb/c nude mice bearing A549-derived xenografts, higher fluorescence intensity was observed on the tumor boundaries as

compared to the core, most likely due to the presence of a higher proton concentration in the extracellular plasma region as compared to the core (**Figure 1.14c**).

1.8.2. Turn-OFF pH Probes

For ON-OFF fluorescent probes, the desired signal is obtained by the continuous decrease in fluorescence intensity after interacting with the target analyte. Though ‘Turn-ON’ probes are preferred as imaging agents due to their advantages in point-of-care detection, a large number of ‘Turn-OFF’ pH probes have been reported in the literature.

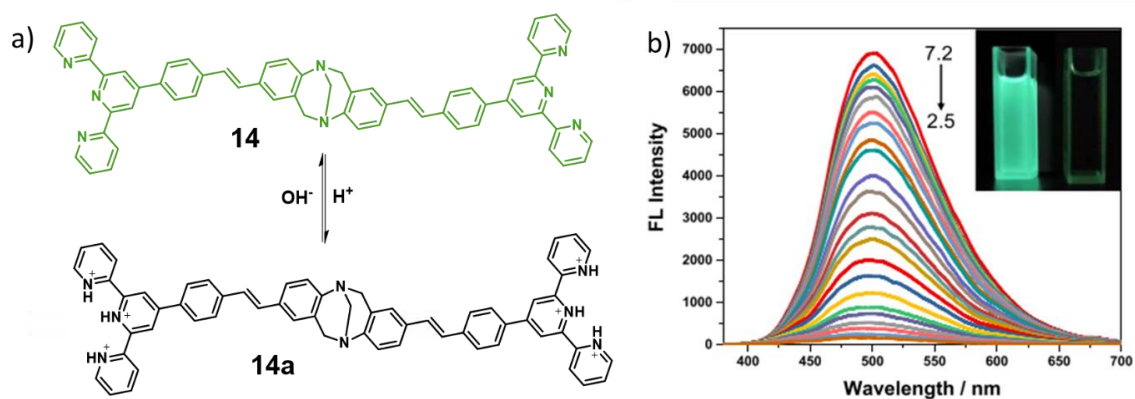


Figure 1.15. (a) Chemical structure and the sensing action of the probe **14** for pH detection. (b) Emission spectra of **14** with increasing H^+ concentration and the photographs of the probe at pH 7.2 and 2.5 under 365 nm light. (Adapted with permission from ref 56).

Yuan and coworkers have reported a terpyridine appended Tröger's base **14** (**Figure 1.15a**) with a strong green fluorescence at neutral pH (pH 7.2) that decreased gradually with a decrease in pH and eventually quenched at pH 2.5, indicating a typical ‘Turn-OFF’ response. (**Figure 1.15b**).⁶⁰ NMR studies confirmed that adding

an acid to **14** resulted in the protonation of the nitrogen atoms in the terpyridine unit, thereby reducing the ICT effect, leading to fluorescence quenching.

Chao *et al.* have reported iridium complex-based probes **15a** and **15b** for monitoring mitochondrial pH fluctuation during apoptosis (**Figure 1.16a**).⁶¹ Both the probes showed characteristic emission at pH 9, and the emission intensity decreased to near-complete quenching at pH 3 for **15b** (**Figure 1.16b**).

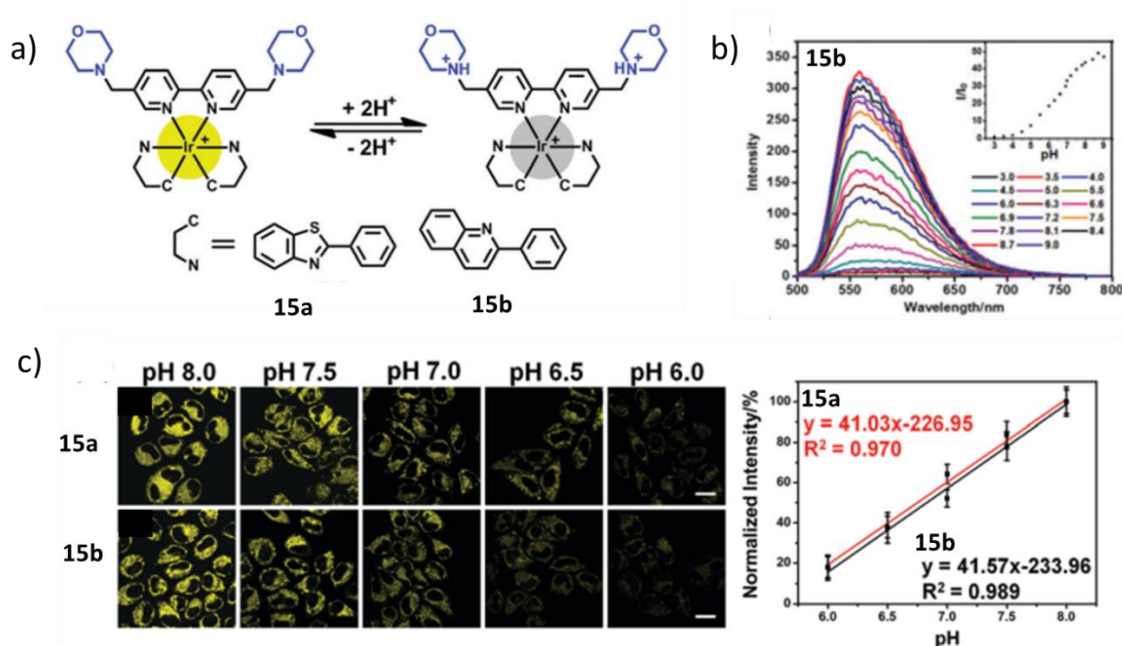


Figure 1.16. (a) Chemical structures and the representative pH-responsive fluorescence of probes **15a-b**. (b) Emission spectra of **15b** at different pH and the secondary plot of the fluorescence maxima vs. its pH (inset). (c) Decrease in the fluorescence intensity of HeLa cells with a decrease in intracellular pH and of the corresponding intracellular pH calibration curve using the probe. (Adapted with permission from ref 57).

Despite having two morpholine units, the probe showed excellent mitochondria localization (Pearson's coefficient = 0.90), most likely due to the positive charges on the iridium. A yellow fluorescence was observed at neutral pH, which gradually decreased with a decrease in pH. A linear decline in emission intensity was observed when the intracellular pH was adjusted in the pH range 8-6 (**Figure 1.16c**). Time-

dependent analysis of apoptosis induced in HeLa cells using carbonyl cyanide *m*-chlorophenyl hydrazone (CCCP) in the presence of the probe corroborated a gradual decrease in mitochondrial pH with progression in apoptosis.

In 2019, Wu *et al.* have reported an NIR pH probe for monitoring chronic wound healing.⁶² The probe **16** was synthesized by conjugating a benzoyl hydrazine group to a cyanine dye (**Figure 1.17a**). It exhibited an absorbance maximum at 770 nm that decreased with an increase in pH from 4.5 to 10.5. The emission intensity of **16** remained nearly constant in an acidic medium as pH was gradually changed from 4.5 to 7. Fluorescence intensity decreased nearly 10-fold in the pH range 7-9.5, and pKa of the probe was found to be 8.01 (**Figure 1.17b**).

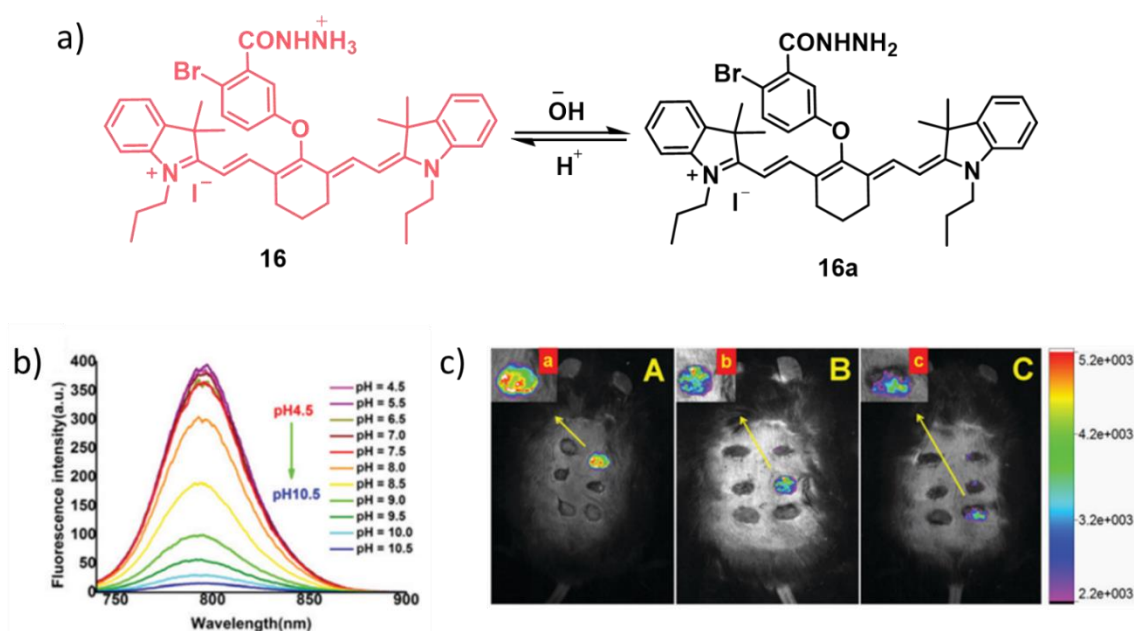


Figure 1.17. (a) Chemical structure of the NIR fluorescent probe **16**, its structural change in response to pH. (b) pH-responsive emission spectra of **16**. (c) Fluorescence pseudo color images of the wound beds at different time points: A (day 1), B (day 4), and C (day 7). Partially enlarged views of the pseudo color images are shown in the inset. (Adapted with permission from ref 58).

Intracellular imaging at a pH range of 4 to 9.5 confirmed a gradual decrease in fluorescence intensity with increase in pH. An intensity variation of ~8% was

observed in the pH range 4.5 and 7.0, whereas ~77% decline in emission intensity was observed when the intracellular pH was increased from pH 7 to 9. The probe **16** was later used to investigate chronic wound healing in diabetic foot ulcers using a transgenic diabetes-impaired db/db mouse model. It was sprayed on each wound bed, and fluorescence images were recorded after 1, 4, and 7 days. Fluorescence intensity was found to decrease by almost 45% from day 1 to day 7, indicating a concomitant pH increase with wound healing. This observation was corroborated via pH measurements on the wound using a flat glass pH electrode, which showed an increase of pH from 6.97 to 8.06 within 7 days (**Figure 1.17c**). Also, the fluorescence distribution within the wound was uneven, confirming different pH at different parts of the wound.

1.9. Ratiometric pH Probes

Though ‘ON-OFF’ probes possess several advantages in terms of point of care applications, they suffer from several limitations also. For example, quantification of analyte concentration via fluorescence measurements has been found to give inconsistent results due to various factors such as uneven local concentration of the dye, the influence of cellular microenvironment, aggregation-induced quenching of fluorescence, etc. These limitations of an ‘ON-OFF’ probe can be effectively addressed using ratiometric fluorescent probes where the ratio of two signals, rather than individual emission intensities, is considered. Therefore, there has been a renewed interest in the development of novel ratiometric fluorescent probes, particularly for quantitative detection of bioanalytes and related applications.

Kim *et al.* have developed a fluorescent probe **17** for broad range ratiometric pH monitoring.⁶³ A rhodamine moiety was covalently attached to a fluorescein dye leading to a conjugate with two different pKa values, wherein rhodamine exhibited characteristic emission at acidic pH and fluorescein emitted in basic medium (**Figure 1.18a**).

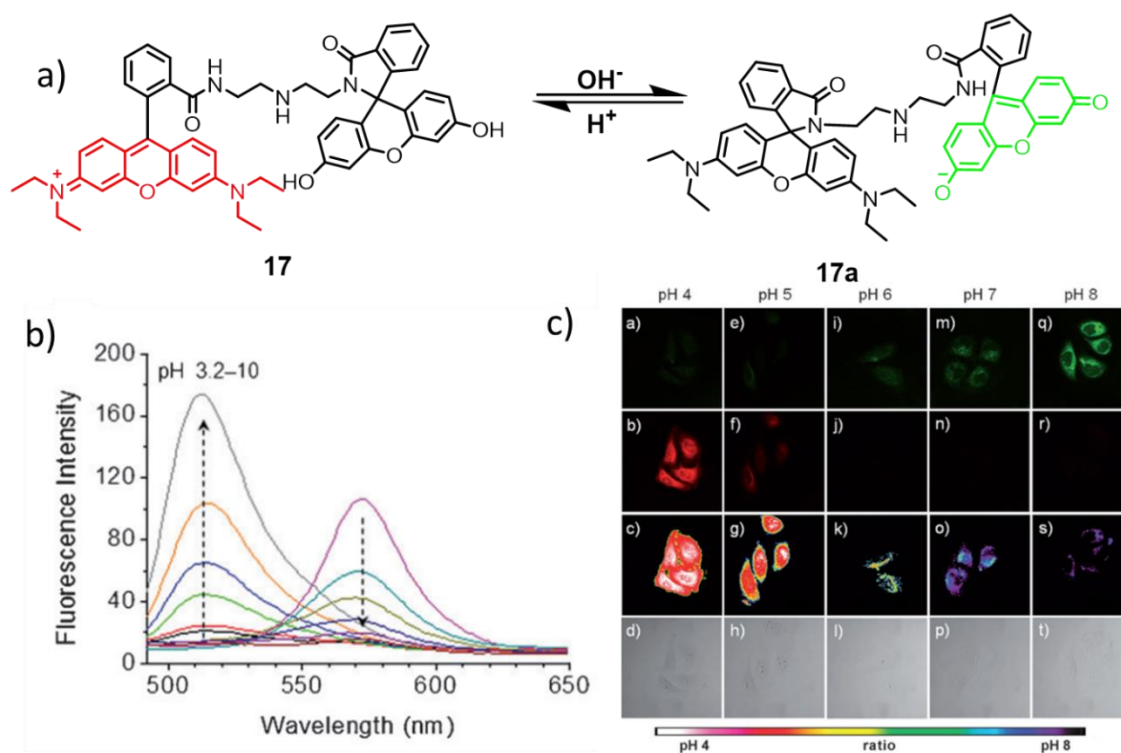


Figure 1.18. (a) Structural change of the probe **17** in acidic and basic media and the representative fluorescent colors, based on structural aspects. (b) Ratiometric change in the emission spectra with change in the pH of the media from 3.2 to 10. (c) Simultaneous change of fluorescence in green and red channels with change of intracellular pH from 4.0 to 8.0 and of the corresponding ratiometric image. (Adapted with permission from ref 59).

Accordingly, a red fluorescence characteristic of rhodamine was observed at acidic pH that decreased with an increase in pH. Typical green fluorescence characteristic of fluorescein was found to gradually increase with the decrease in red emission at basic pH leading to a ratiometric response. (**Figure 1.18b**). Similar ratiometric behavior was observed in pH modulated live cells incubated with the probe, and data

collected in green and red channels were used to generate the ratiometric images (Figure 1.18c). The probe was also used to monitor pH changes in cells during apoptosis induced by H₂O₂ and NAC (*N*-acetylcysteine, a GSH precursor).

Yu and coworkers have reported two ratiometric pH probes (**18a** and **18b**), in which a pyridine moiety provided pH response and coumarin was used as a fluorophore (Figure 1.19a).⁶⁴ **18a** was chosen for cellular experiments due to its superior ratiometric response over the other. Red and green emissions were observed, respectively, at acidic and basic pH, and the pK_a was 6.7. It was found to exhibit ratiometric response in a cellular environment similar to solution photophysics (Figure 1.19b).

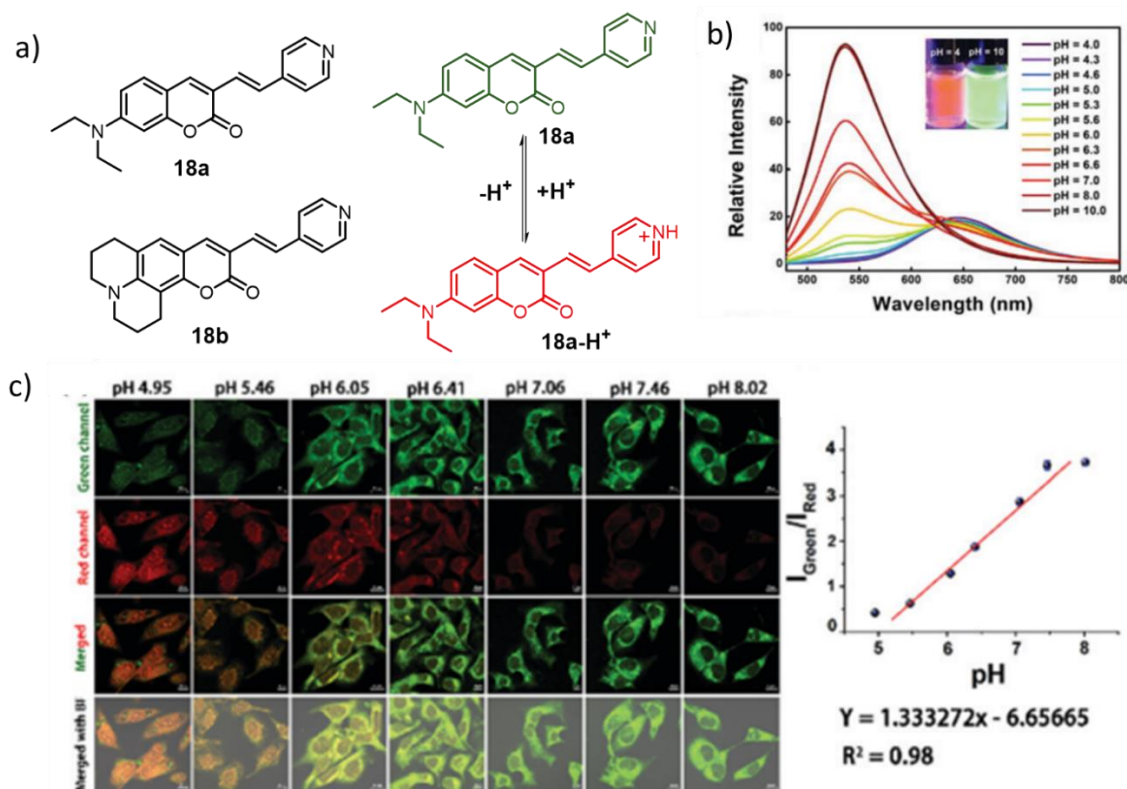


Figure 1.19. (a) Chemical structure of the fluorescent pH probes **18a-b** and fluorescence response mechanism of **18a** via its protonation in acidic medium. (b) Emission spectra of **18a** at different pH. (c) Ratiometric change of emission in the green and red channels with change in intracellular pH and of the corresponding merged and ratiometric images. (Adapted with permission from ref 60).

pH of cells during autophagy induced by drugs such as verapamil, loperamide, rapamycin, and starvation confirmed cellular acidification and the final pH of the cells were quantified from fluorescence intensity analysis.

In 2019, Zhang *et al.* have reported a light-activated ratiometric pH probe, **19a** comprising spiropyran and methylpiperazine moieties.⁶⁵ The probe exhibited a weak yellow fluorescence in PBS buffer at pH 7.4, that increased significantly with UV light (375 nm) irradiation. Further, an increase in the pH of the medium resulted in a decrease of the yellow fluorescence with a concomitant increase in red fluorescence. On the other hand, decreasing the pH of the medium to the acidic range afforded a new green emission (**Figure 1.20a**). It was found to respond to pH changes as low as 0.028, confirming its ultra-sensitive nature. *In vitro* investigations using cells showed good linearity with photophysical data (**Figure 1.20b**).

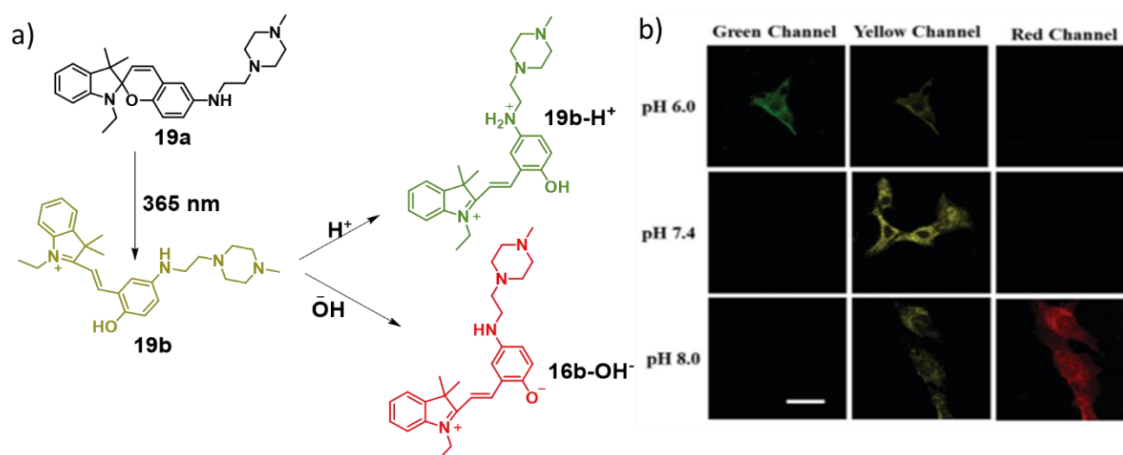


Figure 1.20. (a) Light-activated ring opening of **19a**, enabling fluorescence light up (**19b**), followed by the change in structure and emission color with change in pH (**19b-H⁺** and **19b-OH⁻**). (b) Intracellular pH-dependent fluorescence response of **19a** upon 365 nm UV light irradiation. (Adapted with permission from ref 61).

When apoptosis was induced in cells using UV light irradiation in presence of **19a**, red fluorescence was observed within 120 minutes of irradiation, indicating cellular

basification during the apoptotic process. It was further possible to sort and count the cells for quantification using the fluorescence signal from the probe.

Recently, Tang and coworkers have reported a ratiometric fluorescent probe **20** that showed pH-dependent cellular permeability.⁶⁶ This probe emitted green light at a basic pH and exhibited a hypsochromic shift with acidification of the medium (**Figure 1.21a**). NMR studies revealed that addition of an acid resulted in the protonation of the nitrogen atom in **20**, leading to the observed change in fluorescence.

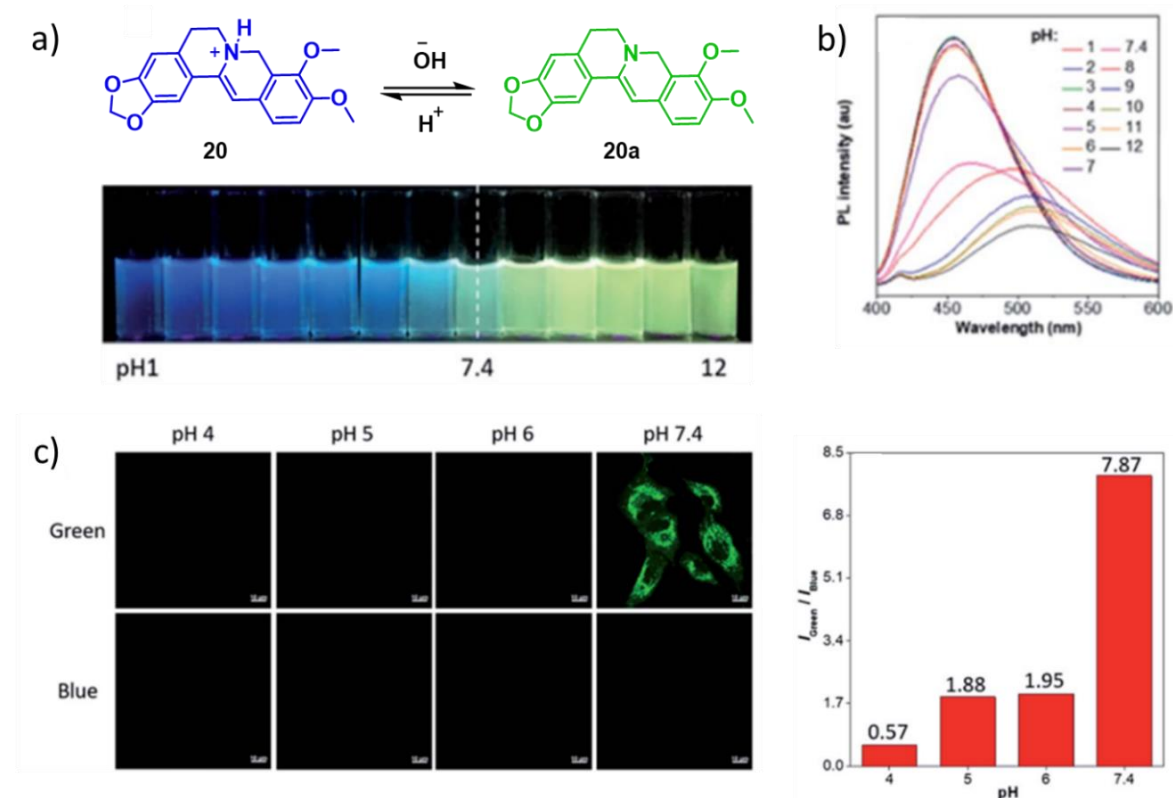


Figure 1.21. (a) Molecular structure of the probe **20** in its protonated and deprotonated forms along with the photograph of its solution at different pH under 365 nm light. (b) pH-dependent emission spectra of **20**. (c) CLSM images of A549 cells incubated with **20** at various pH. Fluorescence intensity ratio in the green/blue channels suggested little to no probe uptake by cell at pH below 7.4. (Adapted with permission from ref 62).

A strong blue emission was observed at acidic pH that decreased gradually upon increasing the pH, and a new peak in the green fluorescence region was found to emerge as pH was changed from neutral to basic region (**Figure 1.21b**). In the case of cellular imaging, unlike other pH probes, the authors did not use ionophores to balance intracellular and extracellular pH. The extracellular medium pH of the cells was altered from pH 4 to 7.4 prior to the addition of **20**. The probe was found to cross the cellular membrane only upon attaining a pH of 7.4 (**Figure 1.21c**), most likely due to the hydrophobic nature of the cellular membrane that allowed only the non-ionized form of **20** to enter the cell.

Single excitation ratiometric probes have recently gained huge popularity due to the ease of experimentation wherein excitation source change is not required during imaging and the background noise emanating from the use of multiple excitation sources is significantly reduced. Song *et al.* have reported a single excitation ratiometric pH probe **21**, based on chromenoquinoline comprising a lysosome targeting group (**Figure 1.22a**).⁶⁷

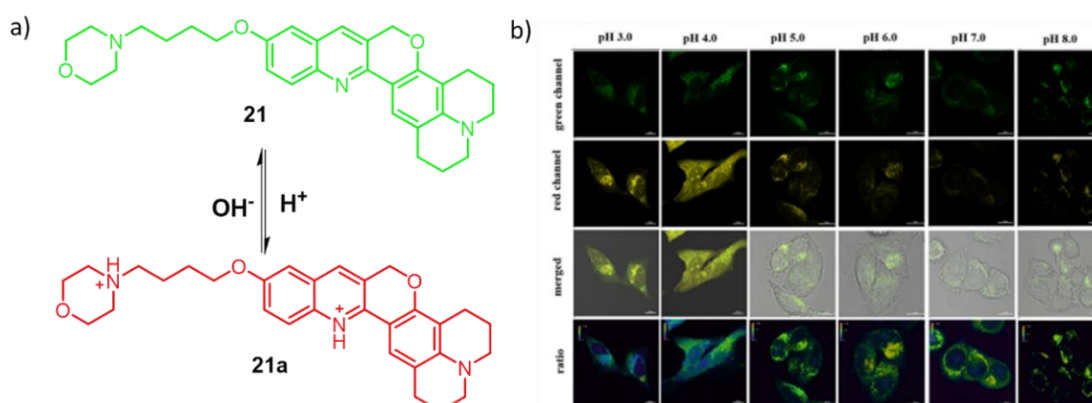


Figure 1.21. (a) Chemical structure of the probe **21** and its changes in acidic and basic medium. (b) Fluorescence images of HeLa cells incubated with **21** at various pH in the green and red channels. The corresponding merged and ratiometric images were also generated. (Adapted with permission from ref 63).

The probe exhibited a long Stokes shift, and excitation at the isosbestic point resulted in a ratiometric fluorescence response from yellow to red upon changing the pH from basic to acidic. Furthermore, it showed excellent lysosomal localization and ratiometric fluorescence change in the green and red channels with variations in the intracellular pH (**Figure 1.22b**). Quantification of lysosomal pH changes during apoptosis was also achieved using the changes in fluorescence intensity of the cells incubated with this probe.

1.10. Development of Novel Fluorescent Cores

A large number of fluorescent sensors and imaging probes for any chosen analyte have been reported in the literature. Most of these probes possess a unique set of functional properties that allows to gather information leading to a better understanding of complex biological systems and processes. However, a detailed survey of the existing literature substantiates the fact that all these probes are derived from a handful of fluorescent core architectures, such as coumarin, BODIPY, fluorescein, rhodamine, cyanine, tetraphenylethylene (TPE), etc. (**Figure 1.23**).^{68–71}

Each core architecture features its own photophysical and physicochemical characteristics, with both pros and cons from a bioimaging perspective. Coumarin has a relatively shorter window for excitation and emission and has been identified as a bottleneck for practical imaging applications, but its excellent photostability and large Stokes shift are highly advantageous. Fluorescein, on the other hand, suffers from high propensity for photobleaching and the narrow Stokes shift limit its use as a preferred contrast agent; however, the exceptionally high molar extinction

coefficients and quantum yields in aqueous medium makes it a reasonably accepted bright dye for imaging applications.

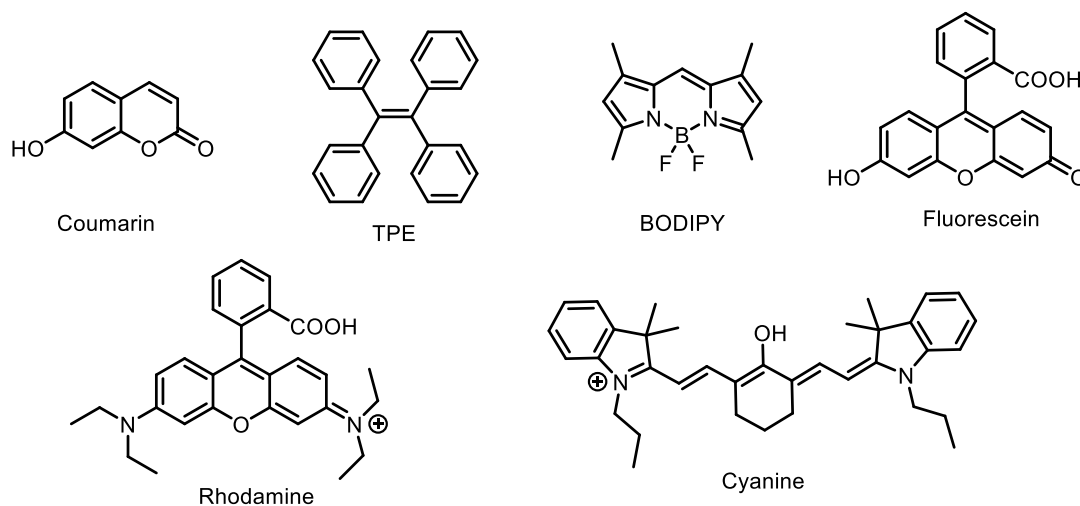


Figure 1.23. Chemical structures of the commonly used fluorescent cores for the development of small molecule-based sensing and imaging probes.

Rhodamine also has a very narrow Stokes shift that seeds in difficulties in choosing the filter set for imaging, leading to autofluorescence; nevertheless, rhodamine derivatives are generally photostable and synthetically accessible. Many of the cyanine dyes are found to have poor stability and low quantum yield, but its NIR emission makes it a potential candidate for *in-vivo* imaging and is preferred over other probes emitting in the visible region. Over the past few decades, these fluorescent core architectures have been synthetically modified with different functional groups for sensing and imaging applications. However, due to the immense scope for new imaging modalities, there is an unmet need for the development of new core architectures that combine the advantages of the existing cores and with possibilities for extensive functional group manipulations for organelle targeting with specificity in bioanalyte recognition. Such a novel core

architecture could eventually be the building block for novel fluorescent probes with new properties and superior performance. Of all major core architectures reported for fluorescence-based bioimaging, the pyrylium and pyridinium derivatives are highly promising, however are least investigated.

Almost four decades ago, Katritzky and coworkers published a series of reports on the synthesis of sterically constrained pyrylium and pyridinium salts (**22a-h**) having a varying number of aromatic rings (**Figure 1.24**).^{72,73} Substituted α -tetralones and chalcones, upon condensation with aldehydes in the presence of an acid afforded heteroatomic polycyclic pyrylium derivatives.

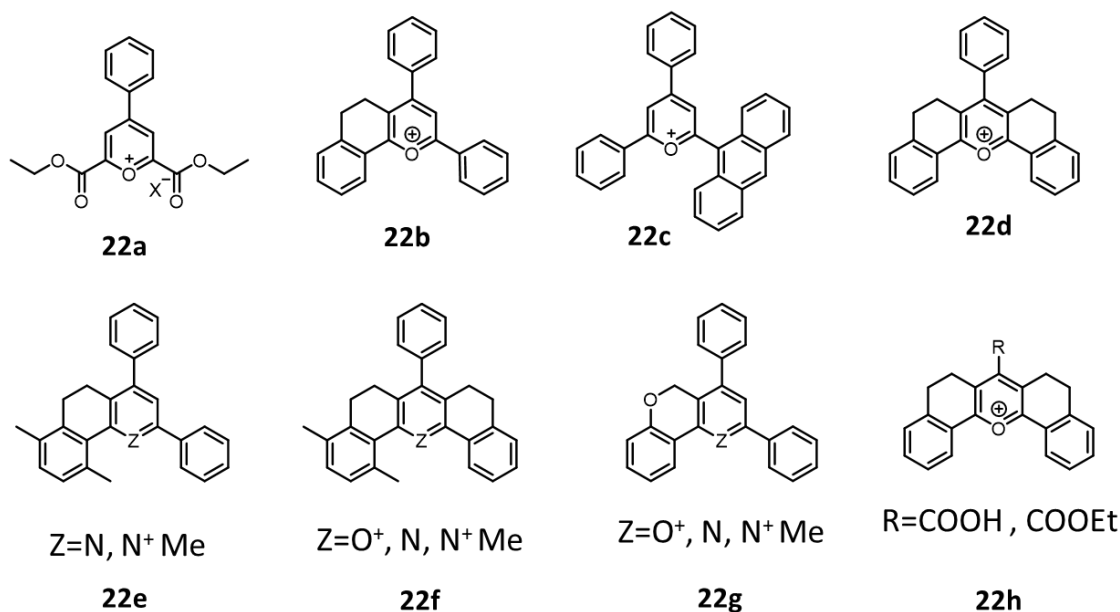


Figure 1.24. Chemical structures of the pyrylium and pyridinium-based molecules having different numbers of aromatic rings and varying functionality.

These pyrylium salts further react with primary and aromatic amines yielding pyridinium derivatives. The developed strategy allowed the gram-scale synthesis of

both pyrylium and pyridinium derivatives, leading to emissive cores with high prospects of scalability.

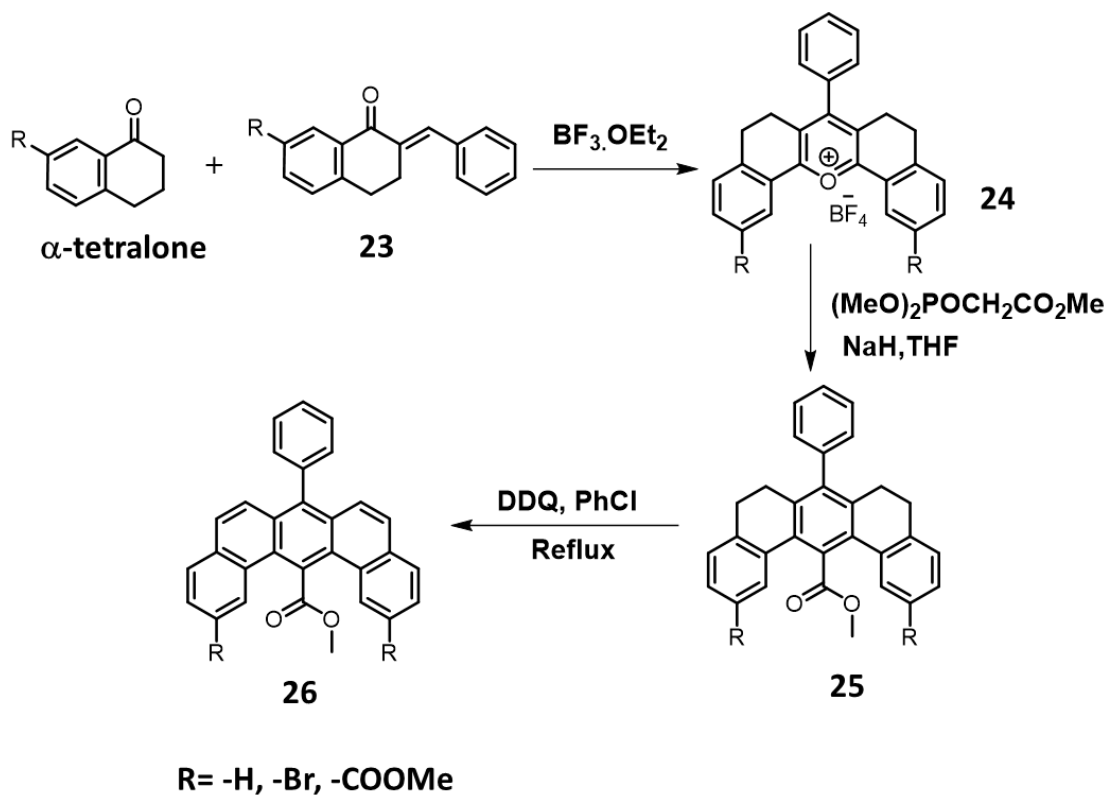


Figure 1.25. Synthetic scheme for the semi-helical aromatic molecules with different functionality using a rigid pyrylium molecule.

Zimmerman *et al.* have also reported similar pyrylium molecule **24**, with different functional groups. With further synthetic modification, they afforded rigid semi-helical aromatic molecule **25** and **26** possessing various functional groups for further derivatization (**Figure 1.25**).⁷⁴

In 2015, Aliaga and coworkers have synthesized a library of pyrylium and pyridinium molecules and reported their extensive photophysical characteristics.⁷⁵ The emission intensity was found to increase with increasing rigidity of the core architecture in these derivatives. Conjugating a radical species (TEMPO) with

pyridinium fluorophores (**27** and **28**, **Figure 1.26a**) resulted in the quenching of the emission due to the spin-exchange process involving the nitroxyl radical.

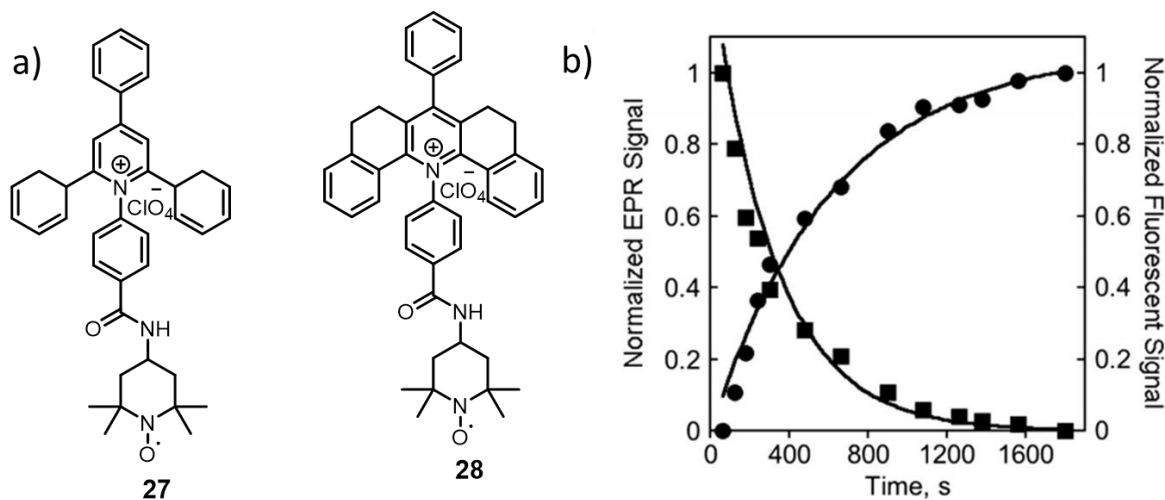


Figure 1.26. (a) Chemical structure of TEMPO-attached flexible and rigid pyridinium molecules **27** and **28**. (b) The secondary plot of the probe's EPR signal and fluorescence signal maxima with time for radical quenching. As radical started quenching, the corresponding EPR signal decreased with a concomitant increase in fluorescence intensity. (Adapted with permission from ref 71).

The original emission of the molecule was restored upon reacting with TROLOX in acetonitrile via the conversion of the nitroxyl radical into diamagnetic hydroxylamine with no possibilities for any spin-exchange process. This radical quenching process was monitored both by fluorescence and EPR methods (**Figure 1.26b**).

Ge *et al.* have reported a nitric oxide sensor using a pyrylium probe that exhibited a turn-ON emission response to the analyte (**Figure 1.27a**).⁷⁶ The non-emissive probe **29** was synthesized by condensing 6-aminonaphthalen-1-ol derivatives and *N*-(2-amino-4-formylphenyl)acetamide. When 1-hydroxy-2-oxo-3-(3-aminopropyl)-3-methyl-1-triazene (NOC13), a nitric oxide donor, was added to a buffer solution of

the probe, NIR emission was found to gradually increase with increasing concentration of NO (**Figure 1.27b**).

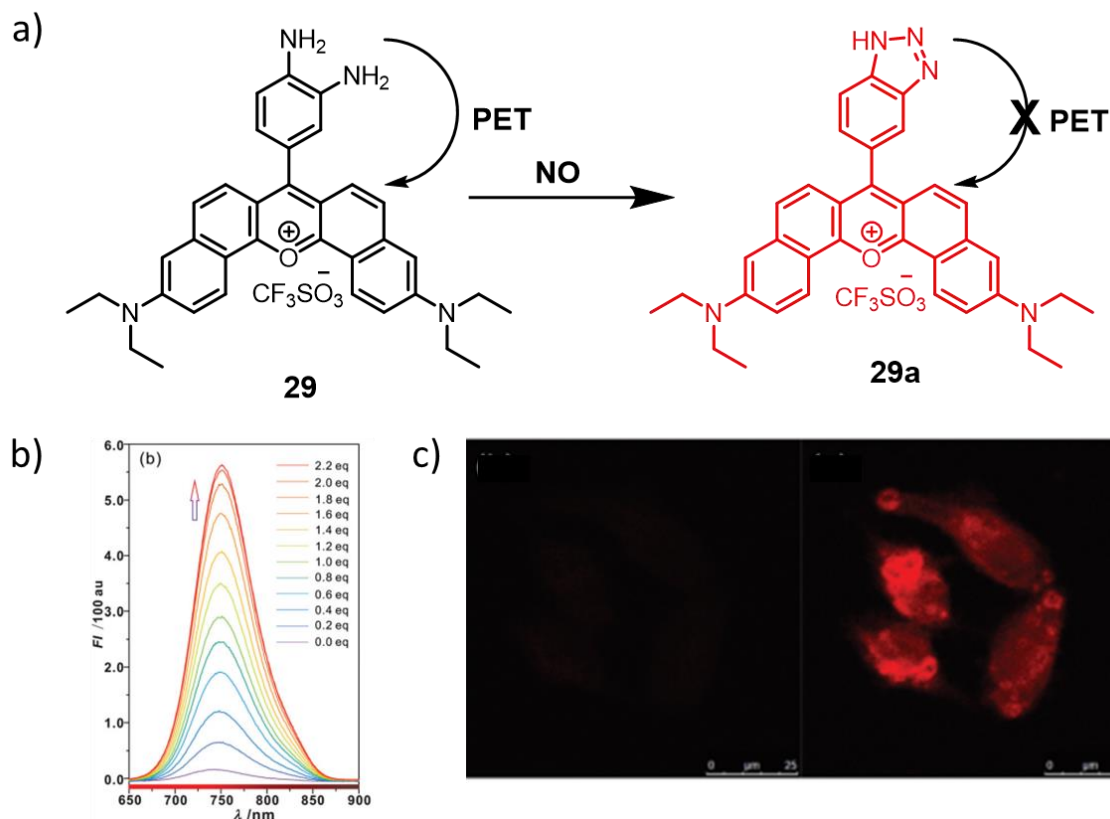


Figure 1.27. (a) Schematic representation of change in the chemical structure of the probe **29** after reaction with NO to form **29a** and its Turn-ON emissive sensing. (b) Change in the emission spectra of the probe with the addition of NOC13. (c) HeLa cells incubated with **29** in the absence and presence of NO. In the absence of NO, there was no emission (left panel), which showed a strong red emission when NO was present (right panel). (Adapted with permission from ref 72).

The promising results thus obtained prompted the authors to use the probe for cellular studies. Incubating HeLa cells with the probe alone did not result in any detectable fluorescence. Upon addition of 100 μM of NOC13 to the cells, an intense red fluorescence was obtained (**Figure 1.27c**).

Cornella and coworkers have synthesized a series of pyrylium and pyridinium probes with varying substitutions and used those for radical C–N borylation of aromatic amines.⁷⁷ Pyrylium molecule **30** was synthesized in a reasonably large

scale (as much as 30 g in a single reaction) and were found to precipitate in their pure form without the need for extensive work-up or purification (**Figure 1.28**). Other pyrylium and pyridinium derivatives were also synthesized in similar scale. Synthesis of any fluorophore in its pure form at such large scales is rather rare and manifests pyrylium and pyridinium derivatives highly attractive for a wider variety of applications.

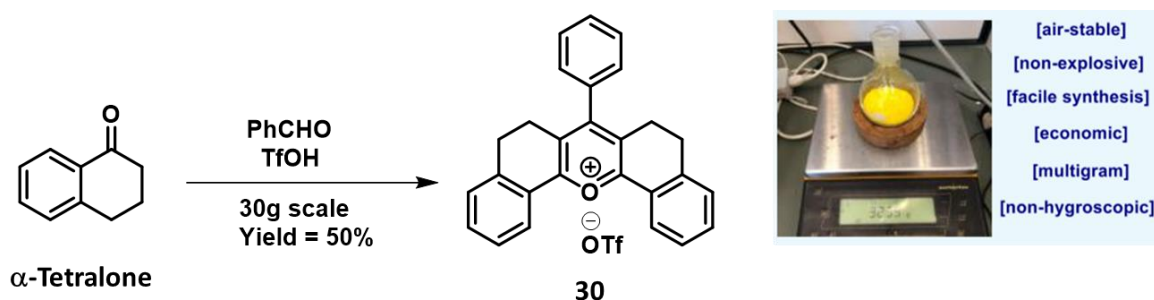


Figure 1.28. (a) Reaction scheme of the large-scale synthesis of the rigid pyrylium salt from tetralone in one step, its daylight photograph, and its advantages as a material for various applications. (Adapted with permission from ref 73).

Recently, Yuan *et al.* have reported a one-step acid-catalyzed condensation reaction for the synthesis of pyrylium derivatives (**31a-f**) (**Figure 1.29a**).⁷⁸ Detailed photophysical studies confirmed that increasing rigidity of the structure leads to better chemical stability and superior emission properties. Altering the aldehyde reagents or the functional groups in these pyrylium salts dictated their quantum yields. Later, a pyrylium-based ratiometric fluorescent probe **31g** for nitroreductase (NTR) detection in cancer cells was proposed by the same research group (**Figure 1.29b**). In this case the initially observed yellow-red emission ($\lambda_{Em} = 575$ nm), was shifted to the far-red region ($\lambda_{Em} = 650$ nm) when exposed to nitroreductase (**Figure 1.29c**).

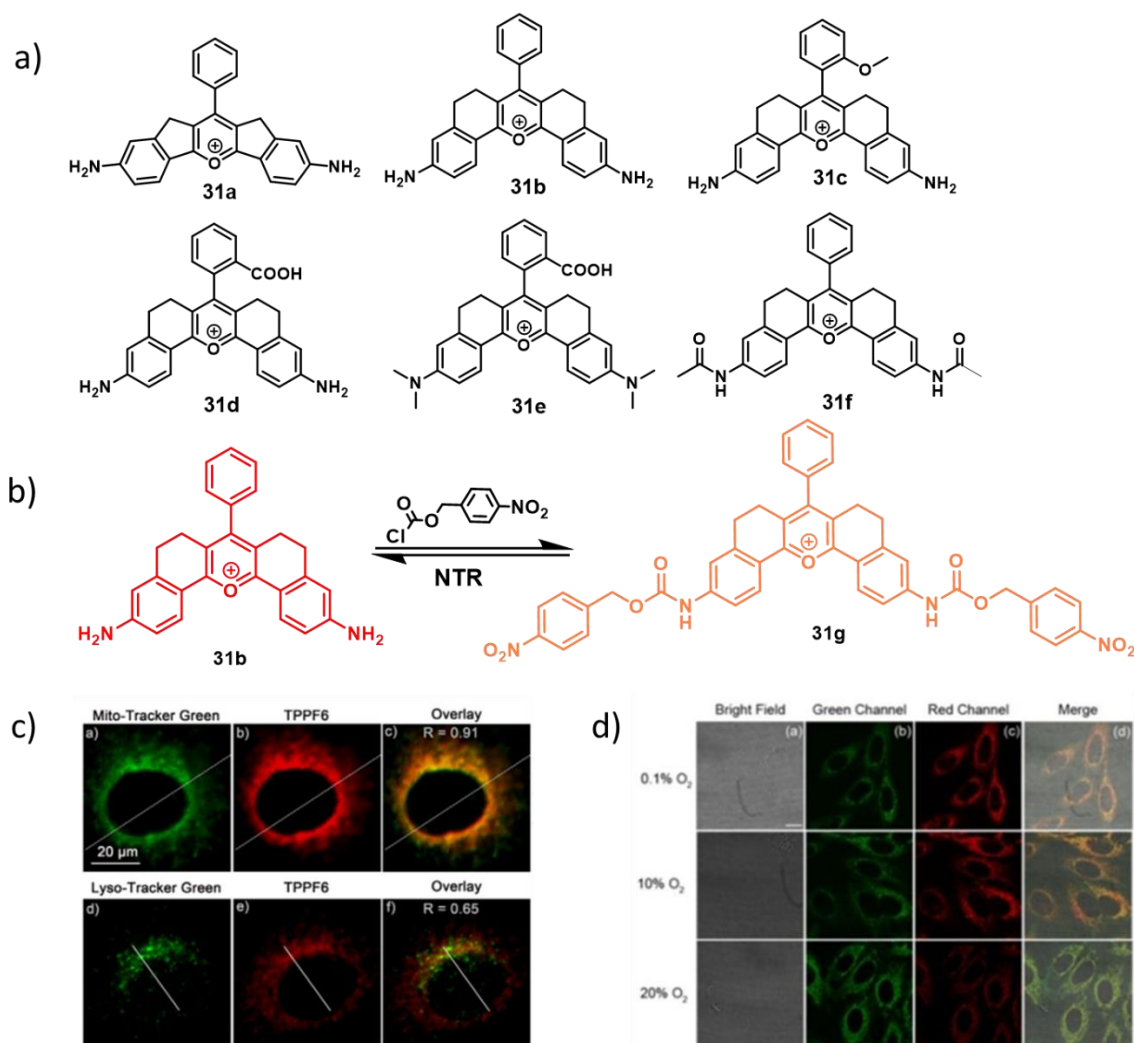


Figure 1.29. (a) Structure of different substituted rigid pyrylium molecules. (b) Scheme for the synthesis of **31** and its use as an NTR sensor. (c) Images of the probe's intracellular organelle localization. HepG2 cells were stained with the probe and commercial Mito-tracker and Lyso-tracker green. Pearson's colocalization coefficient showed a clear mitochondrial localization of the probe. (d) Use of the probe **31g** to differentiate normoxic and hypoxic cells. As hypoxic cells have a higher level of NTR, the probe showed higher fluorescence intensity in cells having lower oxygen concentration which decreased with the increase of intracellular oxygen level. (Adapted with permission from ref 74).

Mitochondrial localization was mostly observed in cellular experiments, most likely due to the presence of the positive charge. As hypoxic cells are known to have a higher level of NTR, HepG2 cells with different concentrations of oxygen (20%, 10% and 0.1%) were incubated with **31g**. Cells having the lowest O₂ levels showed the highest intensity in red channel, which decreased with increase in cellular O₂

level within an hour of incubation (**Figure 1.29d**). These results are indicative of hypoxic cells having a higher level of NTR and the probe's capability for precise detection of NTR in hypoxic environments.

The above discussions clearly depict the significance of small molecule-based pH fluorescent probes for sensing and imaging applications. The previous sections unambiguously corroborate the need to develop new fluorescent core architectures for designing new and efficient probes with unique properties. Construction of new pH probes, tuning their optical properties, sensitivity and operational window, understanding of the response mechanism, and systematic analysis of the output signals have enabled chemists to develop new probes with better utility and promising applications. Use of such probes for subcellular imaging has helped in devising effective protocols for therapy and diagnosis and ensures continued progress in the healthcare sector. Furthermore, well-established synthetic methodologies towards rigid pyrylium and pyridinium salts, their promising photophysical properties, biocompatibility and exceptional physicochemical stability have conveyed the early signs of a new potential fluorescent core architecture with tremendous possibilities for functional group manipulations and application in bioimaging.

1.11. Origin, Objectives and Organization of the Thesis

The work carried out in the present thesis is developed based on a serendipitous formation of a rigid pyrylium fluorophore from a modified Vilsmeier-Haack formylation reaction. The promising reports on the photophysical profiles of

pyrylium and pyridinium derivatives encouraged us to explore this observation in detail. The main objective of the thesis was to synthesize new pyrylium and pyridinium-based fluorescent probes and their use for pH sensing and cellular imaging. Initially, we investigated the mechanism behind the formation of pyrylium salts via Vilsmeier-Haack formylation reaction and developed a new methodology for the synthesis of new pyrylium derivatives with higher yield and better purity under simple experimental conditions and shorter reaction times. The pyrylium salts thus obtained were synthetically modified to develop a pH probe that exhibited a Turn-ON fluorescence response with minute cellular acidification and was used to monitor cellular apoptosis. The results obtained in this study form the subject matter of Chapter 2. In Chapter 3, the pyrylium salts were converted into the corresponding pyridinium derivatives with improved photophysical properties, such as single excitation ratiometric fluorescence response, better chemical stability and photostability, two pKa for a wide range of pH sensitivity, improved solubility, etc. In this chapter, we propose these pyridinium derivatives as an efficient ratiometric pH probe for subcellular bioimaging. In the final chapter, we attached an Endoplasmic Reticulum-targeting group to the pyridinium pH probe and used its mega Stokes shift for converting a single probe into a ‘Turn-ON’, ratiometric, and ‘Turn-OFF’ probe by simply varying the excitation wavelength. The molecules were then used to monitor intracellular pH change during heat shock via simultaneous multi-channel imaging and analysis. Overall, the thesis provides a systematic and detailed investigation of bioimaging at the subcellular level using in-house developed pH probes. The results presented in this thesis are expected to provide

valuable insights into various biochemical processes and envisages the development of new and improved modalities for detection, diagnosis and treatment associated with these systems. We also hope that this work will motivate researchers to adopt similar synthetic methodologies for the development of new and improved bioimaging probes and contrast agents.

1.12. References

- [1] R. Gentili, R. Ambrosini, C. Montagnani, S. Caronni and S. Citterio, *Front. Plant Sci.*, 2018, 9, 1335–1338.
- [2] A. Albu, C.-G. Radu-Rusu, I. M. Pop, G. Frunza and G. Nacu, *Agriculture*, 2021, 11, 247–252.
- [3] P. H. Gleick, *Annu. Rev. Environ. Resour.*, 2003, 28, 275–314.
- [4] Y. Dai, Y. Wu, G. Liu and J. J. Gooding, *Angew. Chem. Int. Ed.*, 2020, 132, 20938–20950.
- [5] J.-T. Hou, W. X. Ren, K. Li, J. Seo, A. Sharma, X.-Q. Yu and J. S. Kim, *Chem. Soc. Rev.*, 2017, 46, 2076–2090.
- [6] D. Wu, A. C. Sedgwick, T. Gunnlaugsson, E. U. Akkaya, J. Yoon and T. D. James, *Chem. Soc. Rev.*, 2017, 46, 7105–7123.
- [7] R. Zhang and J. Yuan, *Acc. Chem. Res.*, 2020, 53, 1316–1329.
- [8] K. P. Carter, A. M. Young and A. E. Palmer, *Chem. Rev.*, 2014, 114, 4564–4601.
- [9] T. D. Ashton, K. A. Jolliffe and F. M. Pfeffer, *Chem. Soc. Rev.*, 2015, 44, 4547–4595.
- [10] Y. He, S. Wang, P. Yu, K. Yan, J. Ming, C. Yao, Z. He, A. M. El-Toni, A. Khan, X. Zhu, C. Sun, Z. Lei and F. Zhang, *Chem. Sci.*, 2021, 12, 10474–10482.
- [11] Y. Wang, G. Song, S. Liao, Q. Qin, Y. Zhao, L. Shi, K. Guan, X. Gong, P. Wang, X. Yin, Q. Chen and X.-B. Zhang, *Angew. Chem. Int. Ed.*, 2021, 60, 19779–19789.

- [12] L. Wu, C. Huang, B. P. Emery, A. C. Sedgwick, S. D. Bull, X.-P. He, H. Tian, J. Yoon, J. L. Sessler and T. D. James, *Chem. Soc. Rev.*, 2020, **49**, 5110–5139.
- [13] A. S. Klymchenko, *Acc. Chem. Res.*, 2017, **50**, 366–375.
- [14] M. Yang, J. Fan, J. Du and X. Peng, *Chem. Sci.*, 2020, **11**, 5127–5141.
- [15] K. J. Bruemmer, S. W. M. Crossley and C. J. Chang, *Angew. Chem. Int. Ed.*, 2020, **59**, 13734–13762.
- [16] M. Vendrell, D. Zhai, J. C. Er and Y.-T. Chang, *Chem. Rev.*, 2012, **112**, 4391–4420.
- [17] W. Xu, Z. Zeng, J.-H. Jiang, Y.-T. Chang and L. Yuan, *Angew. Chemie Int. Ed.*, 2016, **55**, 13658–13699.
- [18] H. Shi, R. T. K. Kwok, J. Liu, B. Xing, B. Z. Tang and B. Liu, *J. Am. Chem. Soc.*, 2012, **134**, 17972–17981.
- [19] R. Blau, Y. Epshtein, E. Pisarevsky, G. Tiram, S. Israeli Dangoor, E. Yeini, A. Krivitsky, A. Eldar-Boock, D. Ben-Shushan, H. Gibori, A. Scomparin, O. Green, Y. Ben-Nun, E. Merquiol, H. Doron, G. Blum, N. Erez, R. Grossman, Z. Ram, D. Shabat and R. Satchi-Fainaro, *Theranostics*, 2018, **8**, 3437–3460.
- [20] C. Heckl, M. Aumiller, A. Rühm, R. Sroka and H. Stepp, *Photochem. Photobiol.*, 2020, **96**, 388–396.
- [21] S. Kim, T. Tachikawa, M. Fujitsuka and T. Majima, *J. Am. Chem. Soc.*, 2014, **136**, 11707–11715.
- [22] Y. Ardeshirpour, V. Chernomordik, J. Capala, M. Hassan, R. Zielinsky, G. Griffiths, S. Achilefu, P. Smith and A. Gandjbakhche, *Technol. Cancer Res. Treat.*, 2011, **10**, 549–560.
- [23] K. Obersioht, *Biochem.Z.*, 1909, 131–304.
- [24] S. R. Values, 1985, **57**, 531–542.
- [25] A. Steinegger, O. S. Wolfbeis and S. M. Borisov, *Chem. Rev.*, 2020, **120**, 12357–12489.
- [26] W. S. Hughes, *J. Am. Chem. Soc.*, 1922, **44**, 2860–2867.

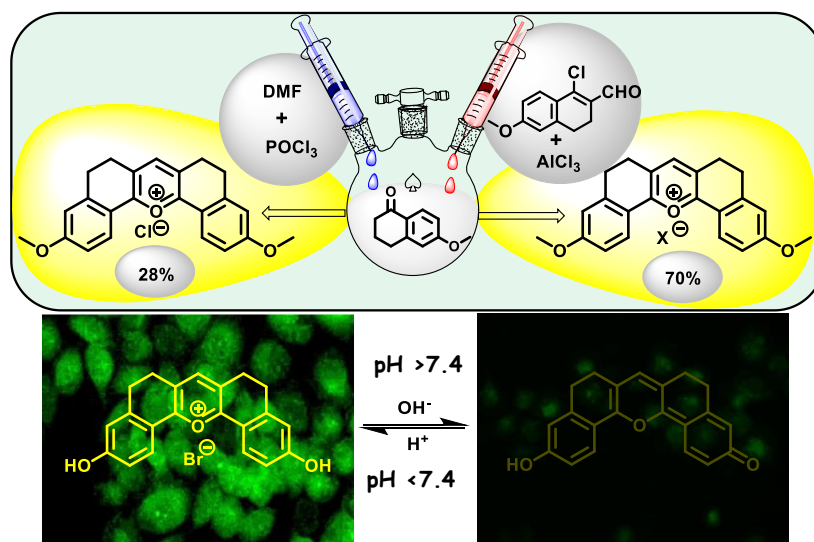
-
- [27] P. T. Kerridge, *Biochem. J.*, 1925, **19**, 611–617.
- [28] B. Walter, *Anal. Chem.*, 1983, **55**, 498A–514A.
- [29] S. R. Goldstein, J. I. Peterson and R. V Fitzgerald, *J. Biomech. Eng.*, 1980, **102**, 141–146.
- [30] M. Bacci, F. Baldini and S. Bracci, *Appl. Spectrosc.*, 1991, **45**, 1508–1515.
- [31] Y. Yue, F. Huo, S. Lee, C. Yin and J. Yoon, *Analyst*, 2017, **142**, 30–41.
- [32] S. T. Whitten and V. J. Hilser, *Proc. Natl. Acad. Sci.*, 2005, **102**, 4282–4287.
- [33] G. Filomeni, D. De Zio and F. Cecconi, *Cell Death Differ.*, 2015, **22**, 377–388.
- [34] D. Lagadic-Gossmann, L. Huc and V. Lecureur, *Cell Death Differ.*, 2004, **11**, 953–961.
- [35] J. R. Casey, S. Grinstein and J. Orłowski, *Nat. Rev. Mol. Cell Biol.*, 2010, **11**, 50–61.
- [36] S. L. Bearne, *J. Chem. Educ.*, 2014, **91**, 84–90.
- [37] B. Fang, D. Wang, M. Huang, G. Yu and H. Li, *Int. J. Neurosci.*, 2010, **120**, 591–595.
- [38] T. Fukuda, L. Ewan, M. Bauer, R. J. Mattaliano, K. Zaal, E. Ralston, P. H. Plotz and N. Raben, *Ann. Neurol.*, 2006, **59**, 700–708.
- [39] R. J. Gillies, Z. Liu and Z. Bhujwalla, *Am. J. Physiol.*, 1994, **267**, C195–203.
- [40] L. Dong, E. A. Krewson and L. V Yang, *Int. J. Mol. Sci.*, 2017, **18**, 278.
- [41] N. V Di Russo, D. A. Estrin, M. A. Martí and A. E. Roitberg, *PLOS Comput. Biol.*, 2012, **8**, e1002761.
- [42] M. Tantama, Y. P. Hung and G. Yellen, *J. Am. Chem. Soc.*, 2011, **133**, 10034–10037.
- [43] Y. Lei, X. He, J. Tang, H. Shi, D. He, L. Yan, J. Liu, Y. Zeng and K. Wang, *Chem. Commun.*, 2018, **54**, 10288–10291.
- [44] M. E. Muroski, K. J. F. Carnevale, R. A. Riskowski and G. F. Strouse, *ACS Nano*, 2015, **9**, 124–133.

- [45] K. J. Robinson, G. T. Huynh, B. P. Kouskousis, N. L. Fletcher, Z. H. Houston, K. J. Thurecht and S. R. Corrie, *ACS Sensors*, 2018, **3**, 967–975.
- [46] G. Kocak, C. Tuncer and V. Bütün, *Polym. Chem.*, 2017, **8**, 144–176.
- [47] A. U. Alam, Y. Qin, S. Nambiar, J. T. W. Yeow, M. M. R. Howlader, N.-X. Hu and M. J. Deen, *Prog. Mater. Sci.*, 2018, **96**, 174–216.
- [48] M. Na, Y. Han, Y. Chen, S. Ma, J. Liu and X. Chen, *Anal. Chem.*, 2021, **93**, 5185–5193.
- [49] X. Wang, M. Tian, Z. Gou and Y. Zuo, *J. Mater. Chem. C*, 2021, **9**, 2392–2397.
- [50] B. S. Stromer and C. V. Kumar, *Adv. Funct. Mater.*, 2017, **27**, 1603874.
- [51] P. Anees, K. V. Sudheesh, P. Jayamurthy, A. R. Chandrika, R. V. Omkumar and A. Ajayaghosh, *Chem. Sci.*, 2016, **7**, 6808–6814.
- [52] M. Zhao, J. Wang, Z. Lei, L. Lu, S. Wang, H. Zhang, B. Li and F. Zhang, *Angew. Chem. Int. Ed.*, 2021, **60**, 5091–5095.
- [53] M. Kneen, J. Farinas, Y. Li and A. S. Verkman, *Biophys. J.*, 1998, **74**, 1591–1599.
- [54] J. Han and K. Burgess, *Chem. Rev.*, 2010, **110**, 2709–2728.
- [55] H. Lee, W. Akers, K. Bhushan, S. Bloch, G. Sudlow, R. Tang and S. Achilefu, *Bioconjug. Chem.*, 2011, **22**, 777–784.
- [56] D. Asanuma, Y. Takaoka, S. Namiki, K. Takikawa, M. Kamiya, T. Nagano, Y. Urano and K. Hirose, *Angew. Chem. Int. Ed.*, 2014, **53**, 6085–6089.
- [57] M. Grossi, M. Morgunova, S. Cheung, D. Scholz, E. Conroy, M. Terrile, A. Panarella, J. C. Simpson, W. M. Gallagher and D. F. O’Shea, *Nat. Commun.*, 2016, **7**, 10855.
- [58] L. Fan, X. Wang, J. Ge, F. Li, C. Zhang, B. Lin, S. Shuang and C. Dong, *Chem. Commun.*, 2019, **55**, 6685–6688.
- [59] S. Y. Kim, A. Podder, H. Lee, Y.-J. Cho, E. H. Han, S. Khatun, J. L. Sessler, K. S. Hong and S. Bhuniya, *Chem. Sci.*, 2020, **11**, 9875–9883.
- [60] X. Zhuge, J. Li, Y. Li and C. Yuan, *Luminescence*, 2020, **35**, 373–378.

- [61] K. Qiu, L. Ke, X. Zhang, Y. Liu, T. W. Rees, L. Ji, J. Diao and H. Chao, *Chem. Commun.*, 2018, **54**, 2421–2424.
- [62] H. Mai, Y. Wang, S. Li, R. Jia, S. Li, Q. Peng, Y. Xie, X. Hu and S. Wu, *Chem. Commun.*, 2019, **55**, 7374–7377.
- [63] M. H. Lee, J. H. Han, J. H. Lee, N. Park, R. Kumar, C. Kang and J. S. Kim, *Angew. Chem. Int. Ed.*, 2013, **52**, 6206–6209.
- [64] S. Wang, B. Wang, L. Zhu, J.-T. Hou and K.-K. Yu, *Chem. Commun.*, 2021, **57**, 1510–1513.
- [65] T. Jiang, X. Wang, G. Wang, Y. Wang, K. Wang, X. Xuan, C. Chen, K. Jiang and H. Zhang, *Chem. Commun.*, 2019, **55**, 5279–5282.
- [66] Y. Gu, Z. Zhao, G. Niu, H. Zhang, Y. Wang, R. T. K. Kwok, J. W. Y. Lam and B. Z. Tang, *Chem. Sci.*, 2020, **11**, 5753–5758.
- [67] X. Liu, Y. Su, H. Tian, L. Yang, H. Zhang, X. Song and J. W. Foley, *Anal. Chem.*, 2017, **89**, 7038–7045.
- [68] D. Cao, Z. Liu, P. Verwilt, S. Koo, P. Jangjili, J. S. Kim and W. Lin, *Chem. Rev.*, 2019, **119**, 10403–10519.
- [69] U. Haris, H. N. Kagalwala, Y. L. Kim and A. R. Lippert, *Acc. Chem. Res.*, 2021, **54**, 2844–2857.
- [70] S. Liu, G. Feng, B. Z. Tang and B. Liu, *Chem. Sci.*, 2021, **12**, 6488–6506.
- [71] X. Tian, L. C. Murfin, L. Wu, S. E. Lewis and T. D. James, *Chem. Sci.*, 2021, **12**, 3406–3426.
- [72] A. R. Katritzky, F. Al-Omran, R. C. Patel and S. S. Thind, *J. Chem. Soc. Perkin Trans. 1*, 1980, 1890–1894.
- [73] A. R. Katritzky, A. Chermrapai, S. Bravo and R. C. Patel, *Tetrahedron*, 1981, **37**, 3603–3607.
- [74] S. C. Zimmerman, *Tetrahedron Lett.*, 1988, **29**, 983–986.
- [75] C. Aliaga, F. Celis, S. Lühr and R. Oñate, *J. Fluoresc.*, 2015, **25**, 979–983.

-
- [76] W. Liu, C. Fan, R. Sun, Y.-J. Xu and J.-F. Ge, *Org. Biomol. Chem.*, 2015, **13**, 4532–4538.
- [77] Y. Ma, Y. Pang, S. Chhabra, E. J. Reijerse, A. Schnegg, J. Niski, M. Leutzsch and J. Cornella, *Chem. Eur. J.*, 2020, **26**, 3738–3743.
- [78] S.-Y. Wen, W. Zhang, T.-B. Ren, Q.-L. Zhang, Y.-P. Liu, L. Shi, R. Hu, X.-B. Zhang and L. Yuan, *Chem. Eur. J.*, 2019, **25**, 6973–6979.

A New Pentacyclic Pyrylium Probe with Distinct Fluorescence Response to pH Imbalance during Apoptosis



2.1. Abstract

Monitoring of apoptotic progression using fluorescence imaging is one among the crucial steps in determining the efficacy of a drug during cancer therapy and personalized medicine. Since, cellular acidification during apoptosis is an important indicator of disease condition, quantification of minute pH variation in cells is of great significance. Therefore, efficient fluorescent probes for monitoring pH imbalance during cellular dysfunction, especially in case of metastatic or invasive carcinoma, are of contemporary interest. To this end, we synthesized a new pentacyclic pyrylium

fluorophore using a modified Vilsmeier-Haack reaction, with a Turn-ON response towards minute acidification of the cells and the cellular environment. We have also demonstrated the application of this fluorophore in monitoring extended and dynamic pH changes during cellular apoptosis. Quantification of intracellular pH at different time points during apoptosis was achieved using image analysis. This new pH probe is indeed a potential small-molecule tool with profound application in drug discovery, identification of leads and dose determination in cancer therapy.

2.2. Introduction

Scientific and technological advancements in clinical diagnosis and medical algorithms have revolutionized the field of cancer therapy in recent years.¹⁻⁴ Several treatment modalities have thus emerged and exhibited high therapeutic efficacy with the possibilities of selectively targeting cancer cells, while minimizing the damage to normal cells.⁵⁻¹¹ However, the efficacy of these drugs or modalities may vary with patients or with their mechanism of action.¹² Therefore, rigorous screening and identification of promising leads have become decisive in drug development.¹³⁻¹⁵ Apoptosis, an organized process for cell death, plays a vital role in eliminating cancer cells during chemo-and radiotherapy and several other treatment modalities.¹⁶⁻¹⁹ Tracking apoptotic progression is probably the best strategy to access the therapeutic response of a patient.²⁰⁻²³ Hence, development of new markers and probes for real-time monitoring of apoptosis has been a thrust area of research in clinical diagnosis.²⁴⁻²⁷

One of the commonly used apoptosis markers is annexin V, that binds selectively with phosphatidylserine (PS). PS expresses itself on the extracellular plasma membrane and moves from the cytoplasm during apoptosis.^{28–30} However, its application is rather restricted as other biological processes such as necrosis also exhibit similar phosphatidylserine expression, leading to false-positives during apoptosis monitoring.³¹ Another widely used strategy for apoptosis marking is the laddering of DNA fragmentation,³² that involves complicated multistep reaction-based detection process. Further, internucleosomal DNA cleavages are not exclusive to apoptosis alone, that limits the reliability of these processes.

To address these issues, a number of small molecule-based fluorescent probes have been developed by various research groups for apoptosis monitoring. Liu and co-workers have reported an AIE-based fluorescent Turn-ON probe **1**, based on Caspase-3/7 specific enzymatic cleavage of the peptide bond (**Figure 2.1a**), and gets overexpressed in apoptotic cells.³³ The peptide-appended TPE was non-fluorescent in buffer solutions of pH 7.4, and peptide cleavage mediated by Caspase-3/7 resulted in an intense emission in the range of 405–585 nm, due to aggregation (**Figure 2.1b**). The fluorescence intensity was found to be linearly dependent on caspase concentration (**Figure 2.1c**). Using lysates of normal and apoptotic MCF-7 cells, the AIE enhancement was observed only for the lysate of apoptotic cells, while normal cell lysate remained non-fluorescent. Moreover, fluorescence intensity increased several folds when apoptosis inducers such as sodium ascorbate, cisplatin and STS were added

to MCF-7 cells, and the results were in agreement with their reported efficacy, thereby confirming apoptosis monitoring ability of probe **1**.

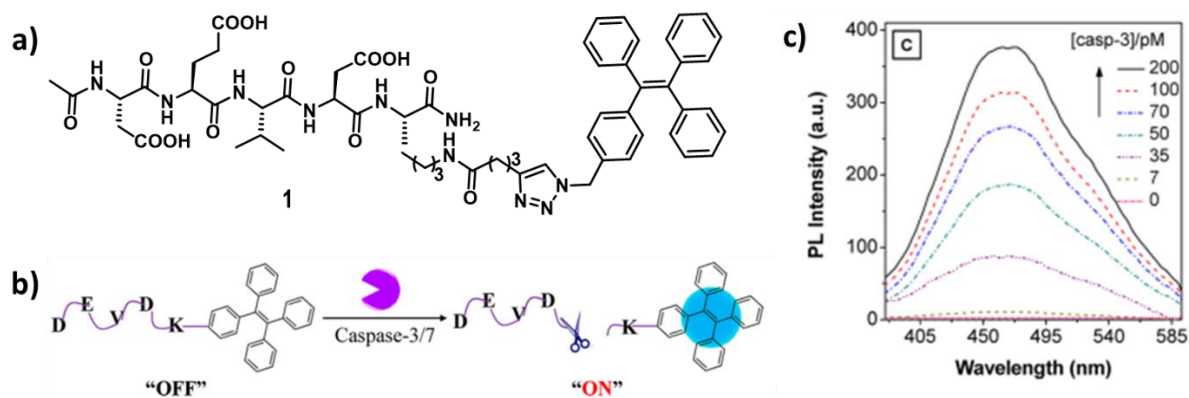


Figure 2.1. (a) Chemical structure of the peptide-based probe **1**. (b) Schematic representation of Caspase-3/7 sensing mechanism of the probe. (c) Emission spectra of the probe **1** in presence of caspase-3 at various concentrations. (Adapted with permission from ref 33).

Depletion in cellular glutathione (GSH) level is another indicator of apoptosis.^{34,35}

Increase in ROS concentration during apoptosis results in the suppression of GSH level, which is a major cellular antioxidant. Ajayaghosh *et. al.* have reported a Squaraine-based ratiometric NIR fluorophore for real-time apoptosis monitoring through GSH sensing.³⁶ This bispyrrole-based π -extended Squaraine dye **2** showed initial emission maximum at 690 nm which bathochromically shifted to 560 nm when the probe reacted with GSH (**Figure 2.2a**). When HepG2 cells were treated with probe **2**, the corresponding fluorescence microscope images showed higher emission intensity in the green channel compared to the red channel. Treating cells with *N*-ethylmaleimide (NEM), a known GSH blocking agent and α -lipoic acid (LPA), a GSH inducer, the fluorescence intensity was found to increase in the red and green channels, respectively

(**Figure 2.2b**). Furthermore, incubating with paclitaxel, an anti-cancer drug, the green fluorescence gradually decreased with concomitant increase in the red fluorescence. These results are indicative of a decrease in GSH level with apoptotic progression and provides a reliable information for monitoring apoptosis in live cells.

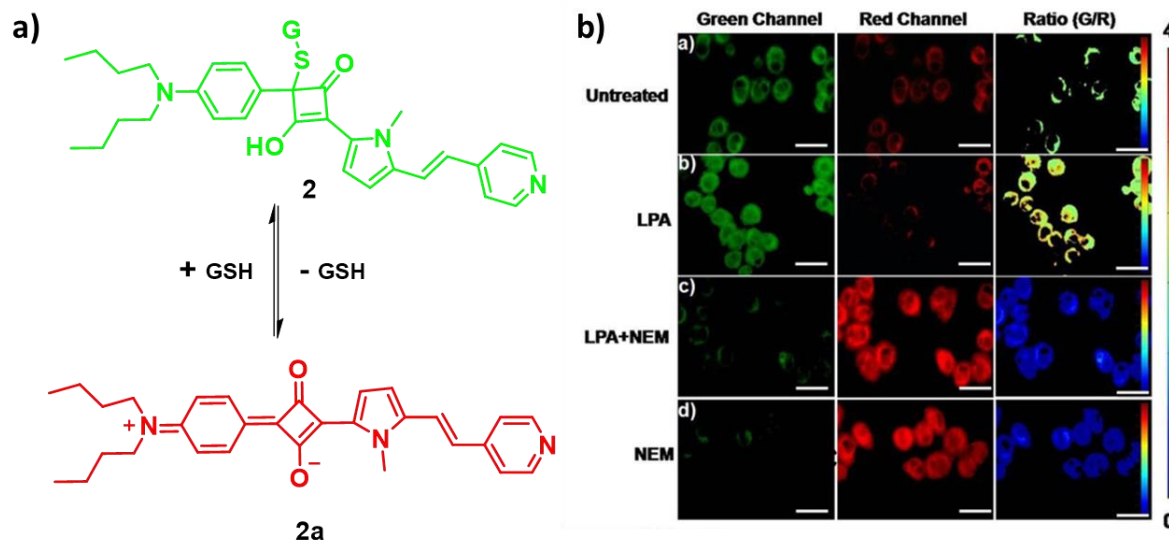


Figure 2.2. (a) Chemical structure and the schematic illustration of ratiometric sensing of GSH during apoptosis using probe **2**. (b) Fluorescence microscope images of HepG2 cells, stained with probe **2** in green and red channels after treatment with different apoptotic inducers to alter intracellular GSH level. Ratiometric images were also constructed for GSH quantification. (Adapted with permission from ref 36).

Cysteine (Cys) is another well-known cellular antioxidant.^{37,38} Meng and co-workers have reported a carbazole-based two-photon ratiometric sensor **3** with two pendent aldehyde groups for selective detection of Cys over Homocysteine (Hcy) (**Figure 2.3a**).³⁹ The initial emission centered at 521 nm was found to be shifted to 390 nm in presence of Cys (**Figure 2.3b**). When HeLa cells were incubated with the probe, a strong emission in the green channel was observed along with a weak blue emission due to the presence of intracellular Cys. HeLa cells stained with the probe were further

treated with H_2O_2 , and as the ROS concentration increased, fluorescence intensity started decreasing in the blue channel with a concomitant increase in the intensity in the green channel. The rate of apoptosis was simultaneously found to increase (0.10% to 17.27%), corroborating the probe's efficacy in monitoring cellular apoptosis. Similar results were also obtained when apoptosis was induced in zebrafish using LPS in presence of the probe under *in-vivo* conditions (**Figure 2.3c**).

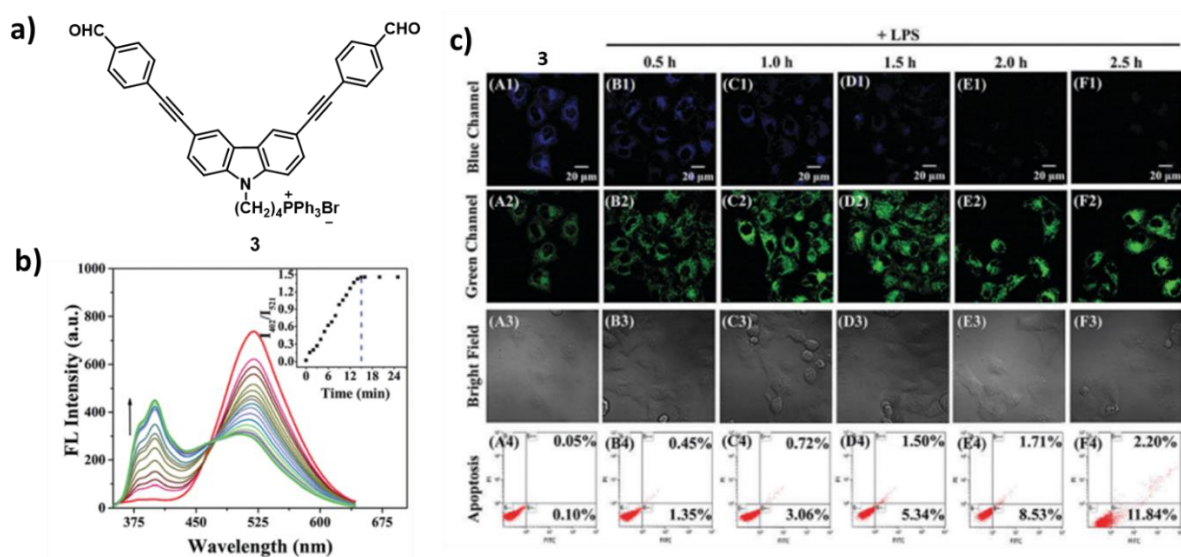


Figure 2.3. (a) Chemical structure of the carbazole-based probe **3**. (b) Fluorescence response of the probe with increasing concentration of Cys. (c) Images of probe **3** incubated HeLa cells in blue and green channels to monitor the depletion of Cys with apoptosis. (Adapted with permission from ref 39).

In an attempt to understand the interaction between various organelles during apoptosis, Yu and co-workers used a single-core fluorescent pH probe for dual-color imaging of nuclei and mitochondria simultaneously. The fluorophore **4** had a hydroxyl group for pH response, benzothiazolium moiety for DNA binding and the positive charge ensured mitochondria targeting (**Figure 2.4a**).⁴⁰ A green fluorescence ($\lambda_{\text{max}} = 550 \text{ nm}$) was observed in acidic medium, that turned red ($\lambda_{\text{max}} = 605 \text{ nm}$) under basic pH with a fast

kinetics. Colocalization experiments confirmed the localization of the probe in the nucleus (colocalization coefficient = 0.93) and mitochondria (colocalization coefficient = 0.87) with distinct green and red emission, respectively, due to distinct organelle-specific pH of the cells. (**Figure 2.4b**) The probe incubated cells were treated with two anti-cancer agents, Paclitaxel and Rotenone for 36 and 24 h, respectively, to induce apoptosis. Image analysis showed a decrease in red fluorescence with no significant change in green fluorescence, indicating changes in mitochondrial pH alone during apoptosis.

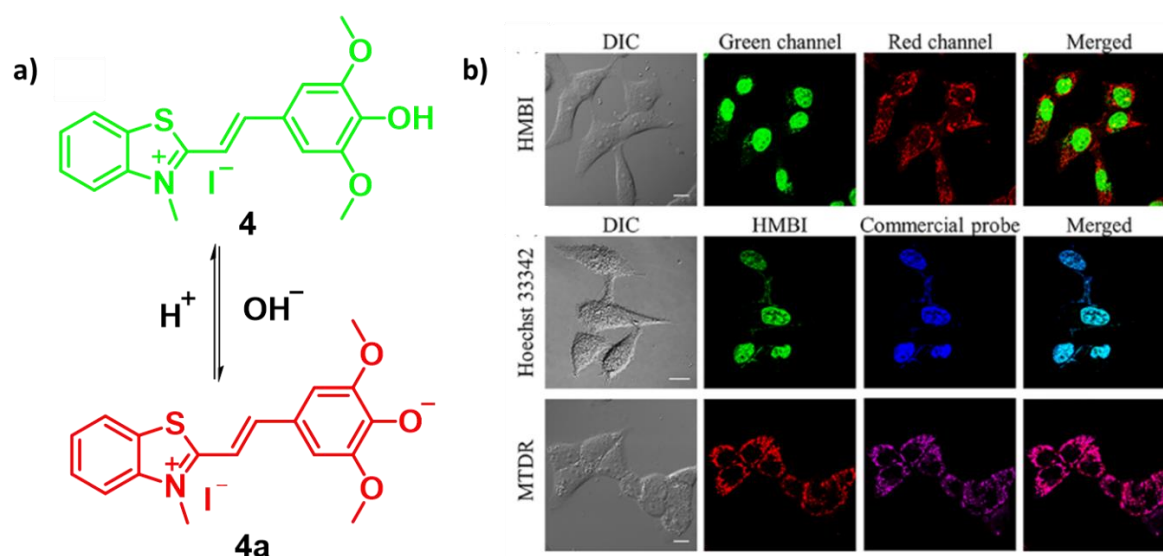


Figure 2.4. (a) Chemical structure and the pH-responsive structural change in the benzothiazolium probe **4**. (b) Fluorescent microscope images showing colocalization of the probe **4** with Hoechst 33342 and MTDR. (Adapted with permission from ref 40).

Though there are several probes for apoptotic monitoring, only a few are capable of tracking cell death precisely and quantitatively.^{41–43} Therefore, we designed a Pentacyclic symmetric pyrylium (**PS-OH**)-based Turn-ON pH probe and developed a new method for the synthesis of rigid pyrylium cores. **PS-OH** has great potential as a

probe to quantify intracellular pH as it shows sharp enhancement in fluorescence with minute acidification of cells. The potential application of **PS-OH** was further explored in monitoring cellular pH with apoptotic progression. The development of a general synthetic strategy towards rigid pyrylium-based fluorophores and application of this new imaging agent in monitoring and quantifying miniscule pH variations in cells are described in the forthcoming sections.

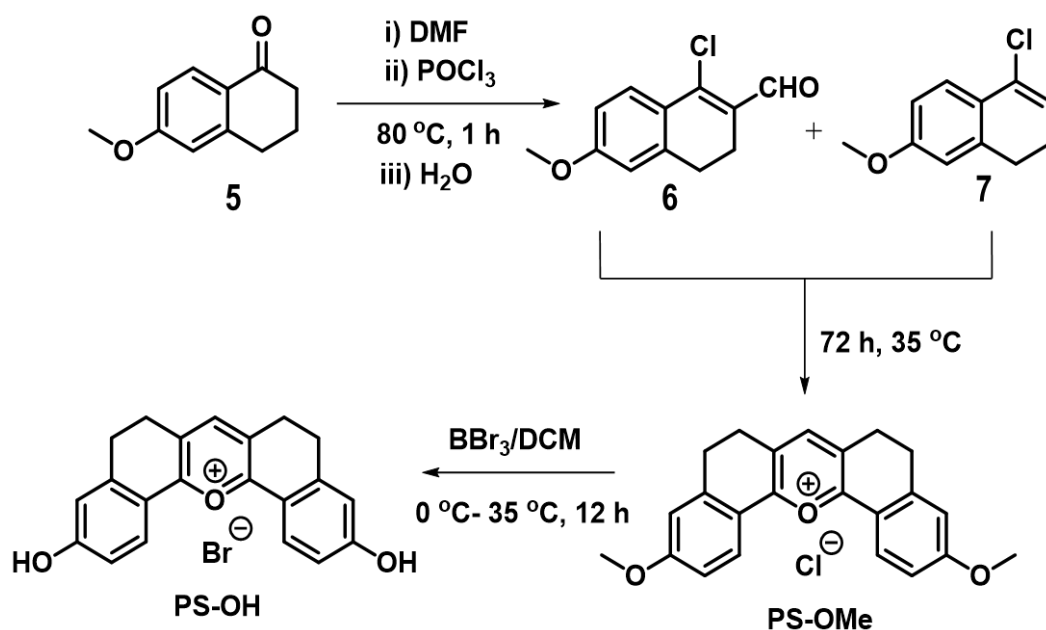
2.3. Results and Discussion

2.3.1. Synthesis of Pyrylium Derivatives

In an attempt to synthesize a new donor-acceptor type fluorescent probe for detecting pH variations in cells, 6-methoxy tetralone **5**, a key intermediate in the synthesis of several heterocycles with diverse pharmacological properties, was subjected to Vilsmeier–Haack reaction.^{44–46} Subsequent demethylation of the Vilsmeier–Haack product afforded a pentacyclic pyrylium core flanked by free hydroxy groups at both ends.

Mechanistically, Vilsmeier–Haack formylation reaction of **5** at 80 °C afforded a reactive 1-chloro-6-methoxy-3,4-dihydronaphthalene-2-carbaldehyde **6**. In ice-cold condition, *N,N*-Dimethylformamide (DMF) and phosphorus oxychloride (POCl₃) were premixed to obtain the Vilsmeier–Haack iminium salt, (*N*-(chloromethylene)-*N*-methylmethanaminium). On the contrary, dropwise addition of POCl₃ to the tetralone **5**

in DMF at 80 °C led to an additional product, 4-chloro-1,2-dihydro-7-methoxynaphthalene **7** along with compound **6**. The formylation reaction was found to be suppressed, unless the Vilsmeier–Haack iminium salts are prepared through a premixed protocol. It was also observed that the tetralone **5** reacts with POCl₃ to afford a reactive intermediate **7** along with the expected product **6**, irrespective of the reaction temperature.

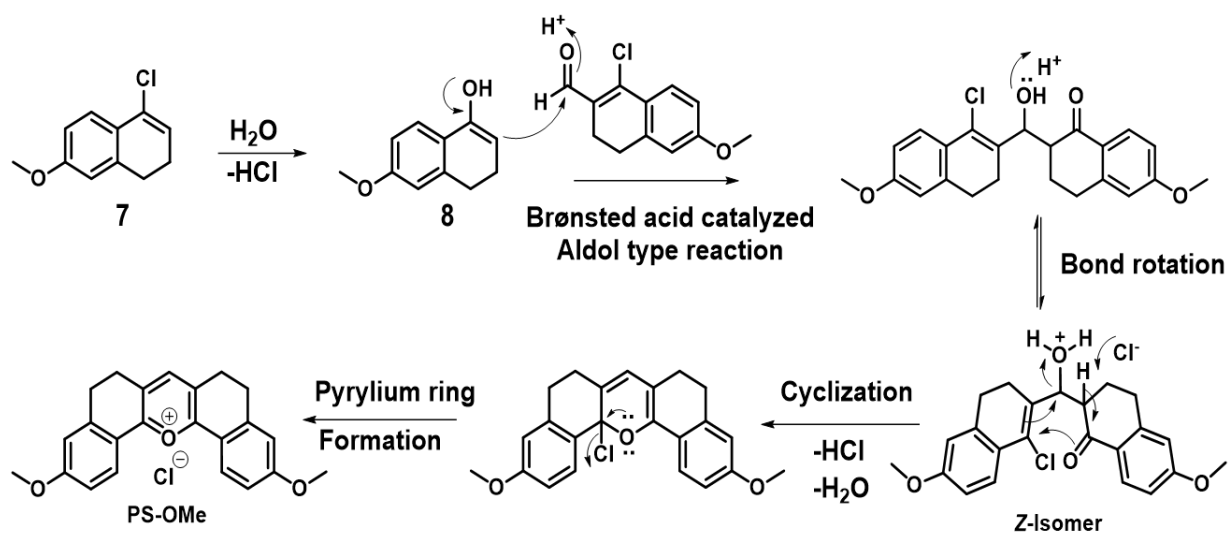


Scheme 2.1. Synthesis of **PS-OMe** using modified Vilsmeier–Haack reaction, followed by demethylation of **PS-OMe** to yield the probe **PS-OH**.

However, the compound **7** is obtained in better yield (~35%) when the reaction mixture is heated to 80 °C, when compared to prior reports.^{47,48} The ethyl acetate extract of a mixture of **6** and **7** thus obtained was concentrated to obtain a colorless oily liquid, which upon standing in air under ambient conditions for 72 h, resulted in a brown solid. After chromatographic purification, the structure of the brown solid was confirmed by

NMR and HRMS. **PS-OMe** was converted to the final probe **PS-OH** using BBr_3 mediated double demethylation reaction (**Scheme 2.1**).

This serendipitous observation corroborated that the vinyl chloride moiety in compound **7** was hydrolyzed upon exposure to moisture to form an unstable enol **8**, that underwent subsequent cyclocondensation with compound **6**, leading to the formation of symmetric pentacyclic pyrylium fluorophore, **PS-OMe** (**Scheme 2.2**).



Scheme 2.2. Postulated mechanism behind the formation of **PS-OMe**.

To confirm the reaction mechanism, the intermediates **6** and **7** were isolated, mixed and kept under inert conditions; however, the formation of the pyrylium fluorophore was not observed even after a week. The proposed mechanism is in good agreement with previous reports, that is indicative of the susceptibility of the vinyl chloride moiety to nucleophilic attack.^{49,50}

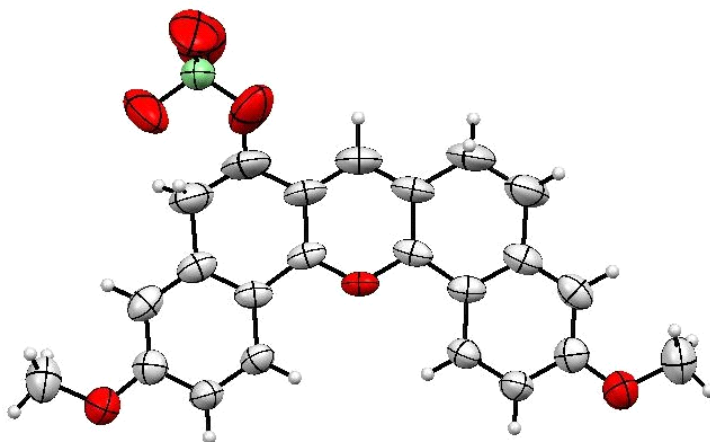
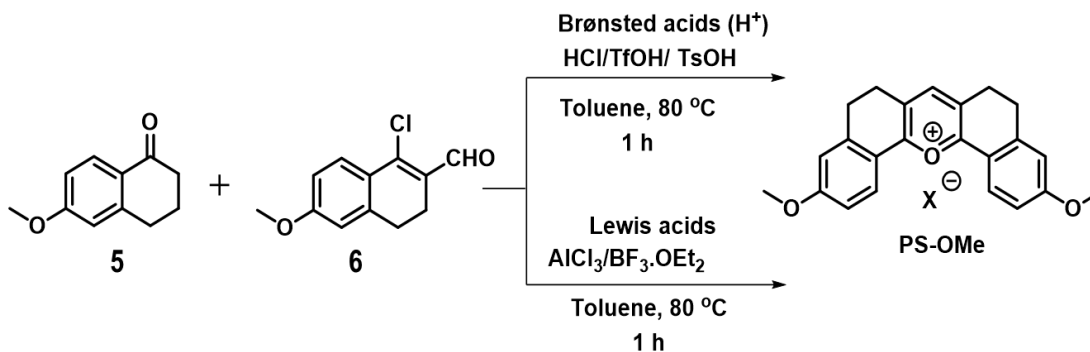


Figure 2.5. The ORTEP diagram of **PS-OMe** with perchlorate as the counter anion. Color codes: grey: carbon, red: oxygen, green: chlorine. Hydrogens are omitted for clarity.

The structure of **PS-OMe** was further confirmed using single crystal XRD analysis. We attempted to crystallize **PS-OMe** from polar solvents containing different acids, that enabled anion exchange assisted crystallization. Single crystals of **PS-OMe**, as its perchlorate salt, suitable for XRD experiments were obtained from a DMF solution containing slight excess of perchloric acid. The crystal structure of **PS-OMe** obtained by single crystal XRD analysis unambiguously confirmed its molecular structure. (**Figure 2.5**).

Since the proposed mechanism involves an aldol type condensation reaction, we chose a few Brønsted and Lewis acids as catalysts to further establish the mechanistic pathway and optimize the yield of **PS-OMe**. Acid-catalyzed condensation of compounds **6** with **5** in the presence of various acids confirmed AlCl_3 to be the best catalyst (yield ~ 70%), followed by triflic acid (yield ~ 61%), among others (**Figure 2.6**). Demethylation of **PS-OMe** using BBr_3 afforded two free hydroxy groups that can exhibit keto-enol

tautomerism under acidic/basic conditions, with concomitant changes in fluorescence as mandated for an efficient optical pH sensor.



Entry	Catalyst (equiv.)	Time (h)	Temp. (°C)	Isolated yield (%)
1	HCl (1)	12	80	15
2	TFA (1)	12	80	n.d.
3	TfOH (0.3)	1	80	61
4	TsOH (0.3)	1	80	29
5	BF ₃ .OEt ₂ (0.1)	1	80	51
6	AlCl ₃ (0.1)	1	80	70

Figure 2.6. Alternate route for the synthesis of symmetric pyrylium dye, **PS-OMe**, using Brønsted and Lewis acid catalysts. A tabulated summary of the reaction conditions and isolated yield of **PS-OMe** is also shown.

2.3.2. Photophysical Studies

The basic photophysical properties of **PS-OMe** and **PS-OH** were investigated in water and chloroform. The absorption (λ_{abs}) and emission maxima (λ_{em}) of **PS-OMe** were found to be centered at 505 nm and 560 nm, respectively in chloroform ($c = 10 \mu\text{M}$), as shown in **Figure 2.7a**; whereas in water, the absorption maximum was

bathochromically shifted to 490 nm, with no detectable shift in emission maximum (Figure 2.7b).

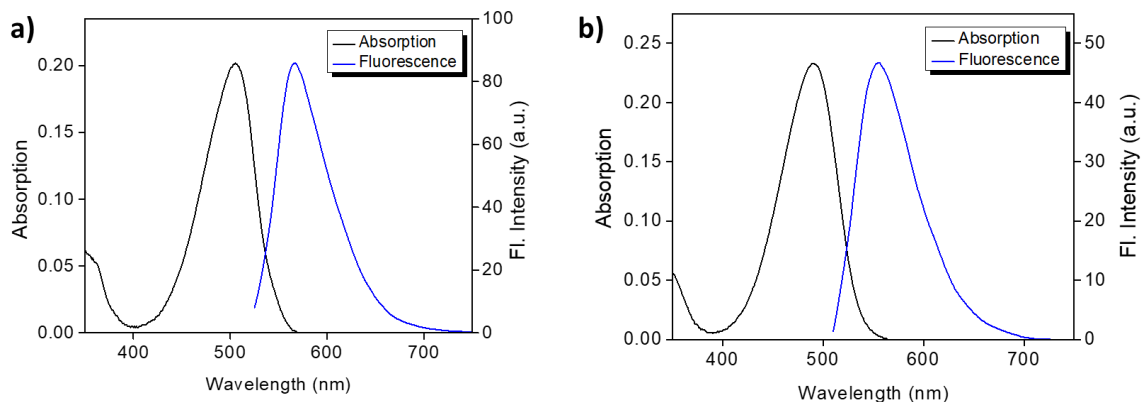


Figure 2.7. Absorption and emission spectra of PS-Ome (10 μM) in (a) CHCl₃ and (b) water.

The absorption maximum (λ_{abs}) of PS-OH in chloroform ($c = 20 \mu\text{M}$) was observed at 490 nm due to weak intramolecular charge transfer (ICT) from the donor to the acceptor (pyrylium ring). The corresponding emission maximum (λ_{em}) appeared at a slightly longer wavelength (577 nm, Figure 2.8a). The absorption (λ_{abs}) and emission (λ_{em}) maxima in water were found to be centered at 460 nm 560 nm, respectively (Figure 2.8b).

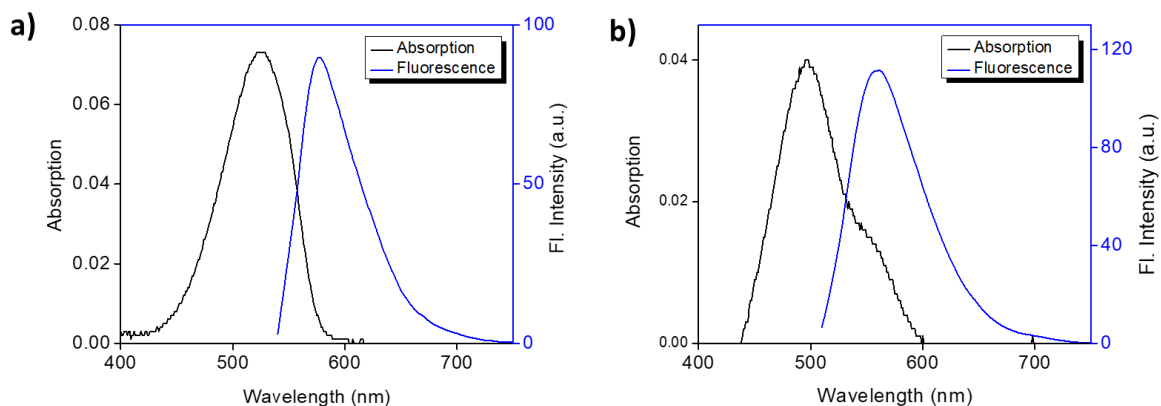


Figure 2.8. Absorption and emission spectra of PS-OH (20 μM) in (a) CHCl₃ and (b) water.

The Stokes shift, absolute quantum yield (Φ_F), and molar extinction coefficients (ϵ) for both the molecules are provided in **Table 2.1**.

Compound	Solvent	Abs. (nm)	Em. (nm)	Stokes Shift (cm ⁻¹)	Extinction Coefficient (ϵ) (M ⁻¹ cm ⁻¹)	Φ_F
PS-OMe	CHCl ₃	505	560	1945	2.01 x 10 ⁴	0.83
	Water	490	560	2551	1.17 x 10 ⁴	
PS-OH	CHCl ₃	490	577	3077	7.33 x 10 ³	0.08
	Water	460	560	3882	3.99 x 10 ³	

Table 2.1. Absorption and emission maxima, Stokes shift, extinction coefficients and quantum yield of PS-OMe and PS-OH in water and CHCl₃.

Fluorophores with large Stokes shift are of great demand due to several advantages in their application as imaging probes. Both PS-OMe and PS-OH exhibited larger Stokes shifts, compared to commonly used fluorescent dyes, like Fluorescein and Rhodamine B (**Table 2.2**).

Dye	Absorption (λ_{max})	Emission (λ_{max})	Stokes Shift (cm ⁻¹)
Rhodamine B	554	581	839
Fluorescein	483	512	1137
PS-OMe	490	560	2551
PS-OH	460	560	3882

Table 2.2. Comparison of absorption and emission maxima and Stokes shift of PS-OMe and PS-OH with commercial dyes, Fluorescein and Rhodamine B.

2.3.3. Aqueous Solubility

Many organic fluorophores suffer from poor aqueous solubility, that restricts their biological applications. Aggregation of fluorophores may cause fluorescence quenching and uneven intracellular distribution, leading to inconsistent signal and data error during cellular imaging. The positively charged core assists **PS-OMe** and **PS-OH** to effectively solubilize in polar organic solvents and buffers. The concentration dependent absorption spectra of **PS-OMe** were recorded in aqueous buffer at pH 4 (**Figure 2.9a**). The absorption intensity at $\lambda_{\max} = 490$ nm increased linearly with concentration, confirming absence of any aggregated state in aqueous medium (**Figure 2.9b**). Similar results were also obtained for **PS-OH** in buffer solution at pH 4 (**Figure 2.10a-b**).

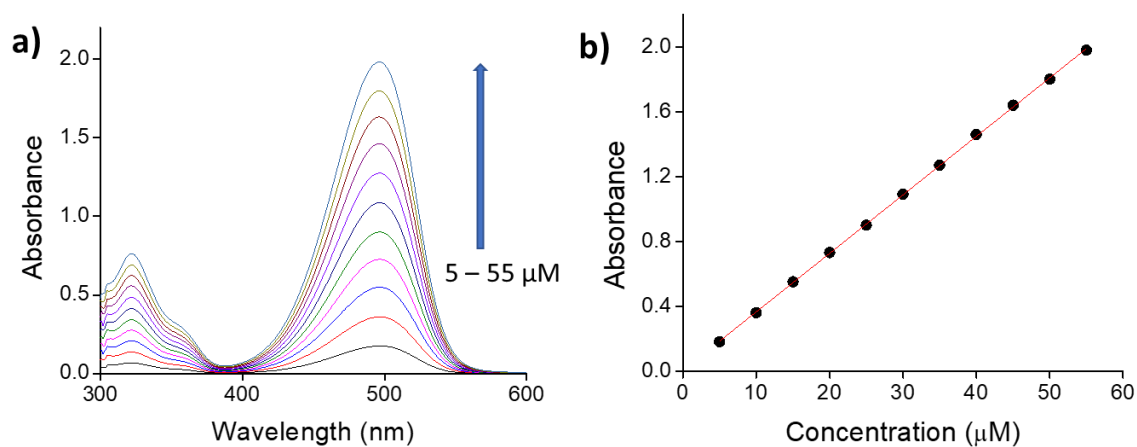


Figure 2.9. (a) The absorption spectra of **PS-OMe** in PBS buffer (pH 4) at various concentrations (5 – 55 μM). (b) Secondary plot of absorbance vs. concentration of **PS-OMe** at $\lambda_{\max} = 490$ nm. $R^2 > 0.99$ for the linear fit.

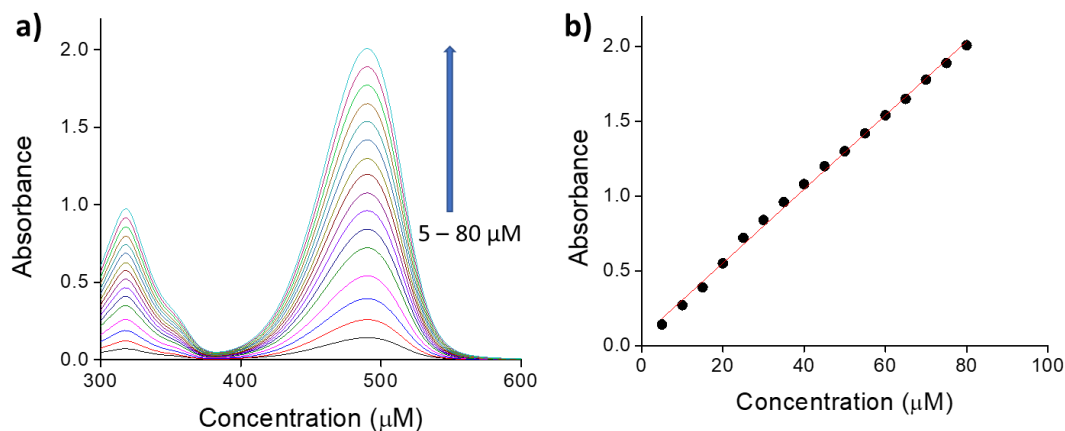


Figure 2.10. (a) Absorption spectra of **PS-OH** in PBS buffer (pH 4) at various concentrations (5 – 80 μM). (b) Secondary plot of absorption vs. concentration of **PS-OH** at $\lambda_{\text{max}} = 460$ nm. $R^2 > 0.99$ for the linear fit.

2.3.4. pH Response and Calculation of pKa

Fluorescence spectra of **PS-OMe** in PBS buffer at various pH (4 - 8) showed no change in λ_{max} (**Figure 2.11a**) or intensity (**Figure 2.11b**), indicative of a pH independent behavior.

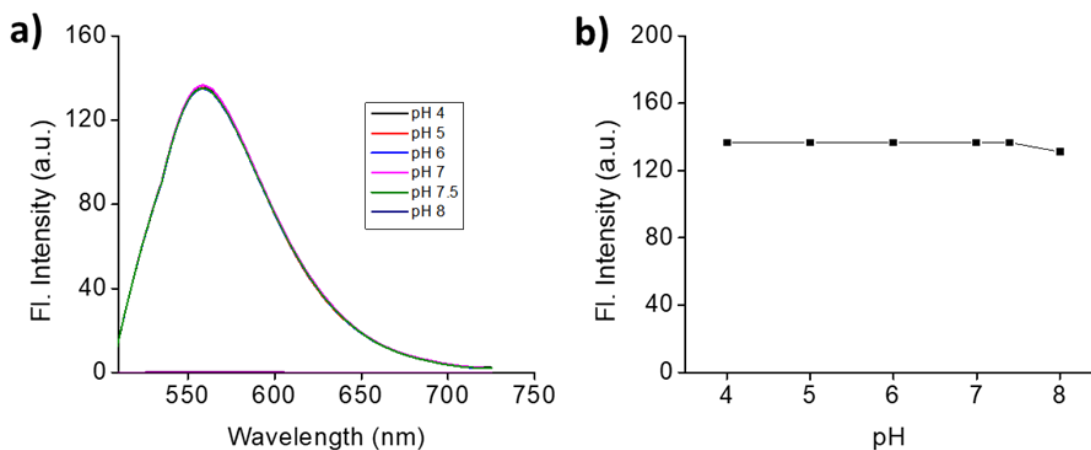


Figure 2.11. (a) Emission spectra of **PS-OMe** (10 μM) in PBS buffer at different pH ($\lambda_{\text{ex}} = 490$ nm). There was no noticeable change in emission intensity or maxima with pH. (b) Emission intensity of **PS-OMe** at different pH.

The absorption maximum of **PS-OH** shifted from 460 nm to 570 nm with an increase in pH from 4 to 10. The color of the solution also changed from orange to purple as the medium changed from acidic to basic (**Figure 2.12a**). The strong emission with $\lambda_{\max} = 560$ nm at pH 4 decreased with increase in pH and exhibited negligible emission at $\lambda_{\max} = 640$ nm under basic conditions (**Figure 2.12b**). This emission profile is indicative of an ON-OFF pH response of **PS-OH**.

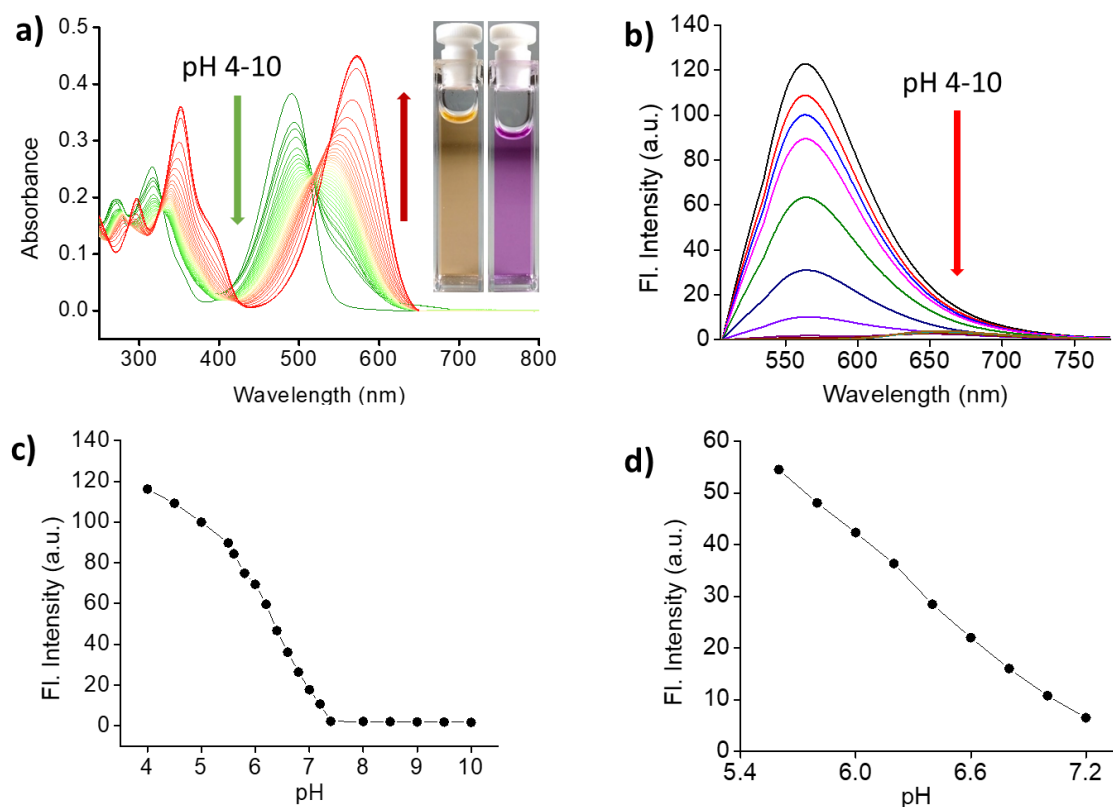


Figure 2.12. (a) Absorption spectra of **PS-OH** (20 μM) in PBS buffer at different pH (4 – 10). The inset shows the daylight photographs of **PS-OH** (20 μM) at pH 4 (left) and pH 10 (right). (b) Corresponding emission spectra of **PS-OH** when excited at $\lambda_{\text{ex}} = 460$ nm. (c) Secondary plot of emission intensity vs pH. (d) Linear increment of fluorescence intensity when pH was decreased from 7.2 to 5.6.

Non-linear regression and Boltzmann fitting of the secondary plot of the emission intensity vs pH was used to calculate the pKa of **PS-OH** and was found to be 6.2 ± 0.03 (**Figure 2.12c**). Starting from pH 10, **PS-OH** remained almost non-fluorescent till pH 7.4, and then fluorescence started to increase linearly with further acidification of the medium. The emission intensity showed a 48-fold enhancement and good linearity ($R^2 > 0.99$) between pH 7.2 and 5.6 (**Figure 2.12d**). Interestingly, a decrease of pH by 0.4 units from normal cellular pH (7.4) was enough to enhance the fluorescence intensity by 5.5-fold. Thus, a miniscule fluctuation of the pH of a normal cell can be accurately monitored using **PS-OH**.

2.3.5. Theoretical Calculations

The ground and excited state properties of **PS-OH** and mono-deprotonated **PS-OH** were studied by time-dependent density functional theory (TD-DFT) at the B3LYP/6-31G level using Gaussian 16. The corresponding energy diagram is shown in Figure 2.12. The calculated absorption and emission maxima of **PS-OH** correlated well with the experimental results. Structural optimization and subsequent frequency calculations on the mono-deprotonated **PS-OH** revealed a mixed state electronic transition from the unsymmetrical highest occupied molecular orbital (HOMO) to symmetrical lowest unoccupied molecular orbital (LUMO) and LUMO + 1. These results are also in good agreement with the experimental data. The mixed excited state resulted in at least two

emission maxima with minimum oscillator strength (f), corroborating the non-emissive nature of **PS-OH** at neutral and basic conditions (**Figure 2.13**).

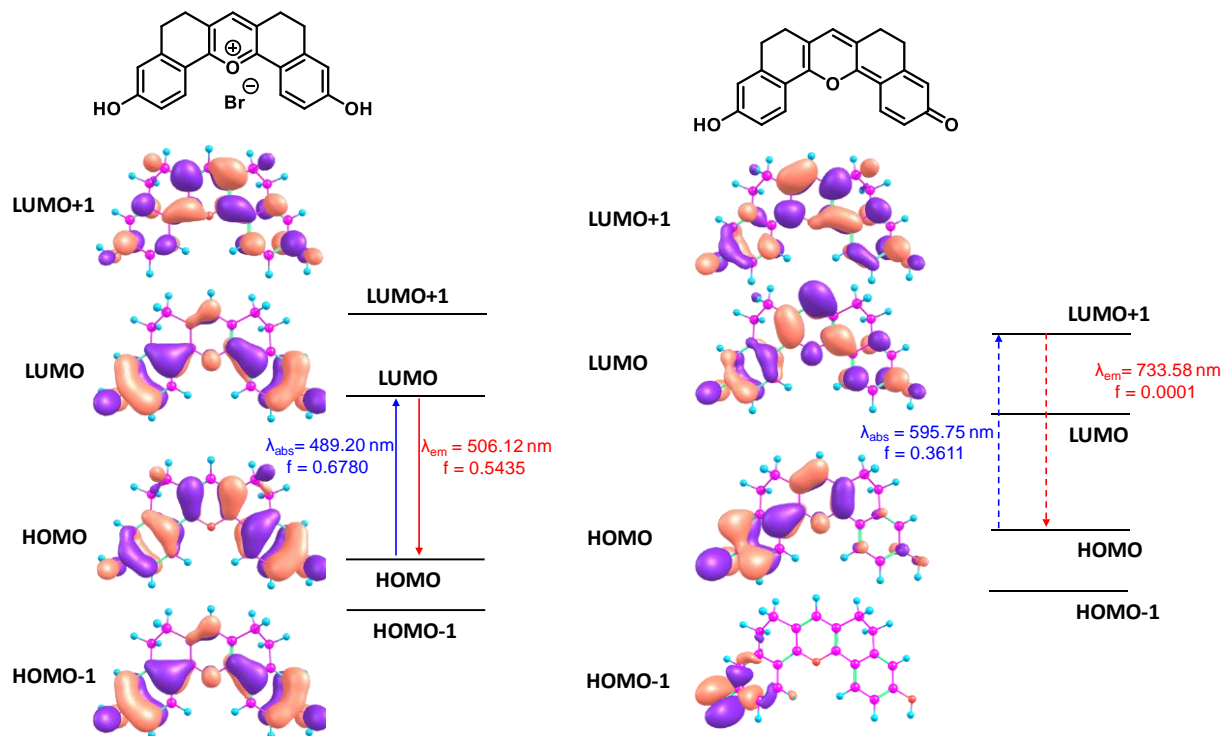


Figure 2.13. HOMO-LUMO energy diagram of **PS-OH** in protonated and deprotonated forms along with the simulated absorption and emission maxima and oscillator strength (f).

2.3.6. Response Time and Reversibility

In order to accurately track cellular changes during various biochemical processes, probes with fast analyte response that exhibit vividly detectable changes are required. Most imaging techniques further demand the optical changes to be reversible for several cycles to ensure their utility in monitoring dynamic variations in cellular environment. A 20 μM of solution of **PS-OH** in PBS buffer at pH 7.4 was nearly non-fluorescent, which upon addition of 20 μL of TFA exhibited a sharp enhancement in fluorescence

at 560 nm. The fluorescence response was found to get saturated within 9 s of changing the pH (**Figure 2.14a**). This observation corroborates the fast response of **PS-OH** towards H^+ , and is highly desirable for any bio-sensor. Furthermore, the retention of fluorescence intensity after four cycles of continuous switching of pH between 4 and 7.4 indicates that **PS-OH** is a potential candidate for monitoring dynamic changes in pH (**Figure 2.14b**).

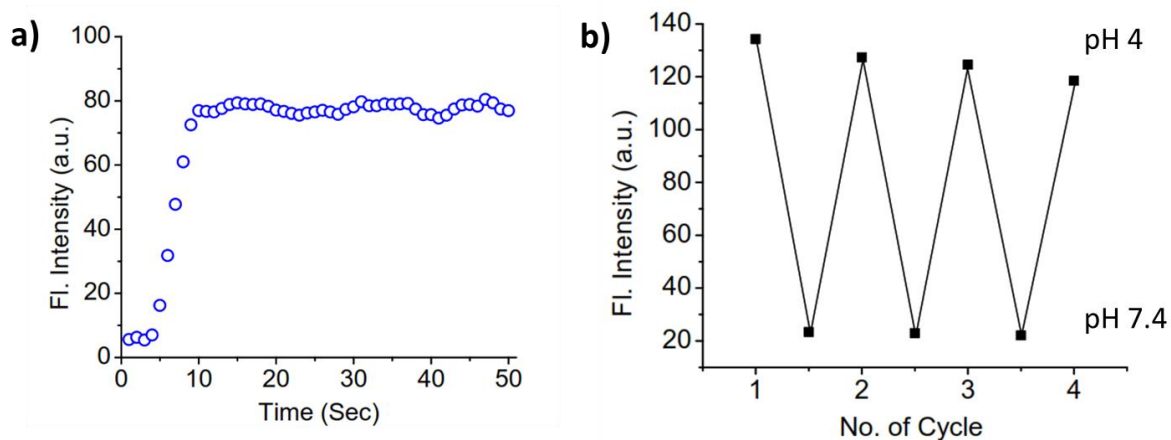


Figure 2.14. (a) Response time of **PS-OH** (20 μ M) upon addition of TFA (20 μ L). (b) Reversible switching of fluorescence intensity upon cycling the pH between 4 and 7.4.

2.3.7. Selectivity of **PS-OH** towards H^+

The response of the **PS-OH** towards different biologically relevant analytes including metal ions (Na^+ , K^+ , Ca^{2+} , Al^{3+} , Mg^{2+} , Zn^{2+} and Fe^{3+}), anions (AcO^- , OH^- , and OCl^-), reactive oxygen species (H_2O_2 , O_2^-), and biothiols (Cys, and GSH), H_2S at pH 4 (**Figure 2.15a**) and 7.4 (**Figure 2.15b**) were studied in order to confirm its selective response to pH. To our satisfaction, none of the analytes interfered the pH-dependent fluorescence

property of **PS-OH**. This observation unambiguously confirmed the potential of **PS-OH** as a versatile pH probe in live cellular imaging.

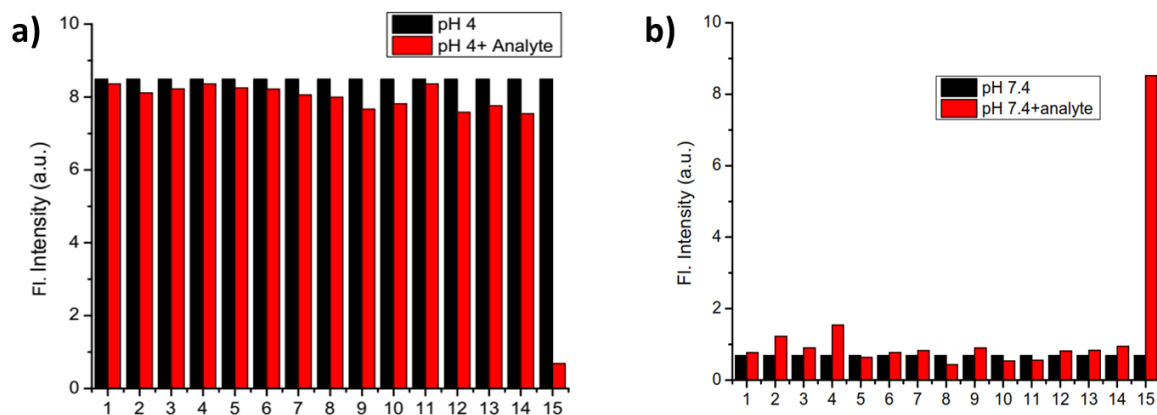


Figure 2.15. Selectivity test for **PS-OH**. 20 μ M of **PS-OH** was taken in PBS buffers at (a) pH 4 and (b) pH 7.4, and emission at $\lambda_{\text{max}} = 560$ nm was measured. Different biologically relevant analytes were added, and the fluorescence spectra were again obtained. Analytes (1mM) 1. Na⁺, 2. K⁺, 3. Ca²⁺, 4. Al³⁺, 5. Mg²⁺, 6. Zn²⁺ and 7. Fe³⁺, 8. AcO⁻, 9. ClO⁻, 10. H₂O₂, 11. O₂⁻, 12. Cys 13. GSH, 14. H₂S and 15. OH⁻/H⁺. $\lambda_{\text{ex}} = 460$ nm.

2.3.8. Biocompatibility and Photostability

Cytotoxicity and photostability are two crucial factors that determine the utility of any fluorophore in sensing and imaging applications. The cytotoxicity of **PS-OH** was checked using human lung adenocarcinoma cancer cell line, A549, up to a concentration of 10 mM under incubation for 48 h. More than 90% of the cells remained unaffected, indicating superior biocompatibility of the probe (**Figure 2.16a**).

The solution state photostability of **PS-OMe** and **PS-OH** were compared with that of Fluorescein and Rhodamine B.

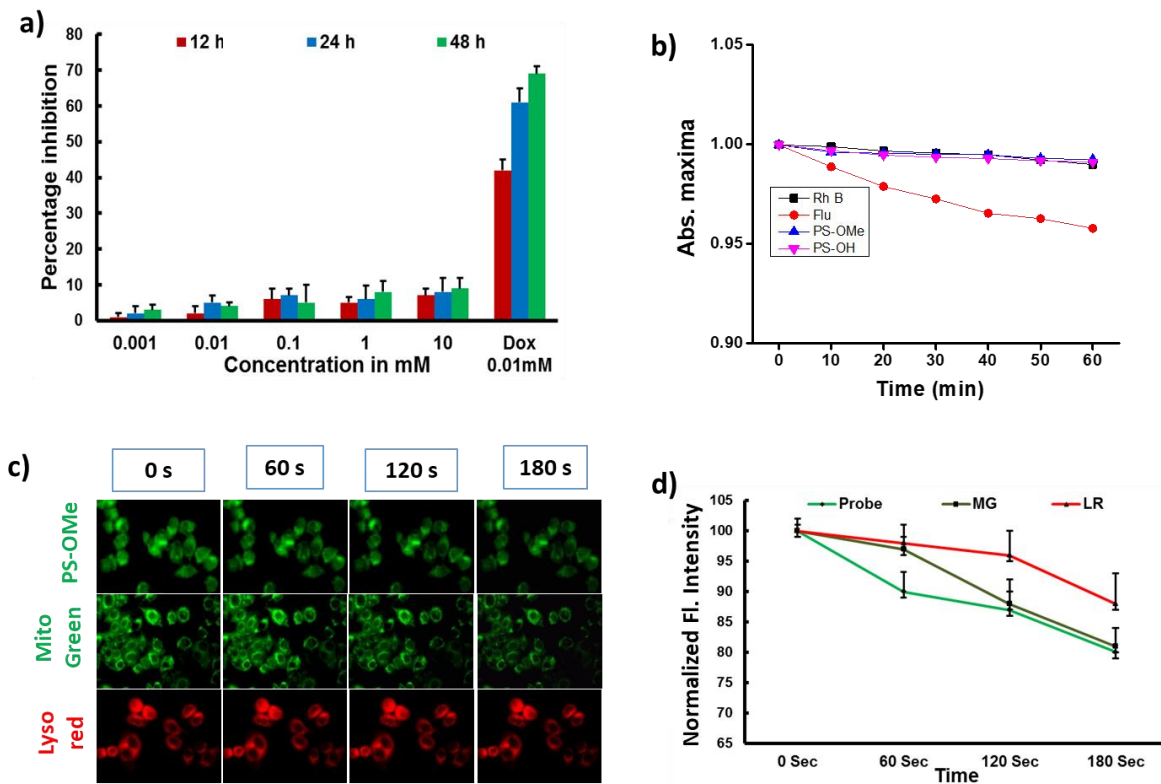


Figure 2.16. (a) Cytotoxicity evaluation using MTT assay on A549 cells treated with **PS-OH** (1 μM to 10 mM) after 12, 24 and 48 h. Doxorubicin (1 μM) was used as a positive control. The mean standard deviation (SD) of three independent experiments is presented. (b) Comparison of solution-state photostability of **PS-OMe** and **PS-OH** with Fluorescein and Rhodamine B. (c) Intracellular photostability imaging of **PS-OMe** (10 μM), Mitotracker green (MG, 100 nM) and Lyotracker red (LR, 100 nM), for 180 s. (d) Plot comparing retention of fluorescent intensity of **PS-OMe**, **MG** and **LR**, after irradiation for 180 s.

All four dyes in PBS buffer solution were irradiated with Hg lamp (200 W) for 30 min, and the emission spectra were recorded every 10 min. Fluorescein is known to be prone to photobleaching, and showed a gradual decrease in emission intensity with time. Rhodamine B, **PS-OMe** and **PS-OH** did not show any significant change in fluorescence, indicating their high photostability (**Figure 2.16b**). **PS-OMe** exhibited good *in-vitro* photostability, similar to commercial probes, such as Mitotracker green

(MG) and LysoTracker Red (LR), and retained nearly 80% fluorescence after continuous light irradiation for 180 s (**Figure 2.16c-d**). Photoinduced radical formation, a common problem associated with pyrylium molecules, was not also observed.

2.3.9. Intracellular pH Response and *In-vitro* pH Quantification

Owing to the superior photophysical properties such as the high Turn-ON sensitivity at acidic pH, excellent photostability and good biocompatibility, we used **PS-OH** to investigate intracellular pH response in A549 cell lines. The pH of the cells was equilibrated with the extracellular medium using Nigericin in the presence of the probe (20 μM), before recording the images. Almost no fluorescence was observed at pH 7.4 using a green emission filter. With a slight decrease in pH (pH 7), a detectable fluorescence signal was observed. Further reduction in pH resulted in gradual enhancement of fluorescence intensity in the green channel (**Figure 2.17a**). Fluorescence intensity obtained from the cells at different pH was found to be in good agreement with the photophysical data (**Figure 2.17b**). This data was then used to construct a calibration curve and was later used for quantification of pH from image analysis (**Figure 2.17c**).

Various anti-cancer drugs and apoptotic agents target cells via different signaling pathways, and result in distinct or characteristic variations in intracellular pH. For example, it has been reported that lipopolysaccharide (LPS) decreases intracellular pH (pH_i) to around 6, and cisplatin induces only a slight decrease in pH_i of cytoplasm. On

the other hand, Mdivi-1 causes apoptosis via mitochondrial hyperfusion, and does not acidify the cell cytoplasm.

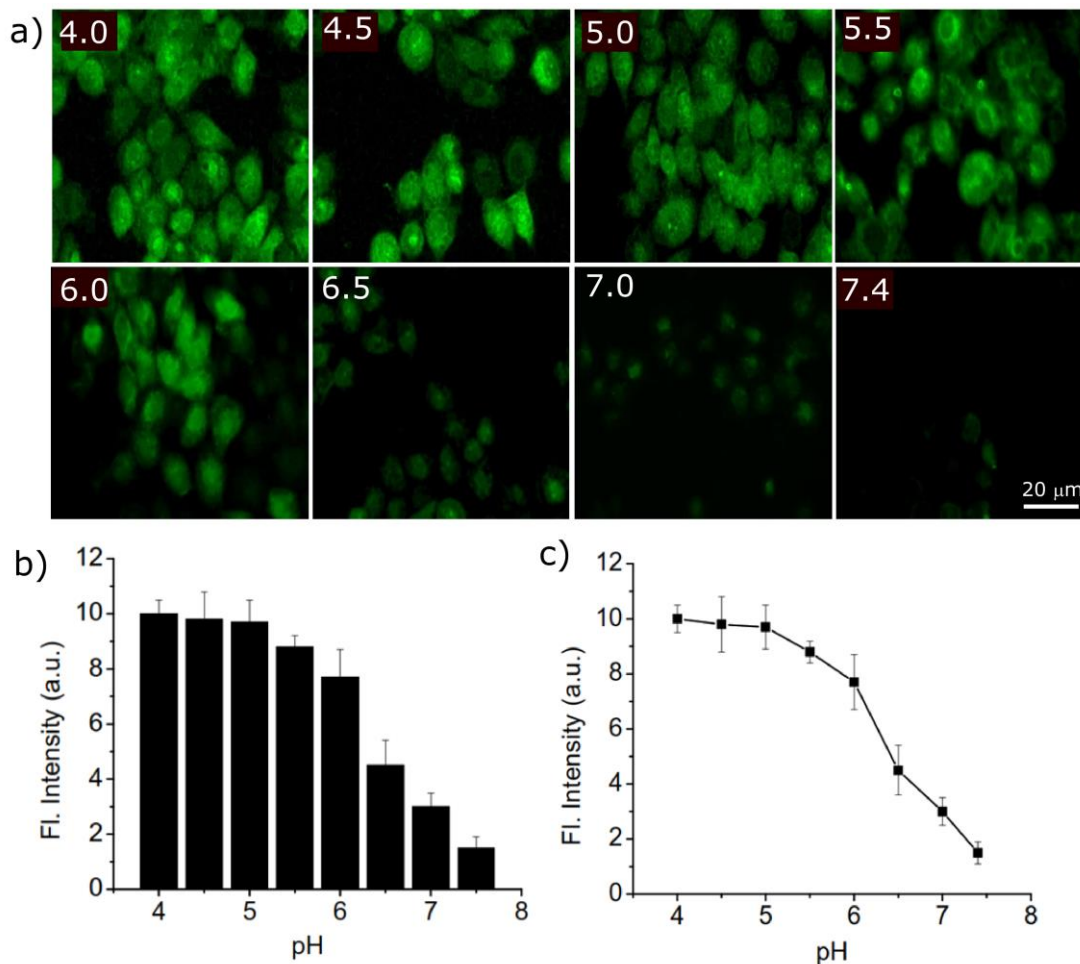


Figure 2.17. (a) Fluorescence Imaging of A549 cells after 10 min incubation with **PS-OH** (20 μM) in buffer solutions of different pH, in presence of 10 μM Nigericin. The corresponding pH is shown in the insets. (b) Fluorescence intensity from cellular imaging at different pH. (c) Intracellular pH calibration curve of **PS-OH** obtained from normalized fluorescence intensity at different pH.

Therefore, we evaluated the cellular pH imbalance caused by the treatment of these anti-cancer drugs or apoptotic agents using **PS-OH** as a probe. A549 cells were incubated with **PS-OH** ($c = 20 \mu\text{M}$) for 10 min. prior to treatment with Mdivi-1 (100 μM), LPS (1 μg/mL) and cisplatin (10 μM).^{51–53} The corresponding fluorescence

images were recorded just before the addition of Mdivi-1, LPS and cisplatin, and 12 h after the addition (**Figure 2.18a-h**).

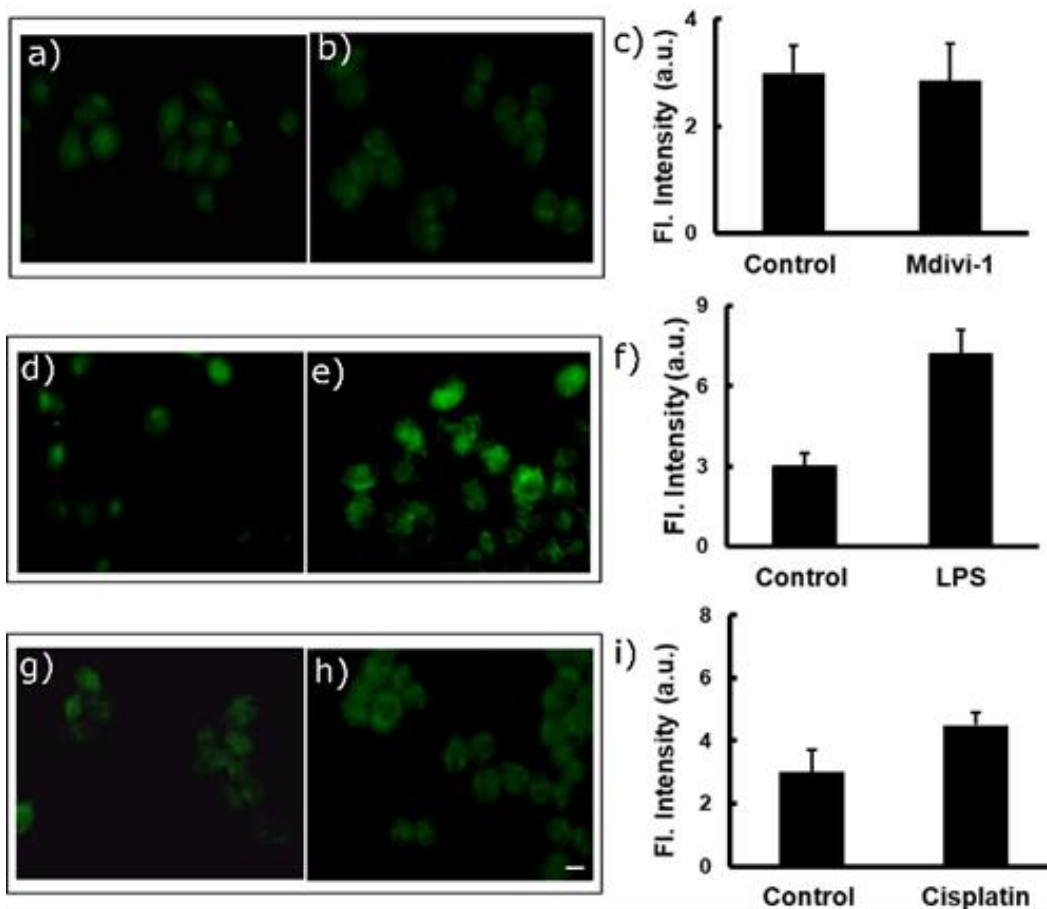


Figure 2.18. Fluorescence images of A549 cells after treatment with different anti-cancer drugs and apoptotic agents. Two sets of A549 cells were taken and incubated with 20 μ M of **PS-OH** for 10 min. in each case. Then, one set of cells were kept as control (a, d, g) and other sets were incubated with (b) Mdivi-1, (e) LPS and (h) Cisplatin, respectively, for 12 h. The final fluorescence intensity of control and treated cells were calculated (c, f, i) and compared with the calibration curve in Fig. 2.16c. Scale bar 20 μ m.

The corresponding fluorescence intensity was calculated from all the images. As expected, treatment with Mdivi-1 did not result in any detectable change in fluorescence intensity (**Figure 2.18c**). However, in the case of cisplatin, a slight change in

fluorescence was observed due to minute acidification of the cells (pH ~ 6.49) compared to control (pH ~ 7) (**Figure 2.18f**). The fluorescence intensity was found to increase significantly upon treatment with LPS that resulted in a reasonable decrease in cellular pH (**Figure 2.18i**). All the pH quantifications were done using the calibration graph obtained previously (**Figure 2.17c**).

These results are in good agreement with prior reports on pH imaging during apoptosis and underlines the applicability of **PS-OH** as a new probe for pH monitoring after chemotherapy.

2.3.10. Dynamic pH Quantification during Apoptosis

Monitoring dynamic changes in pH using a molecular probe is undoubtedly a fundamental aspect of any cancer treatment modality. Hence, we investigated whether **PS-OH** can monitor the dynamic changes in cellular pH during apoptosis, induced by H₂O₂, a known reactive oxygen species which causes rapid cell death.^{54,55} Significantly, addition of H₂O₂ did not have any direct impact on the fluorescence response of **PS-OH**. The cells were initially incubated with the probe **PS-OH** for 10 min, followed by the addition of 500 μM H₂O₂. Fluorescence images were recorded after various time intervals up to 1 h (**Figure 2.19a**). A detectable increase in fluorescence intensity was observed within 5 min of addition. The intensity gradually increased with time, corroborating the continuous decrease in intracellular pH (**Figure 2.19b**). This observation unambiguously established the capability of the probe in monitoring

dynamic changes in cellular pH. The pH changes were quantified at different points of time using the calibration curve obtained previously (**Figure 2.19c**).

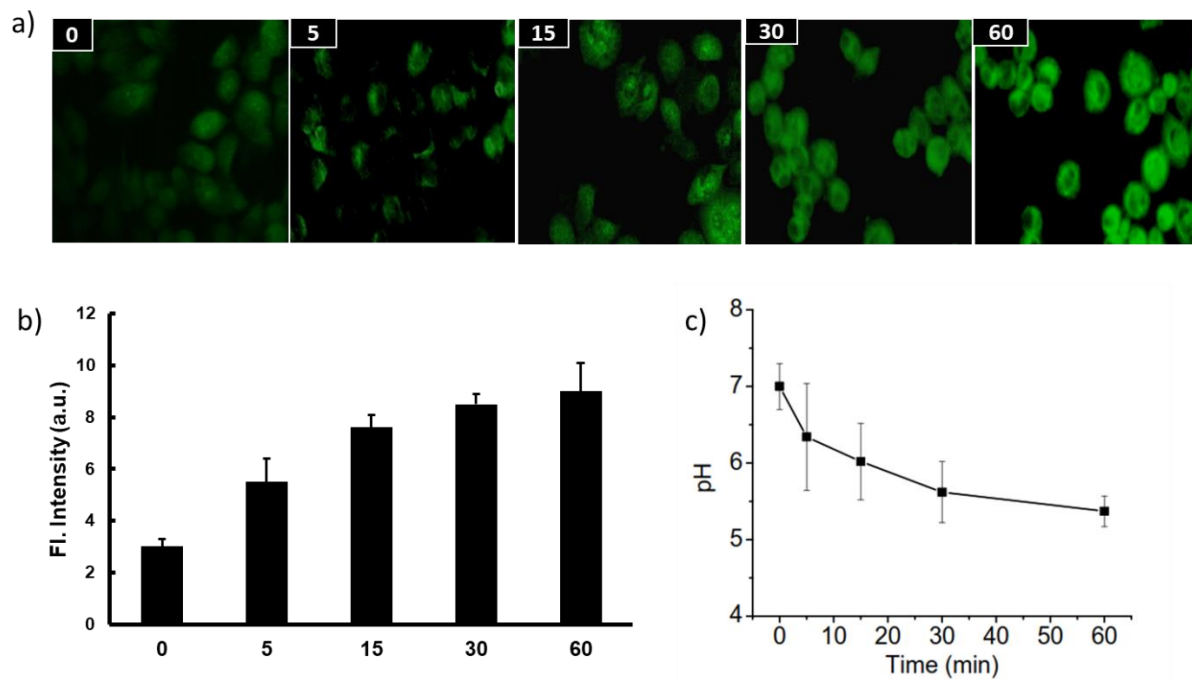


Figure 2.19. (a) Real-time fluorescence imaging of A549 cells stained with the probe **PS-OH** (20 μM) up to 60 minutes after treatment with 500 μM H₂O₂. Corresponding time is shown in the insets. (b) A plot of fluorescence intensity with time during apoptosis. (c) Quantification of the corresponding dynamic changes in pH at different time points in comparison with the calibration curve shown in Fig. 2.16c. Scale bar: 20 μm.

2.4. Conclusions

In conclusion, we have established a new synthetic protocol to prepare a “core scaffold” of a pentacyclic pyrylium dye **PS-OMe**. Mechanistic understanding of the reaction pathways helped to establish an alternate, efficient and general synthetic protocol for pentacyclic pyrylium chromophores with nearly 70% yield. The pyrylium fluorescent probe **PS-OH** exhibited an ‘ON-OFF’ response towards pH variation in cells during

apoptosis. The strong acceptor at the center ring of pyrylium, appended with two hydroxyl groups is the key to the excellent photophysical properties, including photostability, high molar absorptivity, and large Stokes shifts. **PS-OH** exhibited an exceptional ‘Turn-ON’ pH response in the window of biological relevance both in solution state as well as in live cells. This new probe can monitor even miniscule changes in physiological pH (7.4) during therapeutic process using drugs or apoptotic agents in real-time.

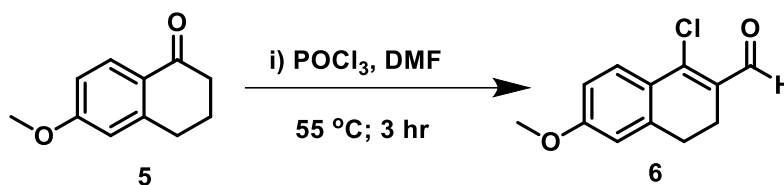
2.5. Experimental Section: Synthesis

2.5.1. Materials and Methods

All reagents and solvents (reagent grade) were used without further purification. Reactions were monitored using silica gel G-60 F254 aluminium TLC and compounds were visualized by short/long-wavelength UV lamps. Column chromatography was done using silica gel 100-200 mesh as a stationary phase. ^1H and ^{13}C NMR were recorded on a Bruker Avance-II spectrometer at 500 and 125 MHz, respectively in deuterated solvents. Data are reported as follows: chemical shift in ppm (δ) and coupling constants (Hz). HRMS data was recorded on a Thermo Scientific Exactive LCMS instrument by electrospray ionization method with ions given in m/z using an Orbitrap analyzer. Cell imaging was carried out in an Epifluorescent Inverted microscope (Olympus 1 x 51, Singapore).

2.5.2. Synthesis and Characterization

Synthesis of 1-chloro-6-methoxy-3,4-dihydronaphthalene-2 carbaldehyde (**6**)

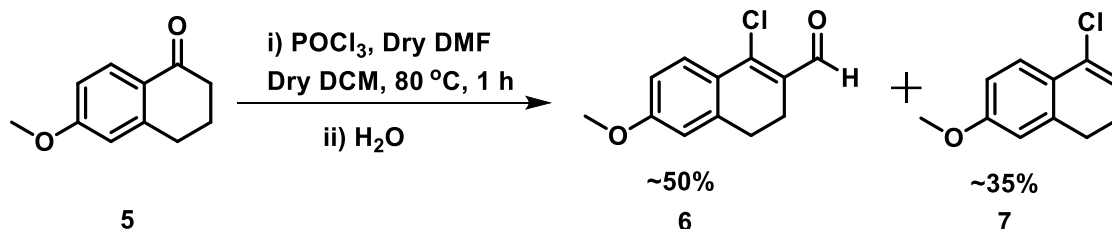


POCl₃ (3.5 mL, 38.25 mmol) was slowly added to DMF (10 mL) at room temperature under stirring and maintained for an additional 30 min at 0 °C. To the reaction mixture, a solution of compound **5** (4.5 g, 25.5 mmol) in DMF (10 mL) was slowly added at room temperature and heated at 55 °C for 3 h. The reaction mixture was cooled to room temperature and poured into ice-cold water with stirring, and was left overnight. The yellowish-white solid was filtered, and the residue was dried in the oven to obtain compound **6** (4.25 g, 85%).

¹H NMR (500 MHz, CDCl₃), δ : 10.33 (s, 1H), 7.81 (d, $J = 10$ Hz, 1H), 6.85 (d, $J = 2.5$ Hz, 1H), 6.75 (d, $J = 5$ Hz, 1H), 3.86 (s, 3H), 2.82-2.80 (m, 2H); 2.64-2.63 (m, 2H).

¹³C NMR: (125 MHz CDCl₃), δ : 190.5, 162.1, 146.2, 141.3, 129.8, 128.4, 124.9, 113.5, 112.1, 55.5, 27.6, 21.5.

HRMS: Calcd (C₁₂H₁₂ClO₂⁺): 223.0520; Found: 223.0561.

Synthesis of 1-chloro-6-methoxy-3,4-dihydronaphthalene-2 carbaldehyde and 4-chloro-1,2-dihydro-7-methoxy-naphthalene (7)

In a two-necked flask, compound **5** (4.5 g, 25.5 mmol) in 10 mL dry DMF was mixed with dry CH_2Cl_2 (20 mL) under ice-cold conditions under continuous stirring. After 30 min, POCl_3 (3.5 mL, 38.25 mmol) was added dropwise to this chilled solution and the temperature was slowly raised to room temperature. The reaction mixture was then heated under reflux ($80\text{ }^\circ\text{C}$) for 1 h and cooled down to room temperature. Ice-cold water was slowly added to the reaction mixture with vigorous stirring for an hour. The mixture was extracted with ethyl acetate. The organic layer was dried over anhydrous Na_2SO_4 , filtered and concentrated under reduced pressure. Chromatographic separation over silica gel afforded compounds **7** and **6**, that eluted using hexane and 10% ethyl acetate/ hexane, respectively.

Compound 6: ^1H NMR (500 MHz, CDCl_3), δ : 10.33 (s, 1H), 7.81 (d, $J = 10$ Hz, 1H), 6.85 (d, $J = 2.5$ Hz, 1H), 6.75 (d, $J = 5$ Hz, 1H), 3.86 (s, 3H), 2.82-2.80 (m, 2H); 2.64-2.63 (m, 2H).

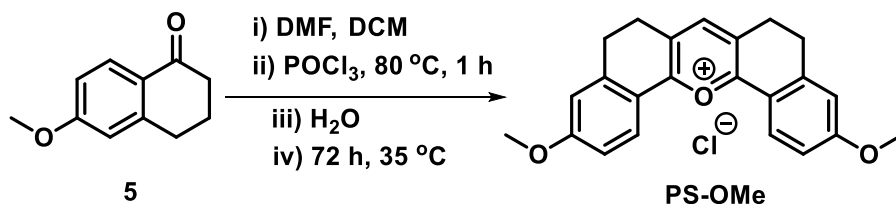
^{13}C NMR: (125 MHz CDCl_3), δ : 190.5, 162.1, 146.2, 141.3, 129.8, 128.4, 124.9, 113.5, 112.1, 55.5, 27.6, 21.5.

HRMS: Calcd (C₁₂H₁₂ClO₂⁺): 223.0520; Found: 223.0561.

Compound 7: ¹H NMR (500 MHz, CDCl₃), δ: 7.48 (d, *J* = 10 Hz, 1H), 6.75 (d, *J* = 10 Hz, 1H), 6.69 (s, 1H), 6.03 (t, *J* = 5 Hz, 1H), 3.8 (s, 3H), 2.8 (t, *J* = 10 Hz, 2H), 2.39-2.34 (m, 2H).

¹³C NMR: (125 MHz CDCl₃), δ: 159.5, 138.2, 130.1, 125.6, 125.48, 123.3, 113.6, 111.0, 55.3, 28.1, 24.1.

Synthesis of PS-OMe



In a two-necked flask, **5** (4.5 g, 25.5 mmol) in 10 mL dry DMF was mixed with dry CH₂Cl₂ (20 mL) under ice-cold conditions with continuous stirring. After 30 min, POCl₃ (3.5 mL, 38.25 mmol) was added dropwise to this chilled solution and temperature was slowly raised to room temperature. The reaction mixture was then refluxed (80 °C) for 1 h, and cooled down to room temperature. Ice-cold water was slowly added to the reaction mixture with vigorous stirring for an hour, followed by extraction with ethyl acetate and the organic layer was dried over anhydrous Na₂SO₄, filtered and concentrated under reduced pressure. The crude mixture was kept at 35 °C for 3 days under ambient atmosphere to obtain a dark reddish solid cake, that was purified by column chromatography on silica gel using 5% MeOH in CH₂Cl₂ to yield

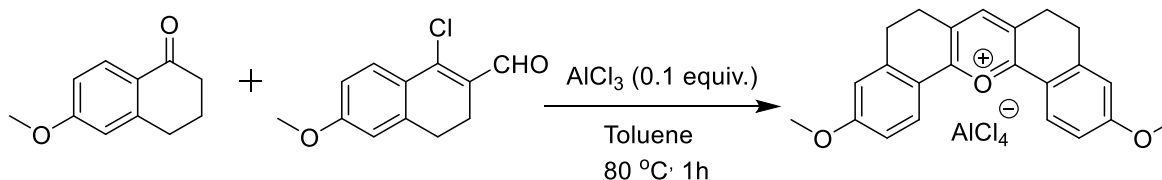
the symmetrical pyrylium fluorophore, **PS-OMe** (2.8 g, 28%), as a brown solid. Single crystals for XRD analysis were obtained from DMF upon addition of a few drops of perchloric acid.

^1H NMR (500 MHz, CDCl_3), δ : 8.85 (s, 1H), 8.07 (d, $J = 10$ Hz, 2H), 7.04 (dd, $J = 5$ Hz, 2H), 6.89 (d, $J = 2$ Hz, 2H), 3.95 (s, 6H), 3.29-3.26 (m, 4H), 3.14-3.10 (m, 4H).

^{13}C NMR (125 MHz, CDCl_3), δ : 165.4, 164.4, 152.9, 144.9, 128.9, 127.7, 118.3, 115.1, 114.2, 56.1, 29.7, 27.1, 25.4.

HRMS: Calcd ($\text{C}_{23}\text{H}_{21}\text{O}_3^+$): 345.1485; Found: 345.14406.

Modified Synthetic Protocol for PS-OMe



Compounds **5** (176 mg, 1 mmol) and **6** (222 mg, 1 mmol) were mixed with toluene (5 mL) in a two-necked flask, equipped with a Liebig condenser, and was heated at $80\text{ }^\circ\text{C}$ for 15 min. Then catalytic amounts (0.1 to 1 equiv.) of Brønsted or Lewis acids was added to the reaction mixture and heating was continued for another 1 h. The reaction mixture was cooled to room temperature, and ~ 10 mL of cold diethyl ether was added to get a precipitate that was collected by filtration followed by washing with diethyl ether (3 times). The crude product thus obtained was redissolve in chloroform (5 mL)

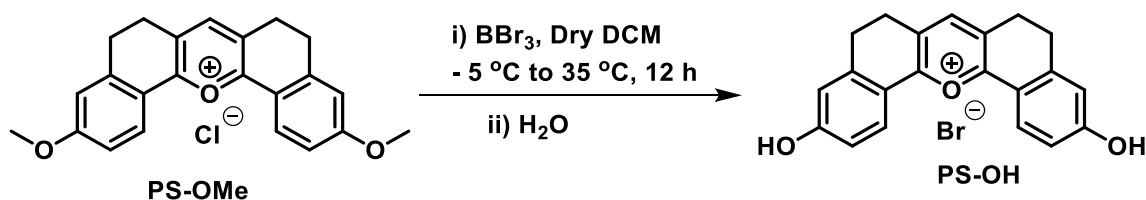
and excess hexane was added to obtain **PS-OMe** as a reddish solid in moderate to good yields.

^1H NMR (500 MHz, CDCl_3), δ : 8.85 (s, 1H), 8.07 (d, $J = 10$ Hz, 2H), 7.04 (dd, $J = 5$ Hz, 2H), 6.89 (d, $J = 2$ Hz, 2H), 3.95 (s, 6H), 3.29-3.26 (m, 4H), 3.14-3.10 (m, 4H).

^{13}C NMR (125 MHz, CDCl_3), δ : 165.4, 164.4, 152.9, 144.9, 128.9, 127.7, 118.3, 115.1, 114.2, 56.1, 29.7, 27.1, 25.4.

HRMS: Calcd. ($\text{C}_{23}\text{H}_{21}\text{O}_3^+$): 345.1485; Found: 345.14406.

Synthesis of PS-OH



PS-OMe (0.5 g, 1.26 mmol) in dry CH_2Cl_2 (10 mL) was added to a two-necked flask and was kept at $-5\text{ }^\circ\text{C}$ for 30 min. BBr_3 in CH_2Cl_2 (~3 mL, 12 mmol) was then added dropwise under an inert atmosphere. The reaction mixture was stirred for 1 h at $-5\text{ }^\circ\text{C}$ and the temperature was raised to $35\text{ }^\circ\text{C}$, with stirring for 12 h. After completion of the reaction, deionized water was added dropwise to neutralize excess BBr_3 until a red precipitate was formed. The red precipitate was filtered, and the residue was washed with cold water for five to six times. The crude mixture thus obtained was purified on

a silica gel column (8% CH₃OH/CHCl₃). **PS-OH** (0.4 g, 76%) was isolated as a solid dark reddish solid.

¹H NMR (500 MHz, MeOD), δ : 8.26 (s, 1H), 8.12 (d, $J = 10$ Hz, 2H), 6.95 (dd, $J_1 = 10$ Hz, $J_2 = 2$ Hz, 2H), 3.09-3.06 (m, 8H).

¹³C NMR (125 MHz, MeOD), δ : 164.8, 164.5, 150.1, 145.1, 128.2, 127.7, 117.2, 115.8, 115.4, 26.4, 25.1.

HRMS: Calcd (C₂₃H₂₁O₃⁺): 317.1172; Found: 317.1164

2.6. Description of Experimental Techniques

2.6.1. UV/Vis Absorption and Emission Spectral Measurements

Electronic absorption spectra were recorded in a Shimadzu UV-2600 spectrophotometer, using quartz cuvettes. Emission spectra were recorded on Horiba Fluorolog — 3 Jovin Yoon with a 1 cm quartz cuvette. Absolute fluorescence quantum yield was measured by the integrating sphere method. All experiments were carried out at 298 K.

2.6.2. Cell Culture

The human lung adenocarcinoma cancer cell line A549 was obtained from American Type Culture Collection (ATCC, Manassas, VA). Cells were maintained in Dulbecco's

modified Eagle's medium (DMEM) with 10% fetal bovine serum and 100 U penicillin/0.1 mg/ mL streptomycin antibiotics under an atmosphere of 5% CO₂ at 37 °C.

2.6.3. Cytotoxicity Studies

The cell viability was evaluated on human lung adenocarcinoma cancer cell line, A549 by colorimetric MTT (3-(4,5-dimethylthiazol-2-yl)-2,5-diphenyltetrazolium bromide) assay as previously reported. Cell suspensions of 5 x 10³ cells/well (100 µL) were seeded in a 96 well plate, and cell lines were grown using DMEM culture media with 10% Foetal Bovine Serum (FBS), 2 mM glutamine and 100 U penicillin / 0.1 mg/mL streptomycin antibiotics. When the cells were approximately 70% confluent, 100 µL of **PS-OH** at various concentrations (1 µM to 10 mM) were added to it. Doxorubicin (Dox, 1 µM) was added as a positive control. The plates were then incubated for 12 h, 24 h and 48 h in a 5% CO₂ incubator. After incubation, 20 µL MTT (5 mg/mL) was added to each well, and incubation was continued for an additional 2 h. The insoluble formazan solid was solubilized by adding 100 µL MTT lysis buffer (SDS and Dimethylformamide) followed by an incubation of 4 h, and the absorbance was measured at 570 nm using a microplate spectrophotometer (BioTek, Power Wave XS).

$$\text{Proliferation [\%]} = A_{\text{Sample}} / A_{\text{Control}} \times 100$$

$$\text{Inhibition [\%]} = 100 - \% \text{ Proliferation}$$

2.6.4. Intracellular pH-dependent Measurement

Cells (A549) were incubated at 37 °C for 30 min in high K⁺ buffer (30 mM NaCl, 120 mM KCl, 1 mM CaCl₂, 0.5 mM MgSO₄, 1 mM Na₂HPO₄, 5 mM glucose, 20 mM sodium acetate and 20 mM MES) of various pH values (pH 4 - 7.4). Next, 25 μL (10 μM) H⁺/K⁺ antiporter nigericin was added and incubated for 15 min to equilibrate the intracellular pH with the pH buffer. The cells were then incubated with 20 μL of the probe **PS-OH** (20 μM) for 10 min, washed and observed under an inverted fluorescence microscope using a green channel (Olympus 1 x 51, Singapore). Image processing was performed using Progress software, and Image analysis was performed using Image J.

2.7. References

- [1] R. L. Siegel, K. D. Miller and A. Jemal, *CA. Cancer J. Clin.*, 2019, **69**, 7–34.
- [2] H. Pei, X. Zuo, D. Zhu, Q. Huang and C. Fan, *Acc. Chem. Res.*, 2014, **47**, 550–559.
- [3] X. Li, S. Lee and J. Yoon, *Chem. Soc. Rev.*, 2018, **47**, 1174–1188.
- [4] J. Li and K. Pu, *Chem. Soc. Rev.*, 2019, **48**, 38–71.
- [5] G. Saranya, M. M. Joseph, V. Karunakaran, J. B. Nair, V. N. Saritha, V. S. Veena, K. Sujathan, A. Ajayaghosh and K. K. Maiti, *ACS Appl. Mater. Interfaces*, 2018, **10**, 38807–38818.
- [6] S. Chakraborty, B. K. Agrawalla, A. Stumper, N. M. Vegi, S. Fischer, C. Reichardt, M. Kögler, B. Dietzek, M. Feuring-Buske, C. Buske, S. Rau and T. Weil, *J. Am. Chem. Soc.*, 2017, **139**, 2512–2519.
- [7] X. Wang, F. Gao and X. Zhang, *Angew. Chem. Int. Ed.*, 2017, **129**, 9157–9161.

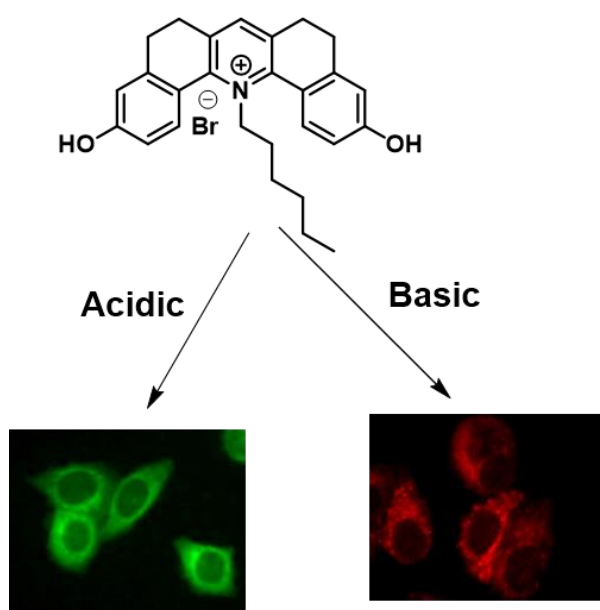
-
- [8] S. Liu, X. Pan and H. Liu, *Angew. Chem.*, 2020, **132**, 5943–5953.
- [9] Y. Liu, P. Bhattarai, Z. Dai and X. Chen, *Chem. Soc. Rev.*, 2019, **48**, 2053–2108.
- [10] J. Liu, L. Song, S. Liu, Q. Jiang, Q. Liu, N. Li, Z.-G. Wang and B. Ding, *Nano Lett.*, 2018, **18**, 3328–3334.
- [11] K. V. Sudheesh, P. S. Jayaram, A. Samanta, K. S. Bejoymohandas, R. S. Jayasree and A. Ajayaghosh, *Chem. Eur. J.*, 2018, **24**, 10999–11007.
- [12] A. M. Gonzalez-Angulo, F. Morales-Vasquez and G. N. Hortobagyi, *Adv. Exp. Med. Biol.*, 2007, **608**, 1–22.
- [13] A. H.-H. Wong, H. Li, Y. Jia, P.-I. Mak, R. P. da S. Martins, Y. Liu, C. M. Vong, H. C. Wong, P. K. Wong, H. Wang, H. Sun and C.-X. Deng, *Sci. Rep.*, 2017, **7**, 9109.
- [14] C. L. Storey, G. G. Hanna and A. Greystoke, *Br. J. Cancer*, 2020, **123**, 28–35.
- [15] Y.-N. Zheng, C.-Y. Xiong, Y. Zhuo, Y.-Q. Chai, W.-B. Liang and R. Yuan, *Chem. Commun.*, 2020, **56**, 8488–8491.
- [16] R. S. Hotchkiss, A. Strasser, J. E. McDunn and P. E. Swanson, *N. Engl. J. Med.*, 2009, **361**, 1570–1583.
- [17] S. Matsuyama, J. Llopis, Q. L. Deveraux, R. Y. Tsien and J. C. Reed, *Nat. Cell Biol.*, 2000, **2**, 318–325.
- [18] E. M. Kniep, C. Roehlecke, N. Özkucur, A. Steinberg, F. Reber, L. Knels and R. H. W. Funk, *Invest. Ophthalmol. Vis. Sci.*, 2006, **47**, 1185–1192.
- [19] P. Wong, C. Lee and I. F. Tannock, *Clin. Cancer Res.*, 2005, **11**, 3553 LP – 3557.
- [20] M. M. Martinez, R. D. Reif and D. Pappas, *Anal. Methods*, 2010, **2**, 996–1004.
- [21] S. Elmore, *Toxicol. Pathol.*, 2007, **35**, 495–516.
- [22] X. Wang, L. Fan, X. Zhang, Q. Zan, W. Dong, S. Shuang and C. Dong, *Analyst*, 2020, **145**, 7018–7024.
- [23] T. Zhang, Y. Li, Z. Zheng, R. Ye, Y. Zhang, R. T. K. Kwok, J. W. Y. Lam and B. Z.

- Tang, *J. Am. Chem. Soc.*, 2019, **141**, 5612–5616.
- [24] W. Zeng, X. Wang, P. Xu, G. Liu, H. S. Eden and X. Chen, *Theranostics*, 2015, **5**, 559–582.
- [25] X. Huang, S. Lee and X. Chen, *Am. J. Nucl. Med. Mol. Imaging*, 2011, **1**, 3–17.
- [26] X. Jiang, E. T. McKinley, J. Xie, H. Li, J. Xu and J. C. Gore, *Sci. Rep.*, 2019, **9**, 9540.
- [27] A. Petrovsky, E. Schellenberger, L. Josephson, R. Weissleder and A. Bogdanov, *Cancer Res.*, 2003, **63**, 1936 LP – 1942.
- [28] O. Krysko, L. de Ridder and M. Cornelissen, *Apoptosis*, 2004, **9**, 495–500.
- [29] L. Wang, A. A. Habib, A. Mintz, K. C. Li and D. Zhao, *Mol. Imaging*, 2017, **16**, 1536012117708722.
- [30] J. Li, B. D. Gray, K. Y. Pak and C. K. Ng, *Nucl. Med. Biol.*, 2019, **78**, 23–30.
- [31] S. Mercille and B. Massie, *Cytotechnology*, 1994, **15**, 117–128.
- [32] D. Matassov, T. Kagan, J. Leblanc, M. Sikorska and Z. Zakeri, *Methods Mol. Biol.*, 2004, **282**, 1–17.
- [33] H. Shi, R. T. K. Kwok, J. Liu, B. Xing, B. Z. Tang and B. Liu, *J. Am. Chem. Soc.*, 2012, **134**, 17972–17981.
- [34] Z. Zhou, H. Wu, R. Yang, A. Xu, Q. Zhang, J. Dong, C. Qian and M. Sun, *Sci. Adv.*, 2020, **6**, eabc4373.
- [35] Y. Guo, X. Zhang and F.-G. Wu, *J. Colloid Interface Sci.*, 2018, **530**, 511–520.
- [36] G. Saranya, P. Anees, M. M. Joseph, K. K. Maiti and A. Ajayaghosh, *Chem. Eur. J.*, 2017, **23**, 7191–7195.
- [37] X. Zhang, N. He, Y. Huang, F. Yu, B. Li, C. Lv and L. Chen, *Sensors Actuators B Chem.*, 2019, **282**, 69–77.
- [38] J. Liu, M. Liu, H. Zhang, X. Wei, J. Wang, M. Xian and W. Guo, *Chem. Sci.*, 2019, **10**, 10065–10071.

- [39] Y. Huang, Q. Zhou, Y. Feng, W. Zhang, G. Fang, M. Fang, M. Chen, C. Xu and X. Meng, *Chem. Commun.*, 2018, **54**, 10495–10498.
- [40] R. Yang, X. He, G. Niu, F. Meng, Q. Lu, Z. Liu and X. Yu, *ACS Sensors*, 2021, **6**, 1552–1559.
- [41] Z. Wang, H. Xia, B. Chen, Y. Wang, Q. Yin, Y. Yan, Y. Yang, M. Tang, J. Liu, R. Zhao, W. Li, Q. Zhang and Y. Wang, *Angew. Chem. Int. Ed.*, 2021, **60**, 14512–14520.
- [42] S. Chen, M. Chen, J. Yang, X. Zeng, Y. Zhou, S. Yang, R. Yang, Q. Yuan and J. Zheng, *Small*, 2021, **17**, e2100243.
- [43] X. Li, P. Wu, W. Cao and H. Xiong, *Chem. Commun.*, 2021, **57**, 10636–10639.
- [44] L. J. Legoabe, A. Petzer and J. P. Petzer, *Chem. Biol. Drug Des.*, 2015, **86**, 895–904.
- [45] B. Gauni, K. Mehariya and A. S. and S. M. Duggirala, *Lett. Drug Des. Discov.*, 2021, **18**, 222–238.
- [46] J. Leng, H.-L. Qin, K. Zhu, I. Jantan, M. A. Hussain, M. Sher, M. W. Amjad, M. Naeem-Ul-Hassan, W. Ahmad and S. N. A. Bukhari, *Chem. Biol. Drug Des.*, 2016, **88**, 889–898.
- [47] A. Lilienkamp, M. P. Johansson and K. Wähälä, *Org. Lett.*, 2003, **5**, 3387–3390.
- [48] Á. Baji, A. Gyovai, J. Wölfling, R. Minorics, I. Ocsovszki, I. Zupkó and É. Frank, *RSC Adv.*, 2016, **6**, 27501–27516.
- [49] H. Chen, Y. Tang, M. Ren and W. Lin, *Chem. Sci.*, 2016, **7**, 1896–1903.
- [50] G. Yin, T. Niu, Y. Gan, T. Yu, P. Yin, H. Chen, Y. Zhang, H. Li and S. Yao, *Angew. Chem. Int. Ed.*, 2018, **57**, 4991–4994.
- [51] Y. Zhang, S. Li and Z. Zhao, *Anal. Chem.*, 2016, **88**, 12380–12385.
- [52] M. V Shirmanova, I. N. Druzhkova, M. M. Lukina, V. V Dudenkova, N. I. Ignatova, L. B. Snopova, V. I. Shcheslavskiy, V. V Belousov and E. V Zagaynova, *Sci. Rep.*, 2017, **7**, 8911.

- [53] W. Zhang, X. Wang, P. Li, H. Xiao, W. Zhang, H. Wang and B. Tang, *Anal. Chem.*, 2017, **89**, 6840–6845.
- [54] L. Lin, J. Zhao, L. Zhang, Y. Huang, F. Ye and S. Zhao, *Chem. Commun.*, 2018, **54**, 9071–9074.
- [55] M. H. Lee, J. H. Han, J. H. Lee, N. Park, R. Kumar, C. Kang and J. S. Kim, *Angew. Chem. Int. Ed.*, 2013, **52**, 6206–6209.

Pyridinium-based Single Excitation Ratiometric pH Probe for Real-Time Autophagy Monitoring in Lysosome



3.1. Abstract

*Progress in cancer therapy is currently facing an enormous challenge due to the apoptotic resistance of several classes of cancer cells. In this context, autophagy provides a potential alternative to non-apoptotic mechanisms in the treatment of cancer. Herein, we report a new aqueous soluble pyridinium-based ratiometric fluorescent probe **PM-C6-OH** for monitoring changes in lysosomal pH during autophagy. The probe, derived from the pyrylium probe **PS-OH** showed yellow ($\lambda_{max} = 550 \text{ nm}$) and red ($\lambda_{max} = 640 \text{ nm}$) emission at acidic and basic pH, respectively. A*

large Stokes shift (5799 cm^{-1} to 5208 cm^{-1}) irrespective of the pH variation enabled ratiometric response using single and multiple excitations. **PM-C₆-OH** also showed excellent lysosomal localization (Pearson's coefficient = 0.94) without creating any alkalizing effect. Rapamycin and starvation were used to induce autophagy in **PM-C₆-OH** stained HeLa cells, and lysosomal acidification was monitored by following the ratiometric variations in the green and red channels. Our studies envision this probe to be an essential part of the chemical toolbox for monitoring autophagy progression and assists in screening new autophagy inducers and inhibitors.

3.2. Introduction

New tools and techniques for inducing and monitoring apoptosis in cancer cells are indeed steering significant advancements in tumor theranostics.¹⁻⁷ However, chemo- and apoptotic-resistance are identified to be the major bottlenecks in cancer therapy.^{8,9} Therefore, devising new therapeutic strategies that exploit non-conventional cell destruction mechanisms have become all the more attractive in cancer research.^{10,11} In this context, autophagy, another pathway for programmed cell death akin to apoptosis, has demonstrated huge potential in targeted therapy. This organized catabolic process,^{12,13} progresses through a double-membrane vesicle formation (autophagosome) that engulfs cellular proteins and organelles and delivers to lysosomes.¹⁴ Several studies have confirmed autophagy to operate via a cytoprotective process, that helps cells to maintain intracellular homeostasis.¹⁵ Cancer cells have been found to be more susceptible towards autophagy compared to normal cells.¹⁶ Recent literature suggest that inducing autophagy can prevent

cancer progression in pre-malignant lesions.¹⁷ On the other hand, autophagy inducers and inhibitors have also been found to be effective as therapeutic agents in advanced stages of cancer.^{18,19} An increased interest in autophagy has put-forth an unprecedented demand for suitable imaging agents for tracking the effectiveness of such inducers and inhibitors for real-time monitoring and understanding the mechanistic pathways behind targeted cell death.²⁰⁻²²

Currently used autophagy monitoring techniques such as TEM, western blot, and GFP-based markers are time-consuming, expensive, complicated, and cannot monitor cellular processes in real-time.¹² Therefore, small-molecular organic fluorophores have evolved as an excellent alternative for real-time autophagy monitoring, due to the ease of synthesis, possibilities for structural modification, low cost and membrane-permeable non-invasive detection capabilities.^{23,24}

During autophagy, autophagosomes interact with the lysosome, leading to the formation of auto-lysosomes via a fusion mechanism. Autophagosomes further remove the damaged mitochondria and reduce cellular stress by maintaining ROS levels in a process called mitophagy. Both these processes lead to noticeable changes in cellular pH, since autophagosomes are more acidic than lysosomes and mitochondria. Therefore, autophagy and mitophagy result in moderate to severe cellular acidification. Concomitant with cellular acidification, several other parameters such as viscosity, polarity, ROS level, etc., have also been found to change with autophagy and mitophagy. These changes in cellular parameters

associated with such processes have aroused a renewed interest in developing organic fluorescent sensor-based autophagy monitoring agents.

In this context, Kim and co-workers have reported the use of a naphthalimide-based fluorescent probe **1** for mitophagy monitoring by following the associated variations in cellular pH.²⁵ The probe comprised of a naphthalimide fluorescent core, a piperazine unit for pH response, a triphenylphosphonium moiety for mitochondria targeting, and a benzyl chloride moiety for mitochondrial immobilization via nucleophilic substitution of the chloride by reactive thiols of various proteins (**Figure 3.1a**). The probe **1** that was non-fluorescent at neutral pH due to PET effect exhibited a fluorescence peak at 525 nm at pH 2, and the pKa was found to be 6.18 ± 0.049 . It showed excellent mitochondrial localization with a Pearson's correlation coefficient of 0.87 and the mitochondrial pH of HeLa cells was determined to be 7.99 ± 0.49 .

HeLa cells, kept in a serum-free medium to induce mitophagy through nutrient deprivation, were co-incubated with the probe **1** and Mitotracker red (MTR). The fluorescence intensity of the cells increased with time, indicating cellular acidification and the final pH was found to be 4.87 ± 0.35 . Autophagosomes fuse with lysosomes to form autolysosomes at the final stages of autophagy. Therefore, autophagy was induced in HeLa cells stained with probe **1** and LysoTracker red (LTR). With the progression of autophagy, both the probe **1** and LTR showed higher colocalization, indicating the formation of autolysosomes (**Figure 3.1b**).

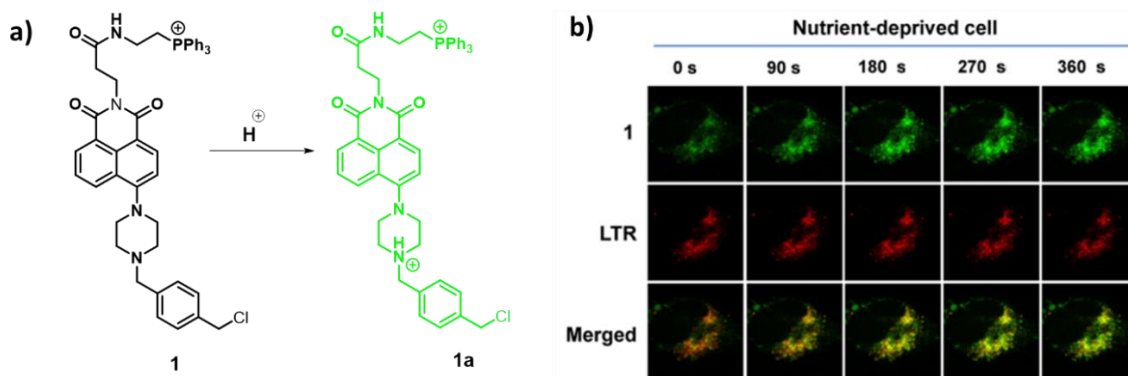


Figure 3.1. (a) Structure of the probe **1** in its protonated and deprotonated forms. (b) Confocal microscope images of nutrient-deprived HeLa cells stained with probe **1** and lysotracker red (LTR) at different time points, indicating cellular acidification during autophagy. (Adapted with permission from ref 25)

Meng *et. al.*, have reported a two-photon fluorescent probe **2** to monitor lysosomal polarity variations during autophagy (**Figure 3.2a**).²⁶ Probe **2** showed strong fluorescence at low polarity, that decreased with an increase in the polarity of the medium, along with a 30 nm red shift in its emission maximum (**Figure 3.2b**). The quantum yield and lifetime of the probe also exhibited a similar trend, while pH and viscosity were found to have negligible effect on the photophysical properties. Two-photon cross-section at 760 nm also showed a dip with an increase in the polarity of the medium.

Probe **2** showed excellent lysosomal colocalization in MCF-7 cells (Pearson's Coefficient = 0.91) with Lysotracker red. When the probe-incubated cells were treated with 10 μ M DMSO, an increase in fluorescence intensity was observed, confirming a decrease in the polarity of the cellular medium. The probe-stained MCF-7 cells were then kept in a nutrient-free medium that triggered autophagy and fluorescence intensity of the cells was found to decrease with time, indicating an

increase in lysosomal polarity concomitant with autophagy progression (**Figure 3.2c**).

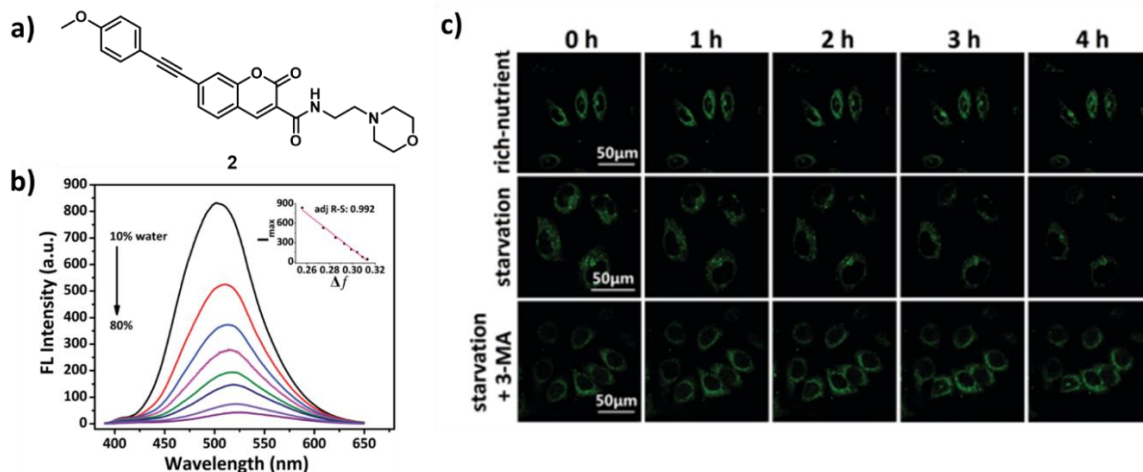


Figure 3.2. (a) Chemical structure of the two-photon probe **2**. (b) Change in the emission spectra of the probe **2** at different polarity. (c) Fluorescence images of the probe **2**-incubated MCF-7 cells under normal, autophagy in the absence and presence of an inhibitor. Cells under starvation showed a gradual decrease in fluorescence, indicating an increase in lysosomal polarity. The normal and autophagy inhibited cells did not show any changes in emission. (Adapted with permission from ref 26)

Since autophagy is relevant to several organelles, Lin and co-workers developed a fluorescent pH probe **3** by covalently connecting 7-hydroxycoumarin (for monitoring cytoplasmic pH) and amino-rhodamine (to visualize lysosomal pH) (**Figure 3.3a**).²⁷ The probe showed a weak blue emission ($\lambda_{\text{max}} = 455 \text{ nm}$) under acidic conditions, that increased drastically with a change in pH to 8, while the bright red emission ($\lambda_{\text{max}} = 588 \text{ nm}$) exhibited an opposite trend leading to a ratiometric response (**Figure 3.3b**). Subsequent experiments confirmed two pKa values of 3.5 and 6.2, that makes the probe suitable for pH monitoring in lysosome and cytoplasm.

When HepG2 cells were incubated with probe **3**, an intense emission in the blue channel was observed with a weak red emission. The red emission was found to emerge from predominant localization in lysosomes (colocalization coefficient =

0.89), and blue emission from Endoplasmic Reticulum (Pearson's Coefficient = 0.85), where the pH is comparable to that of the cytoplasm. The emission properties while altering the intracellular pH of the probe incubated cells was found to be in good agreement with the photophysical data. The probe-stained cells were kept in PBS buffer to induce autophagy, and validated using a western blot experiment. Probe **3** stained cells, under autophagy, showed a slightly decreased blue emission with significantly increased red emission after 60 min, as compared to the control. The potential of the probe for mapping cellular autophagy was further corroborated by monitoring the emission changes after 120 min (**Figure 3.3c**).

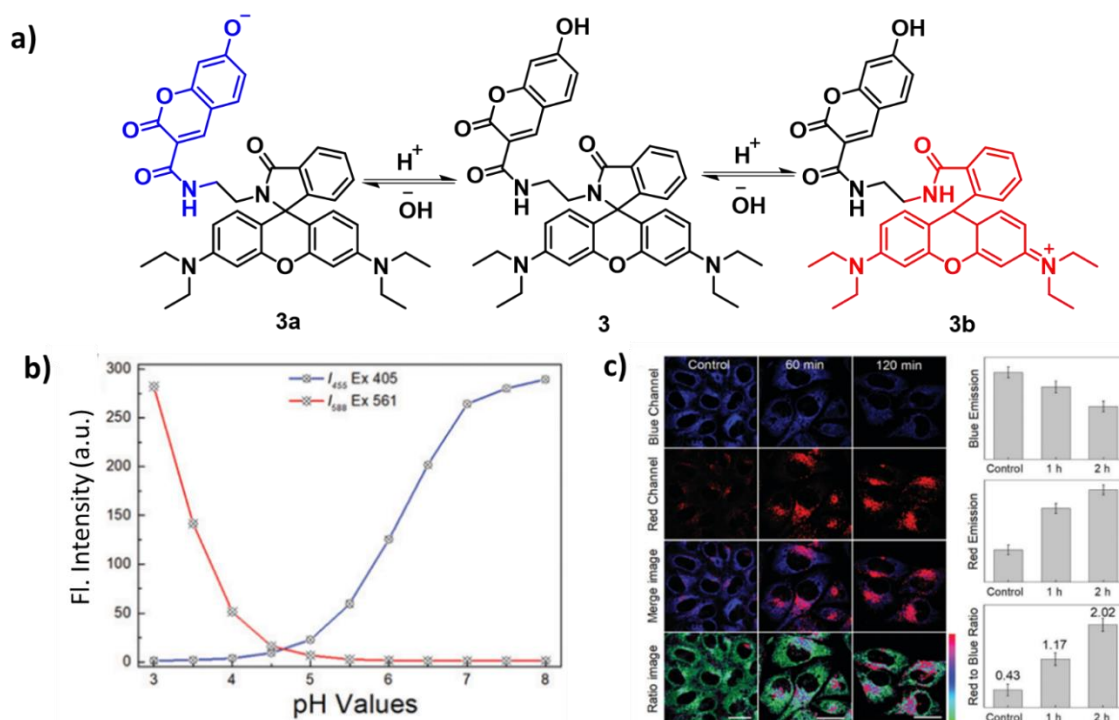


Figure 3.3. (a) Double protonation-deprotonation mechanism of the probe **3** and the associated changes in its structure. (b) The probe's secondary emission profile at $\lambda_{max} = 455$ and 588 nm with changes in pH. (c) Confocal microscopy images of the probe **3** stained HepG2 cells in blue and red channel under autophagy. Ratiometric images were then constructed and intensity quantification was achieved. (Adapted with permission from ref 27)

Autophagy induced enhancement in cellular H_2O_2 level was reported by Peng and co-workers using a hemicyanine-based fluorophore **4**, having a borate ester moiety for detection of H_2O_2 through a Turn-ON NIR fluorescence signal. The probe exhibited a bathochromic shift in the absorption maxima from 554 nm to 685 nm upon addition of H_2O_2 , along with a new fluorescence peak at $\lambda_{\text{max}} = 709$ nm (**Figure 3.4a**).²⁸ MCF-7 cells incubated with the probe, when treated with 100 μM H_2O_2 , a significant fluorescence enhancement in the red channel was observed. Autophagy was then induced in probe **4**-stained MCF-7 cells using Rapamycin. A significantly intense red fluorescence was observed after 3 h compared to the control cells (**Figure 3.4b**).

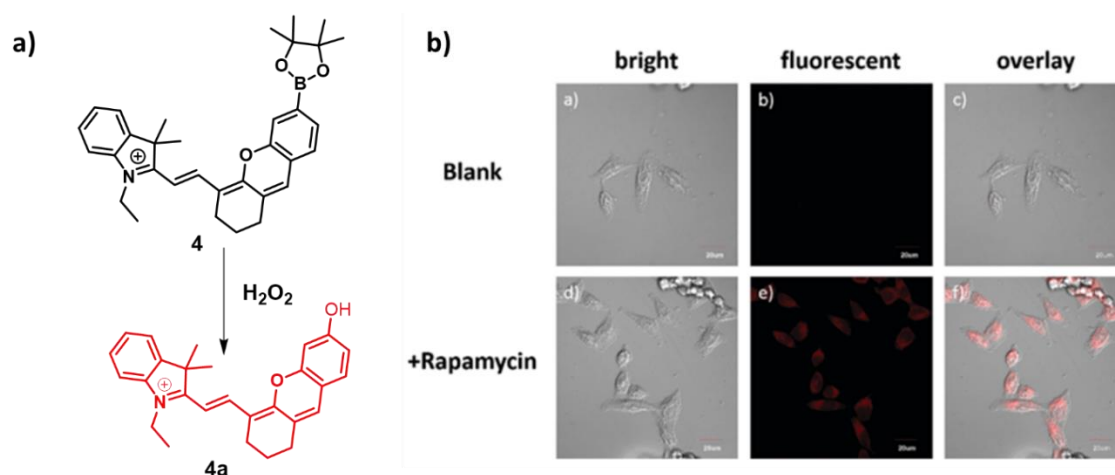


Figure 3.4. (a) Mechanism of the Turn-ON fluorescence response of the probe **4** towards H_2O_2 . (b) Images of MCF-7 cells under autophagy in the presence of the probe and its comparison with a set of control cells, obtained in the red channel. (Adapted with permission from ref 28)

Dong *et al.* have developed a pH probe **5** for monitoring lysosomal pH change during autophagy.²⁹ Unlike most of the lysosome targeting probes, Rhodamine-based fluorophore **5**, that does not feature a protonated moiety, localized in lysosome (Pearson's Coefficient = 0.89) due to the presence of a methylcarbitol unit (**Figure**

3.5a). Almost no fluorescence was observed at physiological pH (7.4) and a sharp 'Turn-ON' emission with a maximum at 583 nm was observed at lysosomal pH (~4.5). When the intracellular pH of HeLa cells was adjusted using Nigericin in the presence of **5**, intense red fluorescence was observed under acidic conditions. HeLa cells were then stained with the probe and autophagy was induced by keeping in a nutrient-free medium. The red fluorescence was found to increase gradually with time, confirming lysosomal acidification during autophagy (**Figure 3.5b-c**).

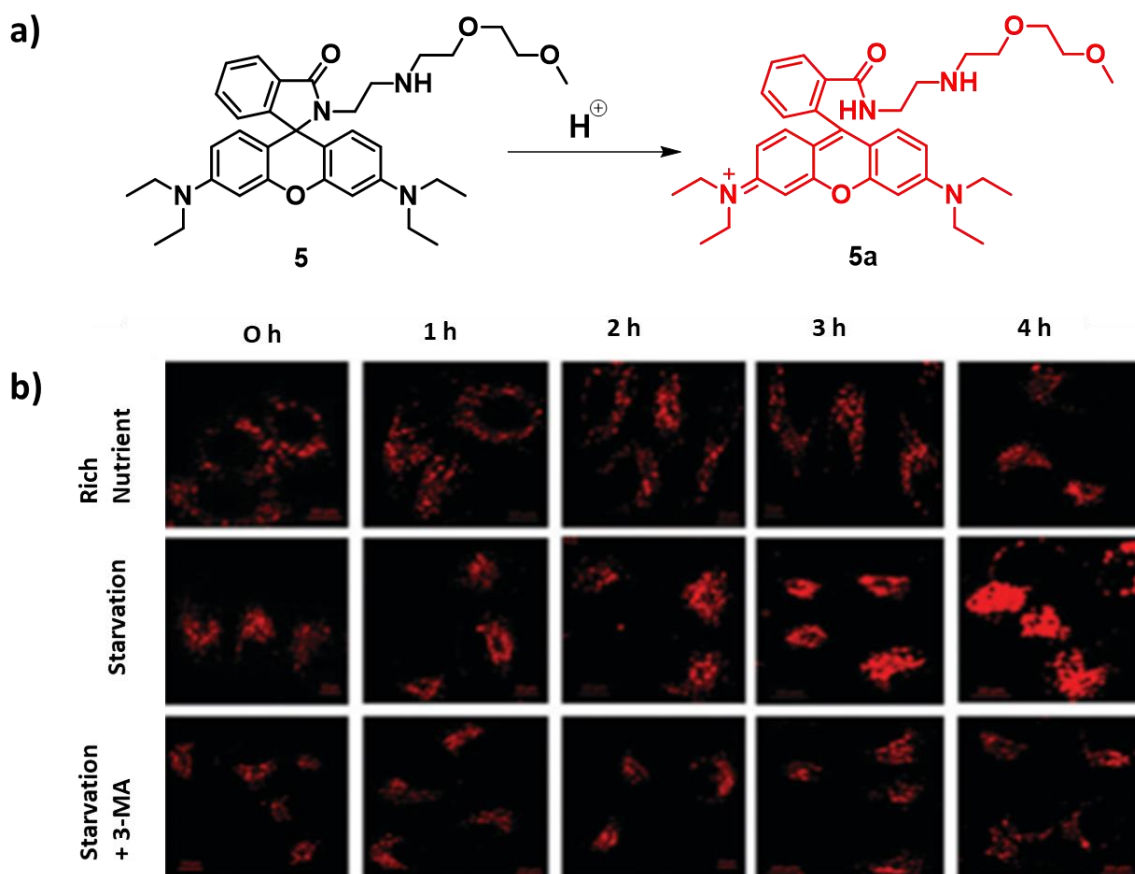


Figure 3.5. (a) Fluorescence Turn-ON mechanism of lysosome targeting probe **5** in the presence of an acid. (b) Change in fluorescence intensity of autophagic HeLa cells incubated with the probe compared to the control cells. (Adapted with permission from ref 29)

A protonation mechanism involving morpholine or amines has been widely used to localize small molecules in lysosomes.^{30–33} The protonation of these molecular

entities disturbs the local pH dynamics and induces alkalizing effect within the cells.^{34,35} A few probes reported recently have been shown to target lysosomes without any protonation mechanism, and exhibited advantages over conventional probes for imaging in live cells.^{36,37} Though a few fluorescent pH probes for monitoring autophagy are reported, none of them targets lysosomes in the absence of a protonation mechanism, leading to a ratiometric response. In this chapter, we report the development of a fluorescent probe, **PM-C₆-OH**, based on a symmetric pentacyclic pyridinium core appended with a hexyl chain to modulate its hydrophobicity. A ratiometric fluorescence change (yellow and red) with good photostability, high stocks shift, and reversibility was observed with pH variation. **PM-C₆-OH** localized predominantly in lysosomes even in the absence of any conventional targeting group or the usual protonation mechanism. The promising potential of the probe towards monitoring the changes in intracellular pH during induced autophagy in real-time was demonstrated using HeLa cells. **PM-C₆-OH**, to the best of our knowledge, is the first lysosome-targeting small-molecular fluorescent probe capable of monitoring pH changes associated with the progression of autophagy without creating any alkalizing effect in cells.

3.3. Results and Discussion

3.3.1. Synthesis of the Pyridinium Derivatives

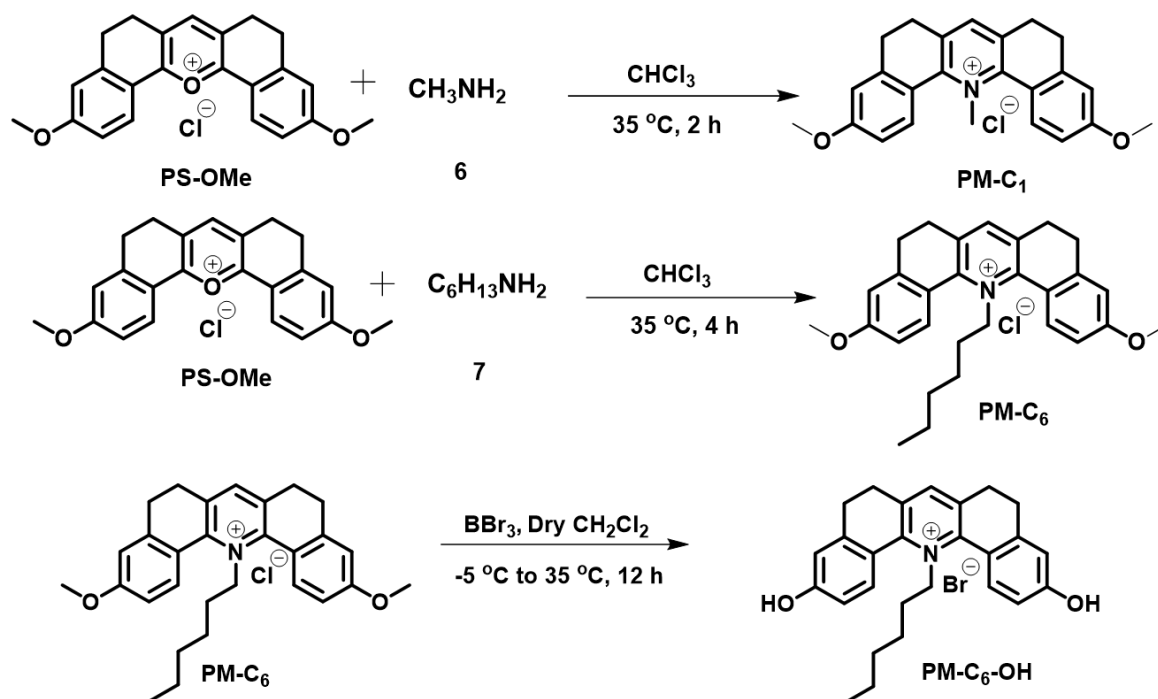
In the previous chapter, we developed a pyrylium fluorophore **PS-OH** for pH monitoring in live cells. The low extinction coefficient and quantum yield of **PS-**

OH leading to reduced brightness is a limiting factor in its sensing and imaging applications. The 'Turn-ON' fluorescence in response to pH change makes **PS-OH** suitable for 'point-of-care' detection, however ratiometric probes are preferred for quantitative experiments.³⁸ Furthermore, **PS-OH** is not specific to the cytoplasm and was found to accumulate in all organelles of the cell, including the nuclei, and is not desirable for a specific imaging agent. A deterrent towards these limitations requires the probe to have the following characteristics:

(i) better extinction coefficient and quantum yield, (ii) reduction in nuclear membrane penetration, and (iii) single excitation ratiometric response.

In a conjugated donor-acceptor-donor (D-A-D) system, reducing the electronegativity of the acceptor moiety assists in better π -cloud delocalization, leading to improved photophysical properties.³⁹ Therefore, the acceptor oxygen atom in **PS-OH** was replaced with a nitrogen atom, thereby converting the pyrylium salt into the corresponding pyridinium moiety and synthesized three pyridinium molecules, **PM-C₁**, **PM-C₆**, and **PM-C₆-OH**.^{40,41}

The pyrylium salt, **PS-OMe** was treated with methylamine and hexylamine in chloroform in room temperature (35 °C) to obtain **PM-C₁** and **PM-C₆**, respectively. **PM-C₆** was demethylated using BBr₃ in dry dichloromethane to yield the pH probe, **PM-C₆-OH** (Scheme 3.1). These molecules were characterized by ¹H and ¹³C NMR spectroscopy and high-resolution mass spectrometry (HRMS).



Scheme 3.1. Synthesis of **PM-C₁**, **PM-C₆**, and **PM-C₆-OH**.

Though **PM-C₁** was found to be soluble in most polar solvents at lower concentrations (μM), complete solubility was observed only in DMF and DMSO at higher concentrations (mM). Moreover, hydrophilic charged molecules may cross the nuclear membrane and this undesired but inherent limitations can be effectively addressed by introducing an alkyl chain. To improve the solubility in organic solvents for feasible synthetic modifications, and to restrict nuclear accumulation, we decided to focus our studies on **PM-C₆** and its demethylated analogue **PM-C₆-OH**.

3.3.2. Photophysical Studies

To understand the photophysical properties of the pyridinium molecules, solvent-dependent absorption and emission spectra of **PM-C₁**, **PM-C₆**, and **PM-C₆-OH** were

recorded. All the stock solutions (10 mM) were prepared in DMSO and diluted using different solvents, as required.

PM-C₁ showed absorption (λ_{abs}) and emission (λ_{em}) maxima at 400 nm and at 541 nm, respectively, in water. The extinction coefficient of the molecule in water was $4.36 \times 10^{-4} \text{ M}^{-1}\text{cm}^{-1}$ and Stokes shift was found to be 6515 cm^{-1} . In other solvents, such as acetonitrile, acetone, DMF, DMSO, methanol, and chloroform, **PM-C₁** showed a bathochromic shift in both absorption and emission maxima (**Figure 3.6a-b**).

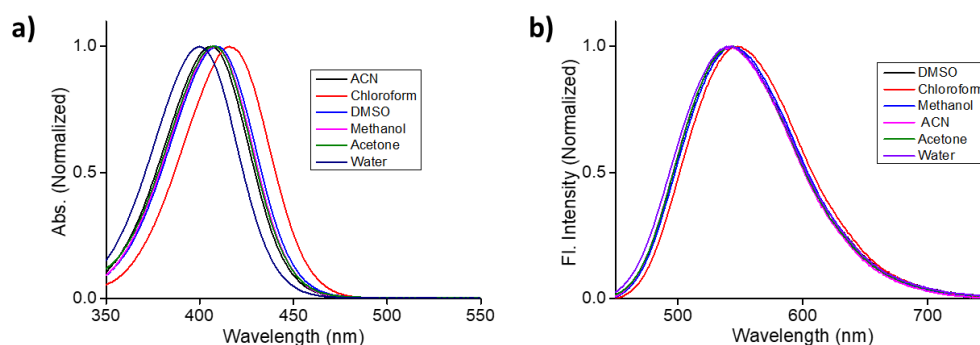


Figure 3.6. Solvent dependent (a) absorption, and (b) emission spectra of **PM-C₁**

Solvent	λ_{max} (nm)		Extinction Coefficient (ϵ) ($\text{M}^{-1}\text{cm}^{-1}$)	Stokes Shift (cm^{-1})
	Abs	Em		
Chloroform	417	548	3.45×10^{-4}	5732
Acetonitrile	405	542	2.62×10^{-4}	6241
Acetone	408	542	4.11×10^{-4}	6059
Methanol	407	543	3.3×10^{-4}	6153
DMSO	408	542	2.96×10^{-4}	6059
Water	400	541	4.36×10^{-4}	6515

Table 3.1. Absorption and emission maxima, extinction coefficient, and Stokes shift of **PM-C₁** in various solvents.

For **PM-C₆**, the absorption and emission maxima shifted to 414 nm and 550 nm, respectively in water (**Figure 3.7a-b**). The extinction coefficient and Stokes shift in water were $3.97 \times 10^{-4} \text{ M}^{-1}\text{cm}^{-1}$ and 5973 cm^{-1} , respectively.

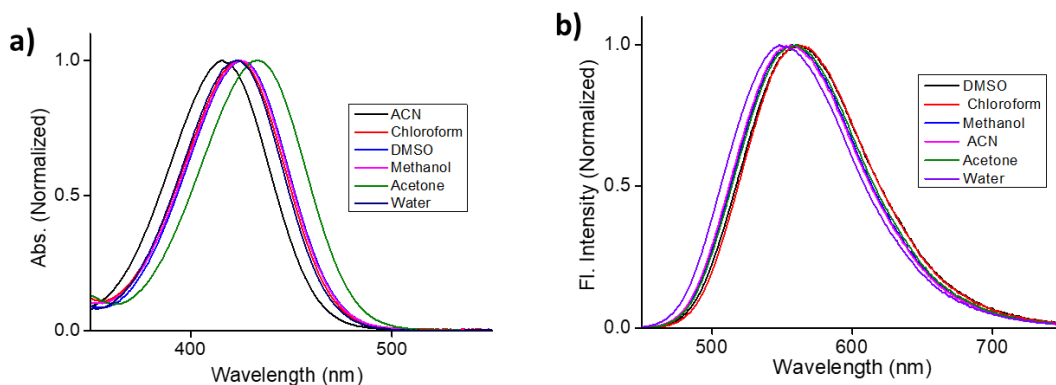


Figure 3.7. Solvent dependent (a) absorption, and (b) emission spectra of **PM-C₆**.

Solvent	λ_{max} (nm)		Extinction Coefficient (ϵ) ($\text{M}^{-1}\text{cm}^{-1}$)	Stokes Shift (cm^{-1})
	Abs	Em		
Chloroform	434	562	3.13×10^{-4}	5247
Acetonitrile	421	556	2.62×10^{-4}	5767
Acetone	423	560	3.52×10^{-4}	5783
Methanol	426	556	3.17×10^{-4}	5488
DMSO	426	561	3.17×10^{-4}	5648
Water	414	550	3.97×10^{-4}	5973

Table 3.2. Absorption and emission maxima, extinction coefficient, and Stokes shift of **PM-C₆** in various solvents.

Similar shift in absorption and emission maxima were observed in other solvents also. **PM-C₆-OH** showed an almost similar absorption ($\lambda_{\text{abs}} = 417 \text{ nm}$) and emission ($\lambda_{\text{em}} = 550 \text{ nm}$) maxima in water, but with even larger bathochromic shifts in other solvents, compared to **PM-C₆** (**Figure 3.8a-b**, **Table 3.2**). The extinction coefficient

in water was found to be $5.46 \times 10^{-4} \text{ M}^{-1}\text{cm}^{-1}$ and was higher than that of **PM-C₆**, with a Stokes shift 5799 cm^{-1} .

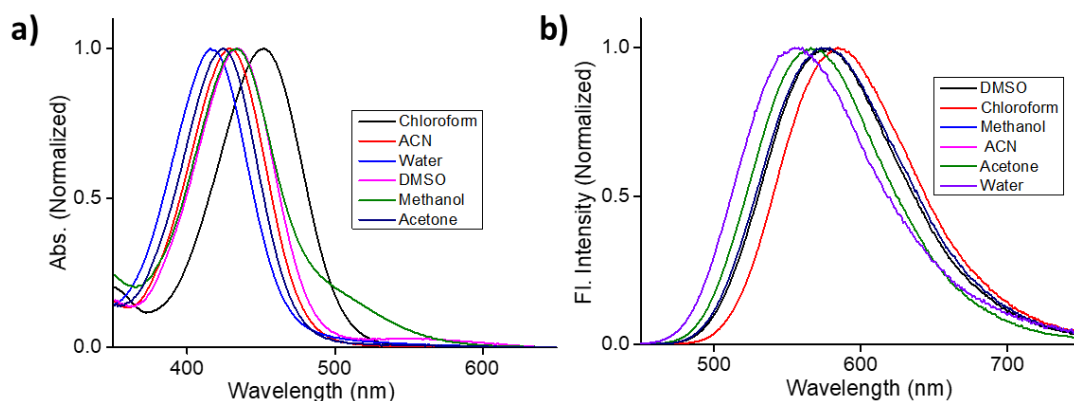


Figure 3.8. Solvent dependent (a) absorption, and (b) emission spectra of **PM-C₆-OH**.

Solvent	λ_{max} (nm)		Extinction Coefficient (ϵ) ($\text{M}^{-1}\text{cm}^{-1}$)	Stokes Shift (cm^{-1})
	Abs	Em		
Chloroform	451	585	6.81×10^{-4}	5079
Acetonitrile	423	560	2.33×10^{-4}	5784
Acetone	428	566	6.69×10^{-4}	5697
Methanol	434	566	2.48×10^{-4}	5373
DMSO	434	576	3.18×10^{-4}	5680
Water	417	550	5.46×10^{-4}	5799

Table 3.2. Absorption and emission maxima, extinction coefficient, and Stokes shift of **PM-C₆-OH** in various solvents. The fluorescence life time data is given in the experimental section.

Though a solvent dependent shift in absorption and emission maxima was observed for all three molecules, the shifts were significantly less than those reported for solvatochromic fluorophores.^{42,43} While the fluorescence maxima did not shift significantly, the absorption maxima of the pyridinium analogs exhibited a hypsochromic shift compared to the pyrylium fluorophores, thereby leading to a

larger Stokes shift. Another significant difference was observed in the extinction coefficients in organic solvents and water. While the extinction coefficient of the pyrylium fluorophore decreased in aqueous solution, the pyridinium molecules exhibited similar extinction coefficient in both organic and aqueous solutions.

Quantum yields of **PM-C₁**, **PM-C₆**, and **PM-C₆-OH** were measured using Coumarin 153 as standard. **PM-C₁** and **PM-C₆** showed lesser quantum yields, compared to the pyrylium analogue **PS-OMe**, probably due to the increased Stokes shift. However, **PM-C₆-OH** showed a 7-fold increase in the quantum yield compared to its pyrylium analogue **PS-OH**, most likely due to the change in the acceptor atom of the molecule. Lower electronegativity of the nitrogen atom allows for better delocalization of the π -electrons, resulting in better orbital matching between HOMO and LUMO. A combination of larger Stokes shift, better extinction coefficients and higher quantum yields make the pyridinium fluorophores better candidates for cellular imaging as compared to their pyrylium analogs.

3.3.3. pH Response and Calculation of pKa

In our previous work, **PS-OH** was found to exhibit an 'ON/OFF' fluorescence response with changes in the pH of the medium. A ratiometric response is always preferred for pH quantification, since the error can be minimized using the ratio of two signals. It can subtract common artifacts caused by both channels due to varying local concentrations of the dye, solubility, background noise, etc.

The pH response of **PM-C₆** was investigated using the photophysical properties of a 10 μ M aqueous solution at different pH (4 – 10). No significant changes in absorption and emission maxima were observed ($\lambda_{\text{abs}} = 414$ and 548 nm) at different pH (**Figure 3.9a**). The secondary plot constructed using fluorescence intensity at different pH also confirmed the negligible pH response of **PM-C₆** (**Figure 3.9b**). The pH response of **PM-C₁** was not investigated due to its structural similarity with **PM-C₆**, except for the alkyl chain length.

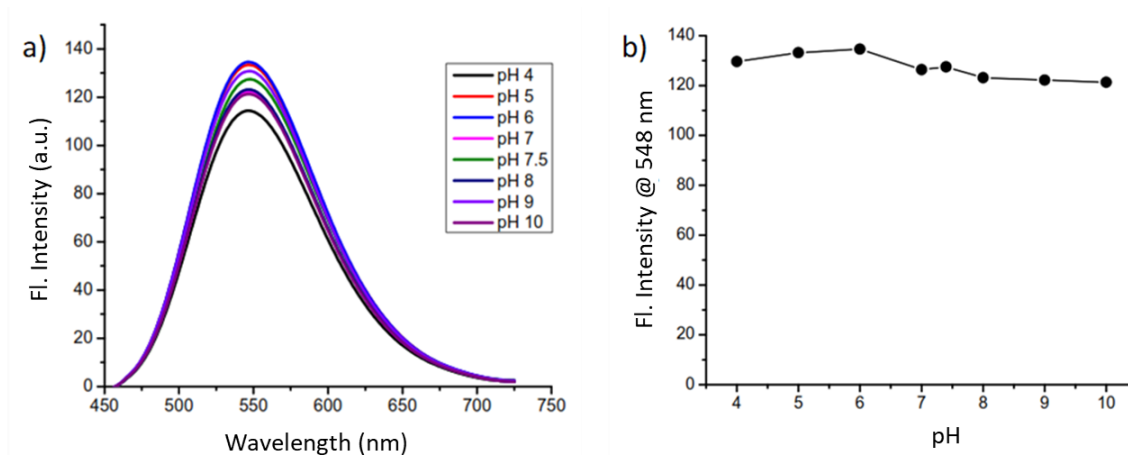


Figure 3.9. (a) Emission of **PM-C₆** (10 μ M) in PBS buffer at different pH ($\lambda_{\text{ex}} = 414$ nm). (b) The secondary plot of emission intensity at different pH, confirming negligible pH response.

For a preliminary understanding of the pH response of **PM-C₆-OH**, its absorption and emission spectra were recorded at pH 4 and 10. The absorption maxima were observed at 417 nm (pH 4) and at 480 nm (pH 10). The emission spectra were recorded using the same buffered solutions of **PM-C₆-OH**, exciting at the corresponding absorption maximum. An yellow fluorescence ($\lambda_{\text{em}} = 550$ nm) was observed at acidic pH and red fluorescence ($\lambda_{\text{em}} = 640$ nm) at basic pH, confirming the ratiometric response of **PM-C₆-OH**. An overlay of normalized absorption and

emission spectra of **PM-C₆-OH** at pH 4 and 10 clearly indicated negligible spectral overlap, irrespective of the pH, due to the large Stokes shift.

There are two types of ratiometric probes, based on the excitation wavelength – single and multiple excitation ratiometric probes. Majority of the reported fluorescent probes have narrow Stokes shifts, and the ratiometric signal is obtained by exciting the molecules at both the absorption maxima.⁴⁴ Only a few molecules having a large Stokes shift are excited at the isosbestic point for recording a ratiometric response.⁴⁵ While multiple excitation ratiometric probes feature a better intensity profile, facile imaging in terms of less background noise and use of single laser source makes single excitation ratiometric probes more appealing.

In order to assess the single and multiple excitation ratiometric behavior of **PM-C₆-OH**, we decided to excite the molecule at both the absorption maxima as well as the isosbestic point. Absorption spectra at different pH (4 - 10) showed an isosbestic point at 440 nm (**Figure 3.10a**). The emission spectra at each pH were recorded using three excitation sources (417, 440, and 480 nm). When **PM-C₆-OH** at pH 4 was excited at 417 nm, an yellow emission with λ_{max} at 550 nm was observed. Fluorescence intensity at 550 nm was found to decrease gradually with increasing pH; however, a new peak with negligible intensity at $\lambda_{\text{max}} = 640$ nm was also observed at basic pH (**Figure 3.10b**). Excitation using a 480 nm source at pH 4 resulted in a weak fluorescence signal at 550 nm, with a strong red emission that appeared at $\lambda_{\text{max}} = 640$ nm at basic pH (**Figure 3.10d**). Exciting **PM-C₆-OH** at 440 nm, both yellow and red emission signals were observed. At pH 4, a strong yellow

emission was predominant that decreased gradually with increasing pH with concomitant emergence of a red emission, resulting in a ratiometric response (Figure 3.10c).

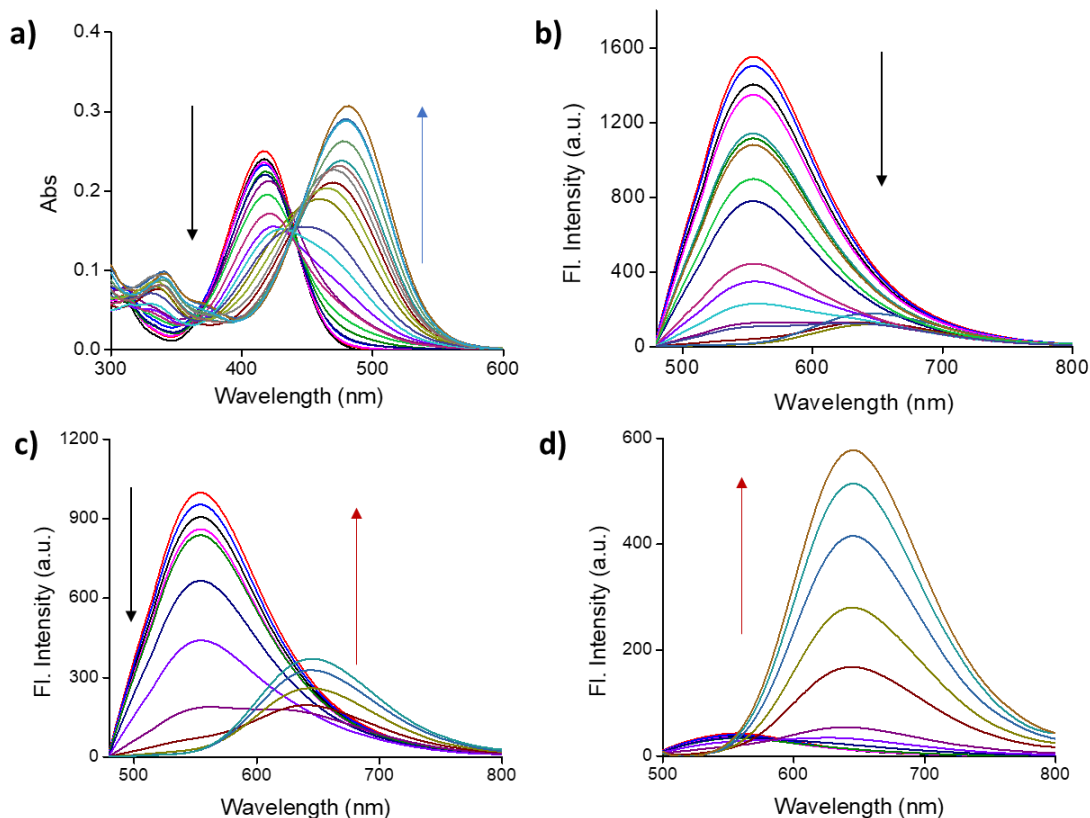


Figure 3.10. (a) Absorption spectra of the probe **PM-C₆-OH** (10 μM) in PBS buffer at different pH (4 – 10). Fluorescence response of **PM-C₆-OH** (10 μM) in PBS buffer of different pH when excited at (b) 417 nm, (c) 440 nm (isosbestic point), and (d) 480 nm (pH 4 - 10).

Two secondary graphs were plotted with fluorescence intensity at 550 nm ($\lambda_{\text{ex}} = 417$ nm) and 640 nm ($\lambda_{\text{ex}} = 480$ nm) against pH. Boltzmann non-linear fitting yielded two pK_a values (pK_{a1} = 7.41 ± 0.03 and pK_{a2} = 8.46 ± 0.07), which indicate that despite being a symmetric molecule, both the hydroxy groups in **PM-C₆-OH** do not simultaneously deprotonate at the same pH (Figure 3.11). Having two pK_a values widens the probe's pH sensitivity range and assists in broad range pH sensing.

Furthermore, **PM-C₆-OH** can be used to monitor the pH in the whole biological pH window (4 - 10), with a sharp change in emission in the pH range 6 - 9.5.

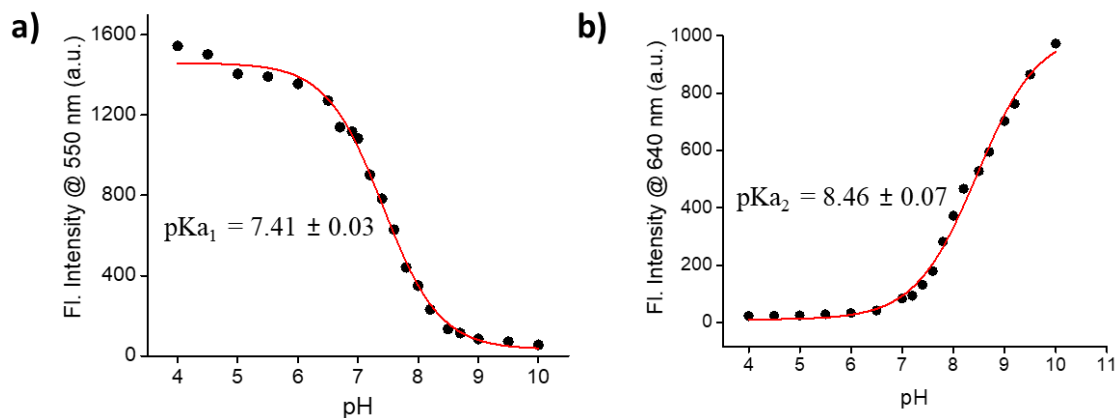
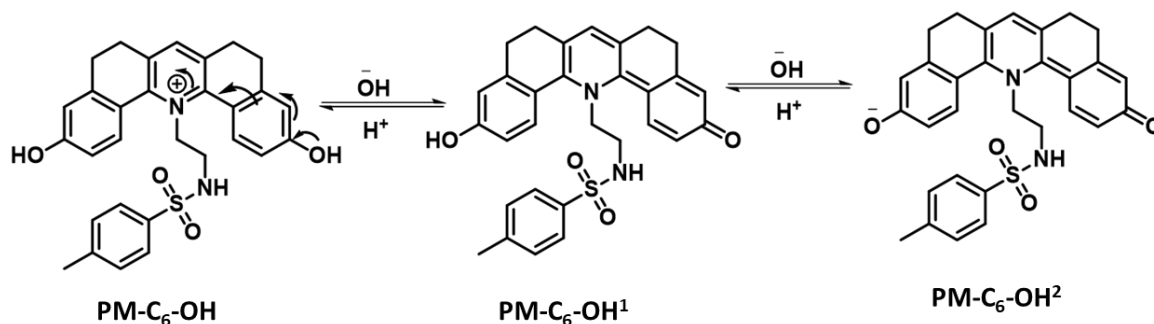


Figure 3.11. Non-linear fitting of the secondary plot of the fluorescence response of the probe **PM-C₆-OH** (10 μ M) at (a) 550 nm (λ_{ex} = 417 nm), and (b) 640 nm (λ_{ex} = 480 nm), and the corresponding fitting to obtain the pKa values.

Most of the pH probes capable of sensing a wide range of pH are made by connecting two molecular moieties with two distinct pKa values.⁴⁶ A single molecule with two pKa values and capable of broad range pH monitoring is rather rare. Possible canonical structures of **PM-C₆-OH** suggest that the initial deprotonation of any of the two hydroxy groups leads to a difference in electronic conjugation and the acceptor from the middle ring, localizes to one side of the molecule. Subsequent deprotonation occurs with an electron push from the donor, localized on the other side of the molecule that assists to emit around a longer wavelength than the fully protonated form of the molecule (**Scheme 3.2**).

The fluorescence quantum yields of **PM-C₆-OH** at pH 4 and 10 in PBS buffer were obtained using Coumarin 153 as a standard and was found to be 0.17, 0.04 at pH 4

and 10, respectively. The comparably lower quantum yield of **PM-C₆-OH** at basic pH is effectively compensated by its high extinction coefficient.



Scheme 3.2. Mechanism of protonation - deprotonation of two hydroxy groups of **PM-C₆-OH** at two different pH, leading to two pK_a values and a wide range of ratiometric pH monitoring.

3.3.4. pH Reversibility and Selectivity

One of the most critical aspects of fluorescent pH probes is their adaptability to monitor pH dynamics in normal cells during any cellular process or abnormalities in real time. Therefore, the reversibility of the fluorescence signal during pH cycling is of utmost importance. **PM-C₆-OH** in PBS buffer of pH 7.4 was subjected to pH switching between pH 4 and 10 using TFA and DBU, respectively. The fluorescence intensity of the probe remained nearly constant for 5 continuous pH cycles, indicating the reversibility of **PM-C₆-OH** in a dynamic pH medium and its utility as a pH probe for real-time sensing and imaging (**Figure 3.12a**).

Another essential prerequisite for any sensor is its selectivity towards the target analyte. We checked the fluorescence response of **PM-C₆-OH** towards various biologically relevant analytes. The emission spectra of the probe were recorded in PBS buffer of pH 7.4 in presence of different metal ions (Na^+ , K^+ , Cu^{2+} , Zn^{2+} , Fe^{2+} , Fe^{3+}), anions (Cl^- , AcO^-), reactive oxygen species (HOCl , H_2O_2 , O_2^-), biothiols (Cys,

GSH, H₂S), acid (H⁺) and base (OH⁻). Fluorescence signals showed significant changes only in response to pH, thereby proving the probe's selectivity towards acid or base (**Figure 3.12b**).

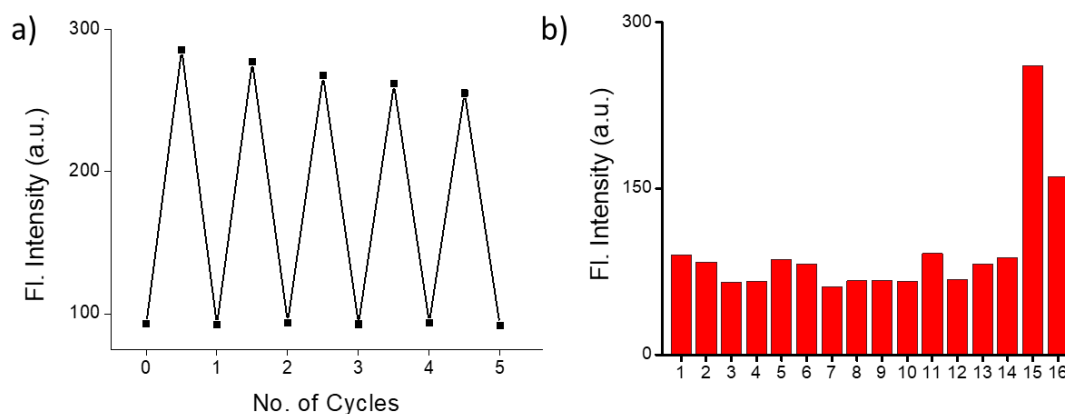


Figure 3.12. (a) Reversibility of **PM-C₆-OH** (10 μ M) under multiple cycles of acid and base treatments. (b) Selectivity of **PM-C₆-OH** (10 μ M) towards different biologically relevant analytes (1. Na⁺, 2. K⁺, 3. Cu²⁺, 4. Zn²⁺, 5. Fe²⁺, 6. Fe³⁺, 7. Cl⁻, 8. AcO⁻, 9. HOCl, 10. H₂O₂, 11. O₂⁻, 12. Cys, 13. GSH, 14. H₂S, 15. H⁺ and 16. OH⁻) at pH 7.4.

3.3.5. Biocompatibility and Photostability

Many optical sensors are not preferred for cellular imaging due to their toxicity towards live cells. Therefore, determination of the cytotoxicity is mandatory before any probe to be used as a cell imaging agent. Cytotoxicity of **PM-C₆-OH** was assayed on a control fibroblast cell line (WI-38) and a cervical cancer cell line (HeLa). MTT assay confirmed that even 100 μ M solution of the probe under incubation for 24 h did not show any notable toxicity on either of the cell lines, corroborating the superior biocompatibility of **PM-C₆-OH**. Doxorubicin was used as a positive control (**Figure 3.13a**).

We further checked the photostability of **PM-C₆-OH** at different pH (4, 7.4, and 10) by irradiating using an Hg lamp (200 W) under a 400 nm long-pass filter followed by recording the emission spectra every 10 min for 30 min. The secondary plot of fluorescence intensity vs. time confirmed no significant photobleaching of **PM-C₆-OH** in presence of acid or base (**Figure 3.13b**). To confirm the photostability in cellular environment, HeLa cells were incubated with **PM-C₆-OH** and was compared with commercial lysotracker red (LTR). Both sets of the cells were irradiated for 180 s at the maximum intensity of the microscope's light source, and images were captured at every 60 s. Quantification of fluorescence intensity from these images confirmed that **PM-C₆-OH** is as photostable as LTR (**Figure 3.13c,d**). Photoinduced radical formation was not also observed during these experiments.

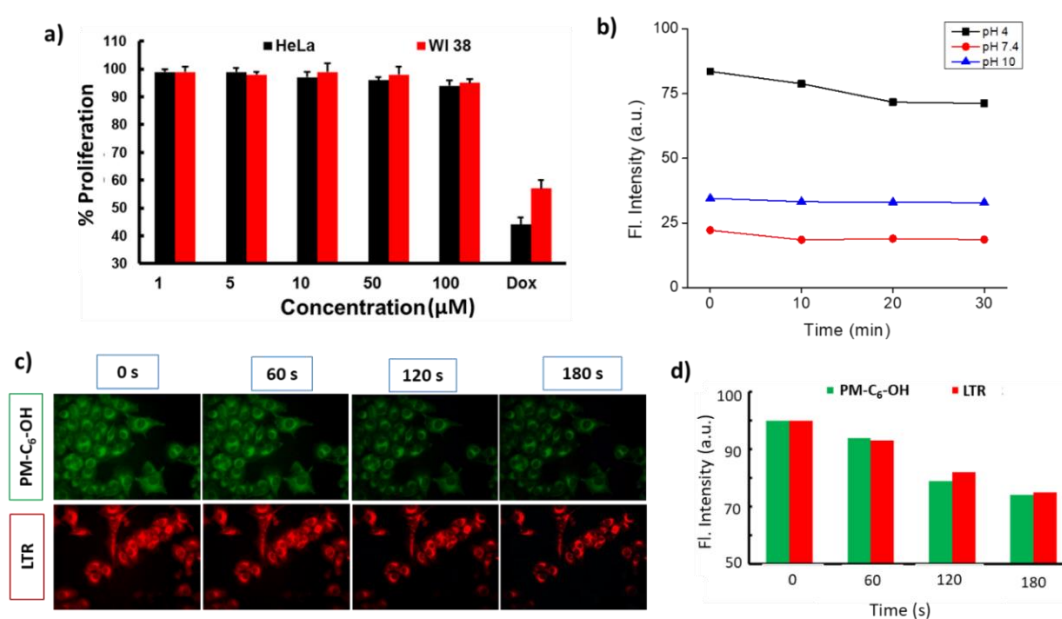


Figure 3.13. (a) Evaluation of the biocompatibility of **PM-C₆-OH** at different concentration on WI-38 and HeLa cells for 24 h by MTT assay using doxorubicin as standard. (b) Determination of photostability of **PM-C₆-OH** (10 µM) at acidic, neutral and basic pH medium. (c) Images of HeLa cells incubated with **PM-C₆-OH** and commercial Lysotracker red (LTR) at different time points under light irradiation. (d) Quantification of fluorescence intensity of HeLa cells, calculated from the image in Figure 3.13c.

3.3.6. Colocalization Experiments

To address the limitations of nuclear membrane penetration by the pyrylium analog **PS-OH**, we introduced a hexyl chain in the pyridinium salt **PM-C₆-OH**. Two sets of HeLa cells were co-stained with **PM-C₆** or **PM-C₆-OH**, and commercial blue fluorescent nucleus staining dye Hoechst-33342. For both probes, merged images of HeLa cells obtained in the blue and green channels showed minimal overlap, indicating a predominant localization of **PM-C₆** and **PM-C₆-OH** within the cell cytoplasm (**Figure 3.14**).

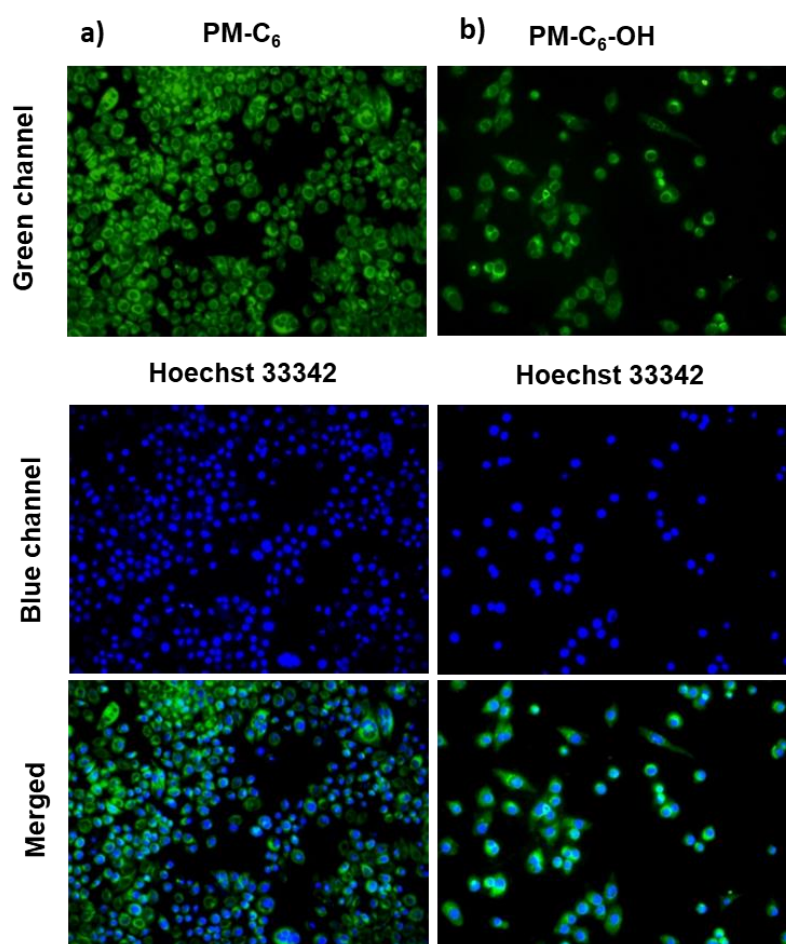


Figure 3.14. Fluorescence images of HeLa cells in green and blue channels, incubated with (a) **PM-C₆** and Hoechst 33342, and (b) **PM-C₆-OH** and Hoechst 33342, and the merged images to confirm cytoplasmic localization of **PM-C₆** and **PM-C₆-OH**.

Due to the presence of a positively charged core, it was expected that both **PM-C₆** and **PM-C₆-OH** may preferentially accumulate in mitochondria, which has a negatively charged membrane. Three sets of HeLa cells were stained with LysoTracker red, Mitotracker red, and Hoechst-33342, along with **PM-C₆** in each set. Images were obtained in blue, green, and red channels and merged using ImageJ software.

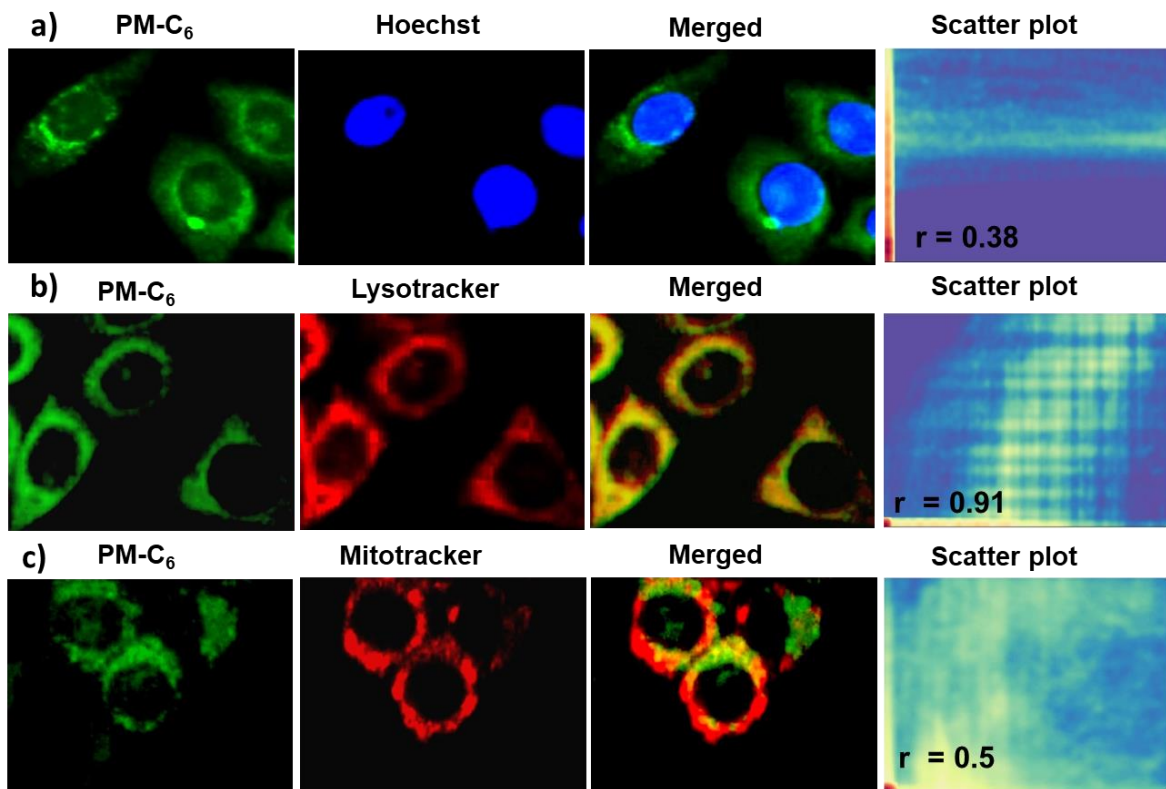


Figure 3.15. Determination of localization of **PM-C₆** (a) HeLa cells were co-incubated with **PM-C₆** and Hoechst 33342, and images were captured in the green and blue channels. Images from both channels were merged to calculate the Pearson's coefficient. (b) **PM-C₆** and LysoTracker red were added to HeLa cells, and images were taken in the green and red channels. Both the images were merged to construct a single image for further analysis. (c) **PM-C₆** and LysoTracker red-stained HeLa cells were imaged in the green and red channels, and a merged image was generated. Finally, all three merged images were analyzed using Matlab software to calculate Pearson's coefficients (r).

From the merged images, Pearson's coefficients (r) were calculated for each organelle. As expected, **PM-C₆** did not show any significant colocalization with the

nuclear staining Hoechst-33342 (Pearson's coefficient = 0.38, **Figure 3.15a**). To our surprise, the probe did not show any significant localization in mitochondria also (Pearson's coefficient = 0.50) despite of having a positive charge (**Figure 3.15c**). The probe was found to be colocalized predominantly in the lysosome (Pearson's coefficient = 0.91), even in the absence of any functional group that can be protonated at lysosomal pH, unlike vastly reported lysosome targeting systems (**Figure 3.15c**).

Similar co-localization experiments on HeLa cells using **PM-C₆-OH** also confirmed negligible accumulation in the nucleus (Pearson's coefficient = 0.40) and mitochondria (Pearson's coefficient = 0.60) (**Figure 3.16a, c**). To our satisfaction, **PM-C₆-OH** exhibited better lysosome targeting (Pearson's coefficient = 0.94) compared to **PM-C₆** (**Figure 3.16b**). It indicated that the structural feature of **PM-C₆** and **PM-C₆-OH** might be the reason of their lysosomal localization.

Recently a few probes with a methylcarbitol unit, without any protonation mechanism, have been found to localize in lysosomes.^{29,37} Most of these probes have a hydrophobic fluorophore which is attached to a hydrophilic methylcarbitol unit. The balance between the hydrophobic core and hydrophilic tag played a crucial role in directing the probe towards the lysosome. On similar grounds, the positively charged hydrophilic fluorophore and the hydrophobic hexyl chain most likely contributed to the lysosomal co-localization of **PM-C₆** and **PM-C₆-OH**.

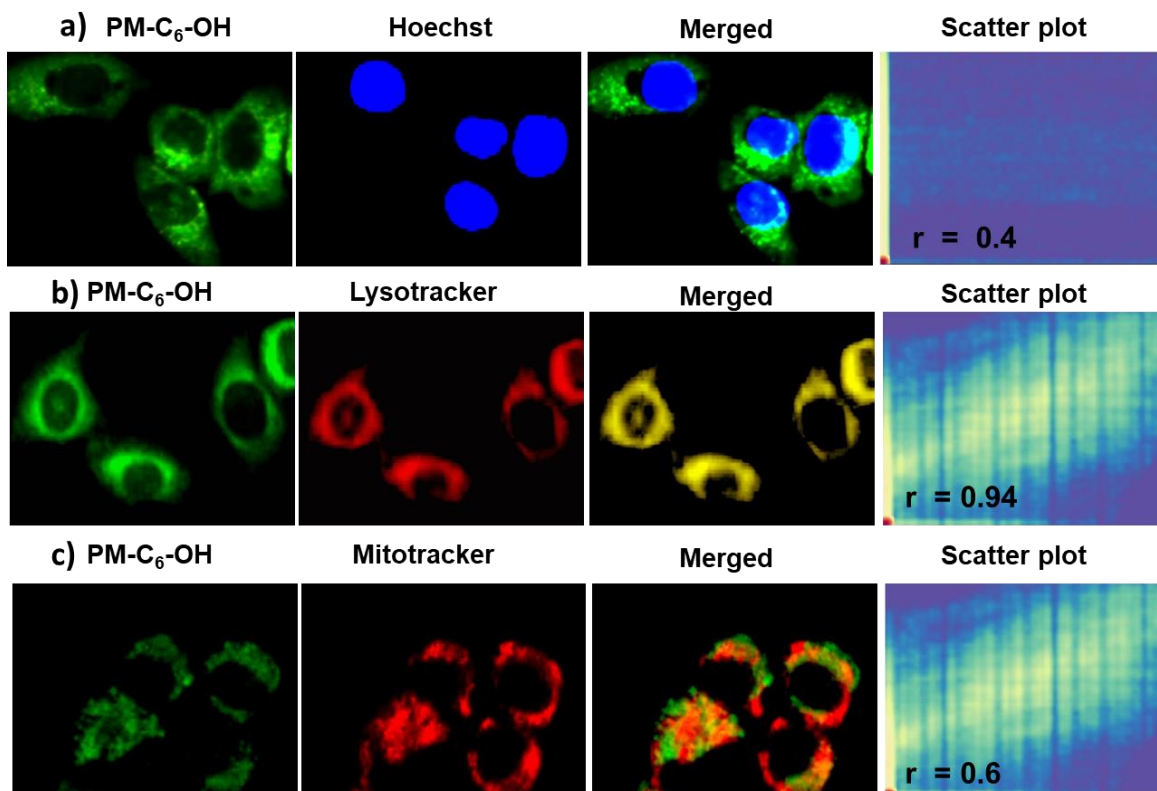


Figure 3.16. Determination of localization of **PM-C₆-OH**. Three sets of HeLa cells were stained with **PM-C₆-OH** and then co-stained with Hoechst 33342, LysoTracker red and Mitotracker red. (a) For **PM-C₆-OH** and Hoechst 33342, images were taken in the green and blue channels. For both (b) **PM-C₆-OH** and LysoTracker red, (c) **PM-C₆-OH** and Mitotracker red, images were taken in the green and red channels. Pearson's coefficients (r) were calculated from the merged images using Matlab software.

3.3.7. Intracellular pH Response

The excellent ratiometric pH response, biocompatibility, photostability and quick cellular internalization of **PM-C₆-OH** prompted us to further explore its potential as a pH imaging agent in live cells. 10 μ M concentration was found to be optimum for imaging experiments using **PM-C₆-OH**. To evaluate the intracellular pH response of **PM-C₆-OH**, HeLa cells were first treated with Nigericin for adjusting the intracellular pH between 4 and 10. Images in green and red channels were obtained after incubating the Nigericin treated cells with **PM-C₆-OH** (**Figure 3.17a**).

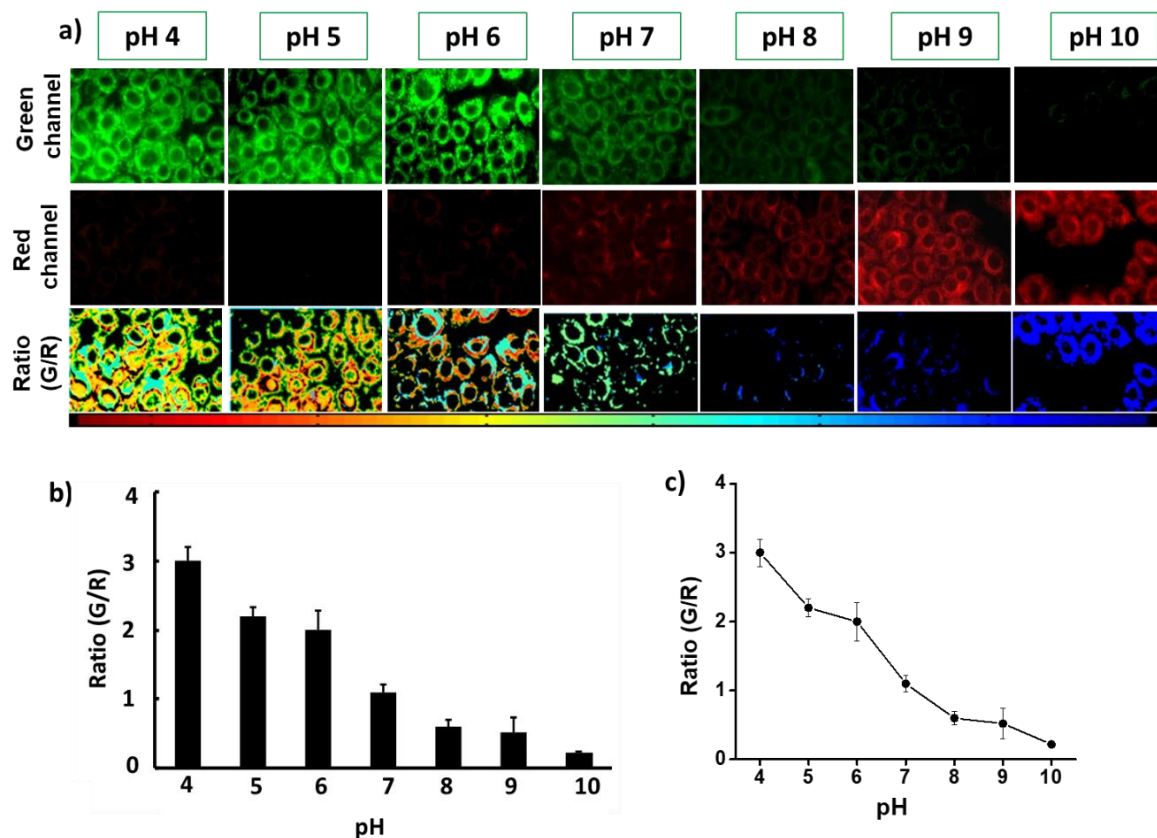


Figure 3.17. (a) Fluorescence microscopy imaging of HeLa cells, incubated with **PM-C₆-OH** at different intracellular pH, induced with the help of 10 μ M Nigericin. Images were taken in the green and red channels. Ratiometric images were constructed using the ratio of green/red intensity. (b) Fluorescence intensity ratio (green/red) from cellular imaging at different pH. (c) Intracellular pH calibration curve of **PM-C₆-OH** obtained from normalized fluorescence intensity at different pH.

The fluorescence intensity in green channel was found to gradually decrease with increasing pH, while that in the red channel showed an opposite trend. Using the images in the green and red channels, ratiometric images were constructed (**Figure 3.17b**). From the intensity of the images in the green and red channels, the green/red intensity ratio was calculated and a calibration plot vs. pH was constructed (**Figure 3.17c**).

3.3.8. Autophagy Monitoring through pH Sensing

Tracking lysosomal pH changes has recently evolved as a key aspect of autophagy monitoring in cancer cells.⁴⁷ **PM-C₆-OH** exhibited ratiometric changes in fluorescence with variations in pH and localized predominantly in lysosome without perturbing its pH dynamics. Hence, we decided to investigate the possibilities of using **PM-C₆-OH** for monitoring the changes in lysosomal pH under induced autophagy conditions.

Autophagy was induced in HeLa cells stained with **PM-C₆-OH**, using Rapamycin, a well-known autophagy inducer.^{48,49} Images were taken in both green and red channels at 0 h and 8 h (**Figure 3.18a**). No significant increment in fluorescence intensity was observed in the green channel. However, a noticeable reduction in fluorescence intensity occurred in the red channel. Ratio of green/red intensity also showed an enhancement, indicating lysosomal acidification caused by autophagy (**Figure 3.18b**).

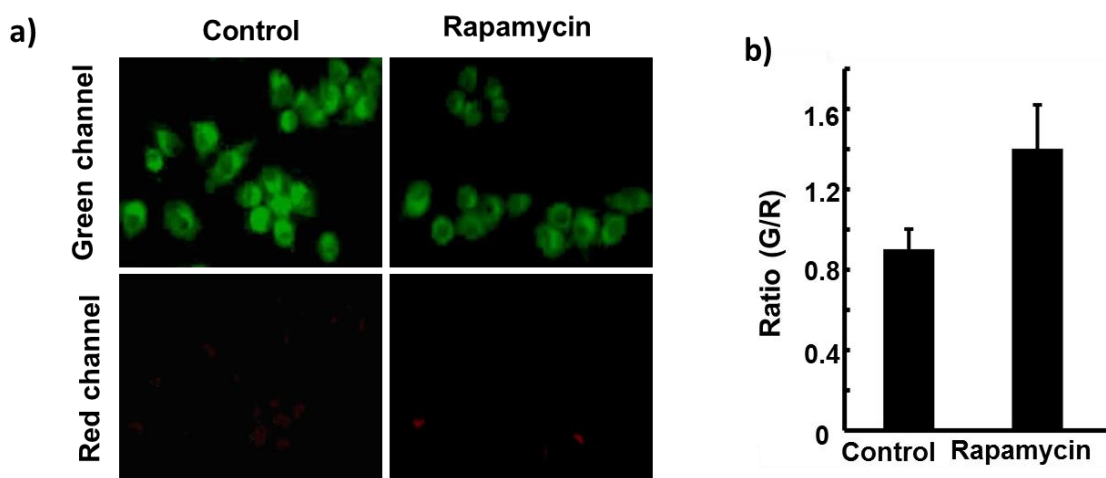


Figure 3.18. (a) Images of **PM-C₆-OH** incubated HeLa cells, with and without Rapamycin treatment. Images of control and autophagic cells were taken in the green and red channels. (b) Fluorescence intensity ratios from green/red channels for control and rapamycin treated cells.

Autophagy was then induced in HeLa cells by starvation.^{50,51} HeLa cells, stained with **PM-C₆-OH**, were kept in a nutrition-free media for 18 h and images were taken at 0, 6 and 18 h, in the green and red channels (**Figure 3.19a**). From the cellular images and green/red intensity ratio, slight acidification of lysosome with the progression of autophagy (till 6 h) was observed. After 18 h incubation, a significant increase in intensity ratio indicated a major drop in lysosomal pH due to induced autophagy (**Figure 3.19b**). These results unambiguously corroborate the potential of **PM-C₆-OH** as a pH-based lysosomal autophagy monitoring agent.

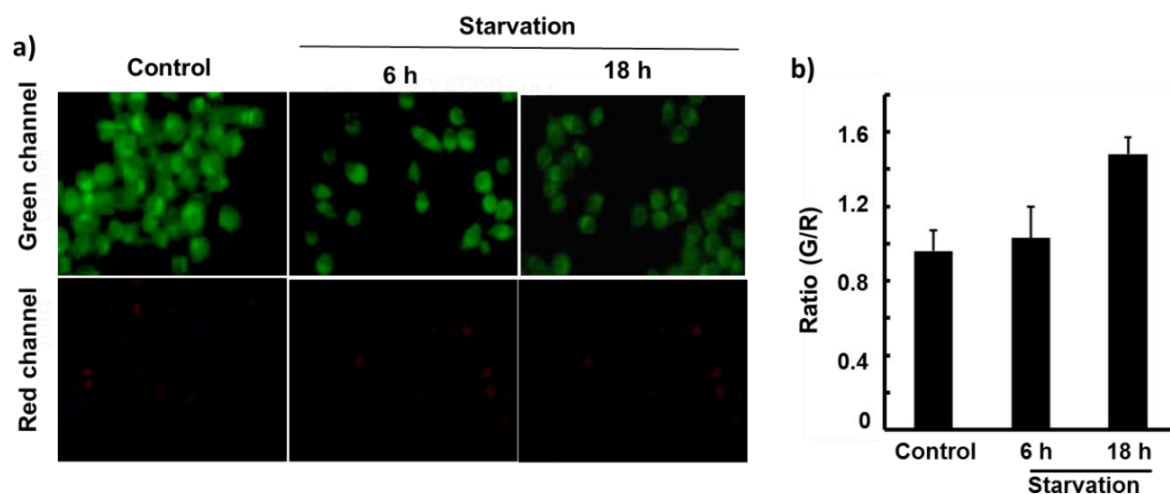


Figure 3.19. (a) Starvation-induced autophagy monitoring of HeLa cells, stained with **PM-C₆-OH**. HeLa cells were kept in nutrition-free medium for 18 h and images were taken at 0, 6, and 18 h in green and red channels. (b) Fluorescence intensity ratio (green/red) for autophagic cells at 0, 6 and 18 h.

3.4. Conclusion

In conclusion, the photophysical characteristics and imaging aspects of our previously developed pyrylium fluorophore were ameliorated by converting it into the pyridinium probes, with better solubility, high extinction coefficient, superior

quantum yield, large Stokes shift, and negligible effect of solvent polarity. **PM-C₆** and **PM-C₆-OH** did not penetrate the nuclear membrane and showed an unusually high lysosomal accumulation without any cellular alkalizing effect due to conventional protonation mechanism. **PM-C₆-OH** exhibited a ratiometric fluorescence response to changes in pH and the large Stokes shift allows for application as single and multiple excitation ratiometric pH probe. **PM-C₆-OH** also features two distinct pK_a values, a characteristic prerequisite for a single core fluorophore to monitor a wide range of pH with high selectivity and sensitivity. This new probe could monitor lysosomal acidification during autophagy and has the potential to monitor autophagy in real-time, thereby leading to break-through achievements in cancer therapy.

3.5. Experimental Section: Synthesis

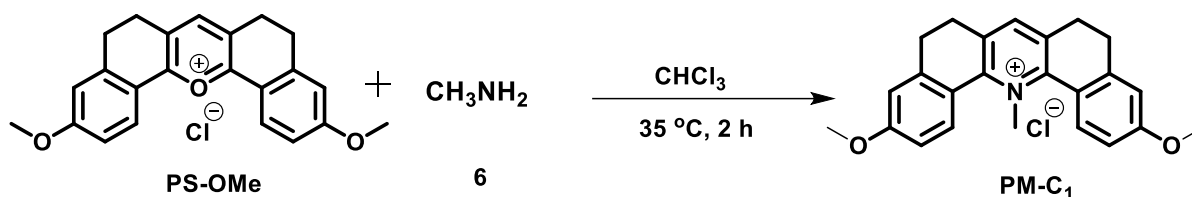
3.5.1. Materials and Methods

All reagents and dry solvents (reagent grade) were used without further purification. Reaction completion was monitored by silica gel G-60 F254 aluminum TLC and compounds were visualized by short/long-wavelength UV lamps. Column chromatography was done using silica gel 100-200 mesh as a stationary phase. ¹H and ¹³C NMR were recorded on a Bruker Advance II spectrometer at 500 and 125 MHz, respectively using deuterated solvents and reported as follows: chemical shift in ppm (δ), multiplicity (s = singlet, d = doublet, t = triplet, q = quartet) and coupling constant (J in Hz). HRMS data were obtained using Thermo Scientific Exactive

LCMS instrument by electrospray ionization method with ions given in m/z using Orbitrap analyzer.

3.5.2. Synthesis and Characterization

Synthesis of PM-C₁

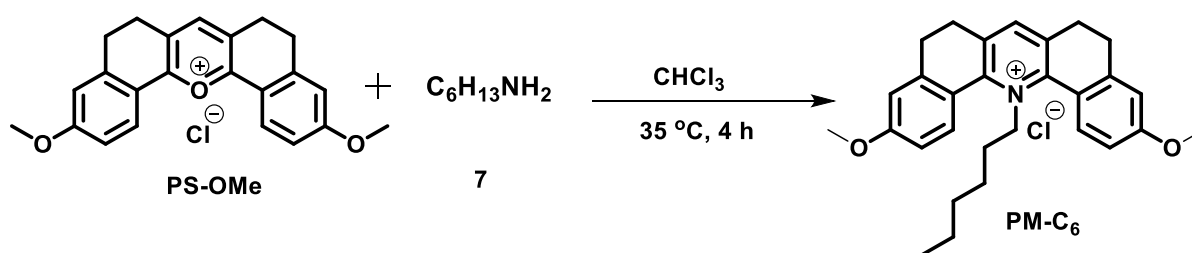


PS-OMe (0.5g, 1.4 mmol) was dissolved in CHCl₃ (200 mL) and stirred for 10 min at 35 °C. Methylamine was added to the above solution dropwise and the reaction mixture was stirred for 2 h at 35 °C. Excess methylamine was then removed by washing three times with water (100 mL). The organic extracts were combined, dried over anhydrous Na₂SO₄. The solvent was removed under reduced pressure and dried at 50 °C to yield **PM-C₁** as a yellow solid (0.36 g, 67 %).

¹H NMR (500 MHz, CDCl₃) δ : 8.22 (d, $J = 5$ Hz, 2H), 7.94 (s, 1H), 7.10 (d, $J = 5$ Hz, 3H), 6.90 (s, 2H), 4.48 (s, 3H), 3.92 (s, 6H), 2.93 (s, 8H).

¹³C NMR (125 MHz CDCl₃) δ : 161.5, 141.5, 139.7, 136.4, 134.1, 129.5, 120.8, 114.4, 113.0, 55.9, 30.3, 28.1

HRMS: Calcd. (C₂₃H₂₁O₃⁺) = 358.4605, Found = 358.4692.

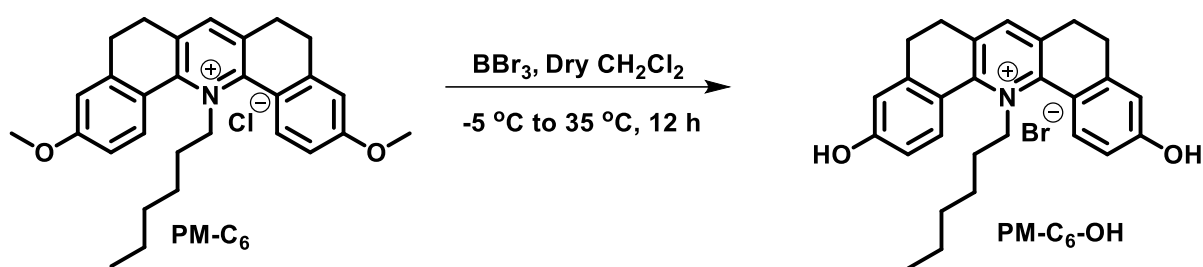
Synthesis of PM-C₆

PS-OMe (0.5 g, 1.26 mmol) was dissolved in CHCl₃ (200 mL) and hexylamine (0.37g, 3.6 mmol) was added dropwise to the stirred solution. The reaction mixture was then stirred at 35 °C for 6 h. Excess hexylamine was removed by washing three times with water (100 mL). The organic extracts were combined, dried over anhydrous Na₂SO₄ and the solvent was removed under reduced pressure. The residue was redissolved in CH₃OH (5 mL) and excess cold diethyl ether was added. The precipitate formed was collected by filtration and dried in an oven at 50 °C to afford **PM-C₆** as an yellow powder (0.41 g, 82%).

¹H NMR (500 MHz, CDCl₃) δ: 8.85 (s, 1H), 8.07 (d, *J* = 10 Hz, 2H), 7.04 (dd, *J*₁ = 5 Hz, *J*₂ = 5 Hz, 2H), 6.89 (d, *J* = 2 Hz, 2H), 5.22 (t, *J* = 5Hz, 2H), 3.95 (s, 6H), 3.29-3.26 (m, 4H), 3.14-3.10 (m, 4H), 1.28-1.26 (m, 2H), 0.98-0.95 (m, 2H), 0.85-0.83 (m, 2H), 0.70 (t, *J* = 10Hz, 3H), 0.67-0.63 (m, 2H).

¹³C NMR (125 MHz CDCl₃) δ: 162.7, 153.8, 144.9, 142.2, 136.8, 130.4, 120.4, 114.4, 113.9, 63.58, 55.6, 30.5, 28.9, 28.2, 27.4, 24.7, 21.8, 12.7

HRMS: Calcd. (C₂₃H₂₁O₃⁺) = 428.2584, Found = 428.2578.

Synthesis of PM-C₆-OH

PM-C₆ (0.1 g, 0.28 mmol) was dissolved in dry CH₂Cl₂ (10 mL) under argon atmosphere and cooled to – 5 °C using an ice-salt mixture. After 30 min, BBr₃ solution (~ 3 mL, 12 mmol) was added dropwise under continuous flow of argon. The reaction mixture was stirred for 1 h at -5 °C and then stirred at 35 °C for 12 h. Deionized water (5 mL) was added dropwise to neutralize excess BBr₃. The precipitate formed was collected by filtration and purified by column chromatography on silica gel (8% CH₃OH in CHCl₃ as eluent). **PM-C₆-OH** was obtained as a reddish-brown solid (0.041 g, 45%).

¹H NMR (500 MHz, CD₃OD) δ : 8.85 (s, 1H), 8.07 (d, $J = 10$ Hz, 2H), 7.04 (dd, $J_1 = 5$ Hz, $J_2 = 5$ Hz, 2H), 6.89 (d, $J = 2$ Hz, 2H), 5.22 (t, $J = 5$ Hz, 2H), 5.0 (s, br, 2H), 3.29-3.26 (m, 4H), 3.14-3.10 (m, 4H), 1.32-1.26 (m, 2H), 1.02-0.98 (m, 2H), 0.88-0.72 (m, 2H), 0.70 (t, $J = 10$ Hz, 3H), 0.66-0.63 (m, 2H).

¹³C NMR: (125 MHz, CD₃OD), δ : 161.6, 153.1, 144.1, 141.16, 136.2, 130.51, 119.9, 114.95, 114.7, 63.58, 30.3, 28.87, 28.10, 27.5, 24.6, 21.7, 12.7

HRMS: Calcd. (C₂₃H₂₁O₃⁺) = 400.2271, Found = 400.2222

3.6. Description of Experimental Techniques

3.6.1. UV/Vis Absorption and Emission Spectral Measurements

Electronic absorption spectra were recorded using a Shimadzu UV-2600 UV-Vis spectrophotometer, and emission studies were conducted using Horiba Fluorolog—3 Jovin Yoon. Stock solutions were prepared in spectroscopy grade DMSO and diluted with spectroscopy grade organic solvents and phosphate buffer as required. The pH solutions were made using phosphate buffer and pH was adjusted using dilute HCl/NaOH solutions.

3.6.2. Fluorescence Quantum Yield Measurements

Fluorescence quantum yields of the molecules were determined using Coumarin 153 as the reference according to the literature method.

Quantum yields were determined using the following equation:

$$\Phi_s = \Phi_f \times (A_r/A_f) \times (F_s/F_r)$$

where the 's' and 'r' represent the synthesized and reference samples, respectively. 'A', 'F' and ' Φ_f ' are the absorbance (≤ 0.07) at λ_{ex} , refractive index of the used spectroscopy grade solvent, and the integrated area under the corrected emission spectrum, respectively.

3.6.3. Cell Culture

Cervical cancer cell line, HeLa was obtained from American Type Culture Collection (ATCC, Manassas, VA). The human lung fibroblast cell line WI-38 was donated by Regional Cancer Centre (Thiruvananthapuram, India). Cells were maintained in Dulbecco's modified Eagle's medium (DMEM) with 10% Foetal Bovine Serum and 100 U penicillin and 0.1 mg/mL streptomycin antibiotics under an atmosphere of 5% CO₂ at 37 °C.

3.6.4. Determination of Cytotoxicity

The cell viability was evaluated on HeLa and WI-38 cell lines by colorimetric MTT (3-(4,5-dimethylthiazol-2-yl)-2,5-diphenyltetrazolium bromide) assay. Cell suspension of 5×10^3 cells/well (100 μ L) were seeded in a 96 well plate and cell lines were grown using DMEM culture media with 10% Foetal Bovine Serum (FBS), 2 mM glutamine and 100 U penicillin and 0.1 mg/mL streptomycin antibiotics. When the cells are approximately 70% confluent, 100 μ L of **PM-C₆-OH** at various concentrations (1 μ M to 100 μ M) and doxorubicin (Dox, 1 μ M) as a positive control were added. The plates were then incubated for 12 h in a 5% CO₂ incubator. After incubation, 20 μ L MTT (5 mg/mL) was added to each well and incubation was continued for an additional 2 h. The insoluble formazan solid were solubilised by the addition of 100 μ L MTT lysis buffer (SDS and Dimethyl formamide) followed by an incubation of 4 h and the absorbance was measured at 570 nm using a

microplate spectrophotometer (BioTek, Power Wave XS). The % proliferation was calculated using the following equation:

$$\text{Proliferation [\%]} = A_{\text{sample}} / A_{\text{control}} \times 100$$

3.6.5. Intracellular Photostability

HeLa cells (5×10^3 cells/well) were seeded in a 96 well plate in DMEM media. The media was replaced with 10 μM **PM-C₆-OH** after 24 h of adherence and allowed to incubate for 30 min in PBS at 37 °C. Similarly, another set of cells were prepared by the incubation of 1 μM LysoTracker red solution for 30 mins. Then, the cells were washed with PBS (3 \times), and imaged under fluorescence microscope with a continuous light irradiation for 180 s. At 0, 60, 120 and 180 s, images were captured in both green and red channels. Image analysis was performed using ImageJ.

3.6.6. Colocalization Experiments

In 96 well plates, three sets of HeLa cells (5×10^3 cells/well) were seeded. Each set of cells were separately incubated with Hoechst 33342 (5 μM), LysoTracker red (1 μM) and Mitotracker red (1 μM), respectively for 20 min. Then the cells of all three sets were washed with PBS (3 \times), and replaced with fresh PBS containing 10 μM of **PM-C₆**. After another 30 minutes, the cells were washed with PBS (3 \times) to wash out excess dye and imaged under fluorescence microscope in blue, green and red channels, as per the emission of the dyes. Image processing was performed using Progress software, Image analysis was performed with ImageJ and matlab software.

Similar process was repeated with **PM-C₆-OH**, in place of **PM-C₆** to determine its colocalization in HeLa cells.

3.6.7. Intracellular pH-Dependent Studies

HeLa cells were incubated at 37 °C for 30 min in high K⁺ buffer (30 mM NaCl, 120 mM KCl, 1 mM CaCl₂, 0.5 mM MgSO₄, 1 mM Na₂HPO₄, 5 mM glucose, 20 mM sodium acetate and 20 mM MES) of various pH (pH 4- 10). Next 25 μL (10 μM), a H⁺/K⁺ antiporter nigericin was added and incubated for 15 min to equilibrate the intracellular pH with the external buffer. The cells were then incubated with 3 μL of the probe **PM-C₆-OH** (10 μM) for 10 min, washed and observed under an inverted fluorescence microscope in the green and red channels. Image processing was performed using Progress software, Image analysis was performed using ImageJ and matlab software.

3.6.8. Autophagy-Induced pH Change Monitoring

HeLa cells were seeded in 4 well plates and incubated at 37 °C for 24 h. Then they were divided into two sets. In first set, one well was treated with **PM-C₆-OH** (10 μM) only, and other well was treated with Rapamycin (5 μM) along with 10 μM of **PM-C₆-OH**. After 1 h, both the wells were washed three times with PBS buffer to remove excess dye and imaged under inverted fluorescence microscope using the green and red channels.

For the other set of cells, both the wells were incubated with **PM-C₆-OH** (10 μM) for 30 min. Then cells from one well were washed with PBS buffer and then kept in

fresh PBS for 18 h to induce autophagy through nutrient deprivation. Images were taken from both wells at 0, 6 and 18 h in both green and red channels.

3.6. References

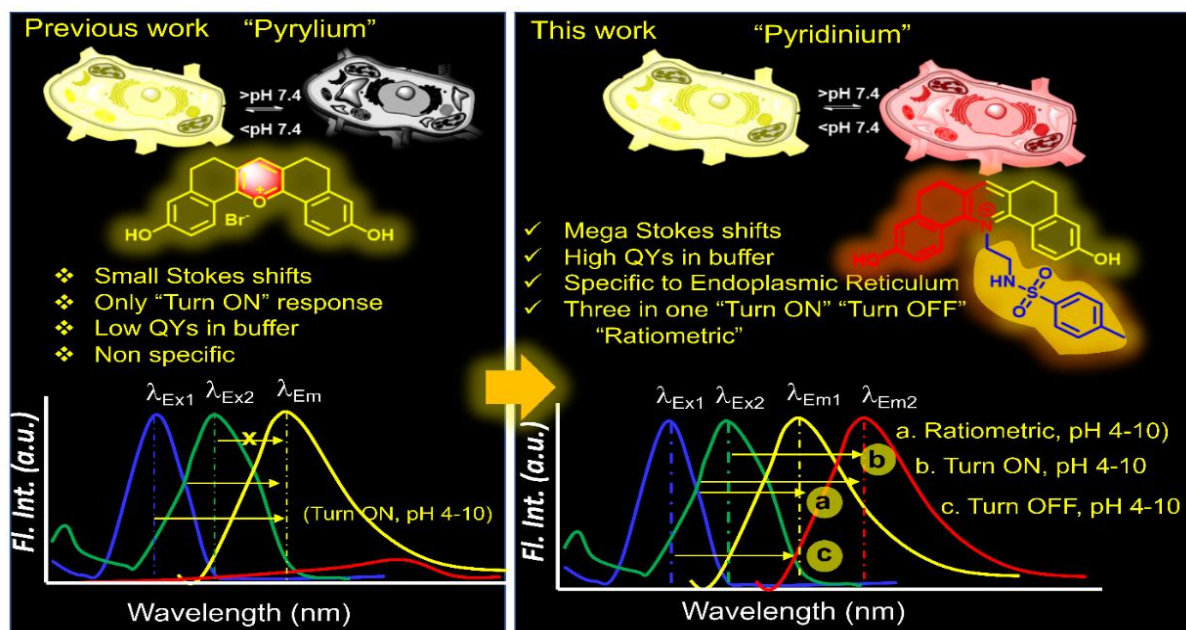
- [1] G. Saranya, M. M. Joseph, V. Karunakaran, J. B. Nair, V. N. Saritha, V. S. Veena, K. Sujathan, A. Ajayaghosh and K. K. Maiti, *ACS Appl. Mater. Interfaces*, 2018, **10**, 38807–38818.
- [2] S. Chakraborty, B. K. Agrawalla, A. Stumper, N. M. Vegi, S. Fischer, C. Reichardt, M. Kögler, B. Dietzek, M. Feuring-Buske, C. Buske, S. Rau and T. Weil, *J. Am. Chem. Soc.*, 2017, **139**, 2512–2519.
- [3] X. Li, S. Lee and J. Yoon, *Chem. Soc. Rev.*, 2018, **47**, 1174–1188.
- [4] J. Li and K. Pu, *Chem. Soc. Rev.*, 2019, **48**, 38–71.
- [5] H. Pei, X. Zuo, D. Zhu, Q. Huang and C. Fan, *Acc. Chem. Res.*, 2014, **47**, 550–559.
- [6] G. Cheng, Q. Zhang, J. Pan, Y. Lee, O. Ouari, M. Hardy, M. Zielonka, C. R. Myers, J. Zielonka, K. Weh, A. C. Chang, G. Chen, L. Kresty, B. Kalyanaraman and M. You, *Nat. Commun.*, 2019, **10**, 2205.
- [7] K. V. Sudheesh, P. S. Jayaram, A. Samanta, K. S. Bejoymohandas, R. S. Jayasree and A. Ajayaghosh, *Chem. Eur. J.*, 2018, **24**, 10999–11007.
- [8] N. Busschaert, S.-H. Park, K.-H. Baek, Y. P. Choi, J. Park, E. N. W. Howe, J. R. Hiscock, L. E. Karagiannidis, I. Marques, V. Félix, W. Namkung, J. L. Sessler, P. A. Gale and I. Shin, *Nat. Chem.*, 2017, **9**, 667–675.
- [9] K. Peynshaert, B. B. Manshian, F. Joris, K. Braeckmans, S. C. De Smedt, J. Demeester and S. J. Soenen, *Chem. Rev.*, 2014, **114**, 7581–7609.
- [10] J. S. Carew, K. R. Kelly and S. T. Nawrocki, *Cancer Manag. Res.*, 2012, **4**, 357–365.
- [11] K. D. Tompkins and A. Thorburn, *Yale J. Biol. Med.*, 2019, **92**, 707–718.
- [12] K.H. Baek, J. Park and I. Shin, *Chem. Soc. Rev.*, 2012, **41**, 3245–3263.
- [13] W. W.Y. Yim and N. Mizushima, *Cell Discov.*, 2020, **6**, 6.

- [14] J. M. M. Levy, C. G. Towers and A. Thorburn, *Nat. Rev. Cancer*, 2017, **17**, 528–542.
- [15] N. Mizushima, B. Levine, A. M. Cuervo and D. J. Klionsky, *Nature*, 2008, **451**, 1069–1075.
- [16] L. Poillet-Perez, X. Xie, L. Zhan, Y. Yang, D. W. Sharp, Z. S. Hu, X. Su, A. Maganti, C. Jiang, W. Lu, H. Zheng, M. W. Bosenberg, J. M. Mehnert, J. Y. Guo, E. Lattime, J. D. Rabinowitz and E. White, *Nature*, 2018, **563**, 569–573.
- [17] I. Dikic and Z. Elazar, *Nat. Rev. Mol. Cell Biol.*, 2018, **19**, 349–364.
- [18] S. Takahiro and K. D. J., *Science*, 2004, **306**, 990–995.
- [19] X. Li, X. Liang, J. Yin and W. Lin, *Chem. Soc. Rev.*, 2021, **50**, 102–119.
- [20] Y. Liu, L. Teng, L. Chen, H. Ma, H.-W. Liu and X.-B. Zhang, *Chem. Sci.*, 2018, **9**, 5347–5353.
- [21] H. Iwashita, S. Torii, N. Nagahora, M. Ishiyama, K. Shioji, K. Sasamoto, S. Shimizu and K. Okuma, *ACS Chem. Biol.*, 2017, **12**, 2546–2551.
- [22] F. Meng, J. Niu, H. Zhang, R. Yang, Q. Lu, G. Niu, Z. Liu and X. Yu, *Anal. Chem.*, 2021, **93**, 11729–11735.
- [23] S. Ding and Y. Hong, *Chem. Soc. Rev.*, 2020, **49**, 8354–8389.
- [24] W. Chen, J. Han, J. She, F. Wang, L. Zhu, R.-Q. Yu and J.-H. Jiang, *Chem. Commun.*, 2020, **56**, 7797–7800.
- [25] M. H. Lee, N. Park, C. Yi, J. H. Han, J. H. Hong, K. P. Kim, D. H. Kang, J. L. Sessler, C. Kang and J. S. Kim, *J. Am. Chem. Soc.*, 2014, **136**, 14136–14142.
- [26] L. Hou, P. Ning, Y. Feng, Y. Ding, L. Bai, L. Li, H. Yu and X. Meng, *Anal. Chem.*, 2018, **90**, 7122–7126.
- [27] M. Tian, C. Liu, B. Dong, Y. Zuo and W. Lin, *Chem. Commun.*, 2019, **55**, 10440–10443.
- [28] F. Xu, H. Li, Q. Yao, J. Fan, J. Wang and X. Peng, *J. Mater. Chem. B*, 2016, **4**, 7363–7367.
- [29] X. Wang, L. Fan, Y. Wang, C. Zhang, W. Liang, S. Shuang and C. Dong, *J. Mater. Chem. B*, 2020, **8**, 1466–1471.

- [30] Y. Yue, F. Huo, S. Lee, C. Yin and J. Yoon, *Analyst*, 2017, **142**, 30–41.
- [31] J.-T. Hou, W. X. Ren, K. Li, J. Seo, A. Sharma, X.-Q. Yu and J. S. Kim, *Chem. Soc. Rev.*, 2017, **46**, 2076–2090.
- [32] M. Yang, J. Fan, J. Du and X. Peng, *Chem. Sci.*, 2020, **11**, 5127–5141.
- [33] W. Xu, Z. Zeng, J.-H. Jiang, Y.-T. Chang and L. Yuan, *Angew. Chem., Int. Ed.*, 2016, **55**, 13658–13699.
- [34] W. Zhang, F. Huo, Y. Yue, Y. Zhang, J. Chao, F. Cheng and C. Yin, *J. Am. Chem. Soc.*, 2020, **142**, 3262–3268.
- [35] J. Zhang, Y. Jia, X. Xing, M. Qin, Z. Wu, Y. Zhong, L. Liu, S. Sun, P. Li, H. Wang and G. Zhao, *SmartMat*, , DOI:<https://doi.org/10.1002/smm2.1054>.
- [36] C. S. Abeywickrama, K. A. Bertman, C. B. Plescia, R. V Stahelin and Y. Pang, *ACS Appl. Bio Mater.*, 2019, **2**, 5174–5181.
- [37] Q. Xia, S. Feng, J. Hong and G. Feng, *Talanta*, 2021, **228**, 122184.
- [38] S. Chakraborty, M. M. Joseph, S. Varughese, S. Ghosh, K. K. Maiti, A. Samanta and A. Ajayaghosh, *Chem. Sci.*, 2020, **11**, 12695–12700.
- [39] Y. He, S. Wang, P. Yu, K. Yan, J. Ming, C. Yao, Z. He, A. M. El-Toni, A. Khan, X. Zhu, C. Sun, Z. Lei and F. Zhang, *Chem. Sci.*, , DOI:10.1039/D1SC02763H.
- [40] A. R. Katritzky, A. Chermprapai, S. Bravo and R. C. Patel, *Tetrahedron*, 1981, **37**, 3603–3607.
- [41] A. R. Katritzky, F. Al-Omran, R. C. Patel and S. S. Thind, *J. Chem. Soc. Perkin Trans. 1*, 1980, 1890–1894.
- [42] J. Valanciunaite, E. Kempf, H. Seki, D. I. Danylchuk, N. Peyri ras, Y. Niko and A. S. Klymchenko, *Anal. Chem.*, 2020, **92**, 6512–6520.
- [43] A. H. Ashoka, P. Ashokkumar, Y. P. Kovtun and A. S. Klymchenko, *J. Phys. Chem. Lett.*, 2019, **10**, 2414–2421.
- [44] P. Anees, K. V Sudheesh, P. Jayamurthy, A. R. Chandrika, R. V Omkumar and A. Ajayaghosh, *Chem. Sci.*, 2016, **7**, 6808–6814.
- [45] X. Liu, Y. Su, H. Tian, L. Yang, H. Zhang, X. Song and J. W. Foley, *Anal. Chem.*, 2017, **89**, 7038–7045.

-
- [46] M. H. Lee, J. H. Han, J. H. Lee, N. Park, R. Kumar, C. Kang and J. S. Kim, *Angew. Chem. Int. Ed.*, 2013, **52**, 6206–6209.
- [47] H. Xu, Y. Bu, J. Wang, M. Qu, J. Zhang, X. Zhu, G. Liu, Z. Wu, G. Chen and H. Zhou, *Sensors Actuators B Chem.*, 2021, **330**, 129363.
- [48] A. Sotthibundhu, K. McDonagh, A. von Kriegsheim, A. Garcia-Munoz, A. Klawiter, K. Thompson, K. D. Chauhan, J. Krawczyk, V. McInerney, P. Dockery, M. J. Devine, T. Kunath, F. Barry, T. O'Brien and S. Shen, *Stem Cell Res. Ther.*, 2016, **7**, 166.
- [49] Y. Su, J. Lu, P. Gong, X. Chen, C. Liang and J. Zhang, *Mol. Med. Rep.*, 2018, **18**, 5445–5454.
- [50] H. Tong, H. Yin, M. A. Hossain, Y. Wang, F. Wu, X. Dong, S. Gao, K. Zhan and W. He, *J. Cell. Biochem.*, 2019, **120**, 5118–5127.
- [51] L. Li, Y. Chen and S. B. Gibson, *Cell. Signal.*, 2013, **25**, 50–65.

A Pyridinium Fluorophore for pH-assisted ‘Three-in-one’ Imaging of Heat Shock in Endoplasmic Reticulum



4.1. Abstract

Heat Shock has recently emerged as a global health concern as it causes permanent damage to living cells and has a relatively high mortality rate. Therefore, diagnostic tools that facilitate a better understanding of heat shock damage and defense mechanisms at the sub-cellular level are of fundamental interest. In this work, a fluorescent probe **PM-ER-OH** was synthesized, and used to monitor pH changes in Endoplasmic Reticulum during heat shock. The probe exhibited bright yellow fluorescence ($\lambda_{max} = 556 \text{ nm}$) at acidic pH and red fluorescence ($\lambda_{max} = 660 \text{ nm}$) at basic

*pH. By changing the excitation wavelength, we were able to modulate the fluorescence signal in a 'Turn-ON', 'Turn-OFF' and ratiometric modes, making the fluorophore a 'three-in-one' probe. **PM-ER-OH** showed good biocompatibility, good colocalization in Endoplasmic Reticulum and excellent intracellular pH response. The probe was further used to monitor pH changes induced by the application of heat shock, either directly or in a pre-heated manner. The data also provide valuable insights on cellular acidification caused by heat stress. We believe that this study will motivate the development of new probes for heat shock monitoring and multi-channel imaging for clinical diagnosis.*

4.2. Introduction

Due to global warming and the occurrence of heat waves at different parts of the tropical countries, heat shock is expected to emerge as one of the major reasons for global mortality in the near future.¹ A 1.4 - 5.8 °C rise in global temperature is expected to severely impact human health by the end of this century.^{2,3} Though a long-known health concern, the mechanistic understanding behind pathological changes during heat shock is rather poor.⁴ However, elucidating the damage mechanisms of heat shock at sub-cellular level may offer better treatment efficacy.⁵ The rise in body temperature above 40.6 °C can spontaneously cause serious injuries to tissues and damage to the nervous system, leading to multiple organ failure and death.⁶⁻⁸ Depending on its cause, heat shock may be categorized as either classic or exertional.^{9,10} Though both classic and

exertional heat-shock are caused by the failure to dissipate excess body heat, their underlying mechanisms may differ.¹¹ Classical heat shock is due to exposure to environmental heat and poor heat dissipation mechanisms, whereas exertional heat shock is associated with physical exercise during which excessive metabolic heat production overwhelms physiological heat loss mechanisms.^{12,13} Akin to other physiological abnormalities, heat shock is monitored using different methods such as flow cytometry, TEM analysis, protein isolation and fluorescence imaging.^{14–19}

Fluorescence is a strong and sensitive tool for probing sub-cellular activities in real-time.^{20–26} Ma *et al.* have reported the first probe for imaging lysosomal pH change during heat shock, using an NIR probe **1**, having a stable hemicyanine skeleton, a morpholine unit, and a hydroxyl group (**Figure 4.1a**).²⁷ Probe **1** exhibited a ratiometric signal with an initial emission, centered at 670 nm at pH 4, and the concomitant appearance of a new peak at 708 nm at pH 7.4 (**Figure 4.1b**). A sharp change in fluorescence intensity was observed in the pH range of 3.8 – 5.0, as required for monitoring lysosomal pH variations. Temperature up to 45 °C did not impact the fluorescence intensity of probe **1**. Excellent lysosome localization (Pearson's Coefficient = 0.91) allowed accurate monitoring of the variation in lysosomal pH during heat shock. The probe's fluorescence response was quantified at different intracellular pH, which was achieved by using Nigericin, to obtain a pH calibration curve. Fluorescence images of HeLa and MCF-7 cells were collected at the physiological temperature, and at 41 °C and 45 °C. From the calibration curve, the lysosomal pH at

37 °C was found to be 4.58 ± 0.09 and 4.55 ± 0.08 for HeLa and MCF-7 cells, respectively (**Figure 4.1c-d**). At 41 °C, the pH was found to increase to 4.80 ± 0.06 and 4.81 ± 0.07 , respectively. At 45 °C, the pH was found to be even higher: 4.89 ± 0.07 for HeLa and 4.91 ± 0.08 for MCF-7 cells. Cooling the cells back to 37 °C did not restore the normal lysosomal pH, indicating the non-reversible damage during heat shock. The rise in pH during heat shock is most likely due to an increase in lysosomal membrane's permeability, that neutralizes lysosomal acidic pH to some extent with the cytosol.

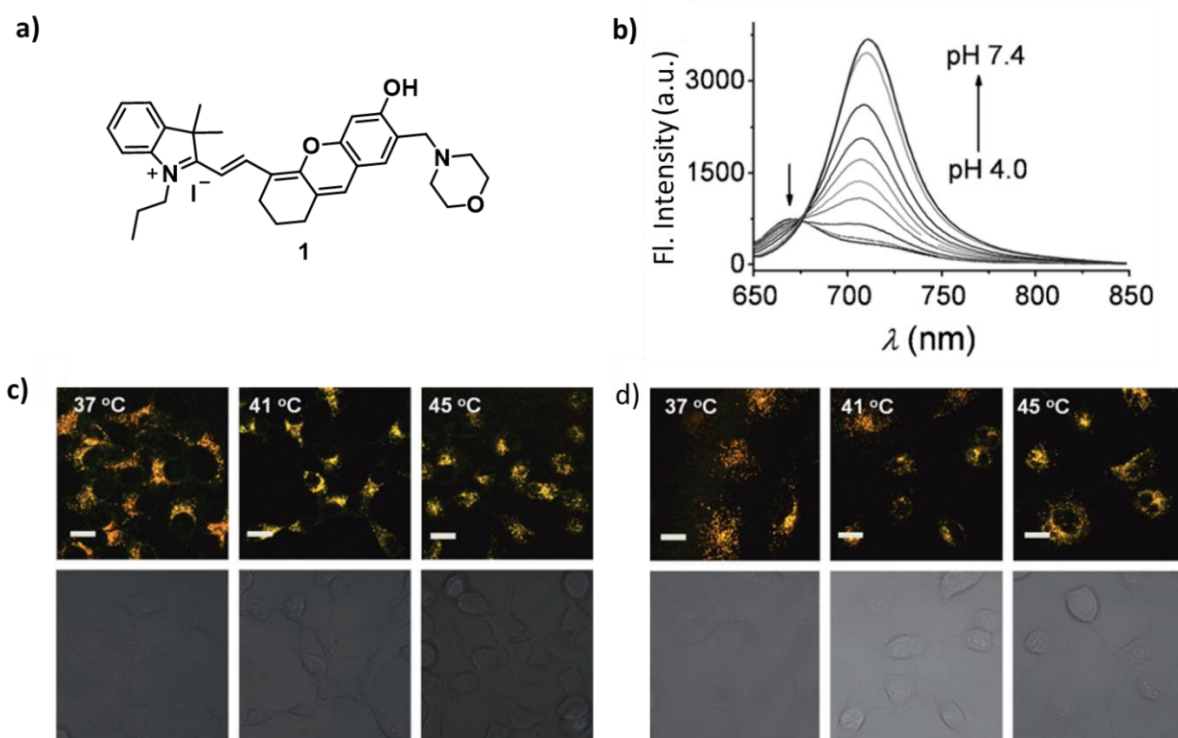


Figure 4.1. (a) Chemical structure of the hemicyanine probe **1**. (b) Emission spectra of **1** at various pH. Ratiometric fluorescence images of probe **1** stained (c) HeLa cells and (d) MCF-7 cells under heat shock. (Adapted with permission from ref 27)

Yin and coworkers have reported a naphthalimide-based fluorescent probe **2** for point of care imaging of lysosomal pH changes during heat shock.²⁸ The 1,8-Naphthalimide-

based fluorophore **2** with a morpholine unit for lysosome localization exhibited an emission maximum at 550 nm, and the intensity increased by 89-fold in the pH range of 3 – 8, with a pKa of 5.67. A steady fluorescence response was observed at pH 4, 6 and 8, when the temperature was increased from physiological temperature to 41 °C and 45 °C. (**Figure 4.2a-b**). Also, it showed excellent lysosomal localization (Pearson's Coefficient = 0.90).

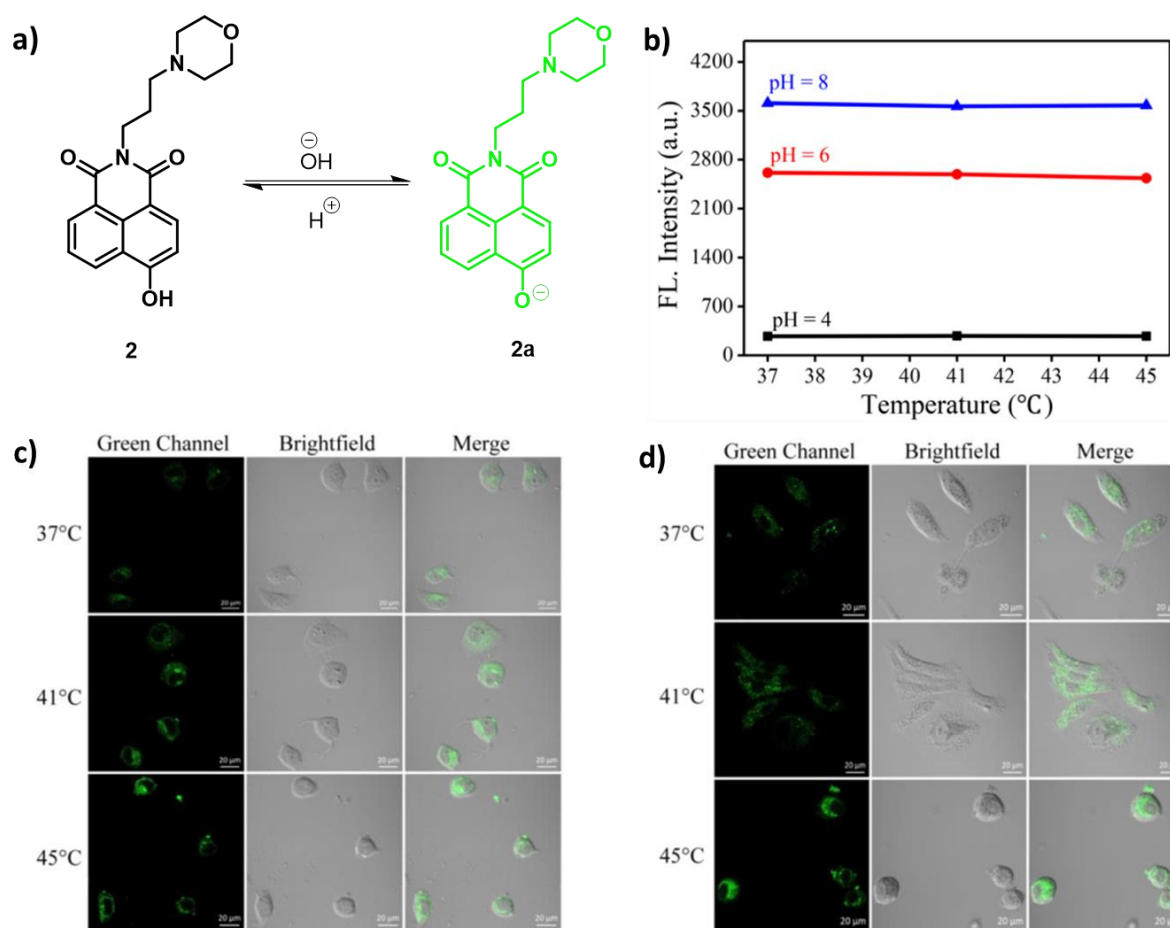


Figure 4.2. (a) Structure of the naphthalimide-based probe **2** in its protonated and deprotonated states. (b) Fluorescence intensity of **2** at different pH and temperature. Confocal microscopy images of probe **2** incubated (c) HeLa and (d) A549 cells, heated at different temperatures. (Adapted with permission from ref 28)

The fluorescence intensity of A549 cells incubated with probe **2** was found to increase with increase in pH. The effect of heat shock on lysosomal pH was investigated using HeLa and A549 cells, incubated with the probe **2** and heated to 41 and 45 °C before recording the images. Quantification of fluorescence intensity using image analysis confirmed an increase in fluorescence intensity with temperature, indicating an increase in lysosomal pH after heat shock (**Figure 4.2c-d**).

In an attempt to understand the defense mechanism of cells to prevent damages caused by heat, Chan and co-workers synthesized a cyanine-based NIR ratiometric probe **3** and monitored cellular glutathione (GSH) level under heat stress.²⁹ GSH is known to play an important role in anti-apoptotic process, both *in-vitro* and *in-vivo* (**Figure 4.3**).^{30–32}

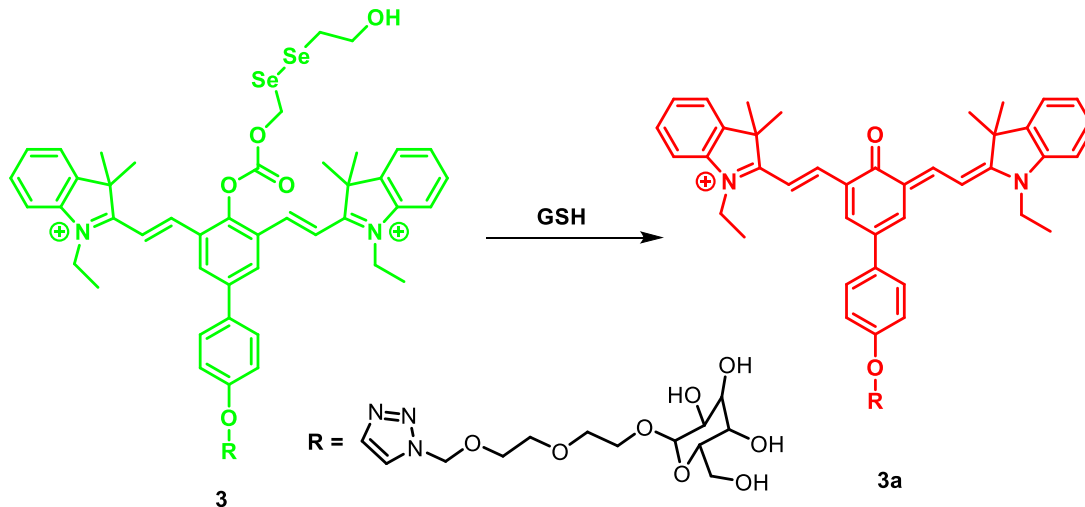


Figure 4.3. (a) Chemical structure of the probe **3** and its interaction with GSH.

The probe **3** showed an initial emission maximum at 785 nm, that hypsochromically shifted to 615 nm upon reaction with GSH. Application of heat shock on HepG2 and HL-7702 cells incubated with probe **3** resulted in an increase in the GSH level as a part

of the cells' inherent mechanism to minimize temperature induced damages. However, when the cells were subjected to heat stress for more than two hours, the GSH level started decreasing, indicating the short-term mechanism of action. A few commercial probes were also used to determine the effect of heat stress on the concentration of Ca^{2+} and mitochondrial membrane potential (MMP). Ca^{2+} level in cells sharply increased with rise in cellular temperature leading to a concomitant decrease in MMP. It was further observed that cancer cells were more susceptible to heat stress as compared to normal cells.

Huang *et al.* have reported a fluorescent probe **4** for monitoring lysosomal pH during heat shock.³³ A previously reported hemicyanine-based pH probe was modified by appending with a morpholine unit to construct the molecule **4**, that exhibited emission maxima at 522 nm and 557 nm, at acidic and basic pH, respectively (**Figure 4.4a**). From the intensity ratio (F_{522}/F_{557}), the pKa was calculated to be 5.96 ($F_{522}/F_{557} = 1.2$ at pH 11 and 0.18 at pH 3).

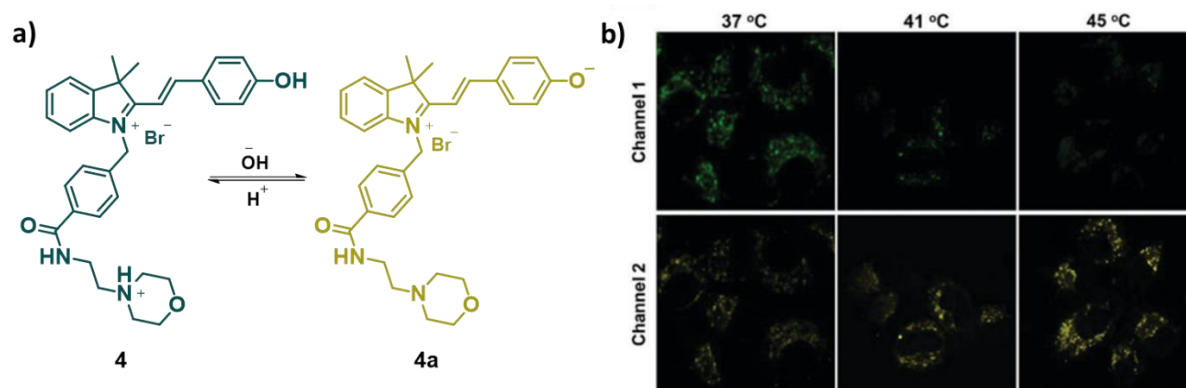


Figure 4.4. (a) Chemical structure of the probe **4** at acidic and basic pH. (b) Fluorescence images of HeLa cells, stained with probe **4** at 37, 41 and 45 °C. (Adapted with permission from ref 33)

The probe **4** showed excellent lysosomal localization as expected, with a Pearson's coefficient of 0.898. When cells were incubated with **4**, fluorescence was observed with a stronger response in green channel indicating the predominant existence of the protonated structure of the probe (**4a**) at lysosomal pH. Subjecting HeLa cells to heat shock resulted in a decrease in fluorescence intensity in the green channel, with a concomitant increase in intensity in the yellow channel (**Figure 4.4b**). Ratiometric image at each temperature (37, 41 and 45 °C) was then generated, that provided visibly evident information on pH distribution in lysosomes under heat shock, and confirmed an uneven distribution of pH in different lysosomes within a single cell.

Yin and coworkers have recently reported a light-controlled fluorescent probe **5** to study the role of SO₂ as an anti-oxidant in protecting lysosomes from heat shock.³⁴⁻³⁶ A morpholine attached 1,8-Naphthalimide-based chromophore was used for lysosome specific Turn-ON fluorescence, that was conjugated to a spiropyran moiety for light-activated FRET and SO₂ detection (**Figure 4.5a**). The naphthalimide part of probe **5** gave an emission maximum at 535 nm at lysosomal pH range (4.5 – 5.5). Irradiating with 365 nm light converted the spiropyran moiety to merocyanine, that absorbed the initial emission from naphthalimide, leading to a new emission maximum at 630 nm. Reaction of merocyanine with SO₂ quenched the emission at 630 nm and the donor emission was restored. The probe **5** was found to be predominantly localized in lysosome. Irradiating the cells, incubated with the probe **5** using UV and visible lights resulted in reversible switching of fluorescence in red and green channels (**Figure 4.5b**).

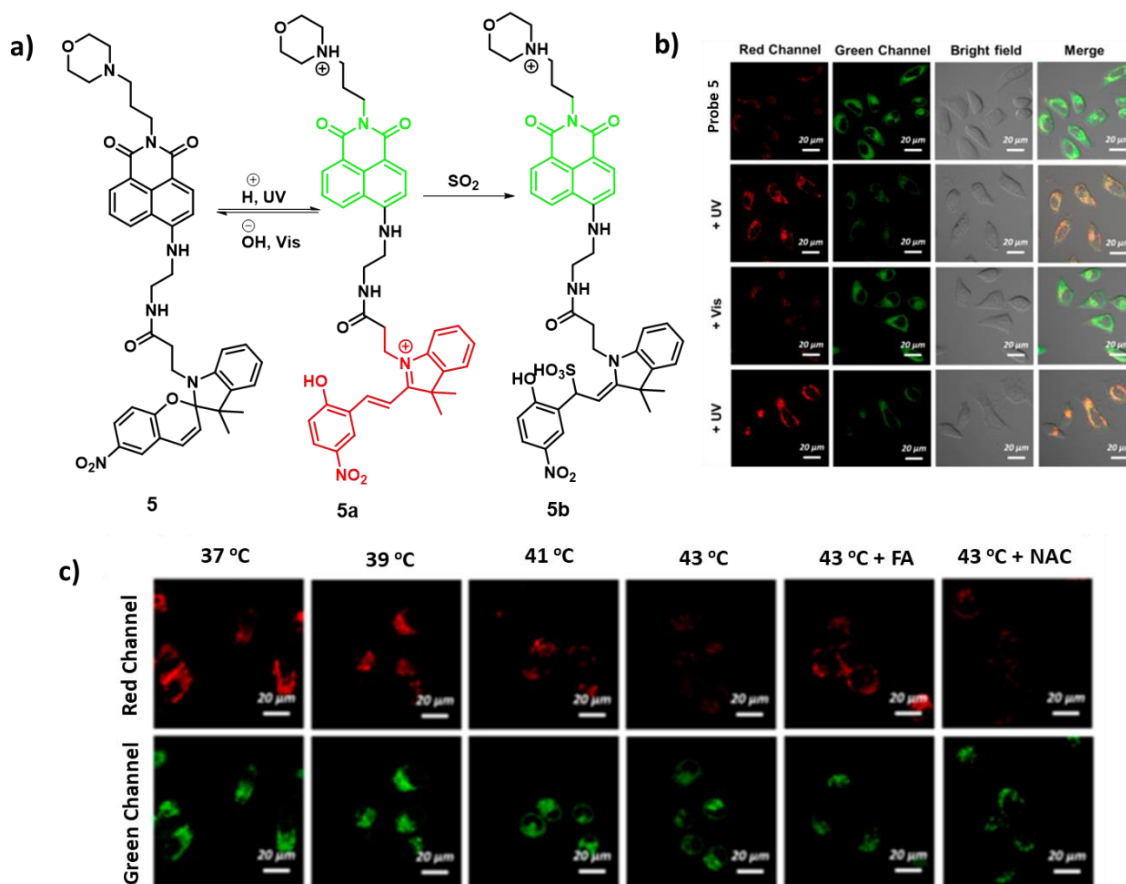


Figure 4.5. (a) Changes in the chemical structure of the probe **5** depending on applied stimuli. (b) Light triggered switching of fluorescence in HeLa cells, stained with **5**. (c) Decrease of emission intensity in the red channel with increase in temperature of HeLa cells, indicative of a higher level of SO_2 . (Adapted with permission from ref 34)

When HeLa cells were subjected to heat shock in the presence of **5**, the red fluorescence was found to gradually decrease with increased temperature. This is indicative of the increased concentration of SO_2 with increase in thermal stress of the cell as a defense mechanism from heat damage. This was further confirmed by the restoration of the red fluorescence when formaldehyde was used as SO_2 scavenger in heat treated cells (**Figure 4.5c**). Similar results were obtained when this probe was used to image the effect of heat shock on the intestinal tissues of mice. These observations corroborate

with the generation of ROS due to heat shock and SO_2 helps in protecting lysosomes and maintaining cellular homeostasis.

Ye and coworkers have developed an AIE probe **6** conjugating a TPE core to a benzopyrylium moiety to monitor changes in mitochondrial SO_2 level during heat shock (**Figure 4.6a**).³⁷ The emission at 455 nm was found to increase with addition of SO_2 . The probe showed an excellent mitochondrial localization (Pearson's coefficient = 0.91), most likely due to the positive charge on benzopyrylium moiety.

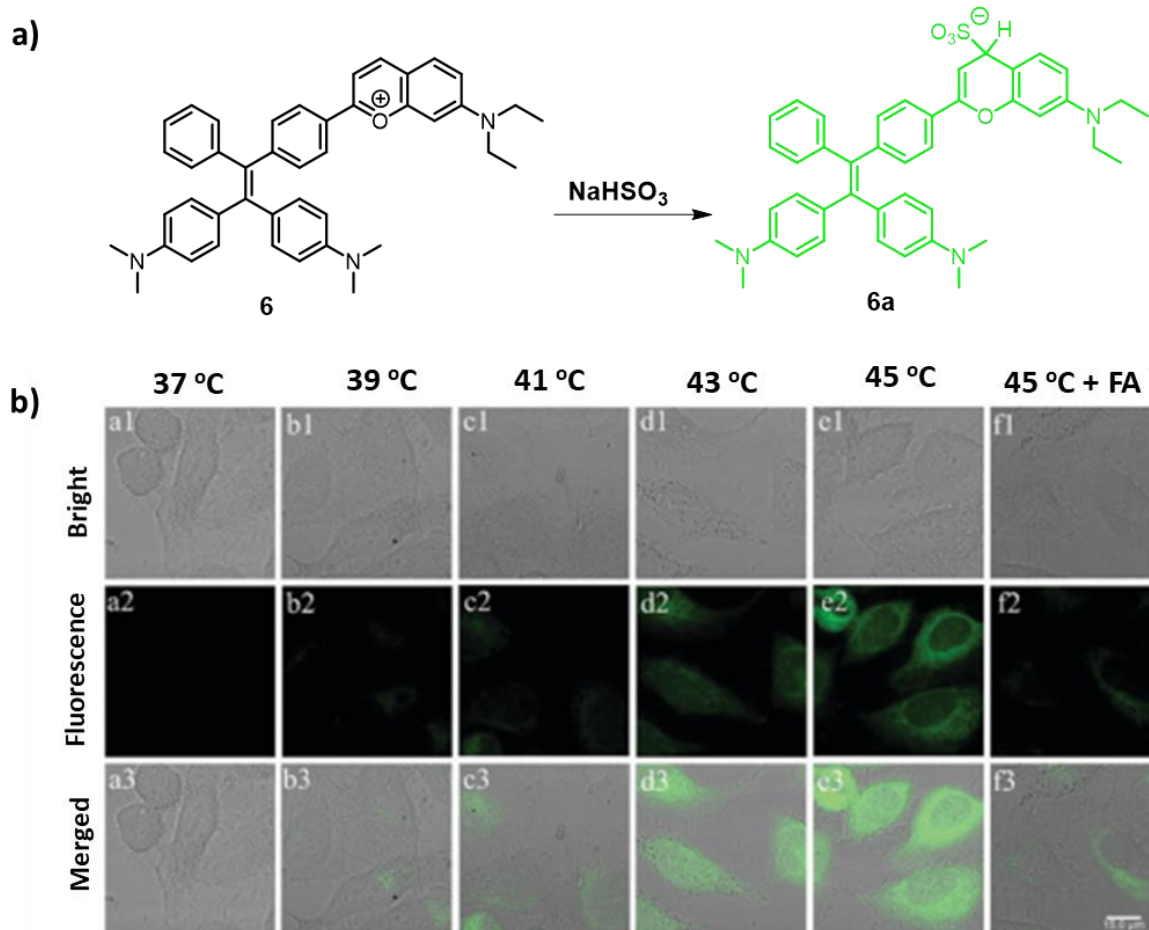


Figure 4.6. (a) Chemical structure of the probe **6** and its SO_2 detection mechanism. (b) Monitoring the rise of SO_2 level with increase in temperature via fluorescence imaging in the green channel using the probe incubated HeLa cells. (Adapted with permission from ref 27)

When the probe-loaded HeLa cells were subjected to heat shock, fluorescence intensity in the green channel increased with increase in temperature (**Figure 4.6b**), indicating a rise in mitochondrial SO₂ level along with a similar phenomenon in the lysosomes.

Though there are a few reports on heat shock monitoring using small-molecule fluorescent probes, majority of them are lysosome and mitochondria targeting.³⁸⁻⁴⁰ Prior literature suggests that ER is a more relevant organelle for better understanding of the subcellular changes during heat shock.⁴¹ Averill-Bates *et al.* have shown that when a cell comes under heat stress, the ER and the Golgi system get fragmented initially, followed by modest swelling of the mitochondria.⁴² This disturbs the usual process of DNA and RNA synthesis, protein folding and the membrane potential, leading to an increase in the intracellular levels of Na⁺, K⁺ and H⁺, with a simultaneous increase in membrane permeability, and a rise in lysosomal pH.⁴³⁻⁴⁵ Keeping HeLa cells at 40 °C, a temperature just below the heat shock temperature, activates several heat shock proteins (HSPs) in order to resist extensive cellular damage, and is known to be a natural mechanism in cells.

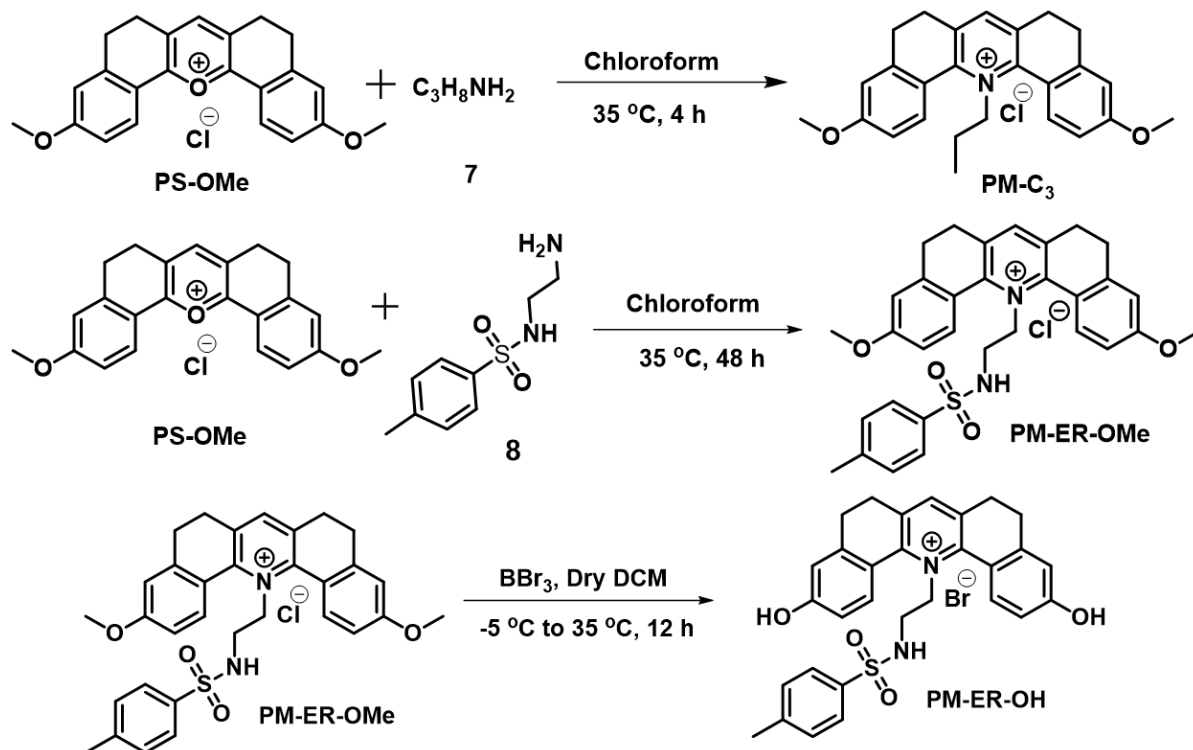
To this end, we have synthesized a pyridinium-based fluorescent probe **PM-ER-OH**, that can track the pH changes in ER during heat shock. Due to the inherently large Stokes shift, this probe behaved as a Turn-ON, Turn-OFF, and single excitation ratiometric probe for pH imaging in live cells, just by changing the excitation wavelengths. **PM-ER-OH** was further used to determine the difference in acidification for normally heated and pre-heated cells to better understand the function of HSPs. **PM-**

ER-OH, to the best of our knowledge, is the first fluorescent probe capable of determining variations in the concentration of any analyte in ER during heat shock.

4.3. Results and Discussion

4.3.1. Synthesis of the Pyridinium Derivatives

Our previous experience with pyrylium and pyridinium fluorophores helped us to design three new pyridinium fluorophores, **PM-C₃**, **PM-ER-OMe** and **PM-ER-OH**. The structural design of these molecules involved the introduction of an organelle targeting group for developing a ratiometric fluorophore having stable signals at high temperature in order to monitor intracellular pH variations during heat shock.



Scheme 4.1. Synthesis of **PM-C₃**, **PM-ER-OMe**, and **PM-ER-OH**.

The syntheses of the probes were achieved by converting the pyrylium fluorophore to the corresponding pyridinium moiety, using a reported procedure.^{46,47} The pyrylium dye **PS-OMe** was treated with propylamine and *N*-(2-aminoethyl)-4-methylbenzenesulfonamide to obtain the pyridinium derivatives of **PM-C₃** and **PM-ER-OMe**, respectively in moderate yields. **PM-ER-OH** was obtained via the demethylation of **PM-ER-OMe** using boron tribromide (**Scheme 4.1**). **PM-C₃** does not have a specific targeting group for ER, whereas **PM-ER-OMe** has an ER-targeting *p*-toluene sulfonamide group, but cannot respond to pH variations, and **PM-ER-OH** features the ER-targeting group, as well as hydroxy groups that ratiometrically respond to changes in pH. The probes were characterized by NMR spectroscopy and high-resolution mass spectrometry (HRMS).

4.3.2. Photophysical Studies

PM-C₃ and **PM-ER-OMe** were used as control molecules in this work. For photophysical studies, all three molecules were dissolved in spectroscopy grade DMSO to prepare a 10 mM stock solution and then diluted with PBS buffer (10 mM) as required. PBS buffers were adjusted to different pH using dil. HCl and dil. NaOH solution.

The absorption and emission spectra of all three compounds (10 μM) were recorded in chloroform (**Figure 4.7a-b**). **PM-C₃** showed absorption maximum at 430 nm, and the extinction coefficient (ϵ) was found to be $3.9 \times 10^4 \text{ M}^{-1}\text{cm}^{-1}$. For **PM-ER-OMe**, the

absorption maximum shifted to 436 nm and the extinction coefficient (ϵ) was $2.69 \times 10^4 \text{ M}^{-1}\text{cm}^{-1}$. Both the molecules featured their emission maxima at 566 nm. However, **PM-ER-OH** exhibited a bathochromic shift in absorbance and emission maxima, that appeared at 445 nm and 585 nm, respectively, indicating a better excited state stabilization. Though the emission maxima of all three molecules showed only a minor shift (6-11 nm) in comparison to the analogous pyrylium fluorophores (i.e., **PS-OMe** and **PS-OH**), they showed a major blue shift in absorbance maxima (45-75 nm) significantly increasing the Stokes shift. Also, **PM-C₃** and **PM-ER-OMe** showed an improved extinction coefficient than **PS-OMe** ($\epsilon = 2.01 \times 10^4 \text{ M}^{-1}\text{cm}^{-1}$), whereas **PM-ER-OH** showed a major enhancement in extinction coefficient ($\epsilon = 2.52 \times 10^4 \text{ M}^{-1}\text{cm}^{-1}$), compared to that of **PS-OH** ($\epsilon = 7.33 \times 10^3 \text{ M}^{-1}\text{cm}^{-1}$).

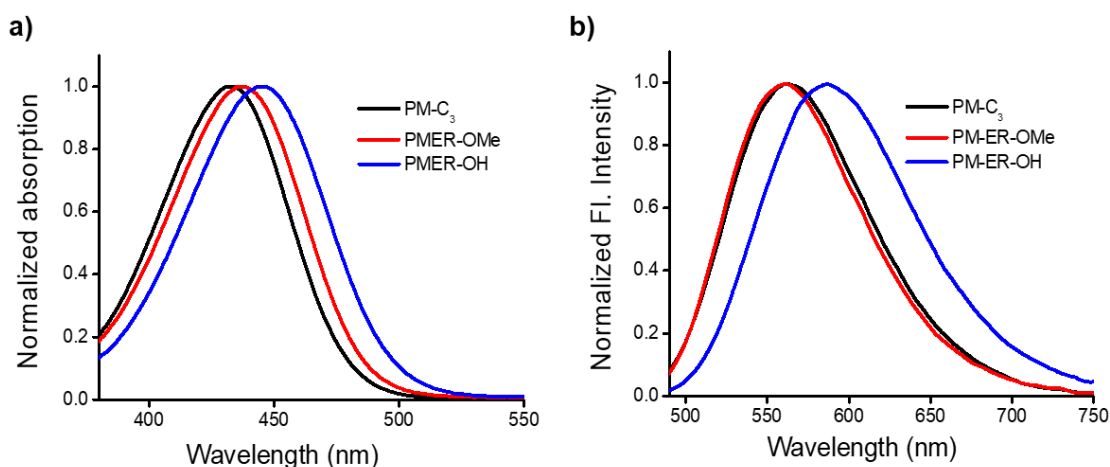


Figure 4.7. (a) Normalized absorption and (b) emission spectra of **PM-C₃**, **PM-ER-OMe** and **PM-ER-OH** in chloroform (10 μM).

We also measured the fluorescence quantum yield of the molecules in EtOH, using Coumarin 153 as standard ($\Phi_f = 0.38$ in EtOH). **PM-C₃** ($\Phi_f = 0.54$ in EtOH) and **PM-**

ER-OMe ($\Phi_f = 0.63$ in EtOH) exhibited $\sim 20\%$ decrease in quantum yield compared to **PS-OMe**. Though both the molecules showed superior extinction coefficients compared to **PS-OMe**, the observed decrease in quantum yield is attributed to the increase in Stokes shift. The quantum yield of **PM-ER-OH** ($\Phi_f = 0.57$ in EtOH) was slightly lower than that of **PM-ER-OMe**, probably due to the decrease in donor strength after demethylation. Nevertheless, enhanced delocalization of electron density on the acceptor nitrogen atom, that is less electronegative, and better possibilities for intramolecular charge transfer in **PM-ER-OH** resulted in a higher quantum yield as compared to **PS-OH**.

4.3.3. pH Response, Calculation of pKa and Microscope Compatibility

No significant change in absorption or emission was observed for **PM-C₃** (10 μ M) in buffer solution of different pH (4 - 10). However, **PM-ER-OMe** exhibited an unexpected pH response with a slight decrease in the intensity of absorption and emission (**Figure 4.8a-b**). It most likely due to the photoinduced electron transfer (PET) from the sulfonamide moiety that is in a close proximity with the acceptor part of the probe.

The expected pH response of **PM-ER-OH** was unambiguously confirmed by the absorption and emission changes exhibited by its buffered solutions. The absorption maxima (λ_{max}) of **PM-ER-OH** in acidic (pH 4) and alkaline (pH 10) solutions were found to be at 420 and 490 nm, respectively with a near-isosbestic point at 450 nm,

indicative of an operational equilibrium between protonated and deprotonated species (**Figure 4.9a**).

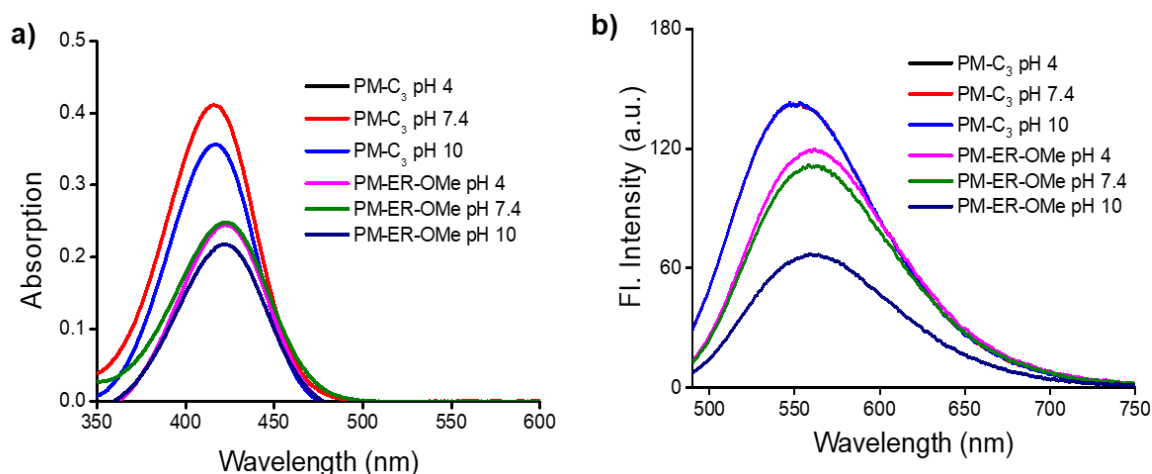


Figure 4.8. (a) Absorption and (b) emission spectra of **PM-C₃** (10 μ M) and **PM-ER-OMe** (10 μ M) in PBS buffer at pH 4, 7.4 and 10.

The emission maximum at 566 nm gradually decreased with increasing pH (pH 4 - 10), with a concomitant increase in a new peak appearing at $\lambda_{max} = 660$ nm upon excitation at the isosbestic wavelength ($\lambda_{ex} = 450$ nm), resulting in a single excitation ratiometric fluorescence response (**Figure 4.9b**). When excited at the first absorbance maximum ($\lambda_{max} = 420$ nm), the emission at 566 nm gradually decreased with increasing pH, with no detectable emission at 660 nm, thereby exhibiting a ‘Turn-OFF’ response at 566 nm (**Figure 4.9c**). Similarly, when excited at the second absorbance maximum ($\lambda_{max} = 490$ nm), the emission at 660 nm steadily increased, with barely any emission at 566 nm, confirming a ‘Turn-ON’ behavior at 660 nm in the same pH range (**Figure 4.9d**).

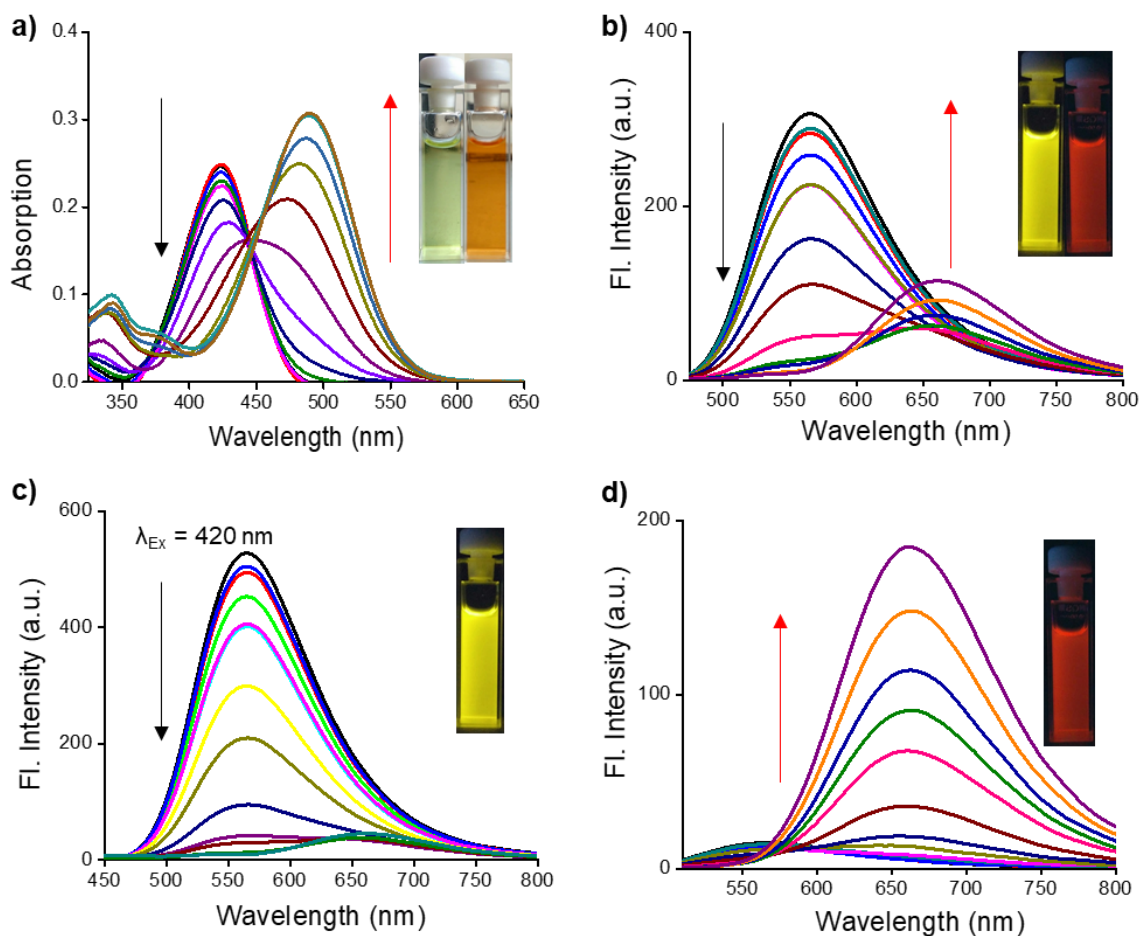


Figure 4.9. (a) Absorption spectra of the probe **PM-ER-OH** (10 μM) in PBS buffer (pH 4 - 10). The corresponding emission spectra of **PM-ER-OH**, when excited at (b) 450 nm, (c) 420 nm and (d) 490 nm. The photographs of the buffered solutions of the probe are shown in the insets.

Thus, the probe **PM-ER-OH** serves as an excitation wavelength-dependent ‘*three-in-one*’ ratiometric, ‘Turn-ON’ or ‘Turn-OFF’ probe without any significant spectral overlap and with high Stokes shifts (pH 4: 6142 cm^{-1} , pH 10: 5257 cm^{-1}). A non-linear Boltzmann fitting of the secondary plots generated from the emission spectra resulted in calculated $\text{pK}_{\text{a}1}$ and $\text{pK}_{\text{a}2}$ values of 7.18 ± 0.02 and 8.28 ± 0.02 , respectively (**Figure 4.10a-b**).

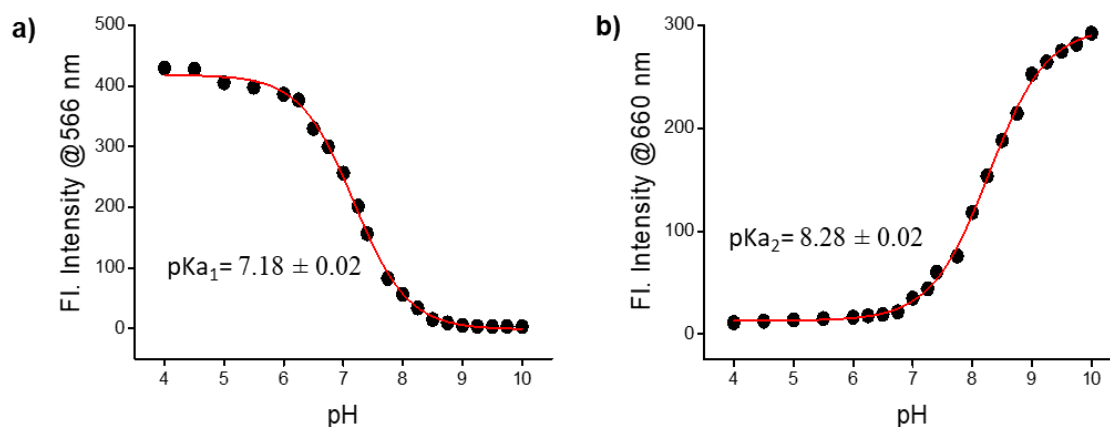
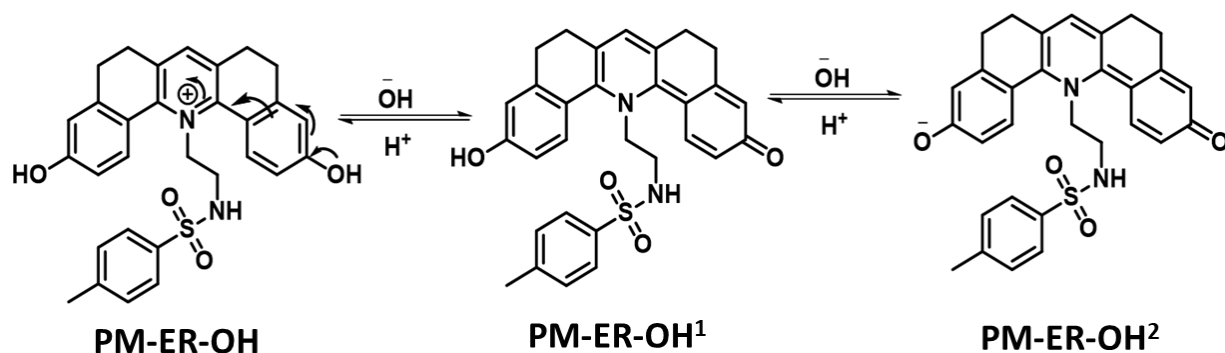


Figure 4.10. The secondary plot of the fluorescence response of the probe **PM-ER-OH** (10 μM) at (a) 566 nm using an excitation source of 420 nm and non-linear fitting to obtain pKa₁, and (b) 660 nm using an excitation source of 490 nm and non-linear fitting to obtain pKa₂.

These observations indicated a two-step deprotonation process involving terminal –OH groups, within the range of physiologically relevant pH (**Scheme 4.2**). These results corroborate the wide range of pH monitoring capability of **PM-ER-OH** inclusive of the normal ER pH (7.2) and its applicability in monitoring heat shock-induced damage of ER by following the corresponding changes in pH.⁴⁸



Scheme 4.2. Two-step protonation - deprotonation mechanism of **PM-ER-OH**, leading to two pKa values and ratiometric emission changes.

The fluorescence quantum yields of **PM-ER-OH** in PBS buffer of pH 4 and 10 were found to be 0.12 and 0.04, respectively. The pH-dependent emission properties of **PM-ER-OH** were obtained using 405, 458 and 488 nm excitations, that are readily available light sources in confocal laser scanning microscopes. Excitation at 405 nm and 488 nm wavelengths resulted in typical pH-dependent ‘ON and OFF’ emission profiles, respectively (**Figure 4.11a, b**). Excitation using a 458 nm laser source showed a single excitation ‘ratiometric’ pH response, without any significant spectral overlap due to the high Stokes shift of **PM-ER-OH** (**Figure 4.11c**). The fluorescence life time data is given in the experimental section.

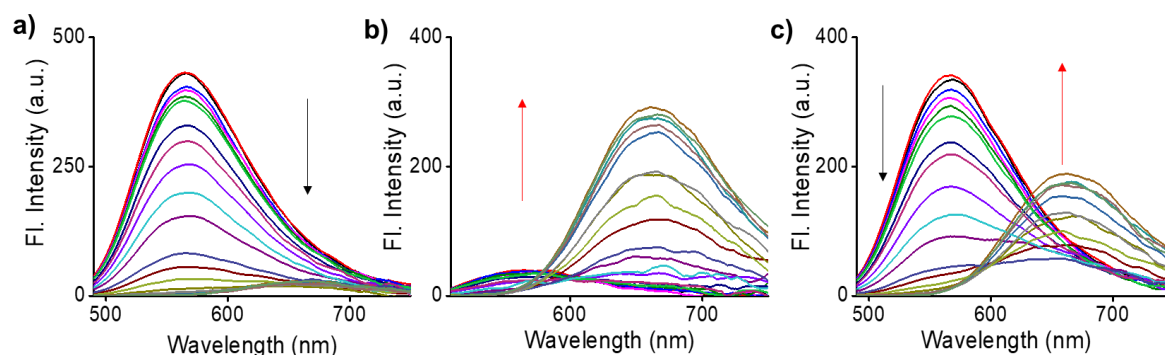


Figure 4.11. Emission Spectra of the probe **PM-ER-OH** (10 μ M) at different pH (4 – 10) using (a) 405 nm, (b) 488 nm, and (c) 458 nm excitation.

4.3.4. Photo and Thermal Stabilities

The photostability of the fluorophore was confirmed by exposing a 10 μ M solution of **PM-ER-OH** in PBS buffer at different pH (pH 4, 7.4 and 10) to a Hg lamp (200 W, 365 nm long-pass filter) for 30 minutes.

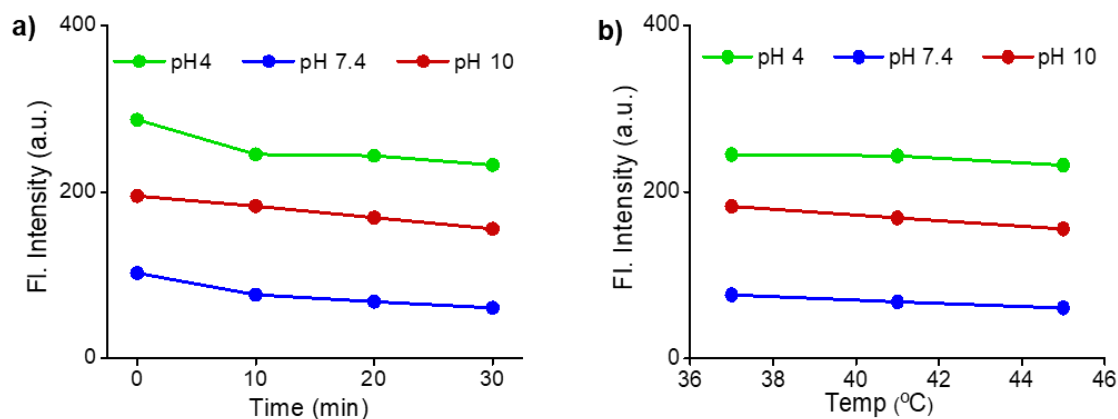


Figure 4.12. (a) Plot showing the photostability of the probe **PM-ER-OH** at pH 4, 7.4 and 10. The emission maximum at the corresponding pH is plotted against time. (b) Effect of temperature on the fluorescence behavior of **PM-ER-OH** at acidic, neutral and basic pH.

The plot of emission intensity ($\lambda_{\max} = 566$ nm for pH 4 and 7.4, and $\lambda_{\max} = 660$ nm for pH 10) vs. time showed >80% fluorescence retention after 30 minutes that is indicative of the superior photostability of **PM-ER-OH** (**Figure 4.12a**). Propensity towards free rotation induced non-radiative transitions in extended conjugated fluorophores with large Stokes shifts makes their fluorescence response susceptible to changes in temperature.⁴⁹ Therefore, we investigated the temperature-dependent emission of **PM-ER-OH** at 35 °C, 41 °C, and 45 °C in acidic (pH 4), neutral (pH 7.4), and basic (pH 10) PBS buffers. To our satisfaction, the emission profiles in terms of wavelength and intensity of this rigid pentacyclic pyridinium fluorophore was found to be unaffected by variations in temperature due to lack of structural flexibility capable of inducing non-radiative pathways (**Figure 4.12b**). Photoinduced radical formation leading to dimerization was not observed during any of these experiments.

4.3.5. Reversibility and Selectivity

As pH is a dynamic parameter, reversibility of the fluorescence response for a few cycles of acid-base treatment is an important criterion for a reliable pH probe. The pH of the buffer solution was switched between 4 and 10 by adding TFA and DBU in the presence of **PM-ER-OH** and recorded the fluorescence response at 566 and 660 nm wavelength, respectively. There was no evident degradation of the probe after 5 cycles, that confirmed its potential to monitor dynamic changes in pH (**Figure 4.13a**).

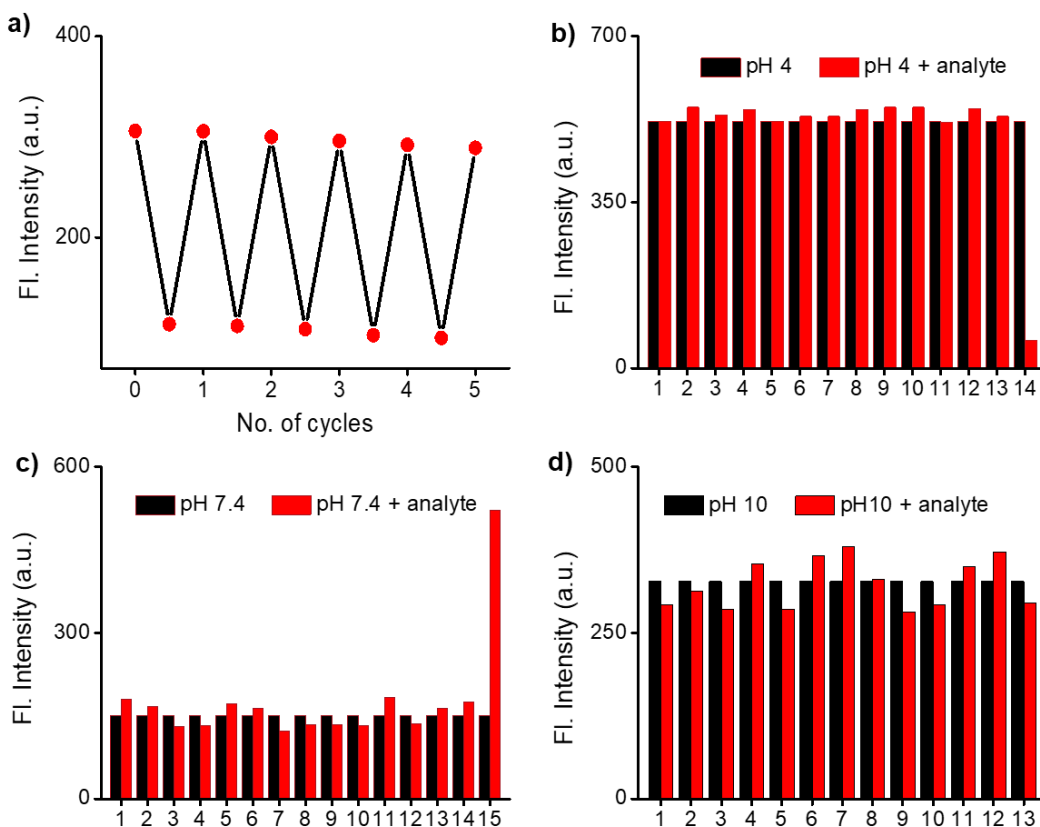


Figure 4.13. (a) Reversibility of the pH response of **PM-ER-OH** (10 μ M) during multiple cycles of acid and base treatments. Selectivity tests using different biologically relevant analytes (1. K^+ , 2. Fe^{2+} , 3. Na^+ , 4. Ca^{2+} , 5. Mg^{2+} , 6. Al^{3+} , 7. Zn^{2+} , 8. AcO^- , 9. $HOCl$, 10. H_2S , 11. H_2O_2 , 12. GSH , 13. O^{2-} , 14. OH^- , 15. H^+) at pH (b) 4, (c) 7.4 and (d) 10.

The selectivity of **PM-ER-OH** towards different biologically relevant analytes including metal ions (K^+ , Fe^{2+} , Na^+ , Ca^{2+} , Mg^{2+} , Al^{3+} , Zn^{2+}), anions (AcO^- , OH^-), reactive oxygen species (H_2O_2 , O_2^- , $HOCl$), and biothiols (GSH, H_2S) at pH 4 and 7.4 and 10 was tested. None of the analytes was found to interfere with the fluorescence profile of **PM-ER-OH** at acidic, neutral and basic pH (**Figure 4.13b-d**). These results unambiguously confirm the selective response of the probe towards changes in pH. The reversibility and selectivity in analyte response is indicative of the potential of **PM-ER-OH** for further exploration as a dynamic pH sensor in live cells capable of monitoring sub-cellular level processes in real-time.

4.3.6. Biocompatibility, Colocalization and Intracellular Photostability

Biocompatibility is an important parameter, that determines the applicability of any fluorophore in biosensing and imaging applications. Cytotoxicity of **PM-ER-OH**, **PM-C₃**, and **PM-ER-OMe** was quantified by incubating these molecules at different concentrations ($c = 0 - 100 \mu M$). Different concentrations of **PM-ER-OMe**, **PM-ER-OH**, and **PM-C₃** were added to HeLa cells seeded in three 96-well plates and incubated for 24 h. After mixing with DMEM for 4 h, the MTT solution was replaced with 100 μL of DMSO, and the absorbance of the formed formazan crystals was measured at 570 nm, that showed excellent cell viability (>85%), confirming the potential application of the probes in cellular experiments (**Figure 4.14**).

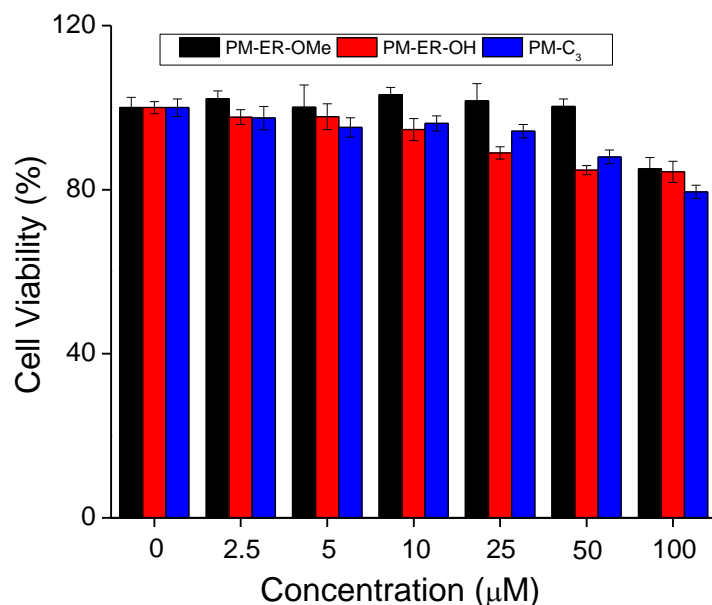


Figure 4.14. Cytotoxicity evaluation of **PM-ER-OMe**, **PM-ER-OH** and **PM-C₃** when incubated with HeLa cells for 24 h via MTT assay.

Colocalization studies were conducted using **PM-ER-OH** and **PM-C₃** (control) in comparison with commercially available ER-tracker blue (**Figure 4.15**). The Pearson's coefficients were found to be 0.77 and 0.50 for **PM-ER-OH**, and **PM-C₃**, respectively. This result suggests moderately efficient colocalization of the probe **PM-ER-OH** in ER and corroborates the vital role of targeting groups for localizing the probe at sub-cellular levels.

In addition to biocompatibility, intracellular photostability is another crucial property for a probe to be applied as a reliable and consistent fluorescence imaging agent. To confirm whether the solution photostability of **PM-ER-OH** is retained in cellular environment, the intracellular photostability of the probe was compared with commercial ER-Tracker blue (**Figure 4.16a**).

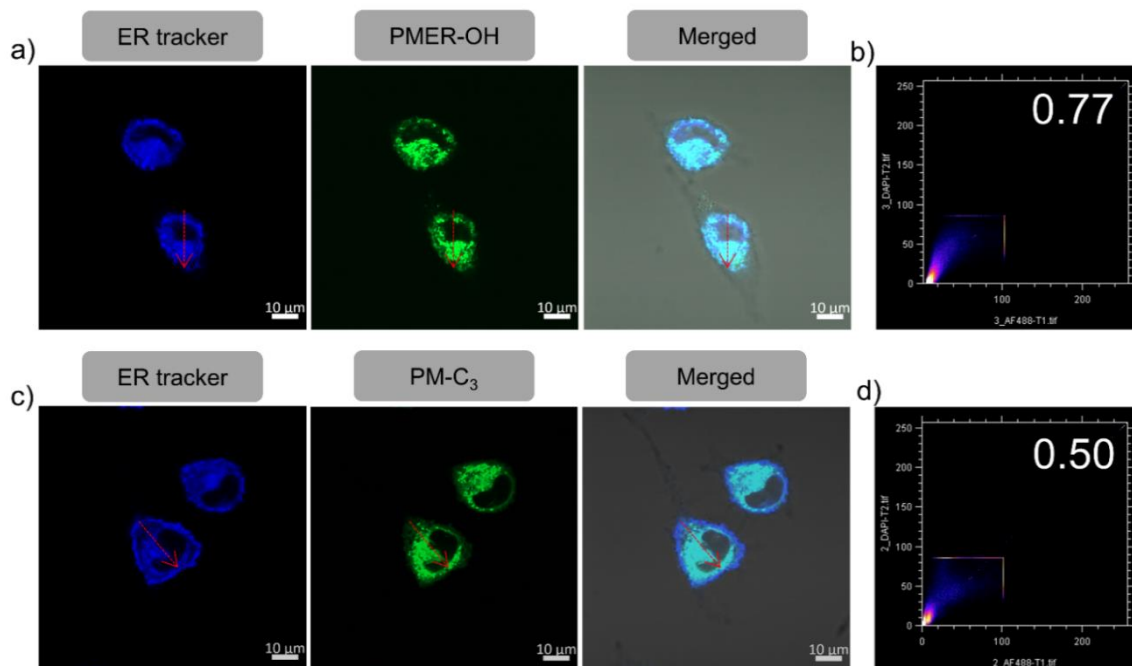


Figure 4.15. CLSM images of live HeLa cells, stained with **ER tracker blue** and (a) **PM-ER-OH** and (c) **PM-C₃** in blue, green and merged channels. Scatter plot-based Pearson's coefficient calculation for (b) **PM-ER-OH** and (d) **PM-C₃**, in comparison to commercial ER tracker blue. Pearson's coefficient values, calculated using ImageJ are mentioned in the inset. Scale bar 10 μm .

Two sets of HeLa cells, each incubated with **PM-ER-OH** and commercial ER tracker, were subjected to light illumination for up to 10 min and images were obtained every 10 s. Intensity analysis indicated that **PM-ER-OH** was more stable compared to the commercial ER-Tracker blue (**Figure 4.16b**). This superior photostability of **PM-ER-OH** could be attributed to the structural rigidity of the pyridinium chromophore, that further underlines the significance of structural design towards stable and effective bioimaging agents. The promising photophysical properties in cellular environment prompted us to further explore the *in vitro* pH response of **PM-ER-OH** using confocal fluorescence imaging.

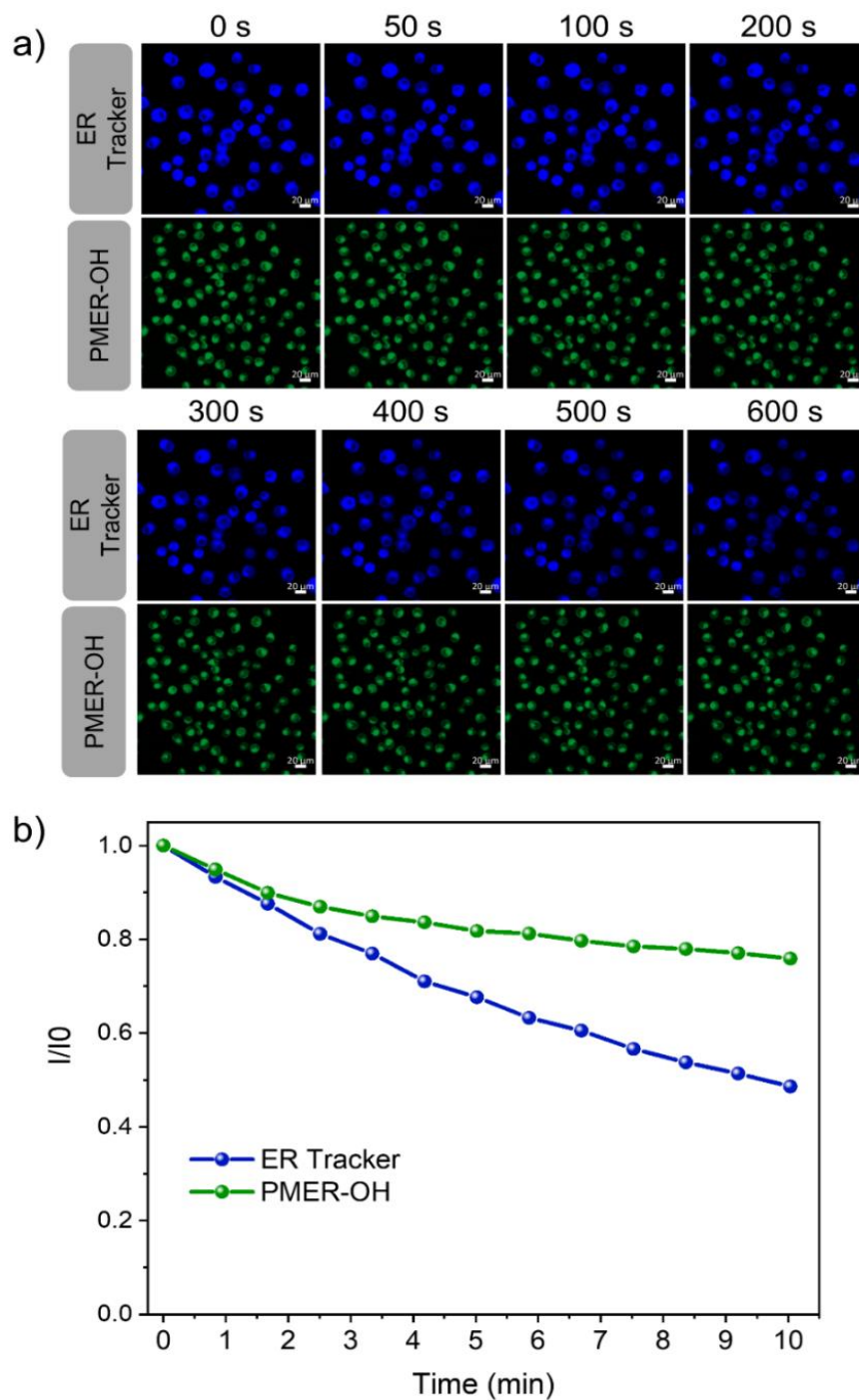


Figure 4.16. Comparison of photostability after treating HeLa cells with **PM-ER-OH** (10 μM) and commercial ER tracker (1 μM) followed by light illumination for 0 – 10 min and (a) images taken with 10 s intervals. (Scale bar is 20 μm). (b) A plot of fluorescence intensity, measured from the cells with time, corroborating better photostability of **PM-ER-OH** in live cells.

4.3.7. In-vitro pH Response

Confocal fluorescence imaging (HeLa cells, 10 minutes incubation) was performed using three excitation laser sources (405, 458, and 488 nm) and the images were captured in the green (500 - 550 nm) and red channels (625 -750 nm). Using Nigericin, intracellular pH was set at 4.2, 7.4, and 9.2, equilibrating with the pH of extracellular buffers, prior to the experiments. Akin to the photophysical experiments in solution, excitation using a 405 nm laser source resulted in a gradual decrease in the fluorescence intensity with increasing pH, when monitored in the green channel (**Figure 4.17a**). The observed fluorescence intensity followed the order: pH 4.2 (intensity = 32.96 a.u.) > pH 7.4 (intensity = 24.25 a.u.) > pH 9.2 (intensity = 12.90 a.u.), with no detectable fluorescence in the red channel (**Figure 4.17b**). This observation confirms a 'Turn-ON' fluorescence response during the acidification of cells upon excitation at 405 nm. On the other hand, the fluorescence intensity in the red channel was found to increase with increasing pH (intensity = 9.05 a.u. at pH 4.2; 14.43 a.u. at pH 7.5 and 20.58 a.u. at pH 9.2), upon excitation at 488 nm (**Figure 4.17c**), with no simultaneous emission change in the green channel (**Figure 4.17d**). The "Turn-OFF" response of **PM-ER-OH** during the cellular acidification process was thus corroborated.

Upon using 458 nm laser excitation, increasing intracellular pH resulted in a decrease in the fluorescence intensity in the green channel (intensity = 30.65 a.u. at pH 4.2; 20.47 a.u. at pH 7.5 and 10.76 a.u. at pH 9.2), with a concomitant increase in the emission intensity in the red channel (intensity = 6.01 a.u. at pH 4.2; 10.66 a.u. at 7.5 and 15.13

a.u. at pH 9.2), leading to a typical single excitation ratiometric response (**Figure 4.17e-f**). These results strongly support the application of a single probe with a 'three-in-one' response for bioimaging, particularly for monitoring intracellular pH changes.

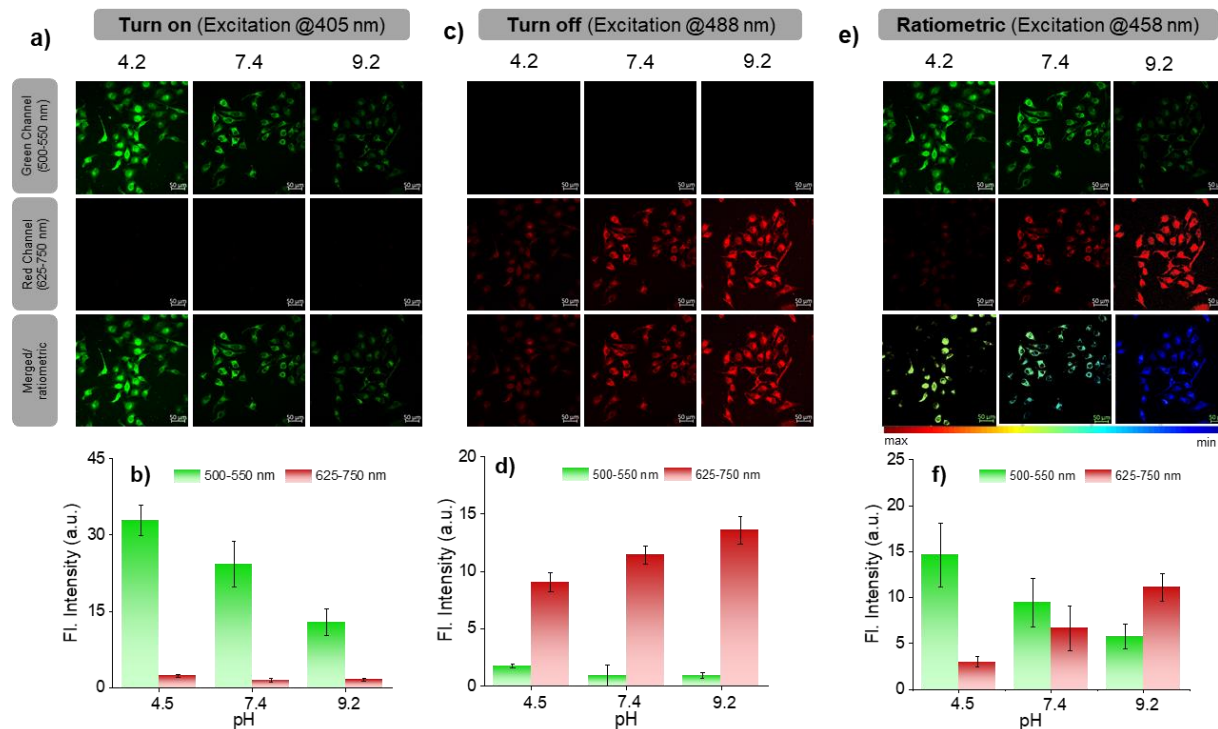


Figure 4.17. CLSM imaging of HeLa cells after 10 minutes incubation with the probe **PM-ER-OH** (10 μ M) in buffer solution of different pH in the presence of 10 μ M nigericin. Images in green and red channels along with merged or ratiometric images, upon using excitation sources: (a) 405 nm laser, (c) 488 nm laser, and (e) 488 nm laser. The bar diagrams represent the values of fluorescence intensities (in a.u.) obtained from the image analysis of (b) a, (d) c and (f) e. The color of the bars represents the corresponding channel.

4.3.8. pH Changes during Heat Shock

Heat-induced cellular damages are generally irreversible even if the cells are later cooled to normal temperature. However, the damage due to heat shock can be significantly curtailed by a process called hormesis, wherein cells are preconditioned at

mild heat for a short period of time.^{50,51} pH is among the factual parameters universally accepted for understanding cellular homeostasis and lysosomal pH probes were recently reported for monitoring heat shock. Since the endoplasmic reticulum (ER) is impacted prior to lysosomes by any heat shock event and the activation of several heat shock proteins located in the ER helps to prevent the heat damage that preserves homeostasis during hormesis. Monitoring pH variations in ER during heat shock can offer better insights into cellular damage pathways at an early stage compared to lysosomal pH probes. Therefore, we believe that ER targeting **PM-ER-OH** is ideal for monitoring heat shock events at sub-cellular level.

Two sets of experiments were designed for heat shock mapping in live HeLa cells. (i) The cells were heated directly to 41 °C and 45 °C from 37 °C, and (ii) the cells were pre-heated for 3 h at 40 °C and then heated to 41 °C and 45 °C. The fluorescence images of both the sets at 41 °C and 45 °C were evaluated after exciting with three laser sources and monitoring two emission channels using **PM-ER-OH** as described earlier. Excitation at 405 nm resulted in an increase in the fluorescence intensity in the green channel with an increase in temperature for directly heated cells (intensity = 1 a.u. at 37 °C; 1.8 a.u. at 41 °C and 3.46 a.u. at 45 °C) and for pre-heated cells (intensity = 1 a.u. at 37 °C; 1.2 a.u. at 41 °C and 2.58 a.u. at 45 °C), with no detectable emission in the red channel (**Figure 4.18a-c**).

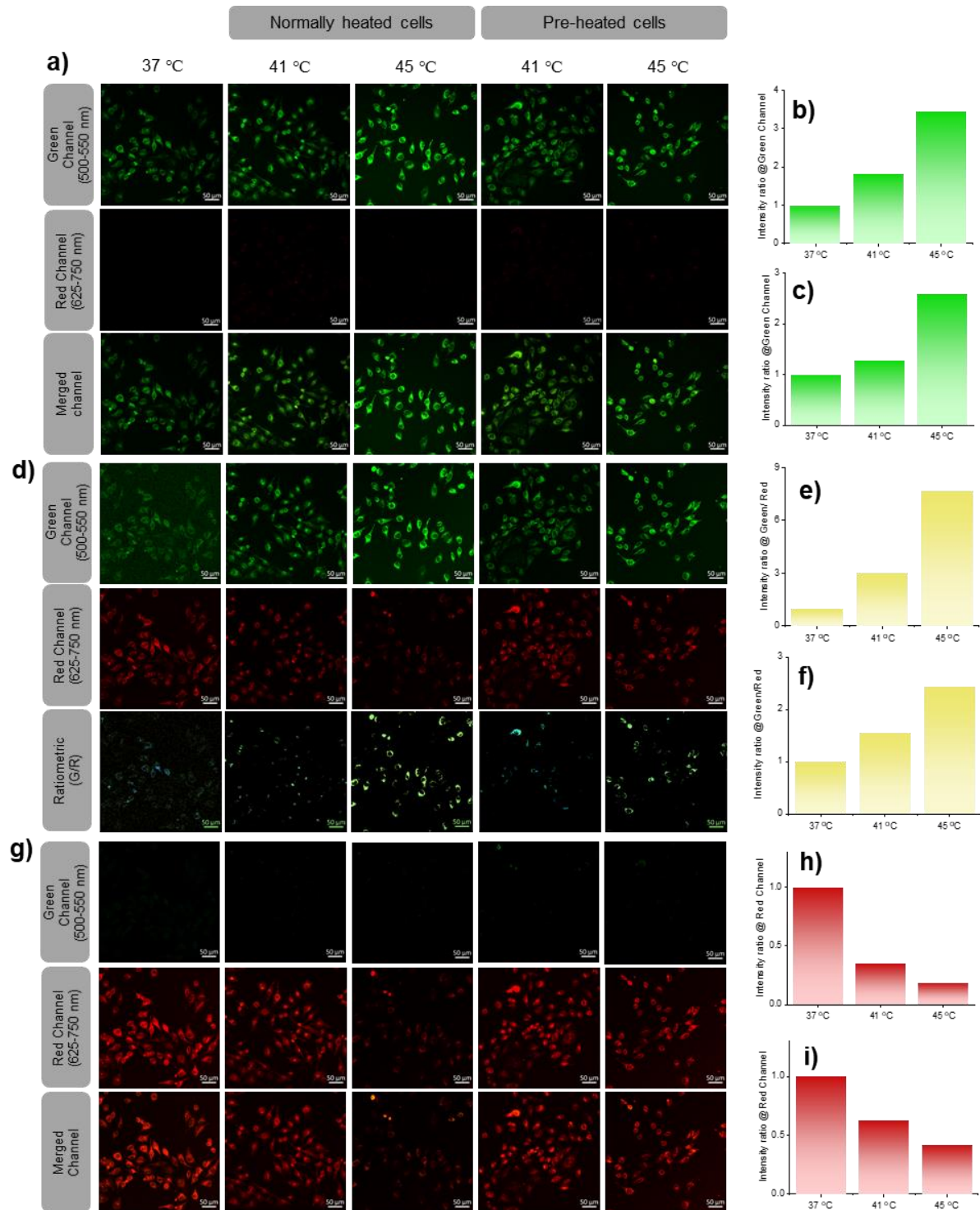


Figure 4.18. *In vitro* heat shock mapping via CLSM imaging of HeLa cells after inducing heat shock in two different ways. (a) Images of heat-treated cells in green, red, and merged channels using 405 nm laser excitation. (b) and (c) represent the fluorescence intensity increment in green channel for directly heated and pre-heated cells, respectively. (d) Green and red channel images along with the constructed

radiometric images (green/red) upon excitation at 458 nm. (e) and (f) represent the calculated ratio of fluorescence intensity increment for both directly heated and pre-heated cells, respectively. (g) Fluorescence images in green and red channels upon excitation at 488 nm. (h), (i) Fluorescence intensity decrease in the red channel for the directly heated and the pre-heated cells, respectively.

For 458 nm laser excitation, a similar result was obtained when monitored in the green channel for the directly heated cells (intensity = 1 a.u. at 37 °C; 1.5 a.u. at 41 °C, and 2.3 a.u. at 45 °C) and for the pre-heated cells (1 a.u. at 37 °C; 1.18 a.u. at 41 °C, and 1.45 a.u. at 45 °C). However, for the directly heated cells, the temperature-dependent increase in fluorescence intensity was higher than the pre-heated cells. Cellular acidification is therefore correlated directly to the increase of temperature (**Figure 4.18d**).

On the contrary, when excited at 458 nm, the fluorescence intensity in the red channel decreased with increasing temperature for both directly heated (intensity = 1 a.u. at 37 °C; 0.5 a.u. at 41 °C and 0.3 a.u. at 45 °C) and pre-heated (intensity = 1 a.u. at 37 °C; 0.76 a.u. at 41 °C and 0.6 a.u. at 45 °C) cells. The ratio of intensities (green/red) also showed an increment for both directly heated (intensity = 1 a.u. at 37 °C; 3.01 a.u. at 41 °C and 7.64 a.u. at 45 °C) and pre-heated (intensity = 1 a.u. at 37 °C; 1.56 a.u. at 41 °C and 2.43 a.u. at 45 °C) cells (**Figure 4.18e-f**).

Images taken in the red channel, using 488 nm laser as the excitation source, showed a similar trend for both directly heated (intensity = 1 a.u. at 37 °C; 0.35 a.u. at 41 °C, and 0.19 a.u. at 45 °C) and pre-heated (intensity = 1 a.u. at 37 °C; 0.63 a.u. at 41 °C and 0.42 a.u. at 45 °C) cells (**Figure 4.18g-i**). Though similar trends in fluorescence changes with

increasing temperature were observed in the green channel upon excitation at 405 nm or 458 nm, the intensity increments for the directly heated cells were significantly higher than those for the pre-heated cells. However, the decrease in the fluorescence intensity was less predominant for the pre-heated cells when compared to that for the directly heated cells under 458 nm and 488 nm excitation.

These observations suggest that conditioning cells at an elevated temperature (40 °C) below hyperthermia could resist cellular acidification far better than direct exposure of cells to hypothermic conditions. Our results confirm that heat shock-induced dysfunction of ER can be directly monitored using the corresponding changes in pH. Pre-heating the cells below hyperthermic conditions signaled the production and activation of HSPs, and as a result, the cells were protected even when the temperature rose above the tolerance level. The acidification of ER reduces the pH of the cell that most likely stimulates an increase in lysosomal pH via a neutralization process as previously reported.

4.4. Conclusion

In conclusion, by virtue of the large Stokes shift exhibited by the newly developed pentacyclic pyridinium fluorescent probe **PM-ER-OH**, ‘*three-in-one*’ fluorescence imaging of pH variations associated with heat shock in live cells could be achieved. The ratiometric changes in the absorbance of **PM-ER-OH** with pH variations and the presence of an isosbestic point that correlates with laser excitation sources of the

confocal fluorescence microscope make this probe an excellent candidate for monitoring pH variations at sub-cellular levels. The lack of backbone flexibility, presence of a subcellular targeting moiety and intrinsic silence towards hyperthermic conditions are ideal prerequisites for live imaging of heat shock-induced dysfunction mechanisms within endoplasmic reticulum. A favorable combination of biocompatibility, physiological solubility, and photo and chemical stabilities, along with reasonable ER colocalization of **PM-ER-OH** facilitated reliable pH monitoring, both exogenously and endogenously. To the best of our knowledge, **PM-ER-OH** is the first fluorescent probe reported for pH-assisted heat shock imaging in the endoplasmic reticulum. As confirmed by our results, cellular exposure to a sudden hyperthermic wave can be more fatal than a slow rise in temperature. We believe that this study will encourage the development of efficient fluorescent probes with large Stokes shifts for wider applications, particularly in bioimaging and diagnostics. Our findings related to variations in pH within endoplasmic reticulum during heat shock is envisioned to assist in elucidating the role of heat shock proteins during hyperthermia, leading to a better understanding of the mechanistic pathways behind heat induced cellular damage and related pathologies, thereby leading to better treatment planning and efficacy.

4.5. Experimental Section: Synthesis

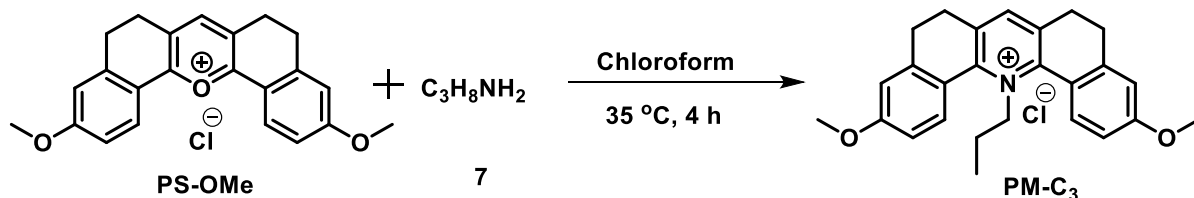
4.5.1. Materials and Methods

All reagents and dry solvents (reagent grade) were used without further purification. Reaction completion was monitored by silica gel G-60 F254 aluminum TLC and compounds were visualized by short/long-wavelength UV lamps. Column chromatography was done using silica gel 100-200 mesh as a stationary phase. ^1H and ^{13}C NMR were recorded on a Bruker Advance II spectrometer at 500 and 125 MHz using deuterated solvents and reported as follows: chemical shift in ppm (δ), multiplicity (s = singlet, d = doublet, t = triplet, q = quartet) and coupling constant (J in Hz). HRMS data were recorded on a Thermo Scientific Exactive LCMS instrument by electrospray ionization method with ions given in m/z using Orbitrap analyzer.

Electronic absorption spectra were recorded in a Shimadzu UV-2600 spectrophotometer. Emission spectra were recorded on Horiba Fluorolog – 3 Jovin Yoon. Cell imaging experiments were carried out using a Zeiss LSM710 Airyscan CLSM (confocal laser scanning microscope). Optical density (OD) for the cellular experiments was recorded using the microplate reader (infinite M200, TECAN).

4.5.2. Synthesis and Characterization

Synthesis of PM-C₃



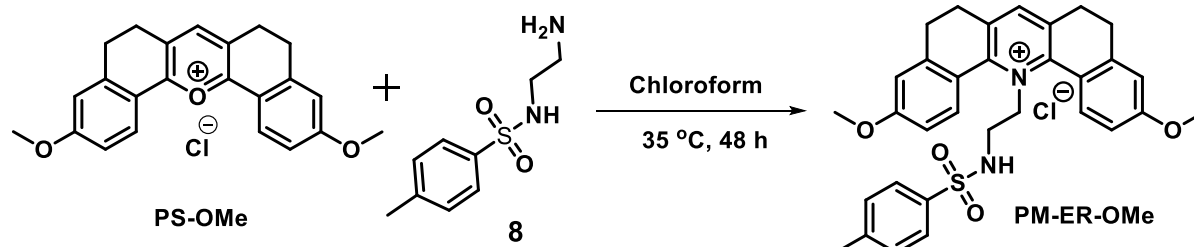
PS-OMe (0.5 g, 1.26 mmol) was dissolved in CHCl₃ (200 mL) and propylamine (0.359 g, 6.08 mmol) was added to the above stirred solution dropwise. The reaction mixture was then stirred at 35 °C for 4 h. Completion of the reaction was confirmed by TLC. Excess amine was removed by washing with water (100 mL, 3×). The organic extract was combined, dried over anhydrous Na₂SO₄ and solvent was removed under reduced pressure. The residue was redissolved in CH₃OH (5 mL) and an excess of cold diethyl ether was added. The precipitate formed was collected by filtration and dried in an oven at 50 °C to afford **PM-C₃** (0.38 g, 71.5%) as a yellow powder.

PM-C₃: ¹H NMR (500 MHz, CDCl₃), δ: 8.29-8.27 (d, *J* = 5 Hz, 2H), 7.99 (s, 1H), 7.14-7.12 (d, *J* = 5 Hz, 2H), 6.90 (s, 2H), 5.24-5.22 (t, *J* = 5 Hz, 2H), 3.91 (s, 6H), 3.05-3.04 (d, *J* = 2.5 Hz, 2H), 2.9-2.89 (d, *J* = 2.5 Hz, 4H), 2.75-2.74 (d, *J* = 2.5 Hz, 2H), 1.31-1.27 (m, 2H), 0.37-0.34 (t, *J* = 7.5 Hz, 3H).

¹³C NMR: (125 MHz CDCl₃), δ: 162.9, 153.3, 142.9, 136.30, 136.35, 120.9, 114.7, 113.5, 65.9, 55.8, 28.6, 28.2, 23.2, 10.2

HRMS: Calcd. ($C_{26}H_{28}NO_2^+$) = 386.2115, Found = 386.2134

Synthesis of PM-ER-OMe



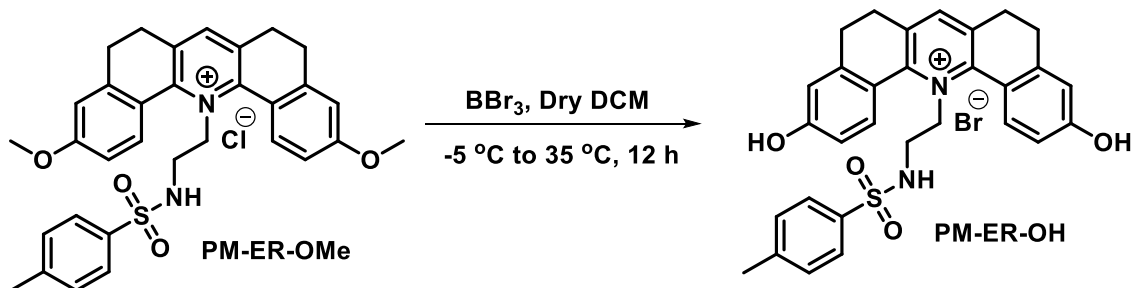
PS-OMe (0.5 g, 1.26 mmol) and *N*-(2-aminoethyl)-4-methylbenzenesulfonamide (0.6 g, 2.8 mmol) were dissolved in $CHCl_3$ (200 mL) and stirred at 35 °C for 48 h. Excess amine was removed by washing with water (100 mL, 3 \times) and the organic layer was collected, dried over anhydrous Na_2SO_4 , solvent was removed under reduced pressure and purified by column chromatography using silica gel as a stationary phase and 5 % methanol/ chloroform as mobile phase to afford **PM-ER-OMe** as a yellow powder (0.232 g, 32%).

PM-ER-OMe: 1H NMR (500 MHz, $CDCl_3$), δ : 8.0 (s, 1H), 7.90 (d, $J = 10$ Hz, 2H), 7.51 (d, $J = 10$ Hz, 2H), 7.14 (d, $J = 10$ Hz, 2H), 7.03 (d, $J = 5$ Hz, 2H), 6.14 (s, 1H), 5.45 (s, 2H), 3.90 (s, 6H), 3.10 (t, $J = 15$ Hz, 2H), 3.12 (d, $J = 15$ Hz, 2H), 2.86-2.69 (m, 6H), 2.31 (s, 3H).

^{13}C NMR: (125 MHz $CDCl_3$), δ : 162.9, 153.9, 144.9, 143.2, 142.7, 136.6, 136.4, 130.2, 129.6, 126.8, 121.0, 114.4, 113.7, 64.2, 55.7, 43.6, 28.3, 28.1, 21.4.

HRMS: Calcd ($C_{32}H_{33}N_2O_4S^+$) = 541.2156, Found = 541.21676.

Synthesis of PM-ER-OH



PM-ER-OMe (0.1 g, 0.17 mmol) was dissolved in dry CH_2Cl_2 (10 mL) and cooled to $-5\text{ }^\circ\text{C}$ using an ice-salt mixture. After 30 min, BBr_3 in CH_2Cl_2 (1.5 mL, 6 mmol) was added dropwise under a flow of argon and was stirred overnight at $35\text{ }^\circ\text{C}$. Excess of BBr_3 was quenched by slowly adding distilled water slowly (5 mL). The precipitate formed was collected by filtration, washed with distilled water (10 mL, 5 \times) to get **PM-ER-OH** as a yellow powder (0.08 g, 86%).

PM-ER-OH: ^1H NMR (500 MHz, MeOD), δ : 8.13 (s, 1H), 7.90 (d, $J = 10$ Hz, 2H), 7.42 (d, $J = 10$ Hz, 2H), 7.27 (d, $J = 10$ Hz, 2H), 6.95 (d, $J = 10$ Hz, 4H), 5.33 (s, 2H), 3.11 (t, $J = 10$ Hz, 4H), 2.90 – 2.77 (m, 4H), 2.66 (s, 2H), 3.09 (s, 3H)

^{13}C NMR: (125 MHz, MeOD), δ : 161.3, 153.4, 144.9, 130.4, 129.5, 126.3, 119.9, 115.1, 114.7, 27.8, 27.7, 20.1.

HRMS: Calcd. ($C_{30}H_{29}N_2O_4S^+$) = 513.1843, Found = 513.18591.

4.6. Description of Experimental Techniques

4.6.1. UV/Vis Absorption and Emission Spectral Measurements

Electronic absorption spectra were recorded using a Shimadzu UV-2600 UV-Vis spectrophotometer, and emission studies were conducted using Horiba Fluorolog – 3 Jovin Yoon. Stock solutions were prepared in spectroscopy grade DMSO and diluted with phosphate buffer as required. The solutions were made by using phosphate buffer and pH was adjusted using dilute HCl/ NaOH solutions.

4.6.2. Fluorescence Quantum Yield and Lifetime Measurements

Fluorescence quantum yields and lifetime of all the molecules were measured as per procedure described in section 3.6.2 using Coumarin 153 as reference.

4.6.3. Cell Culture

HeLa cells were grown in Dulbecco's Modified Eagle's medium (DMEM) supplemented with 10% Fetal Bovine Serum (FBS) and 1% penicillin-streptomycin (PS) antibiotics at 37 °C in humidified environment of 5% CO₂. Cells were plated on 6-well plates and allowed to adhere for 12 h.

4.6.4. Determination of Cytotoxicity

HeLa cells were seeded in three 96-well plates (1×10^4 cells per well) and allowed to adhere for 12 h. Different concentrations of **PM-ER-OMe**, **PM-ER-OH**, and **PM-C₃**

(0, 2.5, 5, 10, 25, 50, and 100 μM) were then added to the wells and incubated for 24 h. Thereafter, MTT solution (5 mg/mL, 10 μL per well) was mixed with DMEM. Following 4 h incubation, the MTT solution was replaced with 100 μL of DMSO, and the absorbance of the formed formazan crystals was measured at 570 nm. The percentage of cellular viability was calculated according to the following equation:

$$\text{Cell viability (\%)} = \frac{\text{OD of treated cells}}{\text{OD of control}} \times 100 (\%)$$

4.6.5. Colocalization Experiments

The HeLa cells (1×10^4 cells) were seeded in μ -Dish 35 mm microscopy dishes. After 24 h of adherence, the media was replaced with 10 μM **PM-ER-OH** and 10 μM **PM-C₃**, and allowed to incubate for 20 min in PBS buffer at 37 °C. Thereafter, the cells were washed three times with PBS, and replaced with PBS containing 1 μM ER tracker solution. The cells were washed after 20 min with PBS (3x) and imaged under Zeiss LSM710 CLSM. The samples were excited at 405 nm and 488 nm. Image analysis was performed using ImageJ.

4.6.6. Intracellular Photostability

HeLa cells (1×10^4 cells) were seeded in μ -Dish 35mm microscopy dishes. The media was replaced with 10 μM **PM-ER-OH** after 24 h of adherence and allowed to incubate for 20 min in PBS at 37 °C. Subsequently, the cells were washed with PBS (3x), and replaced with PBS containing 1 μM ER tracker solution. After 20 minutes, the cells

were washed with PBS (3x) and imaged under Zeiss LSM710 CLSM. With 10 scans using high-intensity of 405 nm laser excitation, images were acquired for both the dyes, for 10 min.

4.6.7. Intracellular pH-Dependent Studies

HeLa cells were incubated at 37 °C for 30 min in high K⁺ buffer (30 mM NaCl, 120 mM KCl, 1 mM CaCl₂, 0.5 mM MgSO₄, 1mM Na₂HPO₄, 5 mM glucose, 20 mM sodium acetate and 20 mM MES) of various pH (pH 4.2 – 9.5). Next, 25 μL (10 μM) of a H⁺/K⁺ antiporter, nigericin, was added and incubated for 20 min to equilibrate the intracellular pH with the pH buffer. The cells were then incubated with 20 μL of the **PM-ER-OH** (10 μM) for 20 min, washed with PBS and observed under CLSM at 405, 458, and 488 nm excitation. Images were obtained on Zeiss software (Zen 3.2) and image analysis was performed using ImageJ.

4.6.8. Heat Shock Experiments

HeLa cells were seeded in 6-well plates and incubated at 37 °C for 24 h. The cells were divided into two sets: (i) normal heating to 41 °C and 45 °C, and (ii) pre-heated at 40 °C for 3 h, followed by heating to 41 °C and 45 °C. For set (i), the cells were kept at 41°C and 45 °C for 30 min each with **PM-ER-OH**. For set (ii), the cells were kept at 40 °C for 3 h, and later incubated with **PM-ER-OH** at 41 °C and 45 °C for 30 min. Both

sets were finally imaged under CLSM in two channels (green and red) using three different excitation sources, i.e., 405 nm, 458 nm, and 488 nm.

4.7. References

- [1] J. A. Patz, D. Campbell-Lendrum, T. Holloway and J. A. Foley, *Nature*, 2005, **438**, 310–317.
- [2] C. D. Butler, *Int. J. Environ. Res. Public Health*, 2018, **15**, 2266.
- [3] J. Hansen, M. Sato, R. Ruedy, K. Lo, D. W. Lea and M. Medina-Elizade, *Proc. Natl. Acad. Sci.*, 2006, **103**, 14288 – 14293.
- [4] N. Kourtis, V. Nikolettou and N. Tavernarakis, *Nature*, 2012, **490**, 213–218.
- [5] A. Bouchama, *Intensive Care Med.*, 1995, **21**, 623–625.
- [6] S. Al Mahri and A. Bouchama, *Handb. Clin. Neurol.*, 2018, **157**, 531–545.
- [7] A. Bouchama and J. P. Knochel, *N. Engl. J. Med.*, 2002, **346**, 1978–1988.
- [8] T. Hifumi, Y. Kondo, K. Shimizu and Y. Miyake, *J. Intensive Care*, 2018, **6**, 30.
- [9] D. J. Casa, L. E. Armstrong, G. P. Kenny, F. G. O’Connor and R. A. Huggins, *Curr. Sports Med. Rep.*, 2012, **11**, 115–123.
- [10] C. Mozzini, G. Xotta, U. Garbin, A. M. F. Pasini and L. Cominacini, *Am. J. Case Rep.*, 2017, **18**, 1058–1065.
- [11] Y. Epstein and W. O. Roberts, *Scand. J. Med. Sci. Sports*, 2011, **21**, 742–748.
- [12] C. L. Lim, *Antioxidants (Basel, Switzerland)*, 2018, **7**, 1–18.
- [13] B. Misset, B. De Jonghe, S. Bastuji-Garin, O. Gattolliat, E. Boughrara, D. Annane, P. Hausfater, M. Garrouste-Orgeas and J. Carlet, *Crit. Care Med.*, 2006, **34**, 1087–1092.
- [14] Z. Li and P. Srivastava, *Curr. Protoc. Immunol.*, 2003, **58**, 552 - 576
- [15] F. D. Cuello-Carrión, M. A. Fanelli, N. Cayado-Gutiérrez, G. Castro and D. R. Ciocca,

- Methods Mol. Biol.*, 2011, **787**, 267–275.
- [16] N. C. Dempsey, F. Leoni, C. Hoyle and J. H. H. Williams, *Methods Mol. Biol.*, 2011, **787**, 155–164.
- [17] C. S. Kumar, D. Sivaramakrishna, S. K. Ravi and M. J. Swamy, *J. Photochem. Photobiol. B Biol.*, 2016, **158**, 89–98.
- [18] E. G. Mimnaugh, W. Xu, M. Vos, X. Yuan, J. S. Isaacs, K. S. Bisht, D. Gius and L. Neckers, *Mol. Cancer Ther.*, 2004, **3**, 551 – 566.
- [19] S. K. B. Taylor, M. H. Minhas, J. Tong, P. R. Selvaganapathy, R. K. Mishra and B. P. Gupta, *Sci. Rep.*, 2021, **11**, 3115.
- [20] P. Gao, W. Pan, N. Li and B. Tang, *Chem. Sci.*, 2019, **10**, 6035–6071.
- [21] M. Gao, F. Yu, C. Lv, J. Choo and L. Chen, *Chem. Soc. Rev.*, 2017, **46**, 2237–2271.
- [22] H. Singh, K. Tiwari, R. Tiwari, S. K. Pramanik and A. Das, *Chem. Rev.*, 2019, **119**, 11718–11760.
- [23] X. Wang, L. Fan, X. Zhang, Q. Zan, W. Dong, S. Shuang and C. Dong, *Analyst*, 2020, **145**, 7018–7024.
- [24] X. Huang, S. Lee and X. Chen, *Am. J. Nucl. Med. Mol. Imaging*, 2011, **1**, 3–17.
- [25] X. Zhang, N. He, Y. Huang, F. Yu, B. Li, C. Lv and L. Chen, *Sensors Actuators B Chem.*, 2019, **282**, 69–77.
- [26] X. Li, P. Wu, W. Cao and H. Xiong, *Chem. Commun.*, 2021, DOI:10.1039/D1CC04408G.
- [27] Q. Wan, S. Chen, W. Shi, L. Li and H. Ma, *Angew. Chem Int. Ed.*, 2014, **53**, 10916–10920.
- [28] Y. Wen, W. Zhang, T. Liu, F. Huo and C. Yin, *Anal. Chem.*, 2017, **89**, 11869–11874.
- [29] X. Han, X. Song, F. Yu and L. Chen, *Chem. Sci.*, 2017, **8**, 6991–7002.
- [30] G. Saranya, P. Anees, M. M. Joseph, K. K. Maiti and A. Ajayaghosh, *Chem. Eur. J.*,

- 2017, **23**, 7191–7195.
- [31] G. Yin, T. Niu, Y. Gan, T. Yu, P. Yin, H. Chen, Y. Zhang, H. Li and S. Yao, *Angew. Chem. Int. Ed.*, 2018, **57**, 4991–4994.
- [32] Z. Zhou, H. Wu, R. Yang, A. Xu, Q. Zhang, J. Dong, C. Qian and M. Sun, *Sci. Adv.*, 2020, **6**, eabc4373.
- [33] L. Wu, Y. Wang, T. D. James, N. Jia and C. Huang, *Chem. Commun.*, 2018, **54**, 5518–5521.
- [34] W. Zhang, F. Huo, Y. Yue, Y. Zhang, J. Chao, F. Cheng and C. Yin, *J. Am. Chem. Soc.*, 2020, **142**, 3262–3268.
- [35] O. Etlik, A. Tomur, M. N. Kutman, S. Yörükan and O. Duman, *Environ. Res.*, 1995, **71**, 25–28.
- [36] K.-K. Sun, D.-B. Zhu, G.-F. Yao, K.-D. Hu and H. Zhang, *Biol. Plant.*, 2018, **62**, 809–816.
- [37] X. Yang, J. Tang, D. Zhang, X. Han, J. Liu, J. Li, Y. Zhao and Y. Ye, *Chem. Commun.*, 2020, **56**, 13217–13220.
- [38] X.-F. Zhang, T.-R. Wang, X.-Q. Cao and S.-L. Shen, *Spectrochim. Acta Part A Mol. Biomol. Spectrosc.*, 2020, **227**, 117761.
- [39] Y. Zhang, S. Wang, X. Wang, Q. Zan, X. Yu, L. Fan and C. Dong, *Anal. Bioanal. Chem.*, 2021, **413**, 3823–3831.
- [40] Q. Xia, S. Feng, J. Hong and G. Feng, *Talanta*, 2021, **228**, 122184.
- [41] D. Kennedy, K. Mnich and A. Samali, *FEBS Open Bio*, 2014, **4**, 813–821.
- [42] A. Bettaieb and D. A. Averill-Bates, *Biochim. Biophys. Acta*, 2015, **1853**, 52–62.
- [43] D. S. Schwarz and M. D. Blower, *Cell. Mol. Life Sci.*, 2016, **73**, 79–94.
- [44] L. Fang, G. Trigiante, R. Crespo-Otero, C. S. Hawes, M. P. Philpott, C. R. Jones and M. Watkinson, *Chem. Sci.*, 2019, **10**, 10881–10887.

- [45] N. Zhang, B. Dong, X. Kong, W. Song and W. Lin, *Anal. Methods*, 2018, **10**, 5702–5706.
- [46] A. R. Katritzky, A. Chermprapai, S. Bravo and R. C. Patel, *Tetrahedron*, 1981, **37**, 3603–3607.
- [47] A. R. Katritzky, F. Al-Omran, R. C. Patel and S. S. Thind, *J. Chem. Soc. Perkin Trans. I*, 1980, 1890–1894.
- [48] M. H. Lee, J. H. Han, J. H. Lee, N. Park, R. Kumar, C. Kang and J. S. Kim, *Angew. Chem. Int. Ed.*, 2013, **52**, 6206–6209.
- [49] J. Yin, M. Peng and W. Lin, *Anal. Chem.*, 2019, **91**, 8415–8421.
- [50] Y.-C. Tsai, K.-K. Lam, Y.-J. Peng, Y.-M. Lee, C.-Y. Yang, Y.-J. Tsai, M.-H. Yen and P.-Y. Cheng, *J. Cell. Mol. Med.*, 2016, **20**, 1889–1897.
- [51] C. Kumsta, J. T. Chang, J. Schmalz and M. Hansen, *Nat. Commun.*, 2017, **8**, 14337.

ABSTRACT

Name of the Student: **Mr. Sandip Chakraborty**
Faculty of Study: Chemical Sciences
AcSIR academic centre/CSIR Lab: CSIR-National
Institute for Interdisciplinary Science
and Technology (CSIR-NIIST)

Registration No.: 10CC17A39001
Year of Submission: 2021

Name of the Supervisor: Prof. A. Ajayaghosh

Title of the thesis: **Pyrylium and Pyridinium Fluorescent Probes for pH Sensing and Imaging in Live Cells**

pH is one among the most critical cellular parameters and its variation in cells gives crucial information about physiological processes and abnormalities. In this context, small-molecular fluorescent probes have provided an unprecedented opportunity to track intracellular pH variations in real-time with high levels of accuracy. Monitoring of pH variations at sub-cellular levels has unveiled a detailed understanding on how the organelle functions under stress induced abnormalities. In the **First Chapter**, we summarize the recent developments in pH probes and their application in understanding the cellular processes, disease diagnosis and tracking, and ideating treatment modalities. We have also discussed the development of pyrylium and pyridinium-based fluorophores and their potential as a prominent core chromophore for sensing and imaging applications.

Apoptosis is an organized process for controlled cell death and has been widely used in cancer therapy. Therefore, understanding various aspects of apoptosis and screening potential apoptotic agents are key steps in ensuring therapeutic efficacy. In the **Second Chapter**, we report a new route for the synthesis of a pentacyclic pyrylium fluorophore **PS-OMe**. An improved synthesis protocol was devised using the mechanistic understanding behind the process. The pH-responsive derivative **PS-OH** showed a 55-fold enhancement in fluorescence response upon varying the pH from pH 7.4 to 4.0, with a concomitant increase in fluorescence quantum yield from 0.03 to 0.11. The water-soluble pH probe was further used to monitor and quantify cellular acidification during apoptosis of A549 cells induced by various apoptotic agents.

In the **Third Chapter**, we have demonstrated the improvement in photophysical properties of the pyrylium probes by converting them to their pyridinium analogs. **PM-C₆** and **PM-C₆-OH**, thus synthesized, showed better emission in aqueous medium, higher Stokes shift and better stability. Presence of two pK_a values allowed high sensitivity and selectivity in a wide range of pH. Unlike **PS-OH**, both **PM-C₆** and **PM-C₆-OH** did not penetrate the nuclear membrane and accumulated predominantly in lysosomes without inducing any alkalizing effect. Owing to its high Stokes shift, **PM-C₆-OH** was used as a single and multiple excitation ratiometric pH probe. Finally, we used this probe to monitor lysosomal pH variations in HeLa cells under induced autophagy, an alternative programmed cell death process and an emerging tool for improved cancer theranostics.

Global warming has resulted in an increase in the average temperature and frequency of heatwaves. As a result, heat shock-related illness and mortality have emerged as a serious health concern. In the **Fourth Chapter**, we report a pyridinium pH probe **PM-ER-OH** for monitoring the effects of heat shock on endoplasmic reticulum. Using the large Stokes shift and distinctly different absorption and emission spectra at pH 4 and 10, we used **PM-ER-OH** as a 'three-in-one' probe, i.e., 'Turn-ON', 'Turn-OFF' and single excitation ratiometric pH probe just by changing the excitation wavelengths. We also showed that heat shock leads to the acidification of the endoplasmic reticulum, and extensive cellular damage can be prevented by activating heat shock proteins in cells through temperature conditioning.

List of Publications from the Thesis Work

1. **S. Chakraborty**, M. M. Joseph, S. Varughese, S. Ghosh, K. K. Maiti, A. Samanta, and A. Ajayaghosh.

“A New Pentacyclic Pyrylium Fluorescent Probe that Responds to pH Imbalance During Apoptosis”

Chem. Sci., **2020**, 11, 12695-12700

2. **S. Chakraborty**, M. M. Joseph, K. K. Maiti, A. Samanta, and A. Ajayaghosh. “Pyridinium Fluorophore for Single Excitation Ratiometric Imaging of Lysosomal pH Imbalance During Autophagy”

(Manuscript Under Preparation)

3. **S. Chakraborty**, A. K. Bindra, S. Munan, A. Samanta, Y. Zhao, and A. Ajayaghosh.

“Pyridinium pH Probe for ‘Three-in-one’ Imaging of Heat Shock in Endoplasmic Reticulum.

(Manuscript Under Preparation)

List of Conference Presentations

1. **S. Chakraborty**, M. M. Joseph, A. Samanta, and A. Ajayaghosh. “Rational Design of Functional Fluorescent Dyes for Formaldehyde (FA) Imaging” 8th East Asia Symposium on Functional Dyes and Advanced Materials (EAS8-2017), CSIR-NIIST, Thiruvananthapuram, India
2. **S. Chakraborty**, M. M. Joseph, A. Samanta, and A. Ajayaghosh. “Synthesis and Utilization of Pyrylium pH Probe for Apoptosis Monitoring” International conference on Chemistry for Human Development, (ICCHD-2020), University of Calcutta, Kolkata, India
3. **S. Chakraborty**, M. M. Joseph, A. Samanta, and A. Ajayaghosh. “A New Pyrylium-based fluorescent probe for monitoring pH imbalance during apoptosis” 14th International Conference on Ecomaterials, 2020, CSIR-NIIST, Thiruvananthapuram, India

Cite this: *Chem. Sci.*, 2020, 11, 12695

All publication charges for this article have been paid for by the Royal Society of Chemistry

Received 8th May 2020
Accepted 14th July 2020

DOI: 10.1039/d0sc02623a

rsc.li/chemical-science

A new pentacyclic pyrylium fluorescent probe that responds to pH imbalance during apoptosis†

Sandip Chakraborty,^{ab} Manu M. Joseph,^a Sunil Varughese,^{ab} Samrat Ghosh,^a Kaustabh K. Maiti,^{ab} Animesh Samanta^{ab*} and Ayyappanpillai Ajayaghosh^{ab*}

Efficient fluorophores with easy synthetic routes and fast responses are of great importance in clinical diagnostics. Herein, we report a new, rigid pentacyclic pyrylium fluorophore, **PS-OMe**, synthesised in a single step by a modified Vilsmeier–Haack reaction. Insights into the reaction mechanism facilitated a new reaction protocol for the efficient synthesis of **PS-OMe** which upon demethylation resulted in a “turn-on” pH sensor, **PS-OH**. This new fluorescent probe has been successfully used to monitor intracellular acidification at physiological pH. From the fluorescence image analysis, we were able to quantify the intracellular dynamic pH change during apoptosis. This new pH probe is a potential chemical tool for screening, drug discovery and dose determination in cancer therapy.

Introduction

Molecular probes that serve as an effective tool for imaging biological tissues and cells play an important role in disease diagnostics and treatment modalities.^{1,2} Over a period of time, a large number of fluorescent probes have been developed for various analyte sensing and imaging applications. However, most of these probes are essentially derived from ‘core scaffolds’ such as squaraine, rhodamine, coumarin, BODIPY *etc.* In this context, developing a new core scaffold with easy synthesis, high yield, and good photophysical properties, stability and biocompatibility is of paramount importance. This may set up a platform for developing new probes with novel sets of advantages for sensing and imaging of cells and tissues for disease diagnosis and therapy.³

Imaging of pH variations in cells is important for proper diagnosis of several types of cancers. The imbalance of pH in cancerous cells during apoptosis caused by chemotherapy needs to be monitored in real time for post treatment wellness of patients.⁴ The extent of pH decrease provides insights into the effectiveness of therapeutic agents, pathways, doses and time needed for apoptosis.⁵ Owing to the significant roles of pH

in many physiological processes within intracellular organelles, enormous efforts have been made for the development of new pH imaging chemical probes with improved optical properties.^{6,7} The imbalance of functional pH within cellular micro-environments is also associated with dysfunctions of enzymes and cellular events. For example, variations of the cytosolic pH are closely associated with cell migration, cellular proliferation and apoptosis. It is evident that extracellular acidic pH is highly favourable for regular growth of cancer cells and metastasis of tumours.⁸ Thus, accurate measurement of pH imbalance in cells is of paramount importance in clinical analysis and disease diagnostics.

Considering its advantages in terms of high sensitivity, simplicity, real-time monitoring, applicability to microenvironments and non-invasive detection with high spatiotemporal resolution, fluorescent imaging is now in the forefront as a diagnostic tool.^{9,10} Fluorescent probes based on organic small molecules are particularly preferred owing to their biocompatibility, solubility and ease of synthetic modifications.¹¹

‘Turn-on’ pH probes have gained attention as they can easily discriminate between “on-off” states during the imbalance of pH. Several “off-on” probes are reported in the literature; however, majority of them have limited use due to difficult synthetic access,¹² poor solubility and partial or strong background fluorescence at physiological pH. Therefore, new fluorescent probes which are easily accessible and highly stable with bright fluorescence are necessary for the advancement of biological imaging and diagnostic applications. Pyrylium derivatives are known as highly fluorescent chromophores, used for a wide range of applications.^{13–15} Herein, we report a modified Vilsmeier–Haack reaction for the synthesis of a pentacyclic pyrylium fluorophore **PS-OMe** which is a precursor of a turn-on fluorescent probe **PS-OH**. A mechanistic

^aChemical Sciences and Technology Division, CSIR-National Institute for Interdisciplinary Science and Technology (CSIR-NIIST), Thiruvananthapuram 695 019, India. E-mail: ajayaghosh@niist.res.in

^bAcademy of Scientific and Innovative Research (AcSIR), CSIR – Human Resource Development Centre, Ghaziabad 201002, India

^cDepartment of Chemistry, Shiv Nadar University, NH91, Dadri, Gautam Buddha Nagar, 201314, India. E-mail: animesh.samanta@snu.edu.in

† Electronic supplementary information (ESI) available: Experimental details, synthesis procedures and characterization data of the compounds, and additional figures. CCDC 1985212. For ESI and crystallographic data in CIF or other electronic format see DOI: 10.1039/d0sc02623a

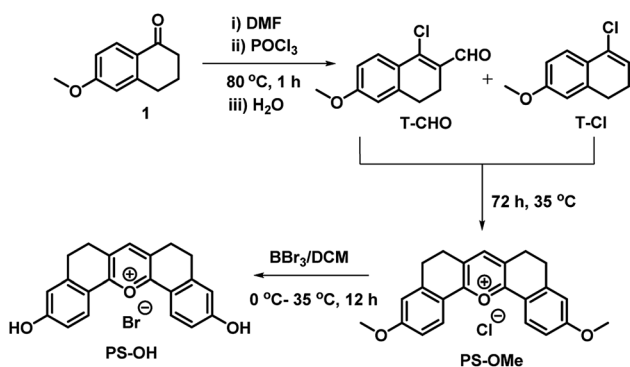


understanding of the synthesis of **PS-OMe** resulted in an alternate efficient route for its synthesis and subsequent demethylation to **PS-OH**. We further describe the use of the new probe for the real time monitoring of pH imbalance during chemotherapy or apoptosis by the fluorescence 'on-off' technique.

Results and discussion

Design and synthesis of the pyrylium fluorophore

The main points considered for the design of the new probe were (i) a simple synthetic strategy to produce an efficient fluorescent probe for pH detection, (ii) to monitor intracellular pH (pH_i) imbalance during apoptotic cellular dysfunction by fluorescence variation and (iii) the real time monitoring of dynamic pH change during the treatment of cells with apoptotic reagents or anticancer drugs. We hypothesized that this approach may provide a unique opportunity to develop an effective sensor to monitor pH imbalance during apoptosis. To achieve these objectives, we have designed a new synthetic protocol for the preparation of the fluorescent pyrylium derivative **PS-OH**, using the modified Vilsmeier–Haack reaction. As illustrated in Scheme 1, we started with 6-methoxy tetralone which is a key intermediate for many heterocyclic syntheses with diverse pharmacological properties. The Vilsmeier–Haack formylation reaction of 6-methoxy tetralone (**1**) at 80 °C produces a reactive 1-chloro-6-methoxy-3,4-dihydronaphthalene-2-carbaldehyde (**T-CHO**) when dimethyl formamide (DMF) and phosphorus oxychloride (POCl_3) were premixed to obtain the Vilsmeier–Haack iminium salts (*N*-(chloromethylene)-*N*-methylmethanaminium). In contrast, dropwise addition of POCl_3 to 6-methoxytetralone in DMF at 80 °C led to an additional product of 4-chloro-1,2-dihydro-7-methoxy-naphthalene (**T-Cl**) along with **T-CHO**. It is noted that if Vilsmeier–Haack iminium salts are not prepared through a premixed protocol, the formylation reaction is suppressed. In contrast, here a part of 6-methoxy tetralone reacts directly with POCl_3 to render a reactive intermediate (**T-Cl**) along with the expected **T-CHO** regardless of the reaction temperature. However, a high temperature (80 °C) leads to better yield (~35%) of **T-Cl** compare to the previous reports^{16,17} (Scheme 1).



Scheme 1 The modified Vilsmeier–Haack synthesis of the symmetrical pyrylium dye, **PS-OMe**, leading to the fluorescent probe **PS-OH** by demethylation using BBr_3 .

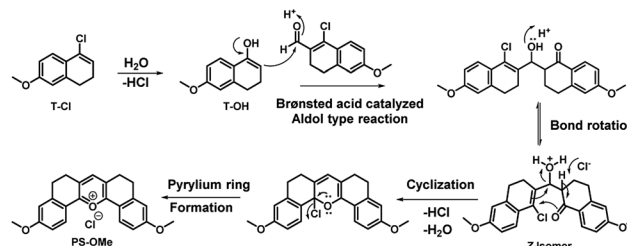
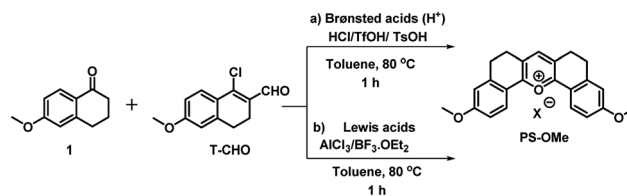


Fig. 1 Possible mechanism of formation of **PS-OMe**.

Interestingly, when the concentrated ethyl acetate extract of the reaction mixture was kept in the ambient atmosphere, a bright yellow fluorescence emitting fluorophore was formed. This serendipitous observation revealed that, the vinyl chloride of **T-Cl** was hydrolysed in contact with moisture to form an unstable enol, **T-OH** (Fig. 1) which undergoes cyclocondensation with **T-CHO** to provide a pentacyclic symmetrical pyrylium fluorophore named **PS-OMe**. To confirm the reaction pathway, firstly, the isolated compounds (**T-CHO**, **T-Cl**) were mixed and kept under inert conditions; however, we could not observe the formation of the pyrylium fluorophore even after one week. The proposed mechanism of **PS-OMe** formation is in good agreement with previous reports which suggest that the vinyl chloro functional group is the one which is labile towards nucleophiles.^{18,19} **PS-OMe** was isolated by column chromatography over silica gel using 6% methanol in chloroform as the eluent in 28% yield. To confirm the reaction pathway in the second step of the mechanism, we chose a few catalysts including Brønsted and Lewis acids since the proposed mechanism (Fig. 1) involved aldol type condensation. Hence, we performed acid catalysed condensation of isolated **T-CHO** and 6-methoxy tetralone in the presence of Brønsted and Lewis acids (Scheme 2). AlCl_3 was found to be the best acid catalyst (~70%) followed by triflic acid (~61%) among other catalysts. The results are summarized in Table 1.

PS-OMe is composed of a donor–acceptor–donor (D–A–D) system where the highly electron deficient pyrylium ring acts as a good acceptor and the corresponding two anisole rings connected to the 2 and 6 positions of the pyrylium ring act as strong donors. Furthermore, the six membered bridges play a crucial role in improving rigidity of the structure to enhance the fluorescence quantum efficiency. The fluorescent probe **PS-OH** was obtained by the demethylation of **PS-OMe** by treating with boron tribromide (Scheme 1). All new products



Scheme 2 A new alternate synthesis of the pentacyclic symmetrical pyrylium dye, **PS-OMe**, using (a) Brønsted acid (H^+) and (b) Lewis acid catalysts.



Table 1 Synthesis of PS-OMe with different Brønsted and Lewis acid catalysts^a

Entry	Catalyst/equiv.	Time/h	Temp./°C	Yield ^b /%
1	HCl (1)	12	80	15
2	TFA (1)	12	80	n.d.
3	TFOH (0.3)	1	80	61
4	PSOH (0.3)	1	80	29
5	BF ₃ ·OEt ₂ (0.1)	1	80	51
6	AlCl ₃ (0.1)	1	80	70

^a Conditions: reaction of 6-methoxy tetralone (1.0 mmol) and T-CHO (1.0 mmol) using different catalysts in toluene at 80 °C. ^b Isolated yield.

obtained were characterized by various spectroscopic techniques such as ¹H NMR, ¹³C NMR, and HRMS analyses. PS-OMe was further crystallized in DMF with the addition of a few drops of perchloric acid. The structure of PS-OMe was unambiguously confirmed from single crystal X-ray analysis as C₂₁H₁₇ClO₇ (Fig. S1†).

Photophysical properties

The absorption and emission spectra of PS-OMe and PS-OH in organic and aqueous solutions are shown in Fig. S2 and S3.† The absorption maximum (λ_{max}) at 505 nm of PS-OMe is shifted to (λ_{max}) 490 nm for PS-OH in chloroform which is attributed to a weak intramolecular charge transfer (ICT) from the donor to the acceptor pyrylium ring. The photophysical properties including maximum absorbance (λ_{max}), emission (λ_{max}), Stokes shift, absolute quantum yield (Φ_{f}) and molar extinction coefficient (ϵ) are summarized in Table S1.† Both PS-OMe and PS-OH have higher Stokes shift when compared to fluorescein and rhodamine B, which can be an added advantage for imaging applications as it can help in setting filter and reduce autofluorescence (Table S2†). The solubility of PS-OMe and PS-OH in PBS buffer (pH 4) was found to be excellent as it shows a linear increase in absorbance till 55 μM and 80 μM for PS-OMe and PS-OH respectively (Fig. S4 and S5†). Subsequently, the absorption and emission spectra were measured with varying pH values in the buffer solution. At first, we checked the pH response of the control molecule, PS-OMe. At pH 4, the molecule exhibited a λ_{max} at 490 nm with a high molar absorptivity ($\epsilon = 1.17 \times 10^4 \text{ L mol}^{-1} \text{ cm}^{-1}$) and exhibited an emission maximum at 560 nm with a 2551 cm^{-1} Stokes shift. With an increase in pH up to 8, there was no shift in either the absorbance or the emission maximum (Fig. S6†).

The maximum absorbance of PS-OH at 460 nm was gradually decreased with increasing pH and a new maximum at 570 nm appeared, indicating the deprotonation of the phenolic -OH (Fig. S7†). In the acidic pH, PS-OH exhibited an intense yellow fluorescence at 560 nm with a large Stokes shift (3882 cm^{-1}) in the acidic region and became almost non-fluorescent at normal physiological pH (pH 7.4). The gradual decrease of the fluorescence intensity with increasing pH from 4 to 7.4 indicates the potential of PS-OH for monitoring apoptosis. Above pH 8, a new peak with a maximum at 640 nm appears which is very weak when compared to the 560 nm emission (Fig. 2a).

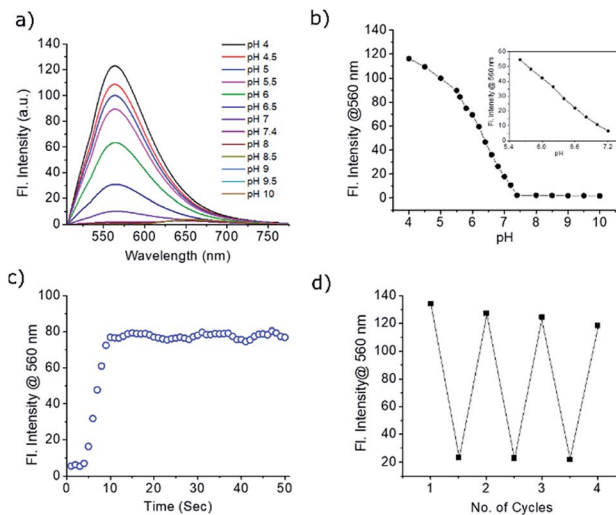


Fig. 2 (a) Fluorescence response of the probe PS-OH (20 μM) in PBS buffer at different pH ranging from 4 to 10. (b) Changes in the fluorescence maximum at 560 nm at different pH. Inset: linear variation of fluorescence intensity with pH between 5.6 and 7.2. (c) Response time of PS-OH upon addition of TFA (20 μL). (d) Reversibility in the fluorescence switching of the probe PS-OH between pH 4 and 7.4.

For a better insight on the “turn on” emission of PS-OH, the frontier orbital energy calculation was performed. The ground and excited state properties of PS-OH and the mono deprotonated PS-OH have been studied by using time-dependent density functional theory (TD-DFT) at the B3LYP/6-31G level using the Gaussian 16 program and compared with experimental absorption and emission spectra. The calculated absorption and emission spectra of PS-OH were well correlated with the experimental results (Fig S8†). However, after deprotonation, structural optimizations and subsequent frequency calculations revealed that a mixed state electronic transition from the unsymmetrical highest occupied molecular orbital (HOMO) to the symmetrical lowest unoccupied molecular orbital (LUMO) and LUMO+1 also correlates with the absorption bands. Due to a mixed excited state, there are at least two emissions with very minimum oscillator strength (f) indicating the non-emissive nature of PS-OH under neutral to basic conditions.

pH monitoring and imaging

The pK_{a} of PS-OH, calculated from the fluorescence titration curve using nonlinear regression by fitting the Boltzmann function was found to be 6.2 ± 0.03 (Fig. 2b). The emission intensity showed good linearity ($R^2 = 0.9962$) from pH 7.2 to 5.6 with a 48-fold enhancement, as shown in Fig. 2b (inset). Interestingly, the decrease of pH by 0.4 unit from normal cellular pH 7.4, enhanced the fluorescence intensity by 5.5-fold. Thus, even a minute fluctuation of the pH of a normal cell can be monitored with PS-OH.

For monitoring the dynamic pH change, a molecule should respond quickly towards pH variation, have good reversibility and photostability. The response of PS-OH was very fast towards



H^+ , as it reaches a maximum fluorescence intensity within 9 s from pH 7.4 upon addition of trifluoroacetic acid (20 μ L) (Fig. 2c). The retention of fluorescence intensity after four cycles between pH 4 and 7.4 (Fig. 2d) indicates that **PS-OH** is a good candidate for monitoring dynamic pH changes in the cellular system. The absolute quantum yields in the PBS buffer of pH 4 and 7.4 were found to be 0.11 and 0.03 respectively. In addition, photostability of **PS-OMe** and **PS-OH** was compared with rhodamine B and fluorescein by irradiation with a 200 W mercury lamp using a 455 nm long pass filter for 60 min. **PS-OMe** and **PS-OH** showed stability similar to rhodamine B and better than fluorescein (Fig. S9[†]).

The selectivity of the **PS-OH** towards different biologically relevant analytes including metal ions (Na^+ , K^+ , Ca^{2+} , Al^{3+} , Mg^{2+} , Zn^{2+} and Fe^{3+}), anions (AcO^- , OH^- , and OCl^-), reactive oxygen species (H_2O_2 and O_2^-), biothiols (Cys and GSH) and H_2S at pH 4 and 7.4 was tested. None of the analytes interfered with the fluorescence property of **PS-OH** (Fig. S10 and S11[†]). The observation indicates the potential for further exploring the response of **PS-OH** as a pH probe in live cells. The cytotoxicity of the probe using the human lung adenocarcinoma cancer cell line A549 was checked by incubating with **PS-OH** up to 10 mM concentration for 48 h. More than 90% cells were unaffected indicating the excellent biocompatibility of the probe (Fig. S12[†]). Also, the photobleaching of **PS-OMe** in the cell was compared with Mitotracker green and Lysotracker red. From the fluorescence intensity data, we could clearly see a comparable stability with Mitotracker green but less stability when compared to Lysotracker red (Fig. S13[†]).

Owing to the high turn-on sensitivity at acidic pH and good biocompatibility, the probe was used to investigate the intracellular pH response in the A549 cell line. At pH 7.4, there was almost no fluorescence observed with a green emission filter at 20 μ M **PS-OH**. Nigericin was used to maintain the pH equilibrium between cells and the medium. With a decrease in pH to 7, a detectable fluorescence signal was observed (Fig. 3a). On further decrease of the pH, the intensity of fluorescence increased gradually (Fig. 3b). The fluorescence intensity obtained from the cells was plotted against pH which shows a good co-linearity with the photophysical data.

The quantitative data of the fluorescence response towards pH imbalance in live cells indicates the efficacy of the probe in cell imaging. Thus, **PS-OH** can be used to quantitatively determine the pH of the cell depending on its fluorescence response (Fig. 3c).

Various anticancer drugs and apoptotic agents target cells in different signalling pathways, varying the pH in each case. For example, it is reported that lipopolysaccharide (LPS) decreases intracellular pH (pH_i) to around 6,²⁰ and cisplatin induces only a slight decrease in pH_i of the cytoplasm,²¹ whereas Mdivi-1 causes apoptosis *via* mitochondrial hyperfusion which does not acidify the cell cytoplasm.²² We tried to evaluate pH imbalance by using the new probe during the treatment of these anticancer drugs or apoptotic agents. Cells were first incubated with **PS-OH** ($c = 20 \mu$ M) for 10 minutes, followed by the treatment of Mdivi-1 (100 μ M) LPS (1 μ g mL^{-1}), and cisplatin (10 μ M) separately for 12 h. The fluorescence images of cells were

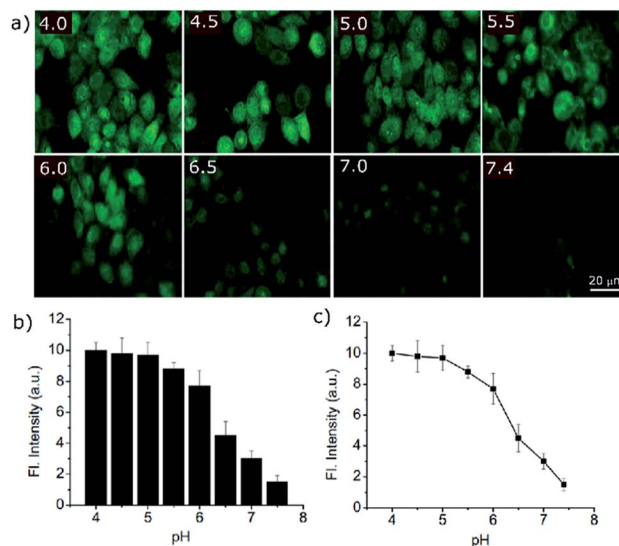


Fig. 3 (a) Fluorescence imaging of A549 cells after 10 min incubation with **PS-OH** (20 μ M) in buffer solutions of different pH, in the presence of 10 μ M nigericin. (b) A plot showing intensity of fluorescence obtained from the intracellular imaging at different pH. (c) Intracellular pH calibration curve of **PS-OH** obtained from the normalized intensity of fluorescence obtained from the cells at different pH.

analysed and it was found that in the case of Mdivi-1, there was no detectable change in fluorescence intensity (Fig. 4a–c). However, in the case of cisplatin, there was a slight change owing to minute acidification of the cells ($pH \sim 6.49$) compared to that of the control ($pH \sim 7$) (Fig. 4g–i), and for LPS treatment, the fluorescence intensity was significantly increased and the

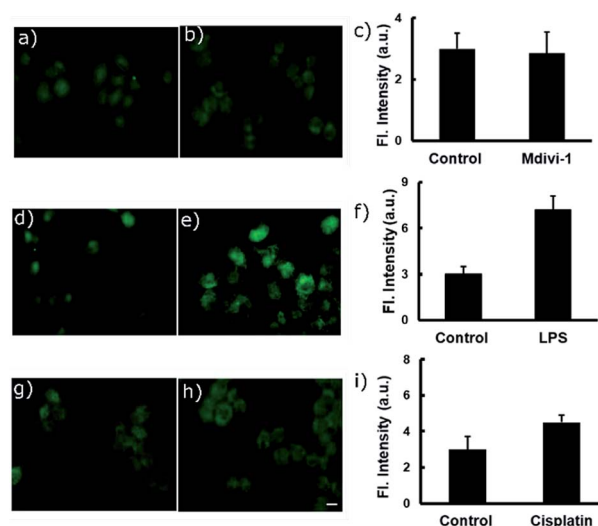


Fig. 4 Fluorescence imaging of A549 cells after treatment with different anti-cancer drugs and apoptotic agents. In each case, two sets of A549 cells were taken and incubated with 20 μ M of **PS-OH** for 20 min. Then, one set of cells was kept as the control (a, d, g) and other sets were treated with (b) Mdivi-1, (e) LPS and (h) cisplatin respectively, for 12 h. The final fluorescence intensities of the control and treated cells were calculated (c, f, i) and compared with the calibration curve in Fig. 3c. Scale 20 μ m.



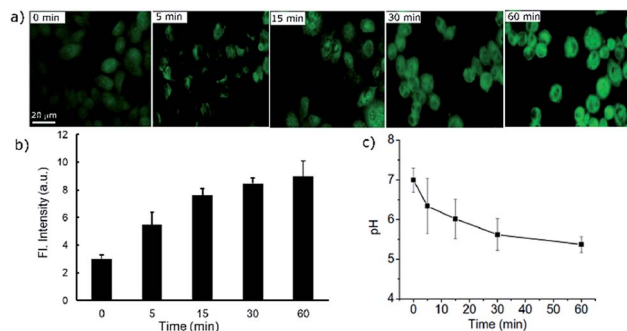


Fig. 5 (a) Real time fluorescence imaging of A549 cells stained with the probe PS-OH (20 μ M) up to 60 minutes after treatment with 500 μ M H_2O_2 . (b) A plot of the fluorescence intensity with time during apoptosis. (c) Quantification of the corresponding dynamic changes in pH at different time points in comparison with the calibration curve in Fig. 3c.

final pH was found to be ~ 6.07 (Fig. 4d–f). These results show a very good agreement with the previous reports,^{20–22} underlining the sensitivity and applicability of the new probe for the pH monitoring of cellular environments after chemotherapy.

Dynamic pH change monitoring with a molecular probe is undoubtedly an important aspect of cancer treatment modality. Thus, we investigated how the new probe can monitor the dynamic pH change in cells during apoptotic treatment. For this purpose, H_2O_2 was chosen as a reactive oxygen species which causes rapid cell death.^{23,24} In the selectivity test, we have found that H_2O_2 does not affect the fluorescence response directly. Therefore, initially the cells were treated with the probe PS-OH for 10 min and then 500 μ M of H_2O_2 was added to the medium. At 0, 5, 15, 30 and 60 min, fluorescence images were taken (Fig. 5a). An obvious increase in fluorescence was found within 5 min. With increase in time, the intensity further increased which is attributed to the continuous pH_i value decrease of the cells (Fig. 5b). This result proves the capability of the probe in monitoring the dynamic cellular pH change. From the previously calibrated graph, we could quantify the pH change at each time point (Fig. 5c).

Conclusions

In conclusion, we have established a new synthetic protocol to prepare a “core scaffold” of a pentacyclic pyrylium dye PS-OMe. A mechanistic understanding of the reaction pathways helped to establish an alternate efficient synthetic protocol of PS-OMe with nearly 70% yield. The pyrylium fluorescent probe PS-OH exhibited an ‘on-off’ response against the pH variation in cells during apoptosis. The strong acceptor at the centre ring of pyrylium, connected through two hydroxyl groups is the key to the bright fluorescent dye with excellent photophysical properties, including photostability, high molar absorptivity and large Stokes shifts. PS-OH exhibited an exceptional ‘turn-on’ pH response in the window of biological relevance both in solution state and in live cells. The new probe is capable of monitoring even a minute change of physiological pH (7.4) in cells during

the therapeutic process with chemo drugs or apoptotic agents in real time.

Conflicts of interest

There are no conflicts to declare.

Acknowledgements

A. A. is thankful to the DST-SERB, Govt. of India for a J. C. Bose National Fellowship (SB/S2/JCB-11/2014). A. S. is grateful to the DST-SERB, Govt. of India, for a Ramanujan Fellowship (SB/S2/RJN148/2015). AcSIR Ph.D. student S. C. thanks DST-INSPIRE for a research fellowship. M. M. J. thanks the DST-SERB, Govt. of India for the National Post-Doctoral Research Fellowship (PDF/2016/001391). K. K. M. thanks the CSIR-FTT project (MLP0027, No. 33/Healthcare/FTT/2018(MT)). S. G. is thankful to the facility of Super Computer System, Institute for Chemical Research, Kyoto University, Japan.

References

- (a) M. Mahmoudi, H. Hosseinkhani, M. Hosseinkhani, S. Boutry, A. Simchi, W. S. Journey, K. Subramani and S. Laurent, *Chem. Rev.*, 2011, **111**, 253–280; (b) A. V. Naumova, M. Mado, A. Moore, C. E. Murry and J. A. Frank, *Nat. Biotechnol.*, 2014, **32**, 804–U121.
- E. I. Dumbrava and F. Meric-Bernstam, *Cold Spring Harbor Mol. Case Stud.*, 2018, **4**, a001578.
- (a) S. M. Barbon, V. N. Staroverov and J. B. Gilroy, *J. Org. Chem.*, 2015, **80**, 5226–5235; (b) E. Benedetti, L. S. Kocsis and K. M. Brummond, *J. Am. Chem. Soc.*, 2012, **134**, 12418–12421; (c) A. N. Butkevich, M. V. Sednev, H. Shojaei, V. N. Belov and S. W. Hell, *Org. Lett.*, 2018, **20**, 1261–1264; (d) R. Greiner, D. S. Ziegler, D. Cibu, A. C. Jakowetz, F. Auras, T. Bein and P. Knochel, *Org. Lett.*, 2017, **19**, 6384–6387; (e) V. Jamsheena, R. K. Mishra, K. S. Veena, S. Sini, P. Jayamurthy and R. S. Lankalapalli, *ACS Omega*, 2018, **3**, 856–862; (f) E. Kim, M. Koh, B. J. Lim and S. B. Park, *J. Am. Chem. Soc.*, 2011, **133**, 6642–6649; (g) G. Li, M. Zhao, J. Xie, Y. Yao, L. Mou, X. Zhang, X. Guo, W. Sun, Z. Wang, J. Xu, J. Xue, T. Hu, M. Zhang, M. Li and L. Hong, *Chem. Sci.*, 2020, **11**, 3586–3591.
- (a) J. Hou, W. X. Ren, K. Li, J. Seo, A. Sharma, X. Yu and J. S. Kim, *Chem. Soc. Rev.*, 2017, **46**, 2076–2090; (b) L. Lyniv and S. Kireeva, *Int. J. Cancer*, 2002, 146; (c) L. Y. Lin, J. J. Zhao, L. L. Zhang, Y. Huang, F. G. Ye and S. L. Zhao, *Chem. Commun.*, 2018, **54**, 9071–9074.
- (a) P. Wong, C. Lee and I. F. Tannock, *Clin. Cancer Res.*, 2005, **11**, 3553–3557; (b) E. M. Kniep, C. Roehlecke, N. Ozkucur, A. Steinberg, F. Reber, L. Knels and R. H. W. Funk, *Invest. Ophthalmol. Visual Sci.*, 2006, **47**, 1185–1192; (c) T. Yamashiro, N. Watanabe and Y. Kobayashi, *Biochem. Pharmacol.*, 1997, **54**, 143–148; (d) S. Matsuyama, J. Llopis, Q. L. Deveraux, R. Y. Tsien and J. C. Reed, *Nat. Cell Biol.*, 2000, **2**, 318–325; (e) L. M. Yang, Y. Y. Chen, Z. Z. Yu, W. Pan, H. Y. Wang, N. Li and B. Tang, *ACS Appl. Mater.*



- Interfaces*, 2017, **9**, 27512–27521; (f) D. Lagadic-Gossmann, L. Huc and V. Lecureur, *Cell Death Differ.*, 2004, **11**, 953–961.
- 6 (a) J. Jo, C. H. Lee, R. Kopelman and X. D. Wang, *Nat. Commun.*, 2017, **8**, 3983; (b) A. Jiang, G. Chen, J. Xu, Y. Liu, G. Zhao, Z. Liu, T. Chen, Y. Lia and T. D. James, *Chem. Commun.*, 2019, **55**, 11358–11361; (c) M. Tian, C. Liu, B. Dong, Y. Zuo and W. Lin, *Chem. Commun.*, 2019, **55**, 10440–10443; (d) F. Yu, X. Jing and W. Lin, *Anal. Chem.*, 2019, **91**(23), 15213–15219.
- 7 (a) J. R. Casey, S. Grinstein and J. Orlowski, *Nat. Rev. Mol. Cell Biol.*, 2010, **11**, 50–61; (b) M. H. Lee, J. H. Han, J. H. Lee, N. Park, R. Kumar, C. Kang and J. S. Kim, *Angew. Chem., Int. Ed.*, 2013, **52**, 6206–6209; (c) Y. Ning, S. Cheng, J. Wang, Y. Liu, W. Feng, F. Li and J. Zhang, *Chem. Sci.*, 2019, **10**, 4227–4235.
- 8 E. Persi, M. Duran-Frigola, M. Damaghi, W. R. Roush, P. Aloy, J. L. Cleveland, R. J. Gillies and E. Ruppin, *Nat. Commun.*, 2018, **9**, 2997.
- 9 (a) P. Anees, K. V. Sudheesh, P. Jayamurthy, A. R. Chandrika, R. V. Omkumar and A. Ajayaghosh, *Chem. Sci.*, 2016, **7**, 6808–6814; (b) G. Saranya, P. Anees, M. M. Joseph, K. K. Maiti and A. Ajayaghosh, *Chem.–Eur. J.*, 2017, **23**, 7191–7195; (c) D. S. Philips, S. Sreejith, T. He, N. V. Menon, P. Anees, J. Mathew, S. Sajikumar, Y. Kang, M. C. Stuparu, H. Sun, Y. Zhao and A. Ajayaghosh, *Chem.–Asian J.*, 2016, **11**, 1523–1527; (d) P. Anees, J. Joseph, S. Sreejith, N. V. Menon, Y. Kang, S. Wing-Kwong Yu, A. Ajayaghosh and Y. Zhao, *Chem. Sci.*, 2016, **7**, 4110–4116; (e) N. Gupta, S. I. Reja, V. Bhalla, M. Gupta, G. Kaur and M. Kumar, *J. Mater. Chem. B*, 2016, **4**, 1968–1977; (f) S. I. Reja, M. Gupta, N. Gupta, V. Bhalla, P. Ohri, G. Kaur and M. Kumar, *Chem. Commun.*, 2017, **53**, 3701–3704.
- 10 (a) S. Modi, C. Nizak, S. Surana, S. Halder and Y. Krishnan, *Nat. Nanotechnol.*, 2013, **8**, 459–467; (b) R. Subiros-Funosas, V. C. L. Ho, N. D. Barth, L. M. Tapia, M. Pappalardo, X. Barril, R. Ma, C. B. Zhang, B. Z. Qian, M. Sintes, O. Ghashghaei, R. Lavilla and M. Vendrell, *Chem. Sci.*, 2020, **11**, 1368–1374; (c) S. Benson, A. Fernandez, N. D. Barth, F. Moliner, M. H. Horrocks, C. S. Herrington, J. L. Abad, A. Delgado, L. Kelly, Z. Chang, Y. Feng, M. Nishiura, Y. Hori, K. Kikuchi and M. Vendrell, *Angew. Chem., Int. Ed.*, 2019, **58**, 6911–6915.
- 11 K. Q. Qiu, L. B. Ke, X. P. Zhang, Y. K. Liu, T. W. Rees, L. N. Ji, J. J. Diao and H. Chao, *Chem. Commun.*, 2018, **54**, 2421–2424.
- 12 H. Lee, W. Akers, K. Bhushan, S. Bloch, G. Sudlow, R. Tang and S. Achilefu, *Bioconjugate Chem.*, 2011, **22**, 777–784.
- 13 (a) F. A. Scaramuzzo, A. G. Campo, C.-C. Wu, A. H. Velders, V. Subramaniam, G. Doddi, P. Mencarelli, M. Barteri, P. Jonkheijm and J. Huskens, *Chem. Commun.*, 2010, **46**, 4193–4195; (b) C. T. F. Salfeena, Basavaraja, K. T. Ashitha, V. Praveen Kumar, S. Varughese, C. H. Suresh and B. S. Sasidhar, *Chem. Commun.*, 2018, **54**, 12463–12466; (c) B. S. Sasidhar, C. T. F. Salfeena and A. Ajayaghosh, *Process for the preparation of pyrylium salts*, 2018, PCT/IN2018/050898; (d) N. Manoj, G. Ajayakumar, K. R. Gopidas and C. H. Suresh, *J. Phys. Chem. A*, 2006, **110**, 11338–11345; (e) J. R. Wilt, G. A. Reynolds and J. A. Van Allain, *Tetrahedron*, 1973, **29**, 795–803; (f) D. Basavaraja, D. Dey, T. L. Varsha, C. T. F. Salfeena, M. K. Panda and B. S. Sasidhar, *ACS Appl. Bio Mater.*, 2020, **3**(2), 772–778.
- 14 (a) D. Asanuma, Y. Takaoka, S. Namiki, K. Takikawa, M. Kamiya, T. Nagano, Y. Urano and K. Hirose, *Angew. Chem., Int. Ed.*, 2014, **53**, 6085–6089; (b) M. H. Lee, N. Park, C. Yi, J. H. Han, J. H. Hong, K. P. Kim, D. H. Kang, J. L. Sessler, C. Kang and J. S. Kim, *J. Am. Chem. Soc.*, 2014, **136**, 14136–14142.
- 15 B. Lin, L. Fan, J. Y. Ge, W. J. Zhang, C. H. Zhang, C. Dong and S. M. Shuang, *Analyst*, 2018, **143**, 5054–5060.
- 16 A. Baji, A. Gyovai, J. Wolfoling, R. Minorics, I. Ocsovszki, I. Zupko and E. Frank, *RSC Adv.*, 2016, **6**, 27501–27516.
- 17 A. Lilienkampf, M. P. Johansson and K. Wahala, *Org. Lett.*, 2003, **5**, 3387–3390.
- 18 G. Yin, T. Niu, Y. Gan, T. Yu, P. Yin, H. Chen, Y. Zhang, H. Li and S. Yao, *Angew. Chem., Int. Ed.*, 2018, **57**, 4991–4994.
- 19 H. Chen, Y. Tang, M. Rena and W. Lin, *Chem. Sci.*, 2016, **7**, 1896–1903.
- 20 Y. Y. Zhang, S. L. Li and Z. W. Zhao, *Anal. Chem.*, 2016, **88**, 12380–12385.
- 21 M. V. Shirmanova, I. N. Druzhkova, M. M. Lukina, V. V. Dudenkova, N. I. Ignatova, L. B. Snopova, V. I. Shcheslavskiy, V. V. Belousov and E. V. Zagaynova, *Sci. Rep.*, 2017, **7**, 8911.
- 22 W. Zhang, X. Wang, P. Li, H. B. Xiao, W. Zhang, H. Wang and B. Tang, *Anal. Chem.*, 2017, **89**, 6840–6845.
- 23 M. H. Lee, J. H. Han, J. H. Lee, N. Park, R. Kumar, C. Kang and J. S. Kim, *Angew. Chem., Int. Ed.*, 2013, **52**, 6206–6209.
- 24 L. Y. Lin, J. J. Zhao, L. L. Zhang, Y. Huang, F. G. Ye and S. L. Zhao, *Chem. Commun.*, 2018, **54**, 9071–9074.

